Low Damage Etching and Deposition of Electronic Materials with a Novel RF Plasma Source

Judith Beckman

Thesis submitted for the degree of PhD

University College London

ProQuest Number: 10045682

All rights reserved

INFORMATION TO ALL USERS
The quality of this reproduction is dependent upon the quality of the copy submitted.

In the unlikely event that the author did not send a complete manuscript
and there are missing pages, these will be noted. Also, if material had to be removed,
a note will indicate the deletion.

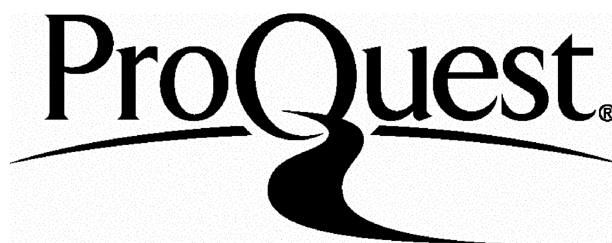

ProQuest 10045682

Published by ProQuest LLC(2016). Copyright of the Dissertation is held by the Author.

All rights reserved.
This work is protected against unauthorized copying under Title 17, United States Code.
Microform Edition © ProQuest LLC.

ProQuest LLC
789 East Eisenhower Parkway
P.O. Box 1346
Ann Arbor, MI 48106-1346

This thesis is dedicated to my children, Eleanor and Adam, for their unfailing moral support throughout the more than three years it has taken.

Acknowledgments

Many thanks to my supervisor, Dr. Richard B. Jackman, for continual consultation, advice and guidance in the pursuance of these studies. I would like to thank Dr. Peter Revell, for providing me with the prototype novel source used for this study, and Mr. Harj Jolly, for advice on its operation. I would like to thank Dr. Paul Chalker of AEA Technology, Harwell for all the Raman spectra he took of my samples, and his interest and advice, and Dr. Don Rodway of DRA, Malvern, for allowing me to use his Raman Spectrometer to take my own spectra of the rest of my samples. Thanks are also due to Duncan Marshall for taking the colour photographs of the source, and for cheerfully providing an extra pair of hands when necessary. I must also acknowledge gratitude to Willow for making sure that I got up early each morning.

Abstract

Plasmas and ion beams produced from plasma are widely used in the processing, etching and deposition, of semiconductor materials. In spite of this, there are many problems with their use with the more delicate, modern materials, such as the III-Vs, which are damaged by the high energy ions created in the plasma.

A novel configuration of a capacitively coupled radio-frequency source was designed and constructed, to overcome these problems. Such a novel source was characterised, and was shown to produce a beam of ions of sufficiently low energy as to avoid causing damage.

The source was used to etch GaAs in both Reactive Ion Beam Etching and Chemically Assisted Ion Beam Etching configurations, and Schottky diodes were manufactured on the etched surfaces. Analysis of the characteristics of the diodes showed that a damage free etch had been achieved.

The growth of diamond films by Plasma Assisted Chemical Vapour Deposition requires a high plasma density with a low ion energy. To achieve this, commonly microwave plasmas are employed, but there are drawbacks to the use of microwaves, chiefly with regard to "scale-up", and also safety. A development of the novel source used in the early part of this study, led to many of the required plasma characteristics but without the drawbacks.

The source was used to grow diamond films, the first successful diamond growth with a capacitive rf source, which were characterised by SEM analysis and Raman spectroscopy.

TABLE OF CONTENTS

Chapter 1: Introduction 10

Chapter 2: Plasma and Ion Beam Sources 14

2.1 Production of Plasmas.. 14

2.1.1 Historical Background 14

2.1.2 Theoretical Considerations................................ 14

2.1.2.1 Temperature Considerations 14

2.1.2.2 Sheath Formation 15

2.1.2.3 Potentials in a Plasma 16

2.1.2.4 Probe Characteristics 20

2.1.2.5 With Magnetic Field................................ 23

2.1.2.6 R.F. Plasmas... 26

2.1.3 Present-day Plasma Sources 29

2.1.3.1 DC Plasma Sources 29

2.1.3.2 Microwaves 29

2.1.3.3 Capacitively Coupled Radio-frequency 30

2.1.3.4 Inductively Coupled Radio-frequency.......... 31

2.2 Ion Beam Sources 33

2.2.1 Arc Discharge Ion Beam Sources in a Magnetic Field 34

2.2.1.1 Homogeneous Field................................ 34

2.2.1.2 Inhomogeneous Field............................. 34

2.2.1.3 The Anti-cathode................................... 35

2.2.1.4 The Cold Cathode.................................. 35

2.2.2 Broad Beam Sources.. 36

2.2.3 Theory of Beam Extraction................................ 37

2.2.3.1 With Two Grids.................................... 38

2.2.3.2 Three Grids 39

2.2.3.3 One Grid 39

2.2.3.4 Focusing 40

2.2.4 High Frequency Ion Sources.............................. 40

2.2.4.1 Inductively Coupled RF Sources................ 40

2.2.4.2 Capacitively Coupled RF Sources................ 42

2.2.4.3 ECR (Electron Cyclotron Resonance).......... 43

Chapter 3: Etching and Deposition of Electronic Materials: Plasma and Ion Beam Source Requirements 46
3.1 Ion- Surface Interactions 47
3.2 Etching 49
3.2.1 Wet-etching 51
3.2.1.1 Factors Affecting Etch Rates 52
3.2.1.2 Chemical Polishing 54
3.2.1.3 Choice of Etching Solution 54
3.2.1.4 Residual Oxide Layers 55
3.2.2 Dry etching 56
3.2.2.1 Reactive Ion Etching 57
3.2.2.2 Ion Beam Etching 58
3.2.2.3 Reactive Ion Beam Etching 60
3.2.2.4 Chemically Assisted Ion Beam Etching 62
3.3 Thin Film Growth: comparison of methods 64
3.3.1 Molecular Beam Epitaxy 66
3.3.2 Chemical Vapour Deposition 67
3.3.2.1 Plasma Enhanced Chemical Vapour Deposition 69
3.3.2.2 Vapour-Phase Epitaxy 70
3.3.2.3 Metalorganic Chemical Vapour Deposition .. 71
3.3.3 Metalorganic Molecular Beam Epitaxy and/or Chemical Beam Epitaxy 72
3.4 Ideal Source Requirements 73
3.4.1 For Etching III-V Materials 73
3.4.2 For Plasma Enhanced CVD 73

Chapter 4: Novel Source Design, Construction and Characterisation 78
4.1 Requirements and Problems 78
4.2 Theoretical solution 79
4.3 Implementation 80
4.4 Characterisation of the source 83
4.4.1 Characterisation of the Plasma 83
4.4.1.1 Electron Temperature 83
4.4.1.2 Plasma Density 86
4.4.1.3 Plasma Potential 88

4.4.2 Characterisation of the Beam............................ 90

Chapter 5: Etching of GaAs with Novel RF Source................. 94
5.1 Reactive Ion Beam Etching...................................... 94
5.1.1 Experimental Procedure.................................. 94
5.1.2 RIBE Etching Results.. 96
5.1.2.1 The Contamination Layer......................... 96
5.1.2.2 Talystep Measurements........................... 98
5.1.2.3 Scanning Electron Microcopy.................... 100
5.2 Chemically Assisted Ion Beam Etching...................... 102
5.2.1 Experimental Procedure.................................. 102
5.2.2 CAIBE Etching Results..................................... 104
5.2.2.1 The Contamination................................ 104
5.2.2.2 Talystep Measurements........................... 104
5.3 Combining Results... 106
5.3.1 Calculation of Chlorine Flux............................. 106
5.3.1.1 Chlorine Flux for RIBE........................... 106
5.3.1.2 Chlorine Flux for CAIBE......................... 107
5.3.2 Combined Data... 108
5.4 The Liner.. 109
5.5 Evaluation of the Novel Source as an Etcher 110

Chapter 6: Device Characterisation of Etched Surface........... 113
6.1 Theory of Schottky Contacts 113
6.1.1 Barrier Height... 113
6.1.1.1 The Ideal Case..................................... 113
6.1.1.2 With a Large Density of Surface States......... 115
6.1.2 Current Transport Processes............................ 116
6.1.2.1 Thermionic Emission Theory.................... 116
6.1.3 Measurement of Barrier Height and Ideality Factor.... 118
6.2 Fabrication of Schottky Diode................................ 119
6.2.1 Preparation of Samples................................... 119
6.2.1.1 Etching... 119
6.2.1.2 Cleaning 119
6.2.2 Deposition of Metal Contacts............................ 120
6.2.2.1 Ohmic Contacts 120
6.2.2.2 Schottky Contacts 120

6.3 Evaluation of Schottky Diodes 121
6.3.1 I-V Characteristics 121
6.3.2 Analysis 122
6.3.2.1 Ideality Factors 122
6.3.2.2 Barrier Heights 123
6.3.3 Summary of Characteristics 124
6.4 Evaluation of Surface Characterisation 124
Chapter 7: Thin Film Diamond 127
7.1 Importance of Diamond 127
7.2 CVD of Diamond 127
7.2.1 Hot Filament Assisted CVD of Diamond 129
7.2.2 Plasma-Assisted CVD of Diamond 130
7.2.2.1 Microwave Plasma-Assisted CVD of Diamond 130
7.2.2.2 Radio-Frequency Plasma-Assisted CVD of Diamond 130
7.2.2.3 Comparison of Characteristics of Plasma Sources 131
7.2.3 Quality of CVD Diamond 132
7.2.4 Surface Preparation 133
7.2.4.1 Bias-enhanced Nucleation 133
7.3 Characterisation of Carbons by Raman Spectroscopy 135
7.4 Diamond-like Carbon (DLC) Film 136
7.4.1 Applications of DLC Films 136
7.4.2 Growth of DLC by RF Plasma-Assisted Chemical Vapour Deposition 137

Chapter 8: Carbon Deposition with Modified Source 142
8.1 Modification of the Source 142
8.1.1 Preliminary tests 143
8.1.2 Preparation of the Liner 144
8.2 First Carbon Deposition 145
8.2.1 Unprepared Silicon 145
8.2.2 Hot Prepared Silicon 145
8.2.2.1 Analysis by Raman Spectroscopy 146
8.2.3 Atomic Hydrogen Addition 156
8.3 Mass Spectroscopic Analysis 156
8.3.1 With Source in Original Configuration 159

8.3.2 With Further Modification of Source 159

Chapter 9: Diamond Deposition 161
9.1 Heating the Sample 161
9.1.1 Direct Heating.. 161
9.1.2 Indirect Heating.. 162
9.1.3 Temperature Measurement 163
9.2 Diamond Depositions: Substrate Preparation Method 1 . 164
9.2.1 Sample Preparation.. 164
9.2.2 Experimental Procedures.................................. 165
9.2.3 Scanning Electron Microscopy............................ 166
9.2.4 Raman Spectroscopic Analysis........................... 166
9.2.5 Summary of Results 171
9.3 Diamond Depositions: Substrate Preparation Method 2.. 172
9.3.1 Sample Preparation... 172
9.3.2 Experimental Procedures 173
9.3.3 Growth at 250W RF Input Power 174
9.3.3.1 Scanning Electron Microscopy 174
9.3.3.2 Raman Spectroscopy............................. 175
9.3.4 Film Growth at 300W RF Input Power 180
9.3.4.1 Scanning Electron Microscopy................. 181
9.3.4.2 Raman Spectroscopy............................. 182
9.3.5 Comparison of Growth at different RF Input Powers 188
9.3.5.1 Assessment of Film Quality....................... 189
9.3.6 Nucleation Density 190
9.3.6.1 Variation with Temperature..................... 190
9.3.6.2 Variation with Input Power....................... 191
9.3.7 Growth at 400W RF Input Power........................ 192
9.3.7.1 Comparison of this work to Bias-enhanced Nucleation (BEN).................................... 197

Chapter 10: Concluding Thoughts 201

CHAPTER 1: INTRODUCTION

Plasma and ion beam sources are widely used in many scientific and industrial applications, including for the etching and deposition of materials in semiconductor device fabrication. Thus these are very important tools for the electronic engineer.

An explanation of the theory of the formation and characterisation of a plasma, with and without magnetic confinement, together with some of the practical problems of performing actual characterisations is given in this thesis. A description of the main features of the different types of plasma sources, excited by dc electric fields, microwaves and both inductively and capacitively coupled radio-frequency fields is given, and the differences in the characteristics of the plasmas they generate outlined. These differences are crucial to the success of a given type of source in a particular application.

An account of the historical development of the various designs of ion beam sources, driven by the requirements of the different applications, is rendered, leading to the designs currently in use for semiconductor device fabrication.

A detailed explanation of etching processes is presented. Wet etching processes, still much in use in device fabrication, are included for comparison, the shortcomings of these techniques for state of the art devices being expounded. Dry etching uses both plasma sources and ion beam sources. These include reactive ion etching, by means of plasma etchers, ion beam etching, reactive ion beam etching and chemically assisted ion beam etching. The advantages and disadvantages of each technique are explained, in terms of reproducibility, anisotropy, exact depth of etch, damage to the substrate etc.

A number of deposition processes, including molecular beam epitaxy, metal-organic molecular beam epitaxy and chemical vapour deposition are described, including plasma-assisted chemical vapour deposition. Again, the advantages and disadvantages of these different processes are explained, the possibilities for growing layers of precise thickness, and of extreme purity, or precise doping levels, for example.

Thus the characteristics of the ideal plasma and beam source for both etching and deposition are arrived at, and a possible design of such a source,

together with its implementation, the novel source used in this study, is developed.

The novel source was then carefully characterised, to determine how closely it met the required specifications of plasma density and ion energy, and of beam uniformity and flux. It appeared to meet the specifications very well indeed.

The source was then used to etch GaAs, a delicate III-V semiconductor material, which has very important applications in opto-electronics. Two different etching configurations were employed, reactive ion beam etching, using chlorine as the reactive etchant, and chemically assisted ion beam etching, using argon to provide the ion beam, with chlorine gas as the chemical agent. This was to test both the ability of the source to etch safely a sensitive material, and also to test the robustness of the source with reactive gases.

The results of the etching processes were analysed in several ways. The etch depths were measured, to find the etching rates for both configurations. The etched samples were examined under a scanning electron microscope, to determine the smoothness of the etched surface, and, using a photo-lithographically masked sample, the anisotropy of the etching process. Schottky diodes were fabricated on the etched surface, and these diodes were tested to determine the quality of the etched surface. This is a useful technique, for determining surface and underlying damage. The results of these tests were compared with those from other etching processes, and showed that the novel source performed etching, on this highly susceptible surface, with far less damage than any other dry etching system, in fact virtually damage -free. This was most encouraging. However, there were a couple of draw-backs too, making the source not quite ideal as an etcher. It had a tendency to etch its own lining, and thereby to deposit a contamination layer, (easily removed), on the sample surface. The presence of this contamination layer slowed the etch rate considerably.

The source was then used for plasma assisted chemical vapour deposition. The material to be deposited was carbon, in the form of diamond. The importance of this material, in particular for electronic applications is demonstrated, and the specific conditions for growing thin film diamond, i.e. the need for high concentrations of atomic hydrogen, and the theoretical model of diamond growth which explains this, together with the various methods of achieving it, are described. The problems with finding suitable substrates are also explained, since a lattice match for hetero-epitaxial growth is impossible to

find, and since diamond grows at the elevated temperature of ~900°C, this is further exacerbated by the differences in thermal expansivity. Diamond has a remarkably low thermal expansivity. The plasmas from various kinds of plasma source, including the novel source, were compared, and it was found that the plasma from the novel source matched the requirements for the deposition of thin film diamond.

An unusual method of introducing the carbon component to the mainly hydrogen plasma was tried, utilising the propensity of the source to etch its lining. A graphitised liner was introduced to the source, and then pure hydrogen was used as the gas source, so that the hydrogen plasma could etch the graphite from the lining, producing the hydrocarbon:hydrogen mixture that is needed for plasma-assisted chemical vapour deposition of thin film diamond. However, this highly original idea was unsuccessful. Carbon was indeed deposited as a thin film on the heated silicon substrate, but only in the form of polycrystalline graphite. The reason for the lack of success was investigated, by determining the final gas composition of the plasma, by means of a quadrupole mass spectrometer. It was found that the plasma contained far too high a concentration of hydrocarbon, and some of it of too heavy a type, although the ratio of atomic to molecular hydrogen was very high, a good sign for future developments. The self-etching was too efficient.

A more conventional gas mixture, 1% methane in hydrogen was used, with the novel source thoroughly cleaned free of carbon. This was still unusual in that, of the non-thermal growth techniques, only microwave plasmas have previously been used successfully to grow thin film diamond. Although good quality film is grown this way, the use of microwaves has some serious disadvantages compared with radio-frequency waves. Microwave plasmas are of generally small dimension, and it is difficult and expensive to scale them up to large wafer size. Also, microwaves are quite hazardous, and extensive shielding of the apparatus is required. Radio-frequency fields, on the other hand, easily sustain plasmas of very large volume, and are much less hazardous.

A range of substrate temperatures, and a range of source conditions, i.e. of gas pressure and RF power, were utilised, and several different pretreatments of the silicon substrate were also used. It is necessary to pretreat the silicon substrate surface, because otherwise the serious lattice constant mismatch makes nucleation very difficult.

This was excitingly successful, and both crystallites and continuous film were grown under a number of values of these variable parameters. They were examined under a scanning electron microscope, and also characterised by Raman spectroscopy, which confirmed that diamond of very high quality had been grown. This is the first time that diamond has been grown in this way, using capacitively coupled radio-frequency plasma-assisted chemical vapour deposition. It was also found that under conditions of higher RF power input, the diamond nucleation layer grown mimicked that from bias-enhanced nucleation, a recently discovered method of greatly improving the quality of film produced.

Because of the inherent advantages of radio-frequency fields, the possibility, demonstrated in this study, of using them to grow this exciting new material, thin film diamond, could be very important in the future.

CHAPTER 2: PLASMA AND ION BEAM SOURCES

2.1 Production of Plasmas

2.1.1 Historical Background

A plasma is electrically energised matter in a gaseous state. It consists of electrically neutral gas molecules, charged particles, ie positive (and maybe negative) ions and electrons, and photons. Discharges in gases have been known and studied since the 19th Century. The first discharges were produced by applying a high voltage across a gas, of order several kilovolts, which caused an electric field sufficiently strong to ionise some of the gas molecules.

In 1927 Hertzberg observed that e-m radiation caused ionisation of gases, and by the late 1930s several groups were researching high frequency breakdown of gases at low pressure.

At the same time, the properties of these gaseous discharges were being investigated, using electrical probe techniques [2.1-2.6], the initial theory of which was carefully propounded by Mott-Smith and Langmuir in 1926 [2.7]. Langmuir first coined the term 'plasma' for such discharges.

2.1.2 Theoretical Considerations

2.1.2.1 Temperature considerations

The charged particles in the plasma move in the presence of electric and magnetic fields, apart from their normal thermal movement, thus a plasma is a conducting medium. Because of their much smaller mass, the electrons move very much faster than the ions, thus the ions appear to be

almost stationary to the electrons. So there are similarities between plasmas and solids as conducting media, but also differences. The early theories of metals assumed that the "electron gas" behaved like a real gas, ie that the electrons obeyed Maxwell-Boltzmann statistics. However, we now know that this was wrong, the electrons in a metal obey Fermi-Dirac statistics. But in a plasma the electrons actually *do* obey Maxwell-Boltzmann statistics [2.7] to a very good approximation, with the proviso that the effective temperature of the electrons is very much higher than the temperature of the neutrals and ions, if the average energy is given in terms of k_BT [2.8]. Because the electron mass is so much less than the ions mass, electrons lose virtually none of the energy they gain from the electric field in eleastic collisions with ions or neutrals. Ions however, having a mass equal to that of the neutrals, will efficiently share any energy they gain with neutrals in collisions. Since there are more neutrals than ions (by several orders of magnitude), the net energy gain of the ions is very small, and leads mainly to a relatively small rise in the temperature of the gas above room temperature. The effective temperature of the electrons is therefore very much higher (again by orders of magnitude) than the gas temperature.

2.1.2.2 Sheath Formation

We now consider what happens to an electrically isolated surface in the plasma. Initially both electrons and ions will strike it with charge fluxes, or current densities, which, from classical kinetic theory will be

$$j_e = \frac{qn_ec_e}{4} \quad \text{for electrons, and} \quad j_i = \frac{qn_ic_i}{4} \quad \text{for ions}$$

where c is the mean speed, n is the particle density and q is the charge [2.9]. A plasma is electrically neutral overall, so, at least initially, $n_e = n_i$. However $c_e >> c_i$, so $j_e >> j_i$. Thus, the surface will quickly gain a negative charge, which will build up until enough electrons are repelled to equalise the charge fluxes. At this point, since c_e is still much greater than c_i, n_i must be very much larger than n_e, ie close to the surface, the ion density is very much greater than the electron density. A region of space charge exists close to the surface. This region is known as the *sheath.*

2.1.2.3 Potentials in a Plasma

(i) Debye Shielding

Around any perturbation in a plasma there will be a potential, varying with the distance from the perturbation, which can be denoted $V(r)$. To find the form of $V(r)$, we use Poisson's equation:

$$-\nabla^2\phi = \rho/\varepsilon_0 \tag{1}$$

where ρ is the charge density.

The plasma as a whole is electrically neutral, but around a perturbation there will be a net charge density, ρ_{net}. Then, in spherical co-ordinates, Poisson's equation becomes

$$\frac{1}{r}\frac{d}{dr}\left(r^2\frac{dV(r)}{dr}\right) = \frac{-\rho_{net}}{\varepsilon_0} \tag{2}$$

where $\rho_{net} = \rho^+ - \rho_\varepsilon = qN^+ - qN_e \exp(-qV/k_BT_e)$

Assuming that N^+, the number per unit volume of positive ions equals N_e, the number per unit volume of electrons, and that $-qV/k_BT_e$ is small

$$\rho_{net} = qN_e\left(1-\exp(-qV/k_BT_e)\right) \approx qN_e.qV/k_BT_e = \frac{q^2N_e}{k_BT_e}V \tag{3}$$

Putting this into Poisson's equation

$$\frac{1}{r^2}\frac{d}{dr}\left(r^2\frac{dV(r)}{dr}\right) = -\frac{q^2N_e}{\varepsilon_0 k_BT_e}V(r) \tag{4}$$

A solution of this equation is

$$V(r) = A\,(q/r)\exp(-r/\lambda_D) \tag{5}$$

where

$\lambda_D = (\varepsilon_0 k_B T_e/q^2N_e)^{1/2}$ is the Debye length, and is of order ~0.1mm . (6)

(ii) Plasma Potential

Thus, no perturbation extends very far within the plasma, at most 2 or 3 Debye lengths, and the bulk plasma is therefore virtually field-free and equipotential. This potential is called the *plasma potential,* V_{pl}, and because of the presence of the sheath around any surface, including boundary walls, electrodes, probes, substrates etc., is positive with respect to any of these.

(iii) Sheath Potential

Returning to the floating surface refered to in the section on sheath formation, the potential reached by the surface when the ion and electron fluxes balance is known as the *floating potential,* V_f. Thus, for this surface, the potential across the sheath is the difference between the floating potential and the plasma potential [2.10].

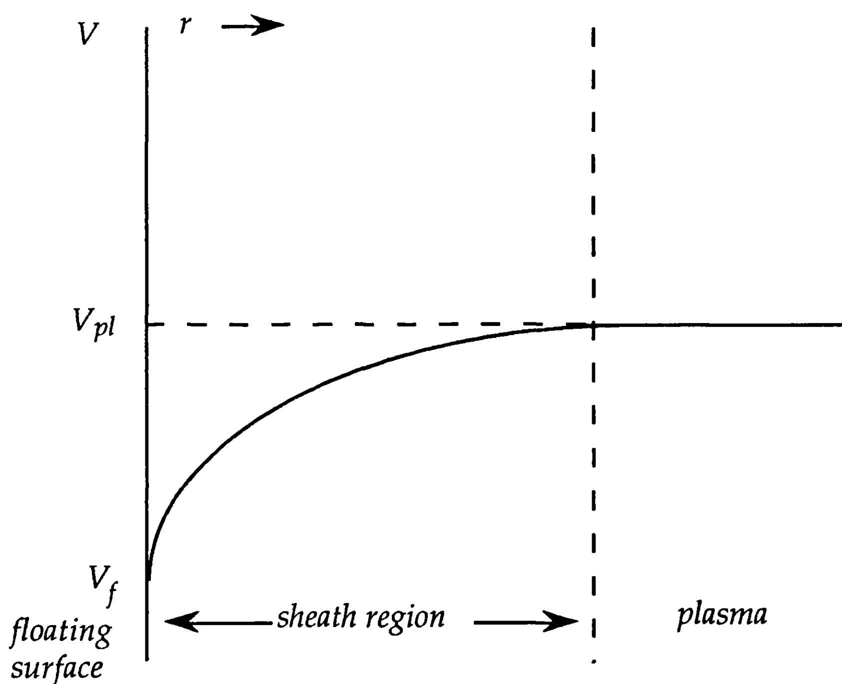

Fig. 2.1(a) Potential across a sheath

(iv) The Pre-sheath and the Bohm Criterion

The boundary between sheath and plasma is taken to be the plane where the ion and electron densities are equal, as in the bulk plasma, but it has been found that the potential at this plane is not the plasma potential. There is, between the sheath and the bulk plasma, a quasi-neutral transition region, of

low electric field, known as the *pre-sheath,* through which ions are accelerated. This acceleration is necessary as otherwise the ions would not in fact be able to cross into the space-charge region of the sheath.

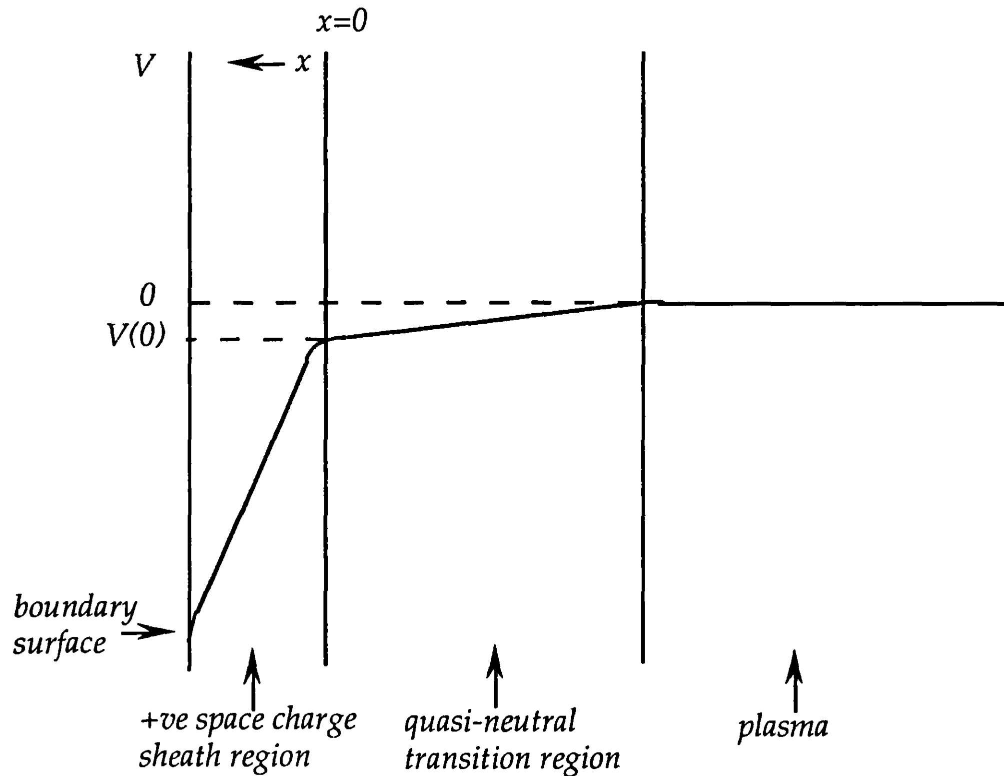

Fig. 2.1(b) Potential across sheath and pre-sheath

In figure 2.1(b), x=0 corresponds to the space-charge sheath boundary with the plasma. At x=0, $n_e(0) = n_i(0)$, that is, there is space charge neutrality. Assuming that the sheath is collisionless, then the ion current $qn_i(x)u(x)$ is constant, where $u(x)$ is the ion velocity.

By conservation of energy for the ions:

$$1/2 m_i u(x)^2 = 1/2 m_i u(0)^2 + q[V(0)-V(x)] \tag{7}$$

$$\therefore\ u(x) = \left\{ u(0)^2 + \frac{2q[V(0)-V(x)]}{m_i} \right\}^{1/2} \tag{8}$$

and

$$n_i(x) = \frac{n_i(0)u(0)}{u(x)} = n_i(0) \left\{ 1 + \frac{2q[V(0) - V(x)]}{m_i u(0)^2} \right\}^{-1/2} \tag{9}$$

By the Boltzmann relation for the electrons:

$$n_e(x) = n_e(0) \exp\left\{\frac{-q[V(0) - V(x)]}{k_B T_e}\right\} \tag{10}$$

But if this is to be a positive space charge region, then

$$n_i(x) > n_e(x)$$

Since $n_i(0) = n_e(0)$, this means

$$\left\{1 + \frac{2q[V(0) - V(x)]}{m_i u(0)^2}\right\}^{-1/2} > \exp\left\{\frac{-q[V(0) - V(x)]}{k_B T_e}\right\} \tag{11}$$

Squaring and inverting:-

$$\exp\left\{\frac{2q[V(0) - V(x)]}{k_B T_e}\right\} > 1 + \frac{2q[V(0) - V(x)]}{m_i u(0)^2} \tag{12}$$

If $[V(0) - V(x)] << k_B T_e$ which is true at the plasma/sheath boundary, then the exponential can be expanded to give:

$$1 + \frac{2q[V(0) - V(x)]}{k_B T_e} > 1 + \frac{2q[V(0) - V(x)]}{m_i u(0)^2} \tag{13}$$

hence $$u(0) > (k_B T_e / m_i)^{1/2} \tag{14}$$

In other words, the ions must have a minimum, directed velocity towards the sheath of $(k_B T_e / m_i)^{1/2}$, to be able to cross into the positive space charge region of the sheath. This is known as the *Bohm criterion*. This velocity is acquired in the pre-sheath region. It is interesting to note that it is the *electron* temperature which enters the Bohm criterion, together with the *ion* mass [2.33].

2.1.2.4 Probe characteristics

The basic technique for investigation of a plasma is the Langmuir probe. This consists essentially of a shielded conductor which is inserted into the plasma. This probe can be biased and the current drawn by it at different voltages constitutes the probe I-V characteristics, from which the plasma parameters may in theory be derived. However, interpretation of these characteristics depends strongly on the model used.

(i) Electron current

For a planar probe (since this was the type of probe used to characterise the plasma of the novel source, Chapter 4), biased near the plasma potential, most of the current collected will be electron current, because the ion mass is so much greater than the electron mass. If the electrons have a Maxwellian distribution function:

$$f(v) = n_e \left(\frac{m_e}{2\pi k_B T_e}\right)^{3/2} \exp\left[-\left(\frac{m_e v^2}{2k_B T_e}\right)\right] \tag{15}$$

The electron current per unit area to a planar probe biased at V can be calculated by taking the integral:

$$\begin{aligned} j_e &= q \int f(v)\, v_z\, dv_x dv_y dv_z \\ &= q n_e \left(\frac{m_e}{2\pi k_B T_e}\right)^{3/2} \int_{v_{min}}^{\infty} \exp\left[-\left(\frac{m_e v^2}{2k_B T_e}\right)\right] v_z\, dv_z \end{aligned} \tag{16}$$

$$\begin{aligned} I_e &= I_e^* \exp\left[\frac{-q(V_{pl} - V_p)}{k_B T_e}\right] & V_p \leq V_{pl} \\ I_e &= I_e^* & V_p > V_{pl} \end{aligned} \tag{17}$$

where $I_e^* = A n_e q (k_B T_e / 2\pi m_e)^{1/2}$

and where V_{pl} is the plasma potential, and A the effective probe area. I_e^* is the electron saturation current.

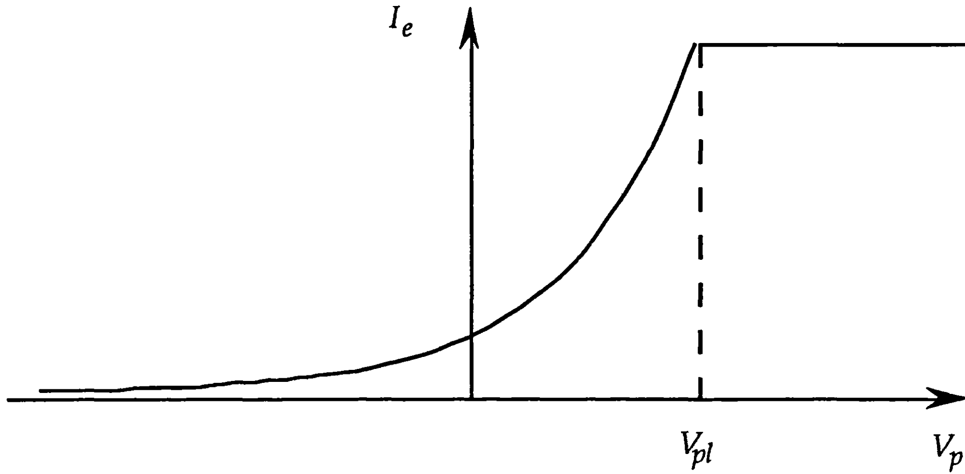

Fig. 2.2(a) Ideal electron current probe characteristics

For such a Maxwellian distribution function, it follows that a plot of $\ln I_e$ against V_p should be linear, up to $V_p = V_{pl}$, with a slope of (q/k_BT_e) from which T_e may be found. Also, the potential at which the electron current reaches saturation should give the plasma potential. The value of this saturation current, with the electron temperature already found, then yields the plasma density, n_e.

(ii) Ion Current

It is only valid to replace electrons with ions in the above discussion if the ion temperature is comparable with the electron temperature, so in the plasmas being described here, the ion saturation current is the Bohm current. This was given in section 2.1.2.3 (iv) as $qn_i(0)u(0)$, where $n_i(0)$ is the ion density at the sheath boundary, and $u(0)$ is the Bohm velocity. But we need to know the value of $n_i(0)$. The ions acquire their velocity by being accelerated across the pre-sheath. This implies that there is a potential drop across the pre-sheath, designated $V(0)$ in figure 2.1(b), with respect to the plasma potential.

Therefore $$\tfrac{1}{2}m_iu(0)^2 = qV(0) \tag{18}$$

$$\therefore \; V(0) = \frac{m_iu(0)^2}{2q} = \frac{m_ik_BT_e}{2qm_i} = \frac{k_BT_e}{2q} \tag{19}$$

By the Boltzmann relation, the electron density, $ne(0)$ at the sheath boundary is given by

$$n_e(0) = n_e \exp\left[\frac{-qV(0)}{k_B T_e}\right]$$

$$= n_e \exp[-1/2]$$

$$= 0.6n_e \qquad (20)$$

But $n_e(0) = n_i(0)$, so the ion flux is given by $n_i(0)u(0) = 0.6n_e u(0)$
Thus the ion saturation current is

$$I_i^* = 0.6n_i qA(k_B T_e/m_i)^{1/2} \qquad (21)$$

(iii) Probe I-V Characteristics

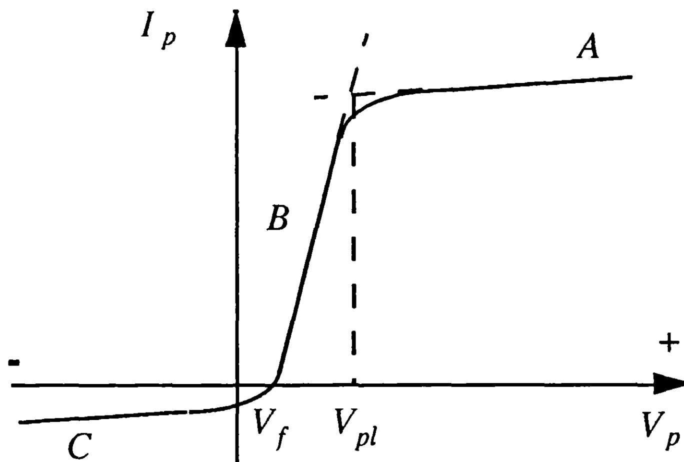

Fig. 2 2 Typical I-V characteristics for a Langmuir probe

The ion current must be added to the electron current to give the complete probe characteristics, shown in figure 2.2(b).

Section C - ion saturation current
Section A - electron saturation current
Section B - mostly electron current, and by extrapolating C the ionic contribution may be removed.

All electron currents measured at $V_p<V_{pl}$ must be measured with respect to the ion current, I_i^*, rather than zero current.

Sometimes the experimentally derived ln I_P-V_P plot may look like this:-

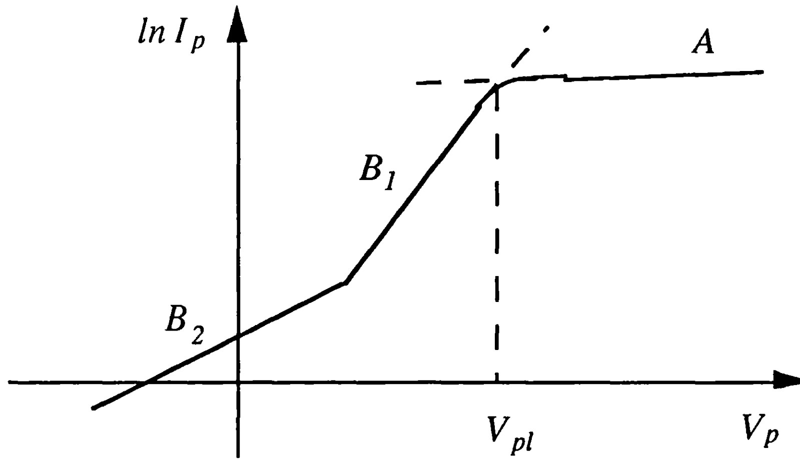

Fig. 2.3 Log plot of probe characteristics showing two electron populations

indicating two populations of electrons at different temperatures. This is probably due to the presence of secondary electrons.

2.1.2.5 With Magnetic Field

Although this all seems quite straightforward, it does not take into account effects on the plasma due to magnetic fields, and the plasma is assumed to be formed by a dc discharge. The main difference is that now the velocity distribution is no longer isotropic, since charged particles will spiral round magnetic field lines [2.11].

When a magnetic field is applied, the most noticeable effect is that the saturation electron current is much less than in the absence of a magnetic field. If the field is not too large, the ion current is basically unaffected. The criterion is that the Larmor radius is large compared with the probe. The Larmor radius is given by:

$$r_L = \frac{1}{B}\left(\frac{2mV}{q}\right)^{\frac{1}{2}} \qquad \text{with energy in eV} \qquad (22)$$

For an ion r_{Li} ~1.9m in a field of 10^{-2}T, so the ion current is virtually unaffected. But for an electron in the same field, r_{Le} ~1mm, so the criterion breaks down.

The effect of the field is to reduce the diffusion rate of electrons perpendicular to the field lines [2.9].

The usual diffusion coefficient D, given by kinetic theory is $\lambda\mathbf{v}/3$ where λ is the mean free path and $\mathbf{v}$ the average speed. In a magnetic field $D_\perp = D/(1+\omega^2\tau^2)$ where ω is the cyclotron frequency (qB/m), and τ the mean collision time. Again in a field of 10^{-2}T, $\omega\tau$ for electrons is $>10^2$ so $D_\perp$ is much less than D, but for ions ω is decreased by (m/M) while τ is increased by $(M/m)^{1/2}$. So $\omega^2\tau^2$ is decreased by (m/M) which is a factor of at least 10^4. Thus $D_\perp$ for ions is almost the same as D.

The presence of a magnetic field does not affect thermodynamic equilibrium, so the slope of the section B of the characteristic will still give the electron temperature. As we have seen, part C, the ion current section will be affected very little unless the field is very strong, but part A, the electron saturation current will be greatly affected, thus finding the value of V_{pl} , the plasma potential will be difficult.

Firstly, imagine a surface **A** around the probe, within which there are no collisions. In the absence of a magnetic field this would be approximately a sphere of radius λ, the mean free path. In the presence of a magnetic field this surface will be distorted. Along the direction of the field the mean free path is still λ, but perpendicular to it, it will be r_L, the Larmor radius.

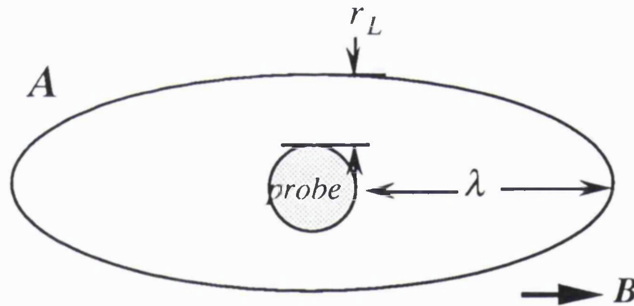

Fig. 2.4 The sheath in a magnetic field

The exact shape of **A** is not important.

In the region outside **A**, collision-dominated equations must be used, also, current is conserved. The electron current is given by:

$$j = -q\mathbf{D}.\nabla n + nq\boldsymbol{\mu}.\nabla V \qquad (23)$$

where **D**, the diffusion coefficient and $\boldsymbol{\mu}$, the mobility are diagonal matrices

$$D = \begin{pmatrix} D_\perp & 0 & 0 \\ 0 & D_\perp & 0 \\ 0 & 0 & D_{\shortparallel} \end{pmatrix} \qquad \mu = \begin{pmatrix} \mu_\perp & 0 & 0 \\ 0 & \mu_\perp & 0 \\ 0 & 0 & \mu_{\shortparallel} \end{pmatrix}$$

If we assume neutrality in the exterior region, $n_e = n_i = n_0 \exp(-qV/k_B T_i)$

so $$\nabla n = n\left(\frac{-q}{k_B T_i}\right)\nabla V$$

By Einstein's relation for classical diffusion, assumed still to be valid,

$$\mu = \frac{qD}{k_B T_e}$$

Putting these into equation (22) gives

$$j = -qD.\nabla n\left(1 + \frac{T_i}{T_e}\right) \tag{24}$$

Since the entire theory is only valid if $T_e >> T_i$ this approximates to

$$j = -qD.\nabla n \tag{25}$$

The probe current is found by integrating j over the surface **A**. This gives

$$I = 4\pi\sqrt{D_\perp D}C(n_0 - n_\lambda) \tag{26}$$

In fairly strong fields $n_0 >> n_\lambda$, so

$$I \approx 4\pi\sqrt{D_\perp D}Cn_0 \tag{27}$$

where C is the capacitance of the surface **A**.
Putting $D = \lambda \mathbf{v} / 3$

$$I = \frac{4\pi n_0 \bar{v}}{3}\sqrt{\frac{D_\perp}{D}}C\lambda \tag{28}$$

But the capacitance of the surface **A**, assumed to be a spheroid, is numerically close to a, the radius of the probe, so approximately

$$I = \frac{n_0 \bar{v}}{3} \frac{A_p}{a} \lambda \sqrt{\frac{D_\perp}{D}} \qquad (29)$$

Thus I varies only as $\sqrt{D_\perp}$, if one could be sure where on the characteristics to take I.

2.1.2.6 R.F. Plasmas

(i) Sheath Formation and Self-bias

A rf excited plasma is different from a dc plasma in a number of ways. One complication is that, due to the high mobikity of the electrons, they can respond instantaneously to the changing fields, whilst the much more massive ions do not, so the actual thickness of the sheath changes during a cycle. In other words, the edge of the sheath oscillates. Electrons in the discharge gain energy by collision with this oscillating sheath edge [2.9].

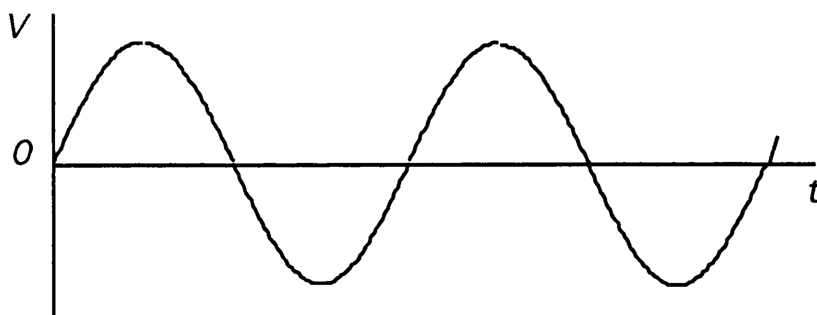

Fig. 2.5(a) Generator voltage wave-form

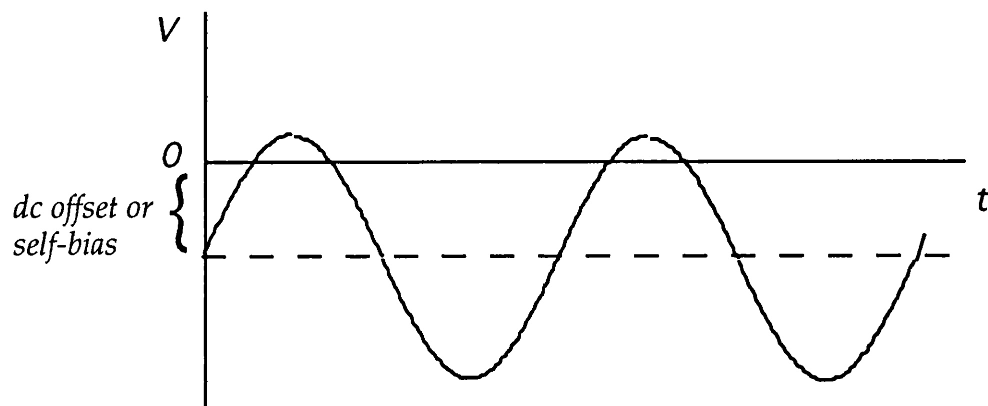

Fig. 2.5(b) Voltage wave-form at substrate surface

On a non-conducting or isolated surface, such as a substrate, in an ac discharge, to equalise the total charge fluxes per cycle, due once again to the very much higher mobility of the electrons, a permanent negative bias quickly builds up, so that the portion of the cycle during which electrons flow is very short compared with the portion of the cycle during which ions flow. This negative self-bias or dc off-set also means that the surface is bombarded by quite high-energy ions throughout most of the cycle.

It can be seen from figure 2.5 that the self-bias is nearly equal to half the peak-to-peak applied voltage. However, not all the ions which reach the surface will have the same energy. In the dc case it was assumed that the sheath was collisionless, but in the case of rf this is far from so. The high value of the self-bias means that sheaths are, on average, much thicker than in the dc case. The ions are therefore more likely to suffer collisions and charge exchange. The energy spread depends very strongly on the number of cycles the ion spends crossing the sheath. If the frequency is very low, then the ion will be able to respond to the phase of the varying sheath voltage, and a very large spread of impact energies will result. If the time taken for the ion to cross the sheath becomes several cycles of the voltage, this response disappears. Thus the energy spread shows an inverse dependence on the ratio between the ion's transit time of the sheath and the rf period, R [2.9]. This ratio, R, can be increased by increasing the rf frequency (reducing the period), by increasing the thickness of the sheath (by changing the pressure), or increasing the mass of the ion (decreasing its velocity). These theoretical predictions have been confirmed by a number of groups [2.14,2.35-36].

(ii) Plasma Potential

Since the sheath edge and sheath potential are oscillating, it follows that the plasma potential is also modulated. Standard probe techniques can only measure an average value for the plasma potential, and due to stray capacitances, this may not even be correct. Several designs of compensating probes have been suggested [2.39-2.40], but are still largely experimental. It does however mean that interpretation of probe characteristics is even more difficult.

(iii) Matching Networks

The purpose of the matching network is to maximise the power dissipation in the plasma.

For a dc circuit, the maximum power dissipation in the load is found when the resistance of the load is equal to the internal resistance of the power supply. In the ac case, if the power supply has an internal impedance of Z=r+is, then the maximum power transfer will occur for a load of impedance Z'=r-is, the conjugate impedance being required to ensure the resultant is purely resistive. In practice, generators have a purely resistive impedance, so a variable reactance is introduced to the circuit to provide the conjugate reactance to that of the load (the plasma). For a capacitive source, the matching unit will be largely capacitive.

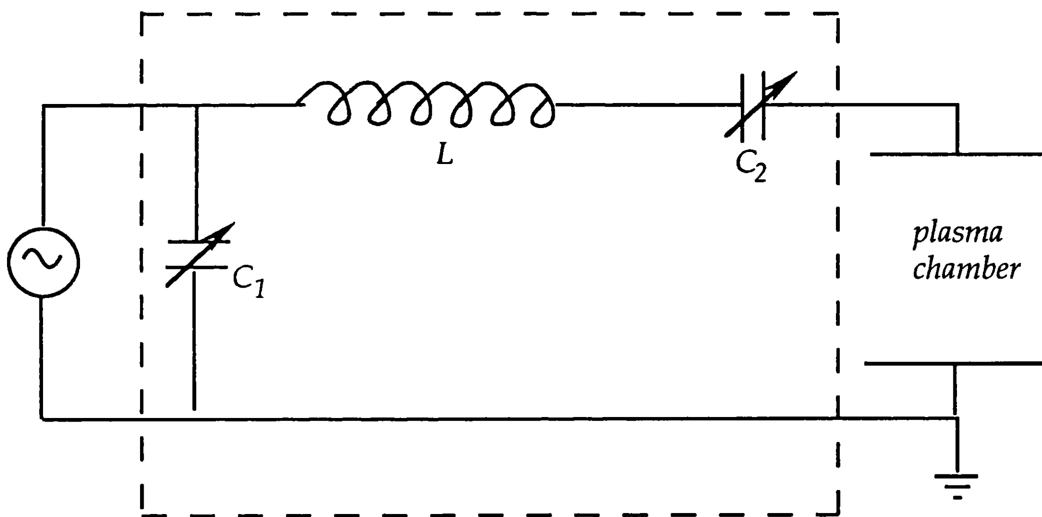

Fig. 2.6 Typical rf matching network

2.1.3 Present-day Plasma Sources

Plasmas can be produced by both dc and ac excitation. There are three main types of ac excitation, directly coupled e-m waves at microwave frequencies, inductively coupled and capacitively coupled fields at radio frequencies.

2.1.3.1 DC Plasma Sources

There are many possible configurations for dc plasma sources. All must include the two electrodes, cathode and anode, across which the potential is developed. Most designs use a central cathode with the anode as a cage surrounding it. There are many variations in both shape and material for both electrodes, depending on the gas to be used, and the specific application.

DC plasmas are now commonly used in sputtering magnetrons, most probably because of their extreme simplicity of operation. Potentials of a few hundred volts are used, together with an external magnetic field of a few hundred gauss, to trap the electrons and thus enhance the plasma density. Such plasmas have a density of charged particles of order 10^{10} cm^{-3}, at pressures of order 10^{-2}mbar [2.12,2.13]. This is a rather low density plasma.

2.1.3.2 Microwaves

To excite a plasma with microwaves, microwave power (commonly at a frequency of 2.45GHz) is passed from an antenna, via a waveguide to the plasma chamber, where a resonant standing wave is formed by adjusting the dimensions of the chamber with a plunger. The electric field component of the e-m wave then accelerates any free electrons to give them sufficient energy to ionise and/or excite molecules of the gas, thus producing the plasma, as shown in figure 2.7. To initiate the plasma, a few electrons must be extracted from somewhere. The volume over which the electric field is strong enough to do this is only a few centimetres diameter for microwaves in the cavity, and

does not ideally extend to the walls (a potential source of electrons), thus microwave plasmas are often difficult to initiate.

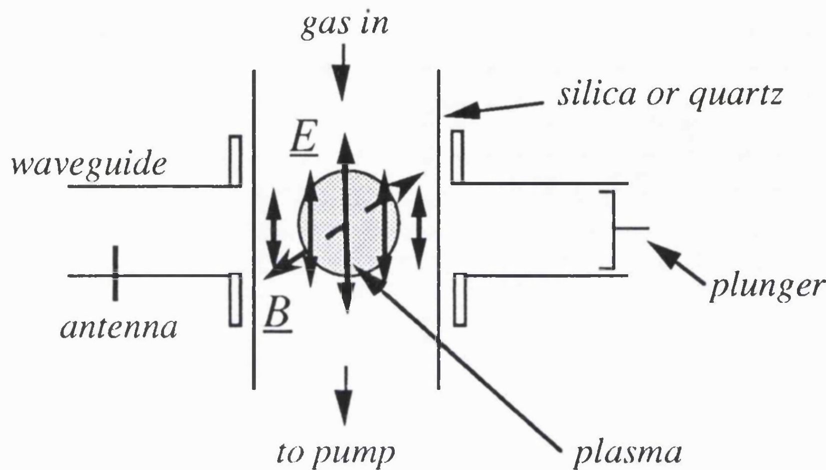

Fig. 2.7 Schematic of typical microwave system

The small dimensions of the strong field region means that the plasma formed is of a limited volume, often in the form of a "plasma ball".

Because the plasma is concentrated by the resonant field, contact with the walls is slight, and electron losses to surroundings are fairly small. Thus within the plasma volume, the plasma density can be very high [2.14], as much as 3×10^{11} cm^{-3}, at a pressure of 10^{-4} mbar.

2.1.3.3 Capacitively Coupled Radio-frequency

Capacitively coupled rf plasmas are frequently used for etching, particularly of silicon. Such plasma etchers usually consist of two parallel plate electrodes, one powered the other earthed, with the plasma formed between them. The substrate to be etched is usually attached to one of the electrodes. An alternating voltage is applied to the powered electrode, producing an oscillating electric field in the space between, as shown in figure 2.8. The frequency of oscillation is very high, 13.56MHz as standard, but as the wavelength of this frequency is large compared with chamber dimensions, the field can be considered uniform and alternating. Powers of a few hundred watts can produce dense plasmas of large volume, of order $10^{11}cm^{-3}$, but high voltages develop across the sheath boundaries of capacitively formed plasmas [2.15].

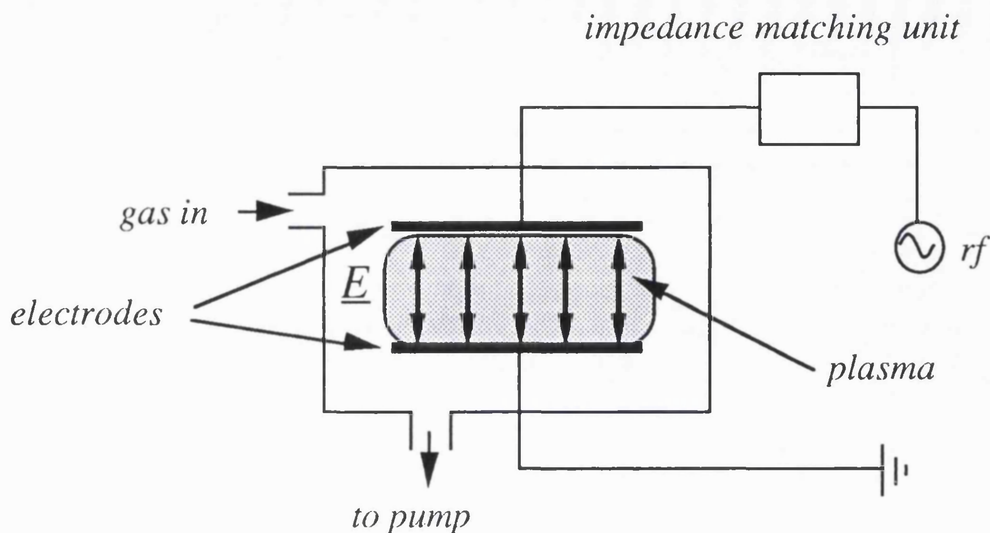

Fig. 2.8 Schematic of typical capacitive system.

These high voltages can lead to sputtering of the electrodes and chamber walls (causing contamination of the plasma) and to damage of any growing film since the substrate normally forms one of the electrodes. It has been shown [2.16] that a magnetic field, parallel to the surface of the electrodes will reduce the electron loss, increasing the plasma density, and reduce the sheath potential through the reduction in electron mobility, which allows equilibrium between electrons and ions at a lower potential. Alternative electrode designs and the incorporation of magnets may therefore enable these shortcomings to be reduced. This is discussed further in a later chapter.

2.1.3.4 Inductively Coupled Radio-frequency

Inductive rf sources come in a number of forms, but the most common uses a helical coil surrounding a chamber, usually pyrex or quartz, which contains the gas to be energised. RF alternating current is passed through the coil, so that the chamber is within an axial alternating magnetic field. This in turn induces an azimuthal alternating electric field, forming closed loops, in the chamber volume as is shown in figure 2.9.

The potential difference across the coil can also cause capacitive field effects within the chamber, and indeed it is believed that it is the capacitive field which ignites the plasma [2.17]. Sometimes the chamber may be surrounded by a split Faraday shield to minimise these effects. Only at high

powers, of the order of kilowatts, does the discharge become predominantly inductive.

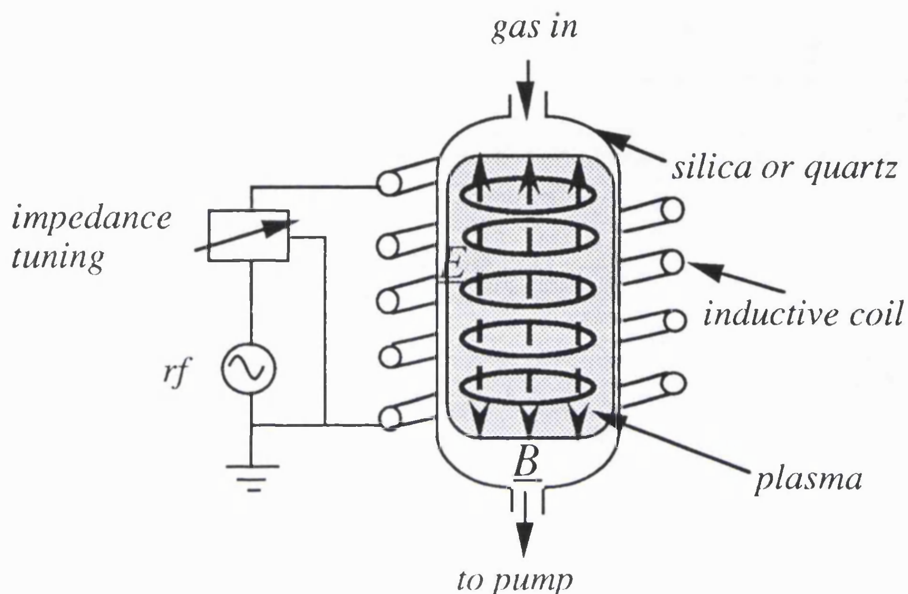

Fig. 2.9 Schematic of typical inductive system

The main advantage of an inductive discharge is the lower sheath voltage and hence reduced sputtering and contamination. However, losses in the inductive circuitry, which may amount to 90%, mean that inductive rf sources are inefficient [2.17].

2.2 Ion Beam Sources

Although plasma sources are neeeded in their own right, for the processing of materials of many types, plasmas are also needed as the starting point for other instruments. In particular, plasmas form the basis for ion beam sources where the source material is a gas.

Ion beams were first investigated at the turn of the century, and the first ion beam source was built by J. J. Thomson in 1910 [2.18]. To create an ion beam, firstly the source material, usually (but not necessarily) a gas, must be ionised, and then the ions formed must be directed into a beam. Here, only ion beam sources for gases will be considered.

The earliest ion beam sources used high voltage discharges to ionise the gas, and another high voltage to accelerate the ions in the required direction. Thomson's ion beam source produced ions with a large energy spread, making collimation of the beam difficult, the discharge was not very stable, and rather a low percentage of the gas molecules were ionised.

By the 1930's, the design had been improved, and stable arc-discharge plasma ion beam sources were being used, to provide ions for use with accelerators in nuclear physics experiments.

A typical source was the design by Allison [2.19], installed in 1940 on the 400kV Cockroft-Walton kevatron for nuclear disintegration experiments. It used a cathode heated by 24A and an anode voltage of 72V to produce the arc discharge, and an extraction voltage which could be varied between 1kV and 5kV, producing a beam current of up to 2mA.

To improve the ionising efficiency, the path of the electrons within the discharge chamber should be lengthened. Two methods were tried, both in the late 1940's, (i) applying a magnetic field to the discharge chamber, and (ii) exciting the discharge with a high frequency power source.

These two development directions will be considered separately.

2.2.1 Arc Discharge Ion Beam Sources in a Magnetic Field

There have been several variations on this theme, homogeneous or inhomogeneous magnetic field, with and without forced oscillations of the electrons, heated or cold cathode.

2.2.1.1 Homogeneous Field

The earliest such source used a solenoid surrounding the anode chamber [2.20], which provided a homogeneous axial magnetic field. An exciting voltage of 250V was needed and it employed an extraction voltage of 3-5kV.

The path of the electrons is lengthened as they travel in spirals around the magnetic field, thereby much increasing their chances of causing ionisation. The ions are extracted through a slit in the anode, a very common design, producing a narrow, high intensity beam, again for high energy applications.

2.2.1.2 Inhomogeneous Field

The next improvement in design, was the inhomogeneous magnetic field, the so-called duoplasmatron [2.21].

The plasma is focused towards the anode by a cone-shaped intermediate electrode, made of soft iron. The anode support is also made of soft iron, and these iron electrodes are magnetised by the field of the large coils, so the magnetic field is very strong close to the anode. The beam is again extracted through a slit in the tungsten anode. The highest concentration of ions is obtained near to the extraction slit. This ion beam source operated in the pressure range 5×10^{-3} Torr to 8×10^{-2} Torr with an extraction voltage of 20kV to 60kV. 92% of the gas is ionised in the environment of the slit.

2.2.1.3 The Anti-cathode

To make the path-length of the electrons within the plasma even longer than magnetic confinement alone, the anti-cathode was introduced. This is another negative electrode, placed beyond the anode, and biased usually ~+10V with respect to the emitting cathode, which reflects the electrons back into the ionisation chamber. This causes the electrons to oscillate between the two cathodes, the emitting, usually hot, cathode, and the reflecting, cold, cathode. An anti-cathode design was also tried with the duoplasmatron type of magnetic field.

2.2.1.4 The Cold Cathode

The main problem with all heated cathode arc-discharge ion beam sources is the short lifetime of the hot emitting cathode. One attempt to improve the cathode lifetime was to use a cold cathode.

There were two main designs, both using the Penning-type electrode configuration, with two cathodes, and the anode between them, generally known as PIG (Penning Ion Gauge) configuration. With no heating of the cathode, a much higher discharge voltage is needed, several kV, the exact value depending on the material of the cathode.

The first design used axial extraction of the beam, as with the previous sources, but later versions used transverse extraction of the beam, ie extracting the beam from near the centre of the plasma, in a direction normal to the magnetic field, from where the ion density was found to be greater. These sources also used a lower extraction voltage, 16kV.

In 1967, Abdelaziz and Ghander [2.22] developed a PIG type of ion source with the anti-cathode in the form of a grid, allowing a broad beam of relatively low energy, a few kV to be extracted.

This reduction in beam energy, without sacrifice of beam intensity has been the long term trend as new uses for ion beams, other than high energy Physics have been found.

2.2.2 Broad Beam Sources

With the growth of the semiconductor industry from the 1970's, ion beam sources for etching and deposition were developed, which attempted to meet specifications for broad uniform beams of high intensity but with energy low enough to avoid damaging the semiconductor material. The standard size of a Silicon wafer is 15cm diameter, and it is therefore necessary to have a beam of uniform intensity over this area at least.

Narrow, higher energy (but still much lower than the earliest sources) beams are used for ion implantation, to dope small regions of a semiconductor wafer, any damage induced being subsequently annealed out, but this damage/anneal cycle cannot be repeated too often, as it induces diffusion which means loss of definition of internal structure.

The first type of broad, low energy ion beam source used an axial magnetic field to confine the electrons, a hot filament cathode inside the chamber, the walls of the chamber as the anode, and extraction grids [2.23] and is illustrated in Fig. 2.8.

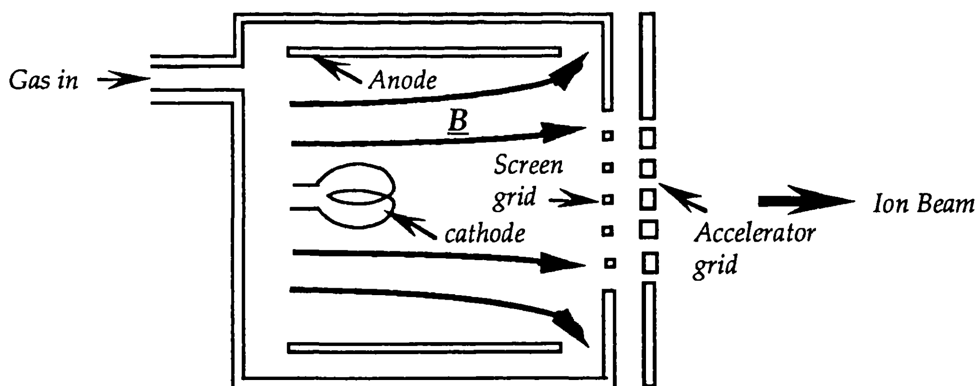

Fig. 2.8 Axial field discharge chamber with two-grid ion optics. The magnet or magnetic winding required to produce the magnetic field is not shown.

Such a magnetic field though does not produce a sufficiently uniform beam.

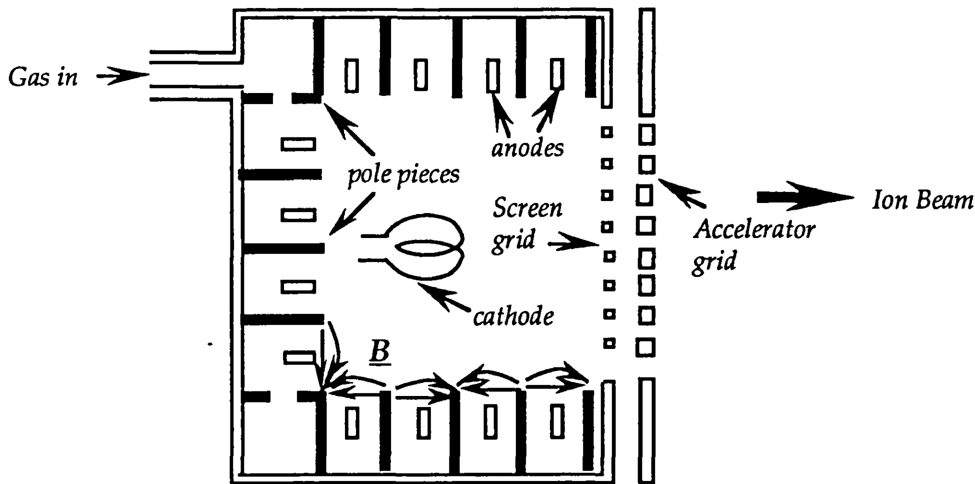

Fig. 2.9 Multipole discharge chamber. The magnets between the pole pieces that are required to produce the magnetic field are not shown.

A new design, since much used, developed in the 1970's [2.24], used a multipole, cusped magnetic field, which is confined mostly to the region of the walls of the chamber, thus still keeping the electrons away from the walls (where they would be lost) and in the plasma, inducing ionisations, but leaving the central region of the plasma virtually field free.

This is illustrated in Fig. 2.9. This type of source uses a discharge voltage of 50V and accelerating voltage of 500V, giving a beam current density of 1mA/cm^2.

2.2.3 Theory of Beam Extraction

The theory behind these designs [2.23], of the so-called Kaufman-type ion beam sources is based on Child's Law:

$$j = (4\varepsilon_0/9)(2e/m)^{1/2}V^{3/2}/l^2$$

where j - maximum current density between planes

V - p.d. between planes

l - spacing between planes

e/m - charge to mass ratio of particles emitted with negligible velocity at one of the planes.

2.2.3.1 With two grids

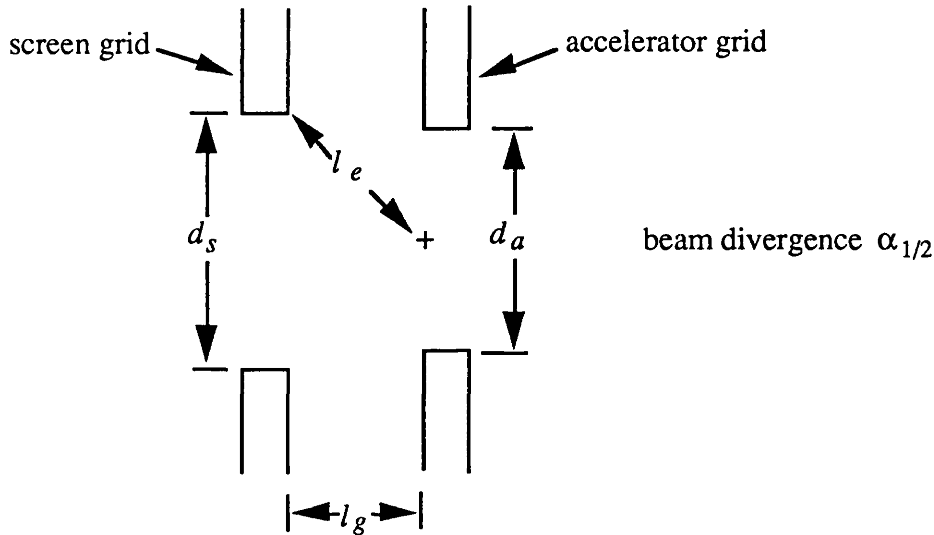

Fig. 2.10 Schematic of grid geometry

For this approximation, V_t, the total voltage drop between grids is used for V, and the diagonal dimension l_e is used for l. The hole diameters d_s and d_a should be about equal. From Child's Law above, it can be seen that the current density varies inversely as l^2. If all the dimensions are varied in proportion, the extraction area of the aperture varies directly as l^2. Total current is the product of current density and extraction area, and is hence independent of aperture size. The extraction current is thus maximised by using many small apertures (the grid). However, it has been found experimentally that current density increasingly falls below Child's Law as the screen hole diameter is decreased below ~2mm.

By Child's Law, the maximum extracted current varies as $V_t^{3/2}$. Thus for lower ion energies, this two grid ion optics gives low current densities.

2.3.3.2 Three grids

A third, grounded, grid can be added after the accelerator grid. This acts as a decelerator grid. Thus V_t can be 2000V, giving a high beam current, whilst the overall net voltage could be only 600V. This ion optics also reduces beam divergence.

2.3.3.3 One grid

This configuration is particularly well suited to low ion energies and high ion current density. With a low plasma density, the ions follow essentially straight line paths and the fraction transmitted corresponds closely to the open-area fraction of the grid. However, the grid is rapidly eroded by ion impingement.

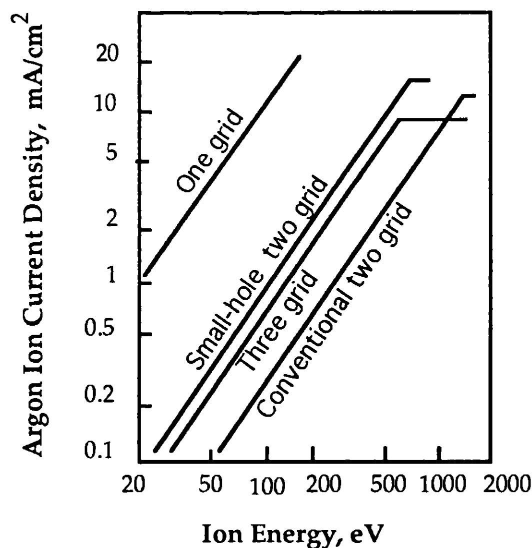

Fig. 2.11 Comparison of gridded optics designs. Beam profile effects not included.

2.3.3.4 Focusing

There are two major methods of focusing ion beams:

(i) *Transverse aperture displacement*, which is difficult with three grids, and of course impossible with only one. This is used mainly to keep the beam from diverging, it cannot alter the actual direction of the beamlet very much.

(ii) *Grid curvature*, which can be used on any grid ion optics. As an example, with grids as segments of concentric spheres and the apertures aligned along radii, considerable beamlet deflection is possible. In one system, a beam of diameter 6.5cm was focused to 2.5cm by two spherical grids, and the current density increased by 6 times. However, curvature of grids is very tricky, and the grids can become very delicate. The problem of erosion also still exists.

2.2.4 High Frequency Ion Sources

One of the main problems with arc discharge ion sources is the frailty of the cathode, particularly if the source is to be used with reactive gases.

High frequency, either microwave or radio-frequency discharges do not use a cathode, so they do not have this problem. This makes them very suitable for reactive gas plasmas.

2.2.4.1 Inductively Coupled RF Sources

The first radio-frequency ion source was made by Bayley and Ward in 1948, and a much improved and more reliable design was built by Thonemann *et al* in 1949 at Oxford [2.25].

It was inductively coupled, with a coil around the outside of the discharge chamber, through which a 20MHz, 150W signal was sent. Its purpose was to provide protons and/or deuterons for an accelerator, (the usual purpose of ion

beam sources at this time) and used an extraction voltage of several kV, producing a beam current of 0.5mA.

Rf ion sources continued to be used as producers of ions for accelerators, as their ionising efficiency is high and they are reliable and long lived, needing very little maintenance. The Thonemann design remained essentially unaltered until Abdelaziz [2.26] in 1962 altered the geometry, to extract the ions (protons) from the centre of the plasma, radially and normally to the rf field and tube axis.

This was because it had been demonstrated that the concentration of suitable ions is greater at the centre of the plasma. This source was also designed for use in conjunction with an accelerator, and was a very high power source, ~30kW, with an extraction voltage of 34kV. A beam current of ~100mA was obtained.

By 1980 sources were using less power and lower extraction voltages, ~200W and a few kV, with a beam current of ~1mA, based on the Abdelaziz design [2.27].

Even as late as 1984, a new rf source was developed based on the Thonemann design but capable of pulsed operation [2.28].

But also in the 1980's there was considerable interest in developing really low energy ion beam sources which could be used with reactive gases for etching and deposition on semiconductor materials. These "dry etching" beam methods have the advantage of greater anisotropy, thus smaller features can be made, but energetic beams can cause damage to the delicate crystal structure of these materials. Also, for processing of semiconductor wafers, a uniform broad beam is preferable.

A completely new design for this application was developed by 1989 by Proudfoot *et al* [2.29] with the following specifications:

Ion energy to be in the range 100-200eV

Uniform beam 15cm in diameter

Beam current density at target 0.5-1.0mA cm^{-2}

Suitable for reactive gases

Pressure in target chamber less than 10^{-4}mbar

However, even these specifications are not adequate for the processing of III-V semiconductor materials.

2.2.3.2 Capacitively Coupled RF Sources

Although it had been known since the 1940's [2.1] that high frequency electric fields can excite a discharge in a gas, this form of excitation was only used in plasma etchers. It was not used in ion beam sources until Guarnieri and Kaufman in 1982 [2.30]. Their paper shows two possible configurations, one with axial magnetic field and the other with radial magnetic field, but includes no quantification.

This demonstrates the major difference between inductively and capacitively coupled sources, that is the greater flexibility of design with capacitively coupled sources.

In 1986 Lossy and Engemann [2.31] developed a capacitively coupled rf ion beam source with two parallel-plate electrodes and three-grid ion optics (the first grid being one of the electrodes), and a magnetic field provided by SmCo-magnets. They experimented with various different magnetic field configurations to optimise this variable, based on the cusped, multipole field described above.

They followed this with the testing of electrode geometries [2.32], together with their optimised magnetic field configuration, a further example of the flexibility of capacitive sources.

At about the same time Lejeune *et al* [2.33] were experimenting with novel forms of electrode, such as a multitube cathode.

Both of these groups have reported that there was some sputtering of the electrodes, and also of the chamber walls, leading to contamination of the beam. With some gases a dielectric coating formed on the electrodes which in no way affected the performance of the source. The exciting electrodes do not need to be in contact with the plasma, as it is only the electric field between them which matters.

The source used in this study, designed by A.C.Evans [2.34] also uses a cusped multipole magnetic field, but with a highly original electrode configuration, and with the electrodes *outside* the chamber. (See Chapter 4)

2.2.3.3 ECR (Electron Cyclotron Resonance)

These sources use microwave excitation of a gas with a tuned magnetic field, usually provided by a coil surrounding the resonance cavity, to produce highly ionised plasmas. They are now very much used instead of other types of ion source in high energy applications because ECR is good at inducing multiple ionisations. This would be a disadvantage in semiconductor applications.

Although there are several commercially available ECR ion beam sources available for low energy work, (a few hundred eV), standardised to use 2.45GHz, and many groups use them to produce reactive ion beams, there seems little interest in developing them further in this energy range.

The main advantage of ECR sources over inductively-coupled rf sources is that they can operate at lower pressures and produce very dense plasmas, but capacitively-coupled rf sources also operate at these lower pressures, between 10^{-4} and 10^{-3}mbar and with magnetic enhancement can produce high plasma densities. So in the future, when they have emerged from the experimental, developmental, stage they may be used preferentially as they are simpler and more flexible than ECR sources.

2.3 References

2.1 D. H. Hale *Phys. Rev.* **73** 1046 (1946)

2.2 M. A. Herlin and S. C. Brown *Phys. Rev.* **74** 291 (1948)

2.3 M. A. Herlin and S. C. Brown *Phys. Rev.* **74** 910 (1948)

2.4 M. A. Herlin and S. C. Brown *Phys. Rev.* **74** 1650 (1948)

2.5 A. D. MacDonald and S. C. Brown *Phys. Rev.* **75** 411 (1949)

2.6 S. C. Brown and A. D. MacDonald *Phys. Rev.* **76** 1629 (1949)

2.7 H. M. Mott-Smith and I. Langmuir *Phys. Rev.* **28** 727 (1926)

2.8 F. F. Chen *Introduction to Plasma Physics* Wiley (1965)

2.9 B. Chapman *Glow Discharge Processes* Wiley (1980)

2.10 N. Hershkowitz in *Plasma Diagnostics* ed. O. Auriello and D. L. Flamm (A.P.) (1989)

2.11 F. F. Chen in *Plasma Diagnostics Techniques* ed. R. H. Huddleston and S. L. Leonard (A.P.) (1965)

2.12 M. J. Goeckner, J. Goree and T. E. Sheridan *J. Vac Sci. Technol.* **A8** 3920 (1990)

2.13 M. J. Goeckner, J. Goree and T. E. Sheridan *IEEE Transactions* **PL19** 301 (1991)

2.14 Z. Zakrzewski, M. Moisan, J. Margot and G. Sauvé *Plasma Sources Sci. Technol.* **1** 28 (1992)

2.15 V. A. Godyak and A. S. Kanneh *IEEE Trans.* **PS14** 112 (1986)

2.16 A. V. Lukyanova, A. T. Rakhinov and N. V. Suetin *IEEE Trans.* **P.S. 19** 197 (1991)

2.17 J. Hopwood *Plasma Sources Sci. Technol.* **1** 109 (1992)

2.18 László Vályi *Atom and Ion Sources* Wiley (1977)

2.19 S. K. Allison *Rev. Sci. Instrum.* **19** 291 (1948)

2.20 C. Bailey, D. L. Druley and F. Oppenheimer *Rev. Sci. Instrum.* **20** 189 (1949)

2.21 C. D. Moak, H. E. Banta, J. N. Thurston, J. W. Johnson and R. F. King *Rev. Sci. Instrum.* **30** 694 (1959)

2.22 M. E. Abdelaziz and A. M. Ghander *IEEE Trans.* **NS14** 53 (1967)

2.23 H. R. Kaufman, J. J. Cuomo and J. M. E. Harper *J. Vac. Sci. Technol.* **21** 725 (1982)

2.24 R. S. Robinson *J. Vac. Sci. Technol.* **15** 277 (1978)

2.25 P. C. Thonemann, J. Moffatt, D. Roaf and J. H. Saunders *Proc. Phys. Soc.* **61** 483 (1948)

2.26 M. E. Abdelaziz *IEEE Trans.* **NS9** 1 (1962)

2.27 M. M. Abd el Baki and S. G. Zakhary *Nucl. Instrum. and Meth.* **178** 311 (1980)

2.28 S. Ahmad, B. W. Farmery, D. Hole and M. W. Thompson *J. Phys. E: Sci. Instrum.* **17** 933 (1984)

2.29 G. Proudfoot, C. M. O. Mahoney and R. Perrin *Nucl. Instrum. and Meth. in Phys. Res.* **B37/38** 136 (1989)

2.30 C. R. Guarnieri and H. R. Kaufman *IBM Technical Disclosure Bulletin* **24** 5833 (1982)

2.31 R. Lossy and J. Engemann *J. Vac. Sci. Technol.* **B6** 284 (1988)

2.32 R. Lossy and J. Engemann *Vacuum* **36** 973 (1986)

2.33 C. Lejeune, J. P. Grandchamp, O. Kessi and J. P. Gilles *Vacuum* **36** 837 (1986)

2.34 A. C. Evans, J. Franks and H. Jolly *Proc. 8th Int. Ion and Plasma Ass. Tech.* 309 (1991)

2.35 W. M. Greene, M. A. Hartney, W. G. Oldham and D. W. Hess *J. Appl. Phys.* **59** 1890 (1986)

2.36 Y. Okamoto and H. Tamagawa *J. Phys. Soc. Jap.* **27** 270 (1969)

2.37 P. A. Chatterton, J. A. Rees, W. L. Wu and K. Al-Assadi *Vacuum* **42** 489 (1990)

2.38 N. St. J. Braithwaite, N. M. P. Benjamin and J. E. Allen *J. Phys. E: Sci. Intrum.* **20** 1046 (1987)2.40

CHAPTER 3: ETCHING AND DEPOSITION OF ELECTRONIC MATERIALS: PLASMA AND ION BEAM SOURCE REQUIREMENTS

The fabrication of devices from semiconductor wafers involves numerous steps, of both removal and addition of material, in selected areas of the surface, to produce the required surface features [3.1].

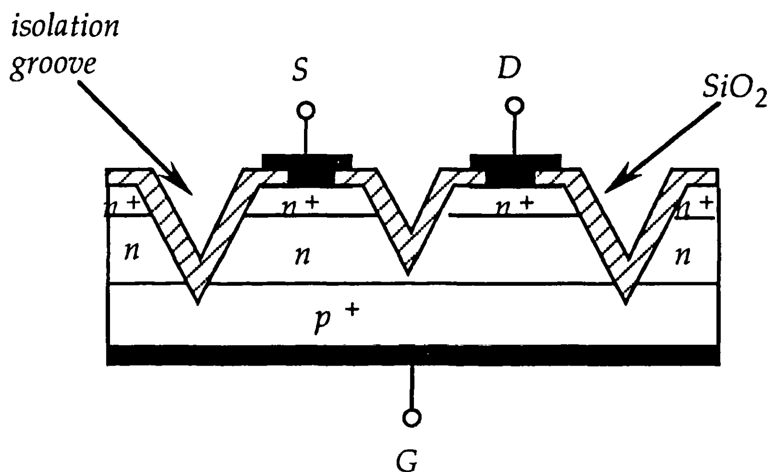

Figure 3.1 V-channel FET [3.2]

Using the example of Fig.3.1, a V-channel field effect transistor, fabricated as part of an integrated circuit, n-type silicon is epitaxially grown on a p-type substrate, followed by a further epitaxially grown layer of n^+-type silicon.

The V-shaped groove to isolate the active part of the device from the rest of the circuit, must then be etched, to the required depth, in the required position, defined by photolithography. After the photolithographic mask has been removed, the SiO_2 will be grown on the surface, and partially etched away, again using a masking technique, to expose areas for metallisation. The purpose of the grooves is to isolate the FET from the rest of the integrated circuit.

The precise etching of material is the key to the definition of device geometry, while the deposition of layers of differing doping levels is vital for

the function of the device. Prior to deposition, surface cleaning and preparation through the removal of thin layers is common.

Thus it can be seen that it is important for the device engineer to have effective deposition and etching tools.

Etching methods and deposition methods typically involve directing energetic particles at the semiconductor surface. It is therefore necessary to take into account the effect of such particles impinging on the surface.

3.1 Ion-Surface Interactions

As a particle collides with a surface, it loses energy, either by interaction with the coulomb field of the electrons surrounding the target atoms, or by more direct collision with the nucleus of a target atom [3.3]. The former, known as electronic stopping, is most strongly dependent on the energy of the incoming ion, since the faster it is travelling, the less time it will spend in the vicinity of the field. The latter is dependent on the energy too, but also on the relative masses of the ion and target atom; the more similar these masses, the more effective will be the energy transfer, as can easily be derived from simple considerations of momentum and energy conservation.

These two sources of energy loss can be combined to give a total energy loss, per unit length:

$$\frac{dE}{dx_{total}} = \frac{dE}{dx_{nucleus}} + \frac{dE}{dx_{electrons}}$$

From these, if known, an estimate of the penetration range of the ion can be made [3.4].

The actual penetration depth will also depend on the direction the ion travels within the target, as some crystallographic orientations offer "channels" which can greatly reduce the number of direct collisions, and thus greatly increase the penetration depth.

The effects within the target material of these collisions are numerous. The target atom may well receive so much energy from the impinging ion that

it is violently dislodged from its lattice position, itself then colliding with other atoms in the host lattice, which may also become dislodged if the energy transferred from the original ion was sufficiently high. Of course, the original ion may still have enough energy to repeat these collision effects as it continues its travels. This therefore leads to a "collisional cascade", whose total volume can be quite large [3.5,3.6]. Some of the collisions within the cascade will lead to backscattering and even ejection of an atom from the surface, i.e. sputtering [3.7]. After about 10^{-13} secs, the moving displaced atoms will no longer have sufficient energy to break lattice bonds [3.8]. A relaxation period of about 10^{-11} secs follows [3.9], in which the remaining energy is thermalised, giving rise to vibrational excitation of neighbouring lattice atoms. Thus a region, fairly deep within the lattice becomes hot, a condition known as "thermal spike" [3.10]. This may encourage the migration of vacancies and interstitials, created in the cascade, deeper into the material, a highly undesirable outcome.

Another effect of the collisions is mixing. To demonstrate the mixing effect of collisional cascades and thermal spikes, especially prepared samples, with ordered layers of different composition were bombarded with ion beams of energy 200keV to 500keV. Mixing of these layers was observed at depths of several hundred Ångstroms by a number of groups [3.5,3.9]. Cheng *et al* [3.11] have shown that this ion mixing is strongly influenced by the heat of mixing. This suggests that diffusion in thermal spikes is the dominant contribution to ion mixing when incident ion energies are above a few keV. They suggest that the mechanism is the same whether ion energies are a few keV or a few hundred keV.

As well as the effects due to direct collisions, the effects of reactions with the electrons in the material, which will lead to excitation and ionisation, must be considered. An excited or ionised atom will be much more easily dislodged by a subsequent collision, and indeed it has been observed from the distribution of kinetic energies of ejected particles, that the threshold energy for ejection of excited atoms is much reduced, or even close to zero, depending on which excited state the atom is in. It has also been observed that the energy at the peak of the distribution is much increased [3.12].

However, in a real situation, we need to consider, not just the effect of one bombarding ion but many collisions per sec. This can lead to multiple displacements of host lattice atoms. Sigmund and Gras-Marti [3.5] have shown that the amount of relocation caused by single events, i.e. a low ion

fluence, is of order 50Å, whilst increasing the bombardment rate can double the amount of relocation to ~100Å. In such a case there may be segregation of components in a binary or tertiary system with the lighter component migrating to the surface, as it is more likely to be backscattered. This will then be followed by preferential sputtering and loss of stoichiometry [3.13].

Sigmund and Gras-Marti [3.5] believe there is a very slow decrease of the range with decreasing energy; it is also reasonable to assume some threshold energy below which no relocation takes place. Low-energy cascade mixing is intimately connected with displacement and replacement processes.

For very much lower energies, up to ~250eV, the volume of the collisional cascade is much reduced [3.6], and the mixing is confined to layers nearer the surface. This can clearly also affect an adsorbed layer on the surface, which can thus be mixed into the upper layers of the surface by quite a low energy beam. Jackman *et al* [3.14] have shown the chemical enhancement effects of this low energy mixing of an adsorbed layer to promote low damage etching of both silicon and III-V semiconductors.

3.2 Etching

Etching can be defined quite simply as the removal of surface material [3.15]. There are two main purposes in etching: surface preparation and device definition.

The semiconductor surface may be covered with an oxide layer, either a native oxide layer, that is, a layer which forms naturally on exposing the surface to air, which typically reaches a thickness of about 30 Å after a few days [3.16], or a residual layer due to a chemical etching process. This oxide layer is a dielectric and will therefore strongly affect the characteristics of any junction formed on the surface. To ensure good characteristics, this layer must be removed, or at least made as thin as possible. The removal of such a layer is part of surface preparation.

The semiconductor surface may not be perfectly smooth. Such irregularities of the surface may also strongly affect the characteristics of a junction or contact, due to localised field effects and surface states. Thus the

surface may require polishing, either mechanical or chemical. This also is a part of surface preparation.

In fabricating devices, etching is used to form mesas to isolate device areas, and to form recesses prior to gate metallisation, as in the MESFET (meta-semiconductor field effect transistor) illustrated in figure 3.2 [3.1]. It has already been mentioned (page 41) that the V-shaped grooves in the V-channel FET are formed by etching.

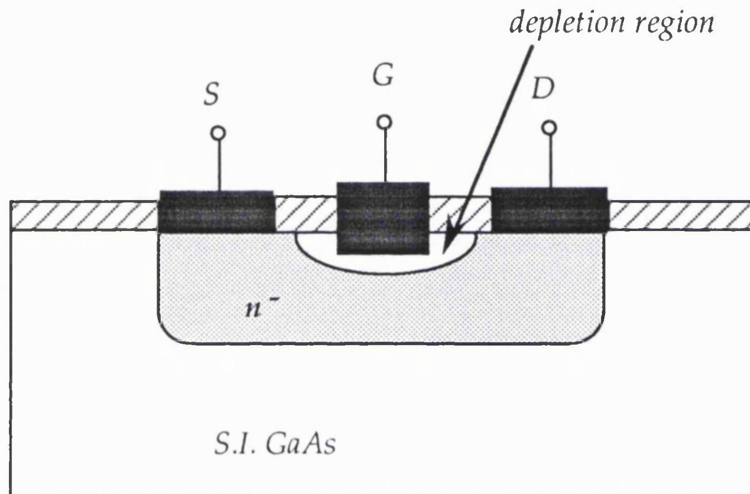

Figure 3.2 Recessed Gate MESFET

Etching processes used in semiconductor technology can be divided into two main groups: wet etching and dry etching. In wet etching, as the name implies, the material is immersed in a liquid, usually an aqueous solution; in dry etching the etchant is gaseous and often ionic, possibly in the form of a beam of particles. There are a considerable number of different processes which come under the general definition of "dry etching", varying from wholly physical, as in inert gas ion beam milling, through combined physical and chemical, as in reactive ion beam etching and chemically assisted ion beam etching, to nearly pure chemical as in reactive ion etching and activated molecular beam etching.

3.2.1 Wet-etching

The object of wet etching is the removal of atoms from the surface of the semiconductor, in a form which is soluble in the etch solution [3.15]. The fundamental reactions underlying semiconductor etching processes are electrochemical in nature. They involve oxidation-reduction reactions, followed by dissolution of the oxidation products, frequently by complexing [3.17].

Oxidation is essentially an electrochemical process in which it is considered that localised anodic and cathodic areas exist at the semiconductor surface. The material goes into solution at anodic sites and the oxidising agent is reduced at cathodic sites. It follows that the more anodic an area, the faster will be its dissolution and as a consequence an etch pit could form. Any external agency which creates electrons and holes at the surface will affect the etch rate, such as illumination or applied currents [3.15].

A considerable variety of possible oxidants and complexing agents may be used, in a considerable variety of relative concentrations, depending on the material to be etched, the required rate of etching, and the possible requirements of preferential etching (etching of a preferred orientation), or selective etching (etching of one material rather than another).

For silicon and germanium, the oxidising agent is usually nitric acid (HNO_3), although hydrogen peroxide (H_2O_2) has also been successfully used with germanium, whilst the complexing agent is hydrofluoric acid (HF) [3.1].

For gallium arsenide and gallium phosphide, the oxidising agent is usually H_2O_2, although others, including HNO_3 have been used, whilst a considerable number of complexing agents have been used, such as sulphuric acid (H_2SO_4), hydrochloric acid (HCl), ammonium hydroxide (NH_4OH) and phosphoric acid (H_3PO_4) [3.1].

The various ongoing steady-state mechanisms in the etching process are:

(a) diffusion of oxidising agent towards the surface;
(b) adsorption of oxidising molecules at active sites on the oxidised surface;
(c) diffusion of oxidising agent or its decomposed product, such as an oxygen atom, through the wholly or partially oxidised surface to reach the oxide-surface interface;

(d) oxidation of the semiconductor atom either at the interface or of an unoxidised atom in the residual layer;
(e) diffusion of the complexing agent molecules towards the oxidised surface;
(f) adsorption of the complexing agent molecules at active sites on the oxidised surface;
(g) complex formation and dissolution of the soluble complexed product into the solvent (usually water) at the liquid-oxide interface;
(h) diffusion of these complexed molecules away from the surface into the bulk of the etching solution.

The process is reaction-rate limited if the supply of oxidant at the surface is always greater than the adsorption rate. This implies a high concentration of oxidising agent compared with complexing agent in the etching solution.

The process is diffusion-rate limited if the supply of oxidising agent through diffusion does not keep up with the adsorption and hence oxidation rate. Diffusion-limited reactions often occur in very viscous etch solutions containing high concentrations of complexing agent and low concentrations of oxidising agent [3.1].

3.2.1.1 Factors affecting etch rates

(i) *Temperature* Etch rates always increase with increasing temperature, since the rates of all the physical and chemical phenomena involved increase as $\exp(-\Delta E/kT)$, with ΔE being the relevant activation energy and T the temperature. Most diffusion phenomena in water-based etchants have activation energies in the range 0.22 to 0.36 eV/molecule, whilst the adsorption process of the oxidising molecule on the surface has an activation energy in the range 0.35 to 0.70 eV/molecule. Hence *reaction-rate* limited etching processes have a stronger temperature dependence than diffusion-rate limited processes.

(ii) *Agitation* The effect of agitation will be to aid the diffusion of oxidising agent towards the surface. Since this is already more than high enough in a reaction-rate limited process, agitation will not affect the etching rate. However, in a *diffusion-rate* limited process, agitation can greatly increase the etching rate.

(iii) *Orientation* All chemical etchants are anisotropic, in that they will etch certain crystal planes preferentially over others. This effect is much more pronounced in a reaction-rate limited etch than in a diffusion-rate limited etch. In a compound semiconductor such as GaAs there is also an effect due to the difference in the readiness with which the two constituent atoms will react with the oxidising agent. A surface exposed trivalent Ga atom in fact has all its bonds satisfied, whilst a similarly surface exposed pentavalent As atom has two dangling bonds and can therefore be oxidised much more readily. Thus the {111}As etch rate is the highest of any orientation in GaAs, and the {111}Ga is the lowest.

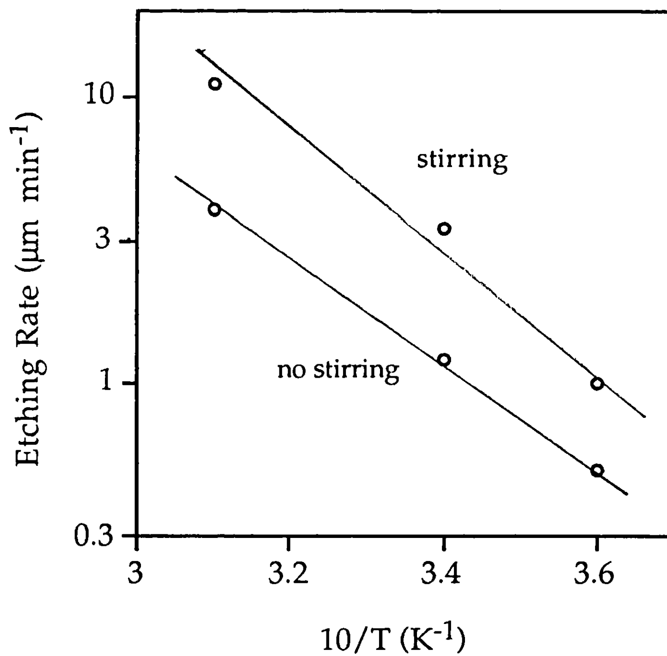

Figure 3.3 The effect of agitation on etching rate for a diffusion-rate limited etch [3.18]

These differences can lead to sloping or undercut edges to etched areas. Sometimes, these effects may be desirable, in which case, aligning of the mask with the crystallographic planes of the wafer should be performed very carefully. More often, these effects are undesirable, and can also lead to non-planar bases to the etched holes [3.19]. If perfectly vertical walls and flat bottoms are desired, it is usually preferable to use a diffusion-rate limited etch solution.

(iv) *Trenching* Another problem may occur with diffusion-rate limited etch processes. This is "trenching", an effect which occurs at the mask edge. In a diffusion-rate limited process, the etch is limited by the supply of oxidising agent. However, at the mask edge, this supply is increased, as there are unused oxidising molecules in the region of the mask itself. Thus, close to the mask, the etch rate can be considerably greater than far from the mask. This is illustrated in figure 3.4.

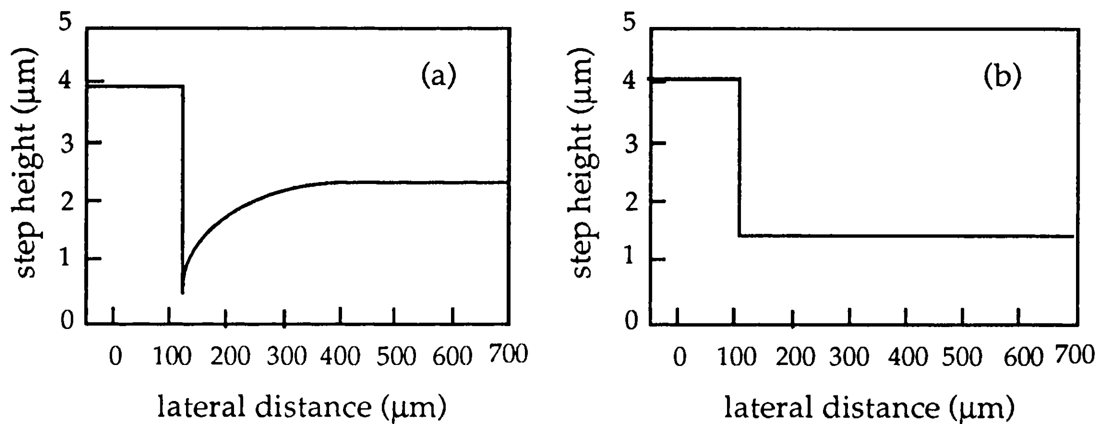

Figure 3.4 Showing (a) the trenching at the mask edge for a diffusion-rate limited etch, (b) flat bottom for a reaction-rate limited etch

3.2.1.2 Chemical Polishing

If the surface has a protrusion, the tip would be exposed to a higher diffusion current of reacting agents than the rest of the surface, and would therefore etch faster. Thus a diffusion-rate limited etchant tends to make a surface smoother [3.1].

3.2.1.3 Choice of Etching Solution

The choice of etchant solution, i.e. which complexing agent to use, and what ratio of reactants to use, will depend on various factors: the etch rate required; whether a reaction-rate limited or diffusion-rate limited etch is

preferred; avoidance of trenching; avoidance of damage to the mask, etc. For example, it has been found [3.20] that $NH_4OH:H_2O_2:H_2O$ will not perceptibly etch SiO_2, although it etches GaAs satisfactorily. However, NH_4OH will attack a photoresist mask, while citric acid does not. H_3PO_4 attacks neither SiO_2 nor photoresist.

Selectivity of etch may also be important. $NH_4OH:H_2O_2:H_2O$, at a pH of 8-8.4 will etch GaAs highly selectively over AlGaAs, (but not if a stainless steel holder is used, due to the galvanic effect) [3.21]. Other pH based selectivities include potassium ferricyanide : potassium ferrocyanide ($K_3Fe(CN)_6:K_4Fe(CN)_6$); $C_6H_4O_2:C_6H_6O_2$; I_2:KI, where changing the pH of the solution changes the selectivity from GaAs over AlGaAs to the reverse. Also $Ce(SO_4)_2.4H_2O : Ce(NO_3)_3.6H_2O$ selects based on doping type [3.22].

3.2.1.4 Residual Oxide Layers

At the end of the etching time, there will be a layer on the surface which has been oxidised, but which has not been dissolved by the complexing agent. Steps (a) to (d) have occurred, but not as yet steps (e) to (h) (see p. 47). The thickness of this residual layer depends on both the etching rate and on the etchant used. In general, the residual layer will be thicker for a slow etchant than for a fast one. Before any further processing can be performed this residual layer must be removed.

This residual oxide layer will be 40Å to 60Å thick, depending on the etchant. Shiota *et al* [3.23] investigated the thickness by monitoring the Auger peaks of oxygen, gallium and arsenic whilst Ar sputtering. They found that this residual oxide layer could be removed by a dip in concentrated HF, followed by a short etch with a slow etchant. The optimal time for the slow etch was 1 minute, after which treatment the oxide layer had been reduced to 10Å or less.

Kohn [3.24] found that only in the case of etching with a high concentration of H_2SO_4 did the residual layer have the properties of a native oxide layer. In all other cases the layer must also have included products of the complexing agent. In the case of citric acid the thickness of the layer *increased* with etching rate, but was very porous and did not adhere well to the surface. It could be removed with a cotton bud.

The most common recipe for removal of the native oxide layer, prior to metallisation to form ohmic or Schottky contacts, is a dip in a moderately concentrated NH_4OH solution. There seems to be considerable leeway in the exact composition of the solution. This gives generally good results.

Wet chemical etching has been used for many years now, and many recipes have been developed, but the inherent problems have not yet been solved. Etching solutions must be prepared with great care and accuracy to ensure that the etch rate and type of etch are as required. A change of concentration can change the type of etch from diffusion-rate limited to reaction-rate limited. As chemicals in the solution are used up, the etch rate will change [3.1], and maybe even the etch type. All etching solutions have the property of etching certain planes preferentially, leading to shapes other than those required for the device. There is always the problem of the residual layer, meaning that the etch itself is a several step process. Wet etching always tends to undercut the mask, leading to loss of definition. The limit of definition for wet etching techniques is of the order ~0.5μm.

3.2.2 Dry etching

Dry-etching involves the use of energetic species, often ionic in nature from a precursor gas in a plasma discharge. The etching process occurs through a combination of chemical reaction (with the formation of volatile compounds containing elements from the semiconductor material) and physical sputtering. For the chemical component of this process, the precursor is often a halogen or halogen containing species.

The imperatives driving the use of dry etching are various.

(i) *Process simplicity* The range of gases used is small compared with the range of chemical solutions used in wet etching, and most are of very general application, they work equally well on most materials, and choice of gas depends as much on choice of dry etching method - whether on mainly physical or chemical - as on material.

The dry etching process is a one, or at most a two, step process, involving direct removal of surface atoms, either elementally or compounded

with a constituent of the beam. There is no prior oxidation required, thus no residual layer to remove subsequently.
(ii) *Better device definition* State of the art device definition, such as VLSI (very large scale integration) or the newest quantum wires and even quantum dots for opto-electronic applications require much better than 0.5μm definition. Quantum wires need to be at most 100Å (or 10nm) wide [3.25], quantum dots, similarly, will be squares of side 10nm. Such accuracy cannot be achieved with any wet etching technique.

To etch specific features on the surface, this process also requires a mask, and can then produce highly anisotropic, straight-walled features through the directionality of the impinging species. However, bombardment of the surface by such energetic species can cause underlying damage, which affects the overall performance of the device.

Alternative dry etching methods, without ion bombardment, involving the use of halogen-containing gaseous species, have also been used [3.26], mainly for *in situ* surface cleaning. Such a technique can indeed produce a damage-free etch, but is not suitable for feature definition as it is no more anisotropic than wet etching.

3.2.2.1 Reactive Ion Etching

Reactive ion etching (RIE) is a commonly used dry etching technique. The standard etcher is a parallel-plate capacitively coupled rf source as described in Chapter 2 (see figure 2.6). The wafer holder is attached to one of the electrodes. A reactive gas, usually a halogen containing species, is introduced and the plasma is fired.

A self bias develops on the electrode due to the sheath potential at the electrode, but an external bias may also be applied.

The etching mechanism involves the spontaneous reaction of the halogen with the material of the semiconductor, such as fluorine with silicon forming SiF_x compounds, or chlorine on GaAs, forming both $GaCl_x$ and $AsCl_3$ volatile compounds. The energy transferred to the surface by the constituents of the plasma then assist in the removal of these products.

Roughness to the surface can be caused by variations in the fluxes of the different constituents, atoms, ions, excited species, electrons and photons,

causing unevenness in the etching of the surface. Damage to underlying layers can be caused by the energy of the impinging species, usually in the range of a few hundred eV.

As plasma potentials of a few hundred volts can develop in parallel-plate etchers, it is to be expected, as described in Section 3.1, that some damage will be caused, due to collisional cascades, in the underlying material of the semiconductor. The question to be answered is whether the amount of damage caused is within acceptable limits.

Damage induced by RIE has been studied, using Rutherford backscattering spectrometry, measuring the barrier heights of Schottky diodes formed on the etched surfaces, Raman spectroscopy and Hall mobility. It was found [3.27] that the number of Ga and As atoms displaced from their lattice sites increased significantly under etching with rf powers of 300W and 500W, the higher power causing more damage. Carrier concentration also decreased significantly [3.27,3.28,3.29], with once again, higher power causing greater depletion, probably due to the formation of traps. The same trend was observed in the barrier heights of Schottky diodes formed on the surfaces, and annealing for 30 min at 400°C did not remove all the damage. Only with the rf power as low as 100W was the surface close to unetched condition. The depth of the damage induced was about 70nm.

ECR plasma etchers are a little less damaging than rf plasma etchers due to the lower sheath potential (see Chapter 2). The increase in displaced atoms after etching is about half that caused by rf plasmas [3.30]. The depth of the amorphous layer formed is about 40 Å. However, there is still a significant degradation of electrical properties.

3.2.2.2 Ion Beam Etching

This is sometimes known as ion milling. A focused beam of ions of an inert gas, usually argon, is directed towards the surface to be etched. This beam is usually provided by a Kaufman type ion beam source, such as those illustrated in Chapter 2, figures 2.10 and 2.11. The energy of the incoming ions is transferred to the substrate, and some substrate atoms are dislodged and removed from the solid surface. This process is known as 'sputtering' [3.8].

This can be a very efficient and highly anisotropic etching process. Sputtering yields (atoms removed/impinging ion) depend on the ion energy and on the relative masses of ion and substrate atom, the latter because this ratio affects the efficiency of energy transfer.

With ion energies in the keV range, sputtering yields between 1 and 3 are found [3.8], but with ion energies of 250eV to 500eV the dependence on ion mass is slight, and sputtering yields are only ~0.5 atoms/ion.

With energies in the keV range, collisional cascades will be important, and as has been shown in Section 3.1, mixing and atomic displacement, as vacancies and interstitials can be caused several hundred Ångstroms beneath the surface.

The damage caused by these energy transfers has been studied by a number of groups. It was found [3.31] that although sputter cleaning of Si with 1keV Ar^+ bombardment, with subsequent annealing left what appeared to be a clean well-ordered surface, as revealed by surface-analysis techniques, TEM examination revealed a considerable increase in density and size of deeper-lying defects.

GaAs and other III-V materials are even more susceptible to underlying damage. The effects of ion mass and energy were investigated [3.32], and lower energy or higher mass was found to introduce less damage. Ar^+ at 500eV and 250eV [3.28] caused considerable damage, which could not be completely annealed out, as shown by attempts to form Schottky diodes on the etched surfaces. These diodes were found to be very leaky. More detail on these Schottky diodes is given in Chapter 5.

Other electrical studies [3.33] of similarly etched GaAs surfaces showed that electrical damage extends several 10s of nm below the surface (hundreds of atom layers). Even for an ion energy of 250eV damage at a depth of 40nm was significant [3.34], and was not completely absent until a depth of 75nm [3.28].

In fact, it has been shown [3.35] by means of deep-level transient spectroscopy that ion energy must be reduced to less than 20eV for perfect damage-free etching.

3.2.2.3 Reactive Ion Beam Etching

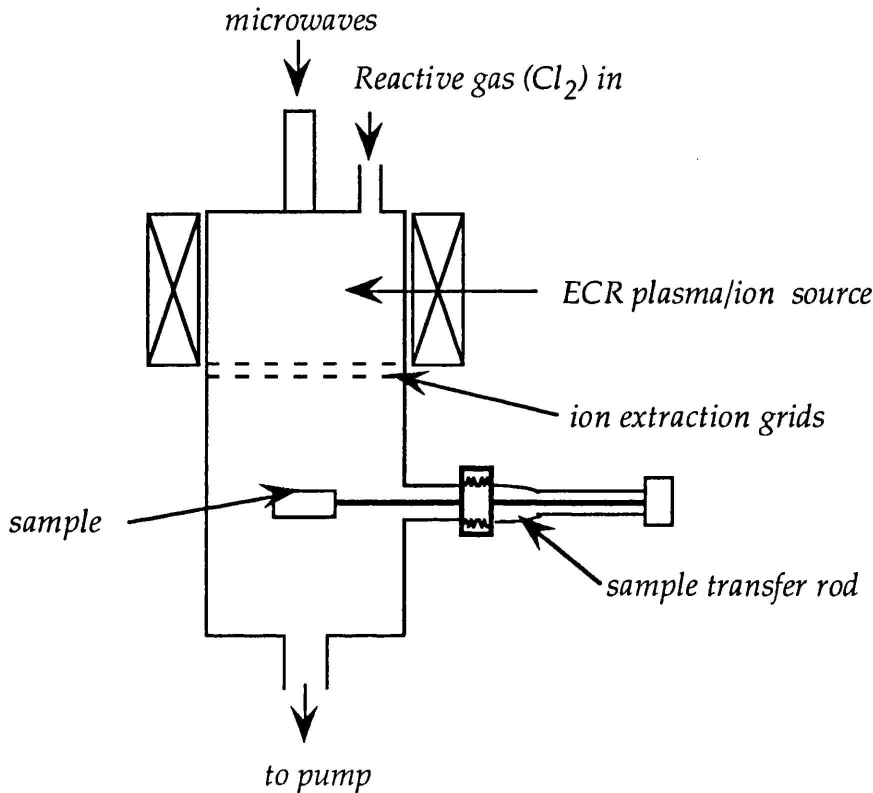

Fig. 3.5 Schematic of a typical RIBE system

The use of a chemically reactive ion beam, rather than an inert ion beam can lead to increases in the sputtering yield. Although the chemical reactions, and formation of volatile products clearly contribute to this increase, the exact mechanisms are more complex than this [3.8].

When a molecular ion is incident on a solid surface it will fragment into its constituent atoms, since the internal binding energy will be low compared with the kinetic energy. Thus it can be expected that the sputtering yield of the molecule will be the sum of the sputtering yields of the constituent atoms. However, experiment has shown that this is not so. Sputtering yields are often less than the predicted sum, as one of the constituent atoms may be deposited on or implanted in the target material. This is particularly common if carbon is a constituent of the impinging molecule (as is often the case).

There is also evidence of some mixing in the surface layer, leading to greater ease of sputtering due to the weaker bonds formed.

The increased sputtering yield means that lower energies or shorter etching times can be utilised, thus reducing the damage caused.

It has been shown that the temperature of the substrate in reactive ion beam etching of GaAs and InP affects the etch rate considerably [3.36]. At room temperature the etch, even with chlorine ions under an extraction voltage of 200V to 500V is little different from ion milling, but at 200°C and energy of 300eV, reactive ions are four times as effective as inert ions, with little voltage dependence over a range 100V to 500V, for the reactive ions. Clearly therefore, at higher temperatures, the chemical component of the etch is dominant over physical sputtering. However, this is accompanied by some loss of anisotropy.

Ormann-Rossiter *et al* [3.37] have shown that not only the energy of the bombarding beam affects the amount of damage caused, but also the ion density. At higher ion densities, >2×10^{16} cm^{-2} the amount of surface damage caused is much reduced, particularly at energies below 500eV. They found, by MEIS (medium energy ion scattering – 100keV H_2^+) that Cl built up in the top 30Å, but that at higher Cl densities, some of the displaced Ga and As atoms in the disturbed surface layers were actually removed, together with some of the Cl, leaving fewer displaced atoms and lower residual chlorine concentration. This is a chemical effect, as it is not predicted by modelling which does not take account of chemistry.

Ormann-Rossiter and Armour [3.38] also studied the interaction of chlorine ions on GaAs at very low energies, 18eV and 108eV, by LEIS (low energy ion scattering – 5keV Ne^+). They found the surface after Cl^+ bombardment to be Ga depleted, the As signal being about twice as strong. This could mean that $GaCl_x$ products were sputtered by the Cl^+ ions, prior to the LEIS analysis. This effect was seen with both Cl^+ ion energies, implying that $GaCl_x$ sputtering needs very little energy, while Ga sputtering by inert Ar^+ ions at 20eV was found to be negligible [3.35].

DLTS of GaAs [3.35] showed that etching by 130eV Cl_2 RIBE induced less underlying damage than 40eV Ar^+ IBE sputter etching. Thus RIBE is less damaging than IBE, but unless the energy, even in this system is ultra-low, some damage will occur.

3.2.2.4 Chemically Assisted Ion Beam Etching

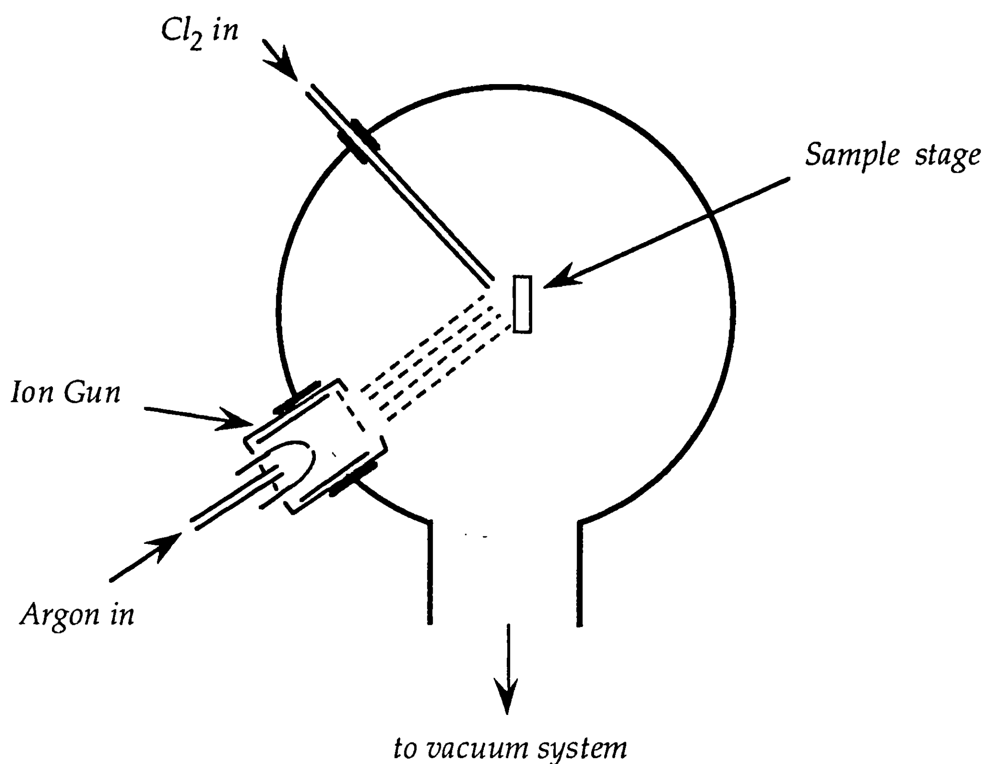

Fig. 3.6 Schematic of a typical CAIBE system

Chemically assisted ion beam etching, sometimes also known as ion beam assisted etching, involves the use of a molecular chemical etchant, which usually contains a halogen, and a separate, inert gas, ion beam. This can be a very closely controlled process to give highly localised and anisotropic etching. There are many variations on the CAIBE theme.

In general, the presence of the ion beam is expected to promote chemical reactions, by producing some mixing of the substrate and the chemical etchant, and giving energy to the process, and the energy of the beam should also help to sputter non-volatile products of the chemical reactions [3.14].

Pang *et al* [3.32] found that adding a flux of chlorine gas directed onto the substrate surface during 500eV Ar^+ bombardment significantly reduced the damage induced, and greatly increased the etch rate. The reduction of

damage was probably due to a combination of adsorption of Cl_2 on the surface as a protective layer, and the increased etch rate. Schottky diodes formed on the etched surface showed only slight reduction in barrier height from the control, and identical ideality factor and breakdown voltage. They also investigated the surface adsorption factor without chemical reaction, using NO_2. Damage was reduced compared with Ar^+ alone, but was greater than with Cl_2 and the etch rate was reduced, compared with Ar^+ alone.

Winters and Coburn [3.39] have shown that the increase in etch rate of ion assisted chemical etching over purely chemical etching is due to ion assistance in the formation of volatile products, and not specifically to bond breaking by the energetic species, nor to sputtering effects. This work concerned the Si-F system, using XeF_2 as the chemical precursor and a 2keV Ar^+ beam. However, the theoretical implications can be applied to other systems where the chemistry is comparable.

Ameen and Mayer [3.40] performed a similar study on GaAs with Cl_2, bombarded with a 1keV Ne^+ beam. This work substantiates that of the previous group [3.39], in that the effect of the ion bombardment appears mainly to be to enhance product formation, and in this way to increase the etch rate. It was found that at high chlorine coverage the main products were $GaCl_3$ and $AsCl_3$, but at low chlorine coverage $GaCl_x$, where $x<3$ were observed too, but at all chlorine levels $AsCl_3$ was predominant. It was also found that after chlorination, the binding energies for atomic Ga and As were much reduced.

Skidmore *et al* [3.41], using Ar^+ at 200eV and Cl_2 found that they could produce a highly anisotropic etch, with a very high etch rate, 0.55μm/min, and smooth resulting surfaces on both the bottom and the side walls if the chlorine was first activated by a plasma. The same system with the plasma off had a much lower etch rate, but was still highly anisotropic. However, there was no investigation of deeper damage.

Meguro *et al* [3.42], used a digital etching technique, whereby Cl_2 gas was allowed to flow onto the surface, the chamber being then purged. This was followed by bombardment with a 100eV electron beam. Each cycle resulted in ~1/3 monolayer being etched, independent of the Cl_2 flux or electron current density. Thus the process must be limited by the chemisorption of chlorine at the surface. This process could allow for very fine control of etch depth. The etched surface appeared mirror-like after 500 cycles.

Kosugi *et al* [3.43] have used a focused Ga^+ ion beam with Cl_2 gas to perform maskless etching, which would be required for a completely *in situ* fabrication process. Damage was observed by measuring photoluminescence intensities. For a beam of 200eV, the PL intensity returned to the unetched value after annealing at 600°C. At higher energies the damage could not be annealed out. A channel 1μm in width was etched with a rough bottom, using a 1keV Ga^+ beam.

CAIBE is a promising technique for highly controlled maskless *in situ* anisotropic etching, but repeated high temperature annealing, as has been mentioned before, can lead to loss of definition in a device. Therefore it will need a very low energy beam to be a damage-free process for III-V materials.

3.3 Thin Film Growth: comparison of methods

The growth of bulk semiconductor materials is generally by a crystallisation from the melt. A small seed crystal is used to initiate it, and from this very large, very pure single crystals can be grown.

However, for the fabrication of actual devices, thin layers of deliberately doped material are needed, to increase the carrier concentration, of either negative (electron) carriers or positive (hole) carriers, by the introduction of donor or acceptor impurities, in carefully controlled amounts. Usually, this will mean growing an epitaxial layer, that is, one in which the crystal structure of the layer matches that of the substrate. However, the composition of the epitaxial layer will be different from that of the substrate. If the layer is mainly of the same material, with or without intentional impurities added, it is known as homoepitaxy. If the layer is chemically different, but has a lattice constant very close to that of the substrate it is known as heteroepitaxy.

Dielectric layers, which are not necessarily crystalline are also needed, and metallisations, in order to complete the device geometry.

There are many ways to grow thin layers, and new ones are continuously being devised, to achieve greater control of the growth conditions. The different growth methods can be arranged acording to the

sources they use, and the pressures at which they operate, which range from atmospheric to ultra-high vacuum. These can be summarised for the growth of III-V materials in the Table 3.1.

METHODS	SOURCES	PRESSURE (torr)	GAS FLOW
High Pressure Chemical Vapour Deposition	Vapour Sources III,V (↕)	760	Viscous Flow (↕)
Low Pressure Chemical Vapour Deposition		300 / 10^{-2}	
Chemical Beam Epitaxy		$\lesssim 10^{-4}$	Molecular Flow (↕)
Metal-Organic Molecular Beam Epitaxy	Vapour Source III Solid Source V	$\lesssim 10^{-5}$	
Gas Source Molecular Beam Epitaxy	Solid Source III Vapour Source V	$\lesssim 10^{-5}$	
Molecular Beam Epitaxy	Solid Sources III,V	$\lesssim 10^{-9}$	

Table 3.1 Relationship between the various epitaxial methods [3.54]

The terms are defined thus; "chemical" is used if there is a definite chemical reaction taking place, that is, if the vapour is a compound containing the species to be deposited which dissociates at the growing surface: "molecular" is usually used if at least one of the species to be deposited is in elemental form.

Among these is a variation on the chemical vapour depositon (CVD) theme, plasma assisted (or sometimes "plasma enhanced") CVD. In this method, the vapour containing the species to be deposited is excited into a plasma, which increases the chemical reactivity, thus promoting the growth process.

3.3.1 Molecular Beam Epitaxy

One of the earliest methods, pioneered in the 1960s is molecular beam epitaxy (MBE) and it is still extensively used [3.44]. The species required for growth are vapourised in heated effusion cells, the vapour produced guided into a molecular beam from the orifice of the effusion cell by a series of slits and shutters. A number of such cells may be incorporated into the system, to vary the composition of the growing layer.

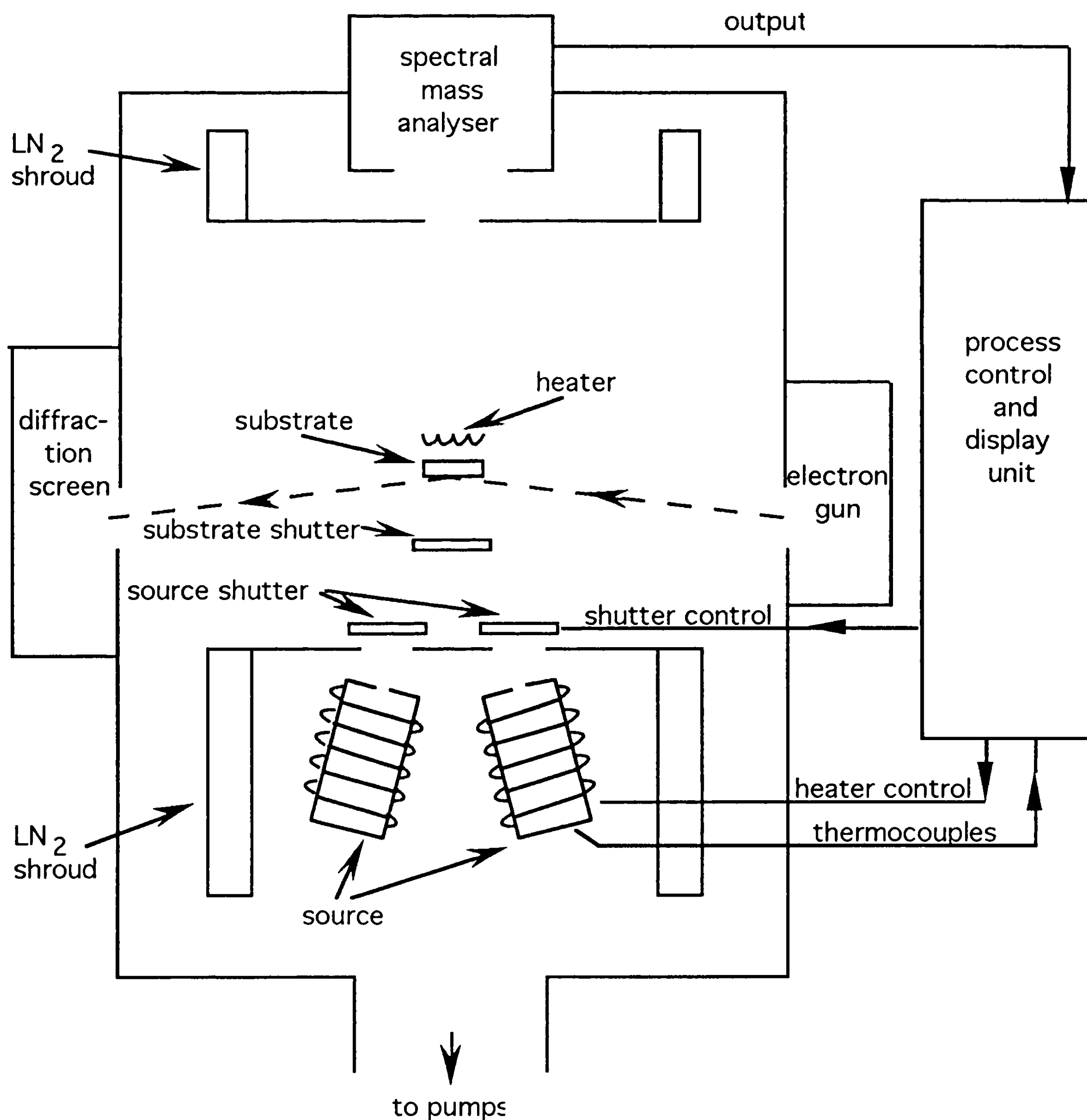

Fig. 3.7 Schematic diagram of a molecular beam epitaxy system

The system must be evacuated to a high vacuum ($<10^{-9}$ Torr) prior to growth, to minimise beam collisions and contamination. The rate of film growth depends not only on the arrival rate of species at the surface, but also on the surface reactions, ie adsorption or capture of impinging molecules, surface diffusion and association of the molecules resulting in nucleation and growth.

For GaAs, the growth rate is essentially determined by the Ga arrival rate, so long as there is a sufficiency of As, as the volatility of As assures a stoichiometric growth over a wide range of As vapour concentration.

The quality of film grown by this technique is very high. By 1972 [3.45] and 1973 [3.46] MBE was used to grow GaAs/GaAlAs superlattices with a period of about 100Å.

3.3.2 Chemical Vapour Deposition

Another early technique still much used is chemical vapour deposition (CVD). This technique, unlike MBE is operated at high pressures, up to atmospheric pressure, with a large excess of a carrier gas, commonly hydrogen, helium or nitrogen [3.47]. The source species are either compounds gaseous at room temperature which contain the species to be deposited, or a vapour at the reactor temperature. The gaseous molecule dissociates on the surface, depositing the species required, the volatile residue being removed by the carrier flow.

Close control of the composition of the epitaxial layer can be exercised by adjusting the flow rates of the source gases. Growth of the layer is under near equilibrium conditions which means fewer crystalline imperfections than some other techniques. Also, it is straightforward to process a number of wafers at the same time, so long as the reactor design allows for variations in gas concentrations and temperatures. Figure 3.8 shows two designs, but there are many others. Sometimes a multi-wafer chamber is tilted, to compensate for the change in concentration of the source gases through the chamber.

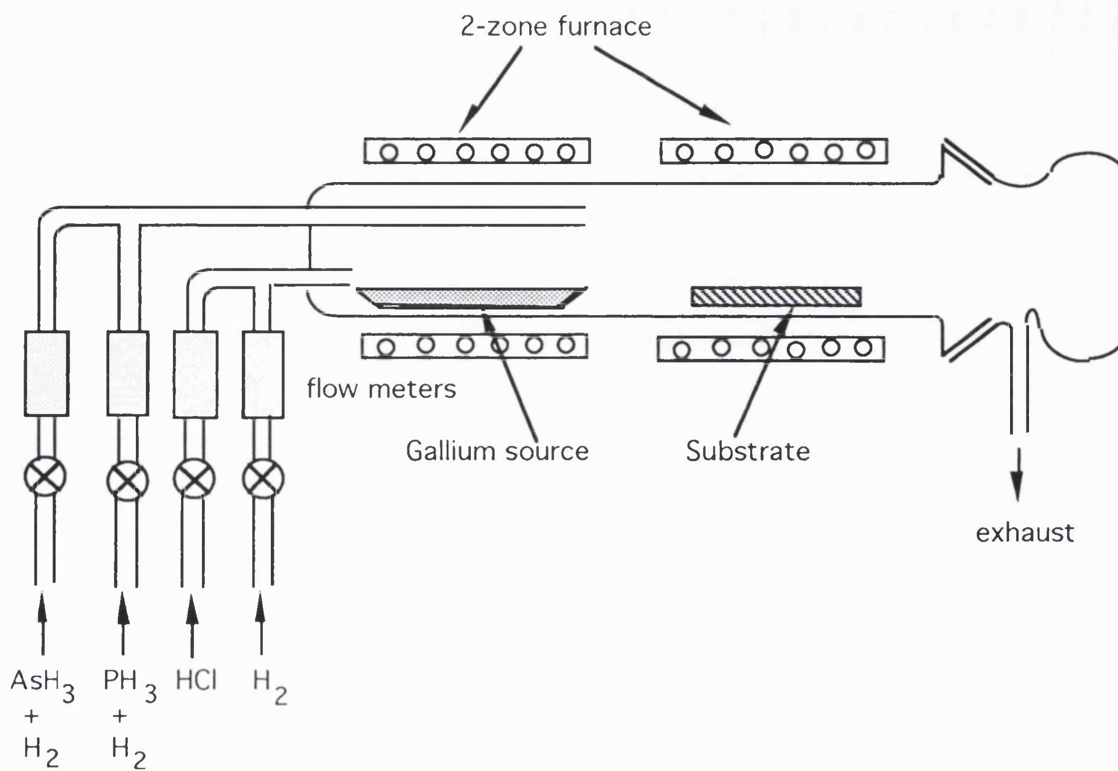

Fig. 3.8 (a) Schematic of a horizontal CVD epitaxial system for a ternary material

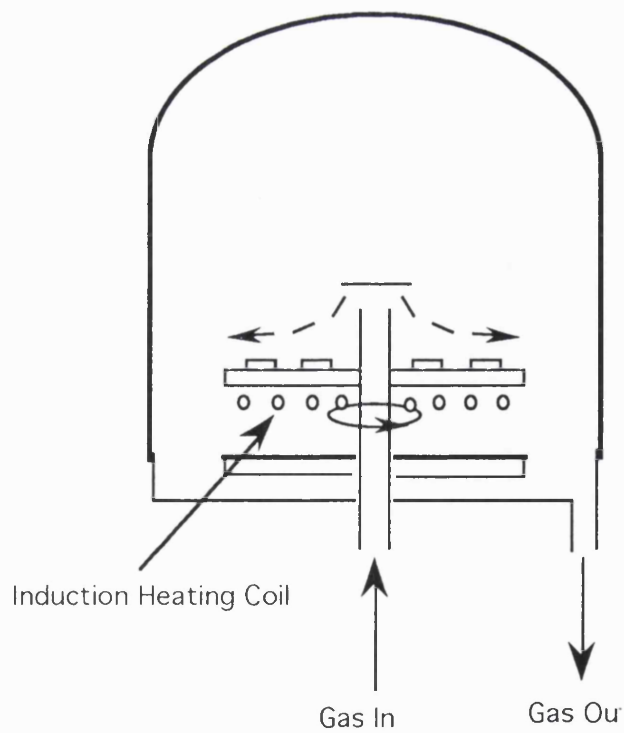

Figure 3.8 (b) Schematic of a vertical CVD epitaxial system

In a CVD reactor, the reactants flow past the growing surfaces, in the stream of the carrier gas. All fluids, including gases, have some viscosity, which means that at the substrate surface there is a boundary layer, within which the reactant gases may become depleted. Thus the growth rate will depend on the diffusion rate of the reactant gases, as well as the surface reaction rate. The diffusion rate will depend on both the diffusivity of the reactant gases, and the thickness of the boundary layer, which in turn depends on the viscosity, the density and the flow rate of the gas [3.47].

The surface reaction rate is always highly temperature dependent. All chemical reactions are in theory reversible. In general, in one direction the reaction will be exothermic, that is the energy released by the reaction is greater than the activation energy, in the reverse direction , the reverse is true, and the reaction is said to be endothermic. If the required reaction at the surface is exothermic, then the surface should be cooler than the walls, where the reverse endothermic reaction may take place. Reactors designed for this type of reaction are "hot wall" reactors, where the substrate is heated by radiation from the walls. If the required reaction is endothermic, the substrate must be the hottest part of the reactor, and is therefore heated directly.

Reduced pressure CVD will improve the rate of diffusion of reactants across the boundary layer, thus improving the uniformity of film growth, allowing greater wafer packing density and higher productivity. But with a low pressure within the reactor, the reactor must be in effect a vacuum system, particularly as the reactant gases are often dangerous, and will be much less dilute than in a high pressure system. The exhaust from such a system must be carefully disposed of.

Chemical vapour deposition is used to grow silicon dioxide, used as an insulating layer between conducting layers, silicon nitride, used as a mask for selective oxidation of substrates, and polycrystalline silicon, often used for the gate of a MOS transistor, as a resistor or as a link between metallisation and substrate to ensure ohmic contact.

3.3.2.1 Plasma Enhanced Chemical Vapour Deposition

For the deposition of some materials, the cracking of the gaseous compounds containing the species to be deposited requires considerable

energy. This is usually provided by heating of the growing surface. However, this heating is not always desirable, some substrate materials may be damaged by it, and another means of activating the chemical reactions has to be found. Creating a plasma in the gas is one well-established method. Plasma enhanced CVD is a low pressure CVD process, since plasmas cannot be maintained at very high pressures.

Commonly, a plasma enhanced CVD apparatus is very similar to a standard plasma etcher, that is, a radio-frequency, capacitive, parallel-plate plasma source, as described in Chapter 2.

Amorphous silicon, silicon dioxide and silicon nitride are commonly grown this way, on a variety of substrates, such as aluminium or polymers, which could not be heated to the >700°C normally required [3.58].

This method has also been used to grow diamond-like carbon (DLC) coatings, a very hard, amorphous, hydrogen-containing carbon material, used mainly as protective coating layers, although it does also have some interesting and useful electronic properties.

PECVD is also used to grow thin film diamond coatings, but in this case, the plasma must be formed by means of microwave excitation, and not by parallel-plate, rf, capacitive excitation as for the other materials cited [7.16-7.18]. The reason is the difference in the properties, plasma density and ion energy, of the plasmas formed by the different methods. The requirements for the growth of diamond are very exacting, and will be described in detail in a later chapter.

3.3.2.2 Vapour-Phase Epitaxy

This is a special case of Chemical Vapour Deposition, in which the layer deposited is grown epitaxially.

To grow a layer epitaxially, the surface must be atomically clean, and the growth rate must be slow enough to allow each atom deposited to move into the correct location. The substrate surface is heated to increase the mobility of surface atoms, thus allowing them to form the required crystal structure.

A number of materials can be grown this way, either undoped or doped, such as silicon from silane, or gallium arsenide from a number of different sources, such as arsine and gallium chloride.

3.3.2.3 Metalorganic Chemical Vapour Deposition

In traditional CVD, the metallic components of any epitaxial layer were still pure metal vapour, as suitable gaseous species for metallic deposition are not naturally occurring. For example, silane, SiH_4 is a simple compound, and gaseous at room temperature, making it a very suitable source of Si, as similarly are $AsCl_3$ and AsH_3 for As. But $GaCl_3$ is not gaseous at room temperature, and indeed no simple Ga containing gaseous species exists, which would deposit Ga on a surface.

But organometallic compounds such as triethylalkyls and trimethylalkyls of Al, Ga etc. can be formed which are gases at room temperature, and on reaching the surface, deposit the metal atom, releasing the simple organic gaseous adducts.

However, promising though this process should be, there are problems. The growth rate can be much reduced by parasitic reactions between the organometallic molecules and the group V hydrides, forming polymeric contamination on the reactor walls upstream from the substrate [3.48]. Another serious problem is carbon contamination of the epitaxial layer [3.49,3.50]. Although in theory the ethyl or methyl adducts should leave the surface as gases to be removed in the flow of carrier gas, some cracking of these groups does occur on the surface, depositing carbon, particularly in the growth of AlGaAs, since the presence of Al very much enhances the tendency for carbon incorporation in the film. This has been attributed to the transfer of of ethyl groups from ethylgallium molecules to atomic aluminium, thus forming ethylaluminium compounds on the surface [3.49]. Lower carbon levels result if ethyl or isobutyl groups replace the methyl ligands in the Group III precursor. But although the carbon level is reduced it is not eliminated.

One possible new type of precursor is a trimethylamine hydride, such as $AlH_3(NMe_3)_2$ and $GaH_3(NMe_3)$. In these species there are no metal-carbon bonds, so the possibility of carbon incorporation is very low indeed.

$AlH_3(NMe_3)_2$ has been used to grow Al film of very high purity [3.51], and to deposit Al on GaAs as a mechanism for AlGaAs growth [3.52,3.53], with no carbon found on the surface.

3.3.3 Metalorganic Molecular Beam Epitaxy and/or Chemical Beam Epitaxy

There is some confusion over the uses of the terms MOMBE and CBE. Tsang [3.54] differentiates between them by the source for the group V element. In his schema MOMBE implies a solid source for the group V element and a vapour source for the group III, while CBE implies a vapour source for both, a differentiation apparently agreed by some [3.55,3.56] while others [3.57] claim to be using MOMBE with all vapour sources. In general, the motivation for the development of this technique is to combine the advantages of MBE and MOCVD. The beam nature allows the preparation of semiconductor heterostructures with monolayer precision, while the use of vapour sources eases multiwafer scaleup and precise reproducibility. CBE is a high vacuum process.

The advantages of CBE over MBE, in other words of having sources which are gaseous at room temperature rather than using heated effusion cells is in the reproducibility. The flux from an effusion cell is highly dependent on the temperature, and also on the surface area of material in the cell, and hence can change with time. The flux of a gaseous source is precisely controllable with electronic flow-meters and is hence very reproducible. Another advantage of CBE is that these vapours can be premixed for the growth of doped layers, making the level of dopant incorporated precise and reproducible [3.54].

With MOCVD thickness and composition variations can occur due to flow patterns in the high pressure gas system. There can also be gas phase reactions. With CBE, these problems are eliminated, as is the doping memory effect. Also, with CBE only very small amounts of material are required, and any residues (which will be minimal) will have been cracked into their constituent elements. Since arsine and phosphine are toxic, disposal of the exhaust gases in MOCVD is a problem, but with CBE there is very little to dispose of, and the likelihood is that it will have become hydrogen and solid

arsenic or phosphorous, thus disposal is much easier and safer. As in MBE, *in situ* monitoring of growth can be incorporated into the system [3.54].

The only problems left are the devising of precursors which do not leave any contaminants.

3.4 Ideal Source Requirements

3.4.1 For Etching III-V Materials

III-V semiconductor materials are effectively etched by chlorine, and the etch rate is much greater for chlorine ions than for Cl_2 gas. Highly anisotropic etching is required.

The source should be an ion beam source, which is tolerant of reactive gases, such as chlorine, freon, and oxygen, but a capacitively coupled rf plasma source would be the simplest and most efficient, so the electrodes would have to be separated from the plasma chamber, which should be lined with a very non-reactive material.

The ion beam should be of very low energy, below 20eV [3.12] to avoid any underlying damage to the semiconductor material, which would perturb the performance of the device.

It would be an advantage if the source could be used with either Cl_2 or Ar, in RIBE or CAIBE configurations, depending on the required etch rate, and depth control.

3.4.2 For Plasma Enhanced CVD

Very high plasma densities with very low energies are required for PECVD thin film growth of sensitive materials. Ideally this would be coupled with a large, uniform, processing area. Thus the ideal would be a capacitively coupled rf plasma source, for large uniform plasma, with efficient and simple

operation, but of much higher plasma density and much lower ion energy than is commonly found in such sources.

This would imply a totally new design of source.

In fact, requirements for both these applications are very similar.

3.5 References

3.1 S. D. Mukherjee and D. W. Woodard in *Gallium Arsenide Materials, Devices and Circuits* ed. M. J. Howes and D. V. Morgan Wiley (1985)

3.2 S. M. Sze *Semiconductor Devices Physics and Technology* Wiley (1985)

3.3 J. Linhard, M. Scharff and H. Schiott *Mat. Fys. Med. Dan. Vid. Selsk* **33** 1 (1963)

3.4 P. Sigmund *Phys. Rev.* **184** 383 (1969)

3.5 P. Sigmund and A. Gras-Marti *Nucl. Instr. & Meth.* **182/3** 25 (1981)

3.6 U. Conrad and H. M. Urbassek *Nucl. Instr. & Meth.* **B48** 399 (1990)

3.7 Y. Yamamura and J. Bohdansky *Vacuum* **35** 561 (1985)

3.8 P. C. Zalm *Vacuum* **36** 787 (1986)

3.9 B. M. Paine and R. S. Averback *Nucl. Instr. & Meth.* **B7/8** 666 (1985)

3.10 R. A. Weller and M. R. Weller *Nucl. Instr. & Meth.* **194** 573 (1982)

3.11 Y. T. Cheng, A. A. Dow and B. M. Clemens *Appl. Phys. Lett.* **53** 1346 (1988)

3.12 M. L. Yu, D. Grishkowsky and A. C. Balent *Phys. Rev. Lett.* **48** 427 (1982)

3.13 P. Sigmund *J. Vac. Sci. Tech.* **A7** 585 (1989)

3.14 R. B. Jackman and G. C. Tyrrell *Proc. of 8th Int. Conf. on I.P.A.T.* 102 (1991)

3.15 D. J. Stirland and B. W. Straughan *Thin Solid Films* **31** 139 (1976)

3.16 A. C. Adams and B. R. Pruniaux *J. Electrochem. Soc.* **120** 408 (1973)

3.17 W. Kern *RCA Rev.* **39** 278 (1978)

3.18 Y. Mori and N. Wanatake *J. Electrochem. Soc.* **125** 1510 (1978)

3.19 S. Iida and K. Ito *J. Electrochem. Soc.* **118** 768 (1971)

3.20 J. J. Gannon and C. J. Nusse *J. Electrochem. Soc.* **121** 1215 (1974)

3.21 K. Kenefick *J. Electrochem. Soc.* **129** 2380 (1982)

3.22 D. P. Tijburg and T. van Dongen *J. Electrochem. Soc.* **123** 687 (1976)

3.23 I. Shiota, K. Motoya, T. Ohmi, N. Miyamoto and J. Nuhizawa *J. Electrochem. Soc.* **124** 155 (1977)

3.24 E. Kohn *J. Electrochem. Soc.* **127** 505 (1980)

3.25 A. Izrael, B. Sermage, J. Y. Marzin, A. Ougazzaden, R. Azoulay, J. Etrillard V. Thierry-mieg and L. Henry *Appl. Phys. Lett.* **56** 830 (1990)

3.26 N. Furuhata, H. Miyamoto, A. Okamoto and K. Ohata *J. Appl.Phys.* **65** 168 (1989)

3.27 T. Hara, H. Suzuki, A. Suga, T, Terada and N. Toyoda *J. Appl. Phys.* **62** 4106 (1987)

3.28 S. W. Pang, G. A. Lincoln, R. W. McClelland, P. D. DeGraff, M. W. Geis and W. J. Piacenti *J. Vac. Sci. Technol.* **B1** 1334 (1983)
3.29 O. J. Glembocki and E. A. Dobisz *J. Vac. Sci. Technol.* **B9** 1403 (1991)
3.30 T. Hara, J. Hiyoshi, H. Hamanaka, M. Sasaki, F. Kobayashi, K. Ukai and T. Okada *J. Appl. Phys.* **67** 2836 (1990)
3.31 J. C. Bean, G. E. Becker, P. M. Petroff and T. E. Seidel *J. Appl. Phys.* **48** 907 (1977)
3.32 S. W. Pang, M. W. Geis, N. N. Efremow and G. A. Lincoln *J. Vac. Sci. Technol.* **B3** 398 (1985)
3.33 A. Scherer, H. G. Craighead, M. L. Roukes and J. P. Harbison *J. Vac. Sci. Technol.* **B6** 277 (1988)
3.34 R. Germann, A. Forchel, M. Bresch and H. P. Meier *J. Vac. Sci. Technol.* **B7** 1475 (1989)
3.35 J-Z. Yu, N. Masui, Y. Yuba, T. Hara, M. Hamagaki, Y. Aioyagi, K. Gamo and S. Namba *Jap. J. Appl. Phys.* **28** 2391 (1989)
3.36 T. Tadakoro, F. Koyama and K. Iga *Jap. J. Appl. Phys.* **65** 168 (1989)
3.37 K. G. Orman-Rossiter, R. S. Bhat, R. Badheka, M. Wadswirth and D. G. Armour *Nucl. Instr. & Meth.* **B36** 446 (1989)
3.38 K. G. Orrman-Rossiter and D. G. Armour *Nucl. Instr. & Meth.* **B42** 334 (1989)
3.39 H. F. Winters and J. W. Coburn *J. Vac. Sci. Technol.* **B3** 1376 (1985)
3.40 M. S. Ameen and T. M. Mayer *J. Appl. Phys.* **63** 1152 (1988)
3.41 J. A. Skidmore, L. A. Coldren, E. L. Hu, J. L. Merz and K. Asakawa *Appl. Phys. Lett.* **53** 2308 (1988)
3.42 T. Megura, M. Hamagaki, S. Modaressi, T. Hara, Y. Aoyagi, M. Ishii and Y. Yamamoto *Appl. Phys. Lett.* **56** 1552 (1990)
3.43 T. Kosugi, K. Gamo, S. Namba and R. Aihara *J. Vac. Sci. Technol.* **B9** 2660 (1991)
3.44 L. L. Chang and R. Ludeke in *Epitaxial Growth Part A* ed. J. W. Matthews Academic Press 37 (1975)
3.45 L. Esaki, L. L. Chang, W. E. Howard and V. L. Rideout *Proc .11th Int. Conf. Phys. Semicond.* 431 (1972)
3.46 L. L. Chang, L. Esaki, W. E. Howard and R. Ludeke *J. Vac. Sci. Technol.* **10** 11 (1973)
3.47 D. W. Shaw in *Epitaxial Growth Part A* ed. J. W. Matthews Academic Press 89 (1975)
3.48 G. B. Stringfellow *J. Cryst. Growth* **70** 133 (1984)

3.49 B. J. Lee, Y, M. Houng, J. N. Miller and J. E. Turner *J. Cryst. Growth* **105** 168 (1990)

3.50 T. F. Keuch, E. Veuhoff, T. S. Kuan, V. Deline and R. Potemski *J. Cryst. Growth* 77 257 (1986)

3.51 W. L. Gladfelter, D. C. Boyd and K. F. Jensen *Chem. Mater.* **1** 339 (1989)

3.52 J. S. Foord, A. J. Murrell, D. O'Hare, N. K. Singh, A. T. S. Wee and T. J. Whitaker *Chemtronics* **4** 262 (1989)

3.53 A. T. S. Wee, A. J. Murrell, N. K. Singh, D. M. O'Hare and J. S. Foord *Vacuum* **41** 968 (1990)

3.54 T. S. Tsang *IEEE Circuits and Devices* **4(5)** 18 (1988)

3.55 K. Ozasa, M. Yuri and H. Matsunami *J. Cryst. Growth* **102** 31 (1990)

3.56 N. Furuhata and A. Okamoto *J. Cryst. Growth* **102** 814 (1990)

3.57 H. Heinecke, K. Werner, M. Weyers, H. Lüth and P. Balk *J. Cryst. Growth* **81** 270 (1987)

3.58 D. W. Hess and D. B. Graves in *Microelectronics Processing: Chemical Engineering Aspects* ed. D. W. Hess and K. F. Jensen A.C.S. (1989)

CHAPTER 4: NOVEL SOURCE DESIGN, CONSTRUCTION, AND CHARACTERISATION

4.1 Requirements and Problems

An ideal plasma source for the applications outlined in the previous chapter is required to have a very high plasma density, with a very low ion energy. It is also required that the ions from the plasma can be directed into a broad uniform beam of high directionality but ultra-low energy, (~20eV), to avoid all possibility of damage to materials such as GaAs, when the source is used for etching.

At present, the highest plasma densities are found in microwave sources, and are approximately 10^{10} cm^{-3} at a pressure of 10^{-3} mbar and a power of 100W [4.1], to $3x10^{11}$ cm^{-3} at a pressure of 10^{-4} mbar and a power of 500W [4.2].

The ideal source would be flexible, so that it could be used for either etching or deposition. Currently available broad beam sources are either dc [4.3,4.4] or rf, both inductively coupled [4.5] and capacitively coupled [4.6,4.7,4.8]. For etching, reactive gases such as chlorine and oxygen are used, and these species cause considerable degradation of the electrodes used in both dc and capacitively coupled sources. Thus it would seem that microwave or inductively coupled rf are superior for use with reactive gases, as these are both electrodeless systems. However, there are other problems with both of these systems. A silicon wafer is of 15 cm diameter, and modern growth methods are producing wafers of up to 25 cm diameter, so the beam needs to be somewhat larger than this, to be uniform over the area of the wafer, and it is not possible to make such a broad beam from a microwave plasma ball of diameter 7.5 cm to 10 cm. There is no problem with scaling up inductively coupled rf plasma sources, and indeed the example quoted, designed by Proudfoot *et al*, [4.5] had a beam uniform over a diameter of nearly 15 cm, which could easily have been made larger. However, it required an input power of 3kW [4.9] to produce a sufficiently dense plasma for their beam.

4.2 Theoretical solution

Gagné and Cantin, in 1972, [4.10] used a capacitively coupled rf plasma source with two ring electrodes around the outside of a pyrex cylinder. This design has some of the requirements of the ideal source, in that the electrodes are separated from the plasma and thus cannot be degraded by any reactive gas used.

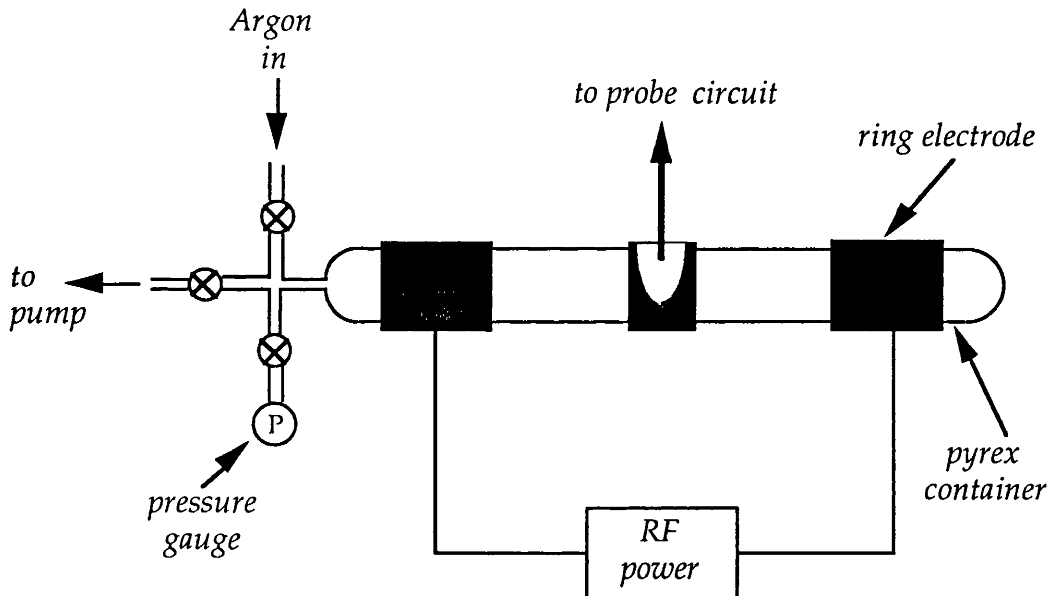

Fig. 4.1 Schematic diagram of the rf plasma facility of Gagné and Cantin

Magnetic enhancement is known to increase the plasma density in capacitively coupled sources, by at least an order of magnitude [4.11]. If the magnetic field is parallel to the electrode surface, electrons will be forced to precess around the magnetic field lines, and will not be lost at the boundary. Magnetic enhancement also reduces the sheath potential. The electron mobility in the direction of the field is reduced, so that equilibrium between ion and electron currents is reached at a lower potential [4.11]. Thus the ion energy will be reduced, which is also one of the requirements. The simplest and most effective way to implement a magnetic field in a capacitively coupled source is with permanent magnets, Sm-Co magnets being commonly used for this [4.6].

4.3 Implementation

In collaboration with Ion Tech Ltd. a novel capacitively coupled rf plasma source has been developed.

To design an ion beam source, meeting the requirements of broad, uniform beam, of ultra-low energy (~20eV) ions, and high current density, without causing erosion of the electrodes, some of the best features of these earlier designs were adopted.

Ring electrodes, (as in the design of Gagné and Cantin), outside the open, cylindical chamber, to stop sputtering and corrosion, were chosen, but to increase the uniformity and density of the plasma, more rings than the two in their design were used. This first prototype version is relatively small, so no more than seven electrodes could be fitted. The rings are alternately powered and earthed, with the earthed rings at the ends of the chamber, to avoid distortion of the beam.

To increase the plasma density further, and also reduce the sheath potential, magnetic enhancement, using a cusped, multipole field, provided by Sm-Co magnets, as in the source designed by Lossy and Engemann [4.6], was incorporated. As the magnetic field must be parallel to the surface of the electrodes, the magnets are between the rings of electrodes, forming similar rings. The polarity of the magnets alternates from ring to ring, with all the magnets in one ring having the same pole facing inwards. In the initial configuration of the source, using the figures published by Lossy and Engemann, and taking into account the smaller dimension of this source, twelve sets of magnets, three to a set, were used for each ring. This allows the magnetic field to penetrate quite far into the chamber. There are also magnets above the base plate, of opposite polarity to that of the nearest ring.

Using this unusual configuration, with the magnetic field parallel to the electrode surfaces, with ring electrodes, the two kinds of field are parallel, instead of crossed as in other magnetically enhanced, capacitively coupled sources. Unfortunately, no models of such a plasma, with parallel fields, have been published.

To keep the energy ultra-low, no accelerating grid is used, the length of the cylindrical chamber, (150mm), providing sufficient collimation for the beam, which is extracted then solely by the action of the vacuum pumping

system. This cylindrical chamber is lined with fused silica, to be non-reactive. To close the chamber at the top end there is a stainless steel base-plate. This is kept at earth potential, matching the potential of the nearest electrode ring. This acts also as a source of electrons to initiate the plasma, which can therefore be fired at very low powers, below 50 W.

If, for other applications of the source, a higher energy ion beam is required, there is provision for the attachment of a grid, but this is not essential to the operation of the source.

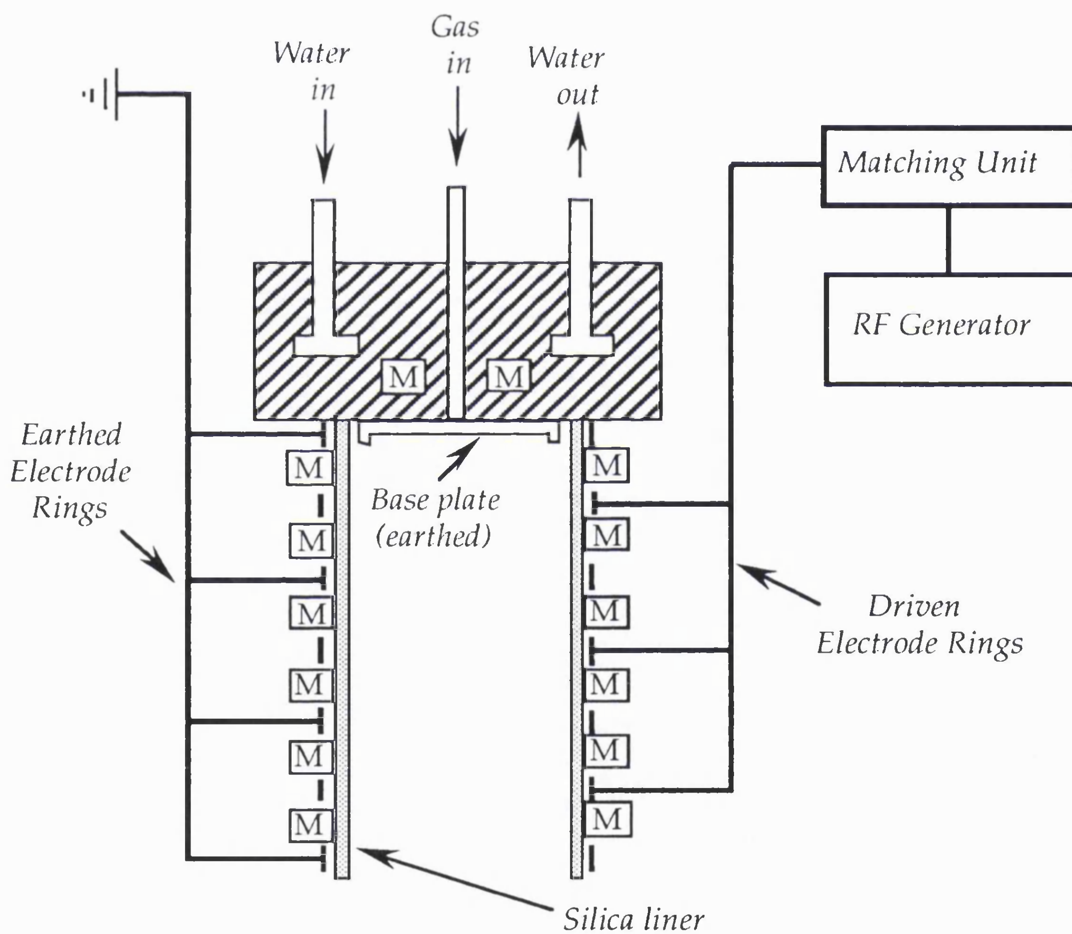

Fig. 4.2 Schematic diagram of the structure of the Ion Tech RF source

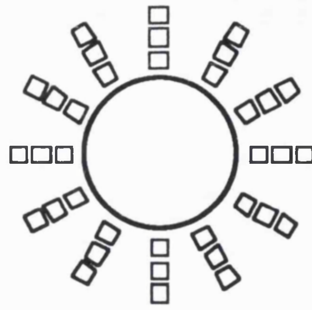

Fig. 4.3 Arrangement of magnets around Ion Tech RF source

The electrode separation is 2 cm, so quite high fields can be achieved without very high voltages, (the maximum output of the power supply used is 500V, so that electrode potentials are routinely much less than this), whilst the multiplicity of electrodes means that a large, uniform plasma volume can be sustained. The power supply is connected to the source via a manually controlled matching unit.

Sm-Co magnets will lose their magnetisation if heated above 200°C, so the source must be cooled whilst in operation. A water cooled chamber is attached to the base plate, and aluminium struts supporting the electrodes also conduct away the heat generated by the plasma to the water cooled chamber.

This prototype experimental source is quite small, the chamber being 90mm internal diameter and 150mm long, but there is no theoretical reason why it could not be larger.

In this design, the substrate to be processed is to be held either at the chamber aperture, if plasma processing is required, where, although immersed in the plasma, the substrate surface is perpendicular to the electric field, and thus the ion bombardment energy should be very low, or, some distance downstream of the plasma, if beam processing is required. The source is encased in a stainless steel jacket, specifically designed to be compatible with a 200mm six-way cross vacuum system. This allows for maximum flexibility in the use and testing of the source. Because of the presence of the Sm-Co magnets the system cannot be baked, and so cannot be used at ultra-high vacuum (UHV) but pressures of less than 10^{-7}mbar were regularly achieved.

In later use of the source with reactive gases, this casing design was found to be less than perfectly satisfactory, as the outer parts of the source were not isolated from the gases in the chamber. Eventually, this led to problems with the operation of the source.

4.4 Characterisation of the source

The initial characterisation measurements were made at Ion Tech Ltd., further measurements and calculations were performed at UCL.

4.4.1 Characterisation of the Plasma

Using a planar Langmuir probe, of effective surface area 0.95 cm^2, I-V measurements were taken, with the probe at the aperture of the source. A range of powers were utilised from 50W to 500W. The gas was argon at a pressure of 7.5×10^{-4} mbar.

Figure 4.4 shows the probe I-V curves obtained at each value of the input power. In accordance with convention (see Chapter 2), the electron current is drawn as positive, and the ion current negative. It can be seen that the ion current for a given probe bias increases with increasing RF power. This is due to the increasing plasma density as the power is increased.

4.4.1.1 Electron Temperature

Figure 4.5 is a logarithmic plot of corrected electron current against probe voltage, and from the slopes of the straight line sections, the electron temperatures can be calculated, in accordance with equation 17 from Chapter 2.

Figure 4.6 shows the variation of calculated electron temperature with input power. Within experimental error, the electron temperature increases linearly with power, but is, at all powers tested, very high compared with conventional capacitively coupled rf plasmas, which commonly have electron temperatures of 3-4eV [4.13,4.14], but with magnetic enhancement electron energies of around 10eV have been measured [4.7]. For microwave plasmas, electron temperatures between ~5eV and ~20eV have been measured [4.1,4.2].

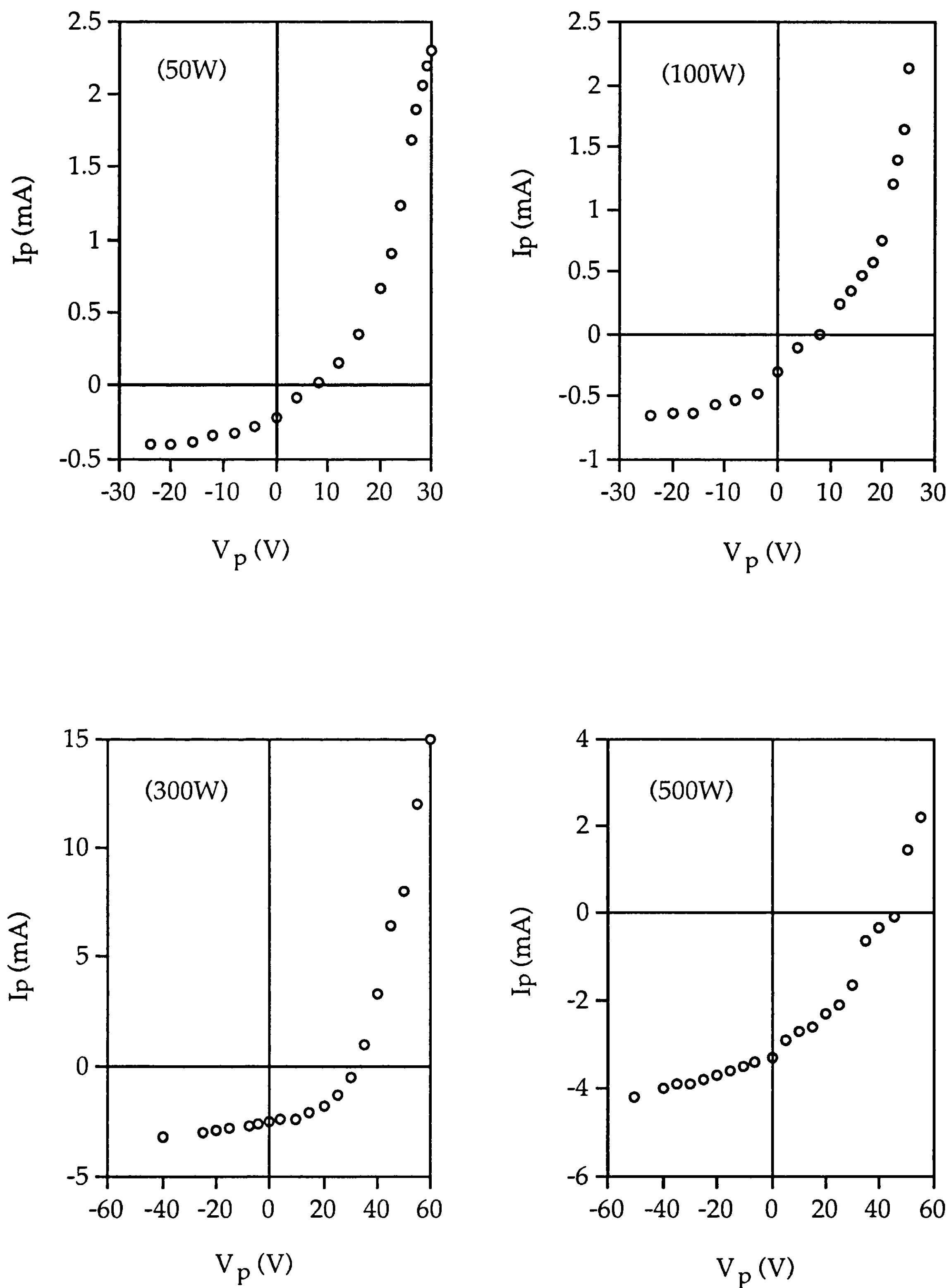

Fig. 4.4 I-V probe characteristics for novel RF plasma source, at vaious input powers

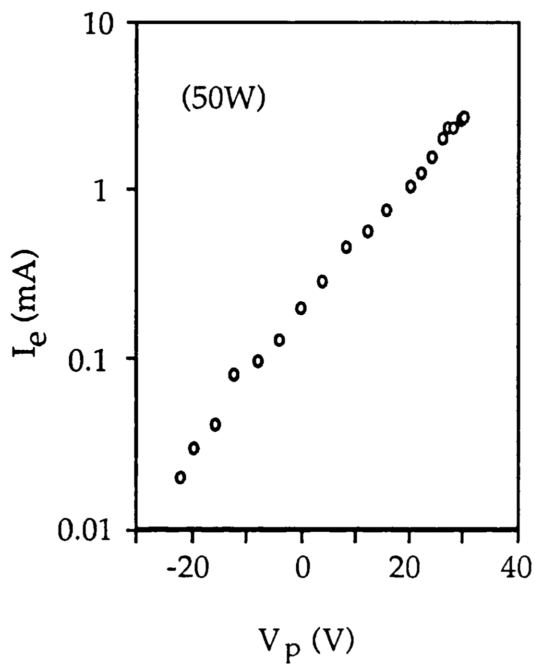

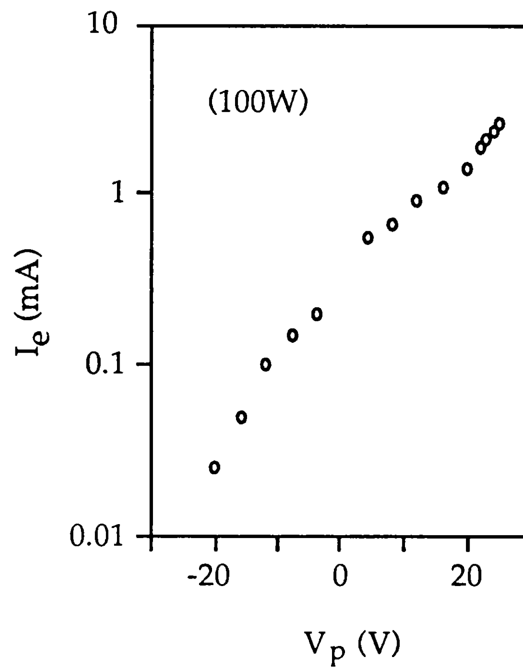

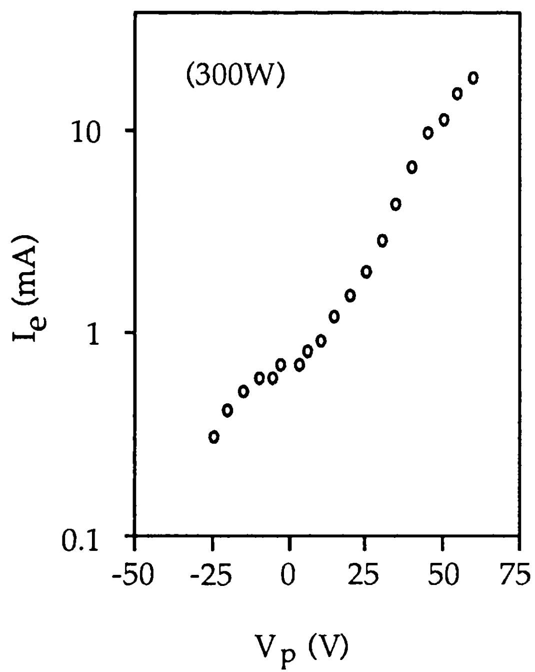

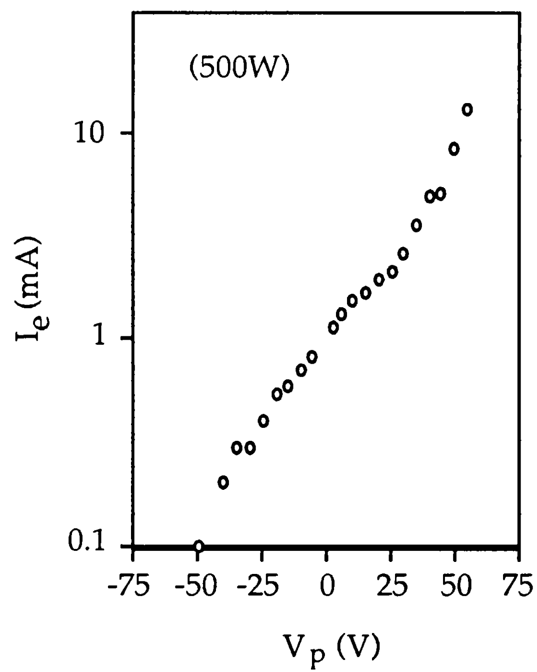

Fig 4.5 Logarithmic plot of I_e against V_p, to find the electron temperature of the plasma at various input powers, with I_e measured from I_i(sat).

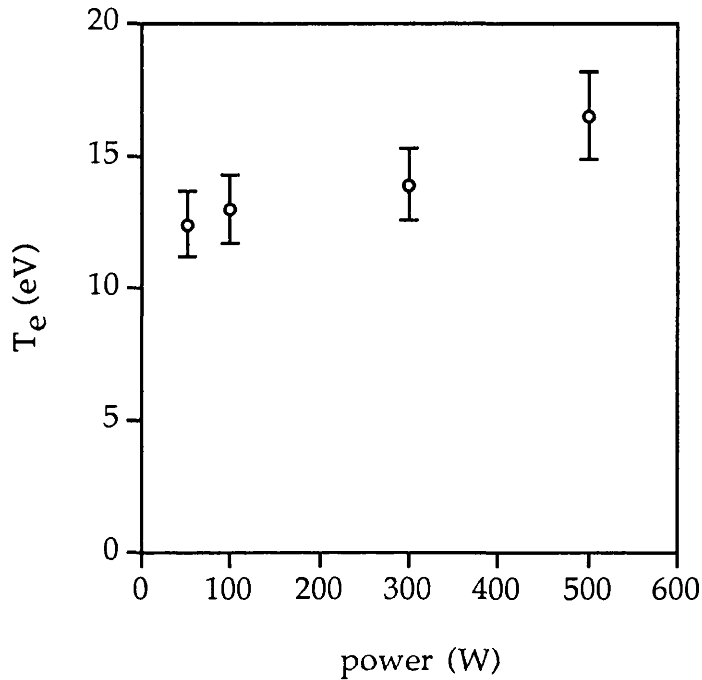

Fig. 4.6 Graph of calculated electron temperature against input power

4.4.1.2 Plasma Density

Since this is a magnetically enhanced plasma source, the saturation electron current will be much less than for a non-magnetic source, due to the reduced mobility of the electrons in the presence of a magnetic field. Thus this measurement cannot be used to derive the electron density.

In this case, the ion saturation current was used instead to derive the ion density, (using equation 21 from Chapter 2), which is an equivalent measure of the plasma density, since the test gas was argon, and therefore the number of negative ions was negligible.

$$I_i^* = e^{-1/2} n_i A q \left(\frac{k_B T_e}{m_i}\right)^{1/2}$$ where A is the probe area

$$n_i = \frac{I_i^*}{(T_e)^{1/2}} \frac{m_i^{1/2}}{e^{-1/2} A q^{3/2}}$$ with T_e in eV

$$= \frac{I_i^*}{(T_e)^{1/2}} (7.02 \times 10^{19})$$ for argon, with A = 0.95cm^2

Power (W)	I_i^*(mA)	T_e(eV)	n_i(cm^{-3})
50	0.42	12.4±1	8.37±0.4 ×10^9
100	0.675	13.0±1	1.31±0.06 ×10^{10}
300	3.3	13.9±1	6.21±0.3 ×10^{10}
500	4.2	16.5±1.5	7.26±0.4 ×10^{10}

Figure 4.7 shows the variation of plasma density with input power. The plasma density increases very rapidly at first, but appears to saturate at about 400W. Increasing the power above 300W seems instead to increase the energy of the ions, as the ion current is still increasing, but so is the electron temperature. Thus the velocity of the ions towards the collector is increasing, rather than the number.

The plasma densities achieved here compare favourably to those achieved with microwave sources [4.1,4.2].

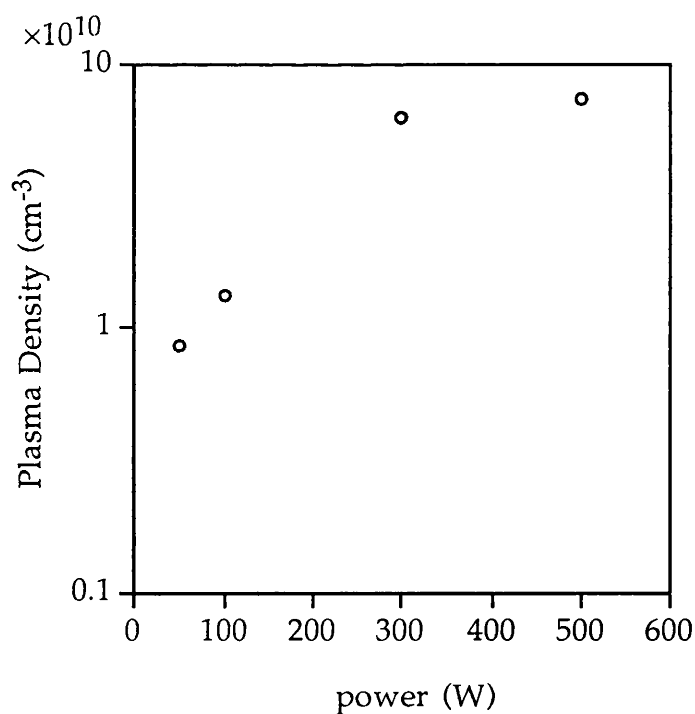

Fig. 4.7 Graph of calculated plasma density against input power

4.4.1.3 Plasma Potential

Because of the magnetic enhancement, the usual method of finding the plasma potential, from the onset of electron saturation current, was not possible. However, an approxiamte calculation method could be used.

At floating potential, electron and ion currents balance. Since $T_e >> T_i$, using equations 17 and 21 from Chapter 2, with $V_p = V_f$, the floating potential,

$$A n_e q \left(\frac{k_B T_e}{2\pi m_e}\right)^{1/2} \exp\left[\frac{-q(V_{pl} - V_f)}{k_B T_e}\right] = 0.6\, A n_i q \left(\frac{k_B T_e}{m_i}\right)^{1/2}$$

$$\exp\left[\frac{-q(V_{pl} - V_f)}{k_B T_e}\right] = 0.6\left(\frac{2\pi m_e}{m_i}\right)^{1/2}$$

inverting $$\exp\left[\frac{q(V_{pl} - V_f)}{k_B T_e}\right] = \frac{1}{0.6}\left(\frac{m_i}{2\pi m_e}\right)^{1/2}$$

$$\left(\frac{q}{k_B T_e}\right)(V_{pl} - V_f) = \ln(1/0.6) + 0.5\ln\left(\frac{m_n}{2\pi m_e}\right) + 0.5\ln\mu$$

where m_n is the mass of a nucleon
μ is the mass number of the ion

$$V_{pl} - V_f = \left(\frac{k_B T_e}{q}\right)[3.35 + 0.5\ln\mu]$$

In this case, the gas was argon, so

$$V_{pl} = [\,T_e(eV)\,]\,[5.2] + V_f$$

Figure 4.8 shows the variation of the calculated plasma potential with input rf power. It can be seen that the plasma potential increases approximately linearly with input power.

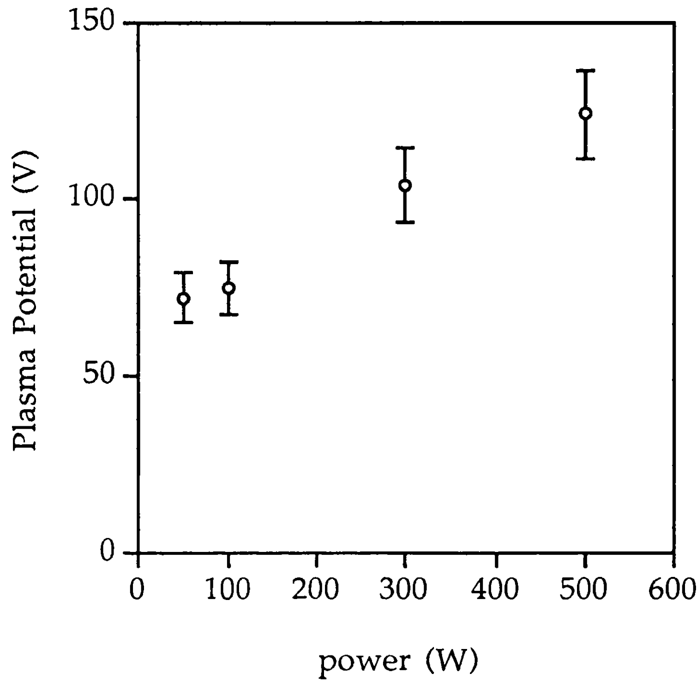

Fig. 4.8 Variation of calculated plasma potential with rf input power

Summary Table of Results

Power(W)	T_e (eV)	n_i ($\times 10^{10}$cm^{-3})	V_f(V)	V_{pl}(V)
50	12.4 (±1)	0.837 (±0.04)	8	~72
100	13.0 (±1)	1.314 (±0.06)	8	~75
300	13.9 (±1)	6.210 (±0.3)	32	~104
500	16.5 (±1.5)	7.26 (±0.4)	38	~124

4.4.2 Characterisation of the beam

Measurements of probe characteristics were made similarly to those for plasma characterisation, but at various distances from the aperture, without any base bias or grid optics.

The most important measurements are the ion current density and the potential at which the ion current is reduced to zero, which is an indication of the ion energy. It was found that the current at only a short distance from the aperture is composed almost entirely of ions, as the electrons are confined to the plasma chamber by the magnetic field. To demonstrate this, the probe characteristics as found in the plasma and 7cm downstream of the plasma, at the same input power of 100W are plotted together in figure 4.9. Due to beam spread, the ion current has dropped a little, but where, in the plasma, the floating potential was 8V, downstream it appears to be ~21V, ie there are very few electrons present in the beam. It is therefore no longer valid to use any equations relating to plasmas, which imply charge neutrality.

Figure 4.10 shows the variation of ion current density with power at two distances, 7.0 cm and 17 cm from the aperture. The current density is between 0.4 mA cm^{-2} and 0.8 mA cm^{-2} at the normal beam conditions of power and working distance, which compares well with other rf beam sources.

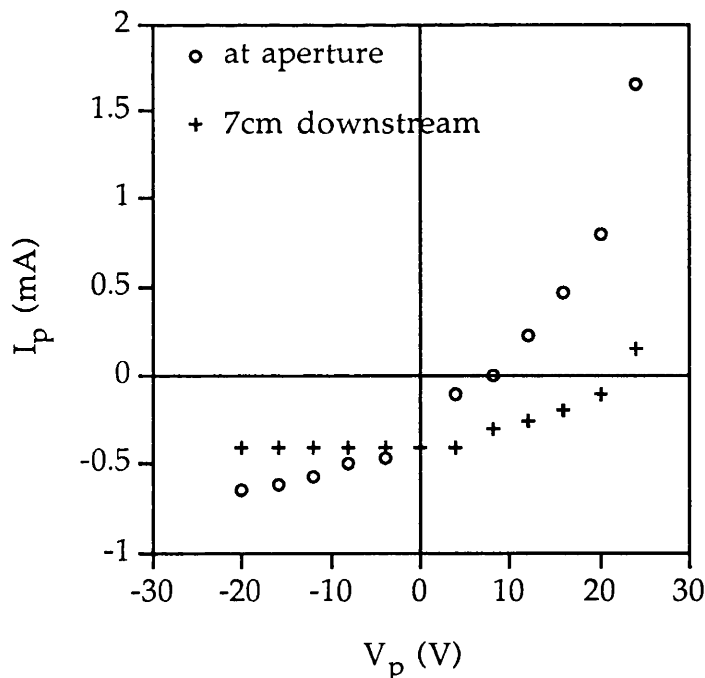

Fig. 4.9 Probe characteristics taken at different positions wrt the plasma, to show electron containment

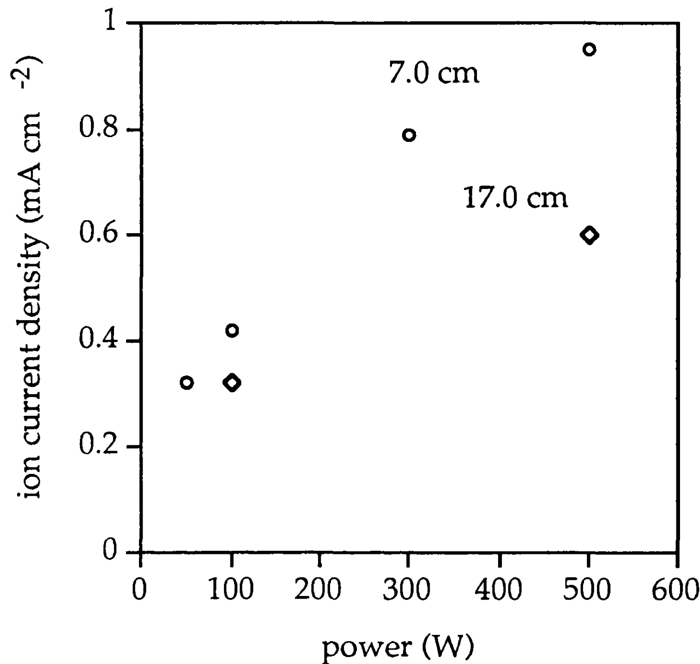

Fig. 4.10 Graph of ion current density at different distances from the aperture.

From the drop of ion current density with distance, assuming total charge conservation, an estimate of the beam divergence for the novel source can be made. However, it can only be a rough estimate as edge effects have not been taken into account. From these measurements the beam divergence is 10.5° (±0.5°), with only the collimation due to the length of the cylindrical lining.

In comparison the inductively coupled rf source of Proudfoot *et al* [4.5] has an ion current density of ~0.4 mA cm^{-2} at a distance of 12 cm from the source and an input power of 700W, with an extraction voltage of 100V. The beam divergence is 20°. Lejeune *et al* [4.8] have an ion current density of 0.9 mA cm^{-2} for an input power of 400W at the plasma, falling off to 0.15 mA cm^{-2} at a distance of 37cm, and their beam divergence is about 5°. The source has 3-grid ion optics with an extraction voltage of 450V.

Figure 4.11 shows the variation of stopping potential, the probe potential at which the ion current falls to zero, against the input power, with the probe at a distance of 7.0 cm from the aperture. This potential changes very little at greater distances from the aperture, and implies an extremely low ion energy.

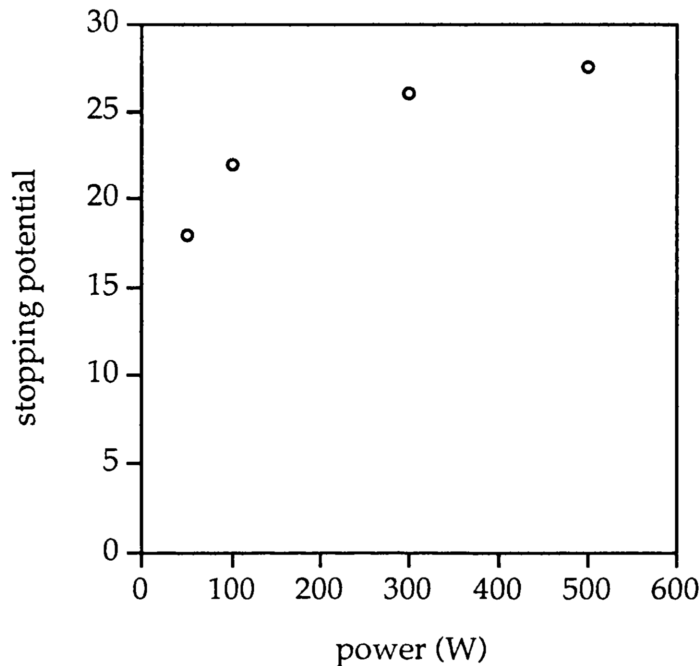

Fig. 4.11 Graph showing variation of stopping potential with power at a distance of 7.0 cm.

The difference in energy between the ions in the plasma and the ions in the beam may be due to the unusual geometry of this source, in that the electrodes are perpendicular to the beam direction. Thus the ions can impinge on the wall of the cylindrical source, behind which is an electrode, with a much higher energy than that with which they emerge into the beam.

Summary

From these characteristics it is apparent that the novel source produces a plasma of high density comparable to that produced by microwaves, and a fairly well collimated ion beam of ultra-low energy and high current density, which should satisfy the requirements for damage-free anisotropic etching and deposition.

4.5 References

4.1 H. Ameniya, K. Shimuzu, S. Kato and Y. Sakamoto *Jap. J. Appl. Phys. Lett.* **27** L927 (1988)

4.2 M. Matsuoka and K. Ono *J. Vac. Sci. Technol.* **A6** 25 (1988)

4.3 H. R. Kaufman, J. J. Cuomo and J. M. E. Harper *J. Vac. Sci. Technol.* **21** 725 (1982)

4.4 H. R. Kaufman and R. S. Robinson *AIAA Journal* **20** 745 (1982)

4.5 G. Proudfoot, C. M. O. Mahoney and R. Perrin *Nucl. Instrum. and Meth. in Phys. Res.* **B37/38** 136 (1989)

4.6 R. Lossy and J. Engemann *J. Vac. Sci. Technol.* **B6** 284 (1988)

4.7 R. Lossy and J. Engemann *Vacuum* **36** 973 (1986)

4.8 C. Lejeune, J. P. Grandchamp, O. Kessi and J. P. Gilles *Vacuum* **36** 837 (1986)

4.9 G. Proudfoot, T. S. Green, M. Inman and C. M. O. Mahoney *Nucl. Instr. and Meth.* **B21** 300 (1987)

4.10 R. R. J. Gagné and A. Cantin *J. Appl. Phys.* **43** 2639 (1972)

4.11 A. D. Kuypers and H. J. Hopman *J. Appl. Phys.* **67** 1229 (1990)

4.12 T. J. Sommerer and M. J. Kushner *J. Appl. Phys.* **71** 1654 (1992)

4.13 V. A. Godyak and A. S. Kanneh *IEEE Trans.* **PS14** 112 (1986)

4.14 T. I. Cox, V. G. I. Deshmukh, D. A. O. Hope, A. J. Hydes, N. St. J. Braithwaite and N. M. P. Benjamin *J. Phys. D: Appl. Phys.* **20** 820 (1987)

CHAPTER 5: ETCHING OF GaAs WITH NOVEL RF SOURCE

The novel rf source is designed to produce a high flux of very low energy ions. As demonstrated in Chapter 4, it produces a large beam current, ~0.8mA, uniform over a considerable area, ~100mm diameter. The energy of the ions which comprise the beam is only ~20eV. It should therefore be possible to perform damage-free etching with the source, even on a delicate material, such as GaAs.

The source was used in two etching configurations, firstly for reactive ion beam etching, using pure chlorine as the reactive etchant, and secondly for chemically assisted ion beam etching, with an argon ion beam and chlorine gas as the chemical component.

5.1 Reactive Ion Beam Etching

5.1.1 Experimental Procedure

The source, in its housing, was fitted onto the top of a 200mm diameter 6-way cross vacuum system. The system was fitted with a turbomolecular pump and a rotary backing pump. The system was routinely evacuated to a base pressure of $\sim 10^{-7}$ mbar.

The sample mounting was on a base of tantalum foil, made with foldable tags for securing the sample. These tags also served as masks for small areas of the surface. This was attached to stainless steel rods, holding the sample ~7 cm below the source aperture, on the axis of the source.

The sample was a $1cm^2$ piece of semi-insulating GaAs.

Pure chlorine gas was admitted to the source through a needle valve to a pressure of 6×10^{-4} mbar. The plasma was sustained with an input power of

300W, chosen as this was the optimum power for good plasma conditions at this pressure. The reflected power was only ~1W after manual tuning of the matching unit.

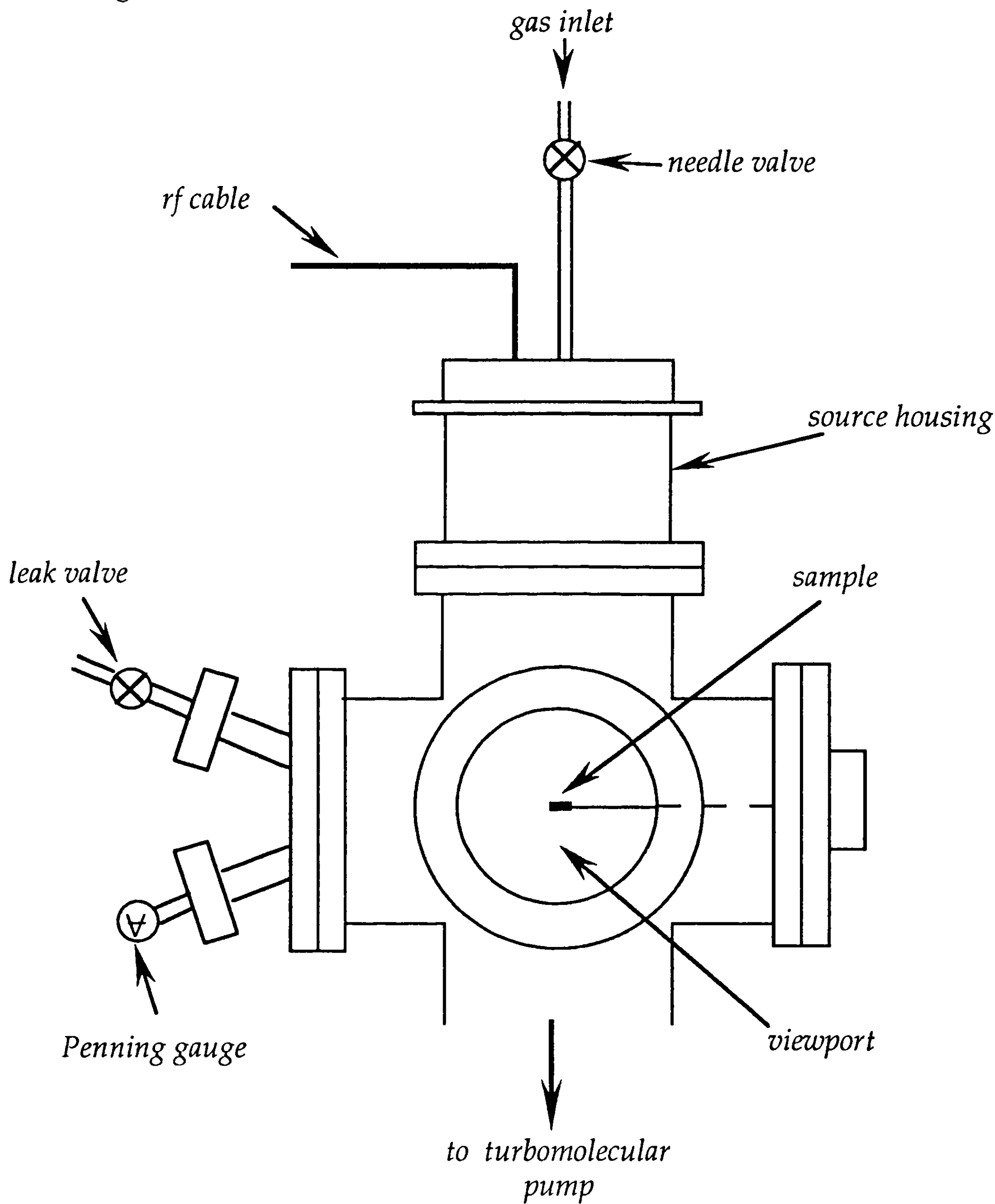

Fig. 5.1 Diagram of experimental setup

For the first experimental run the sample was electrically isolated, but it was noticed that the plasma formed a "cone" reaching from the aperture of the source to the sample. This is illustrated in figure 5.2. For subsequent runs the sample was earthed, and the "cone" did not reappear. This had not been seen

in the testing performed with argon, and was most probably due to the presence of negative ions [5.1].

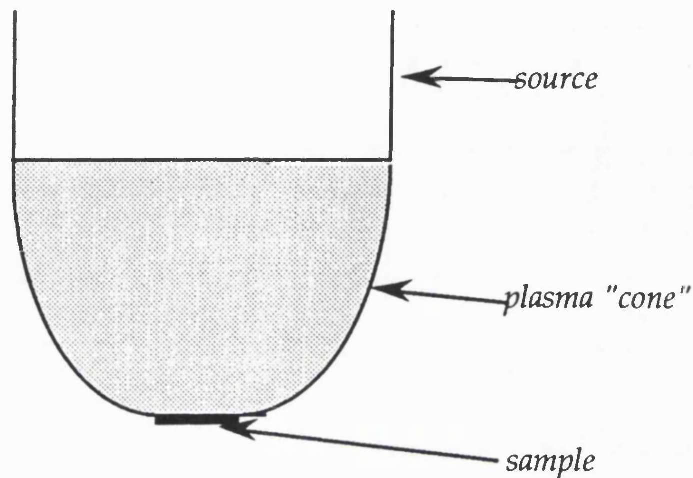

Fig. 5.2 Diagram showing appearance of plasma "cone"

Etches were performed for a range of times from 15 mins to 60 mins. Experiments were performed without the plasma being ignited as a control. In some experiments, the sample was prepared with a photolithographic mask to investigate the anisotropy of the etching process.

5.1.2 RIBE Etching Results

5.1.2.1 The Contamination Layer

On removing each sample from the chamber, it was found to be covered with a bluish coating. This contamination layer was about 60nm thick as measured with a Talystep.

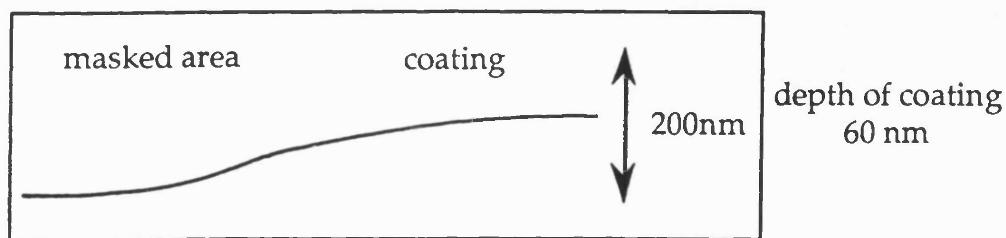

Fig. 5.3 Talystep tracing of etched sample with coating, magnification 10^5

The contamination layer was analysed by EDAX to determine its composition, and thereby its likely origin.

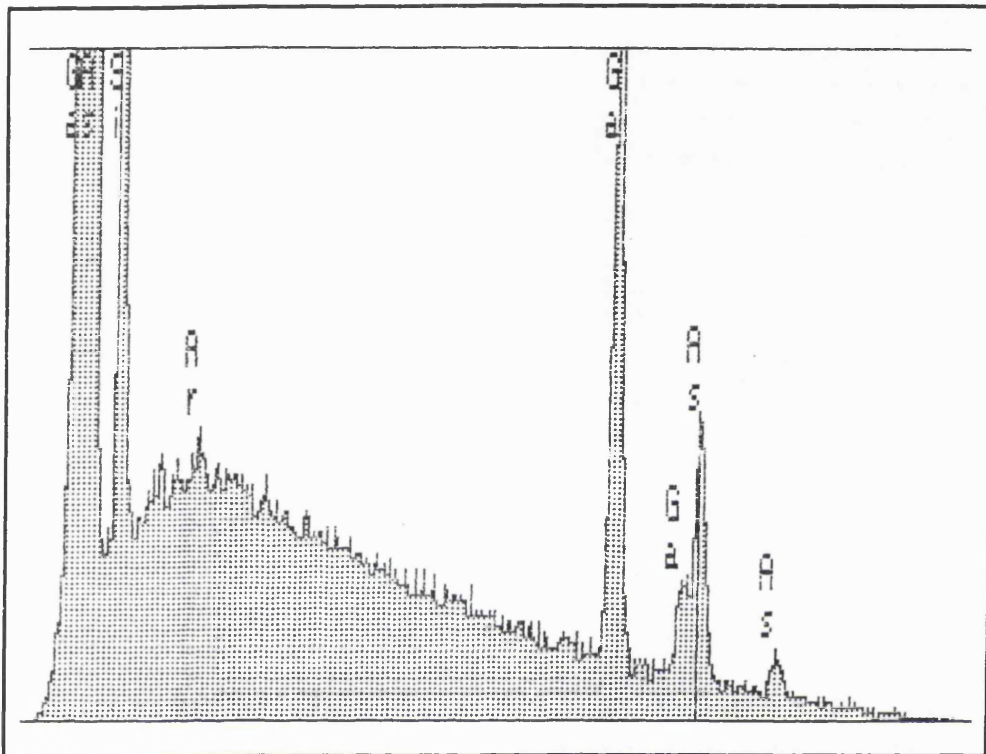

Fig. 5.4 X-ray spectrum of blue contamination layer

As can be seen in the X-ray spectrum shown in Fig. 5.4 the coating was found to contain only silicon and its likely origin was therefore the silica liner of the source. However, it was found that this coating washed off almost completely with isopropyl-alcohol, and a little gentle rubbing with a cotton bud soaked in IPA removed the rest.

5.1.2.2 Talystep Measurements, after Removing the Coating

(i) 15 mins etch — etch depth ~20 nm

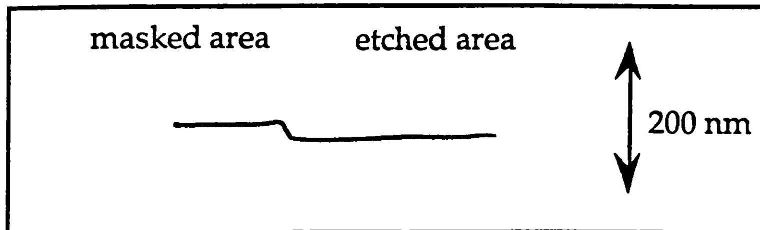

(ii) 30 mins etch — etch depth ~50 nm

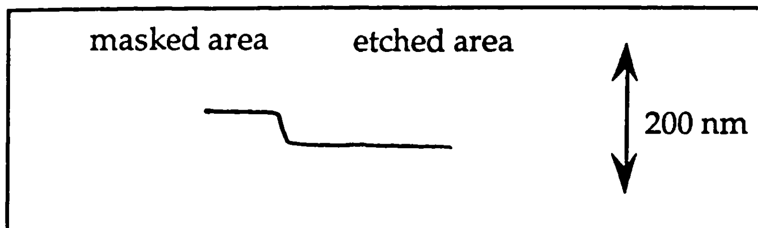

(iii) 40 mins etch — etch depth ~75 nm

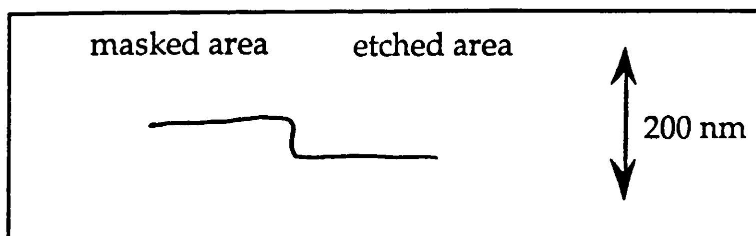

(iv) 60 mins etch — etch depth ~120nm

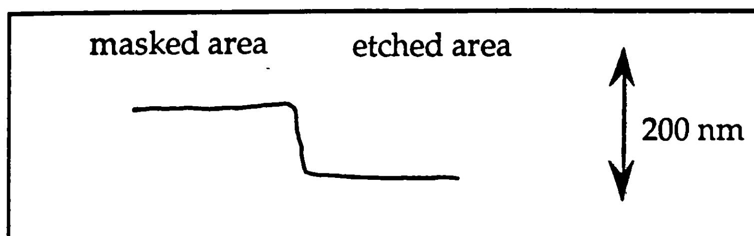

(v) 45 mins etch with lithographic masking at 200W etch depth ~60 nm

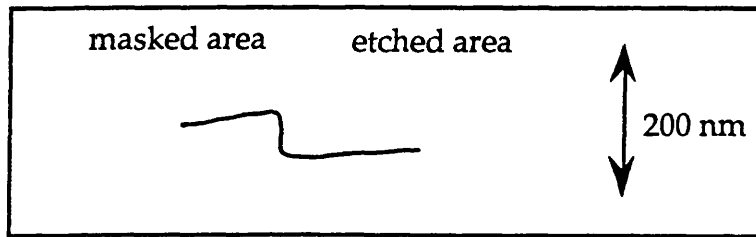

Fig. 5.5 Talystep traces of etched samples

A plot of etch depth against time is linear, but the straight line does not go through the origin.

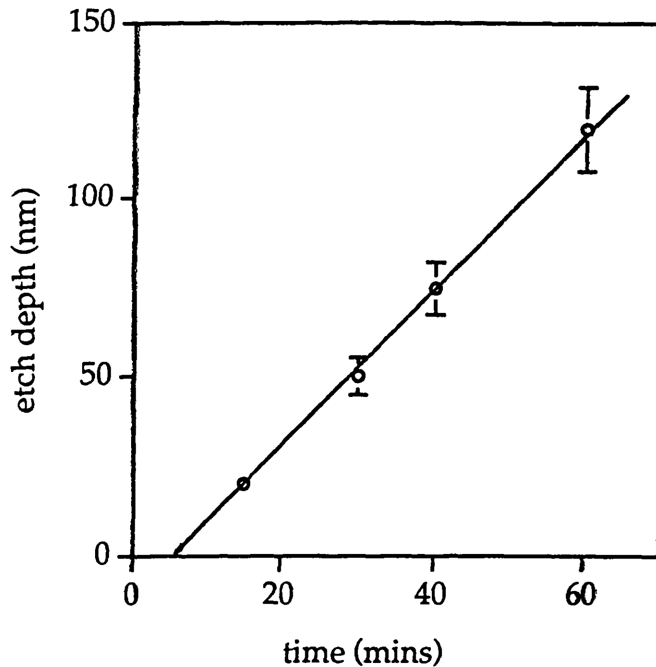

Fig. 5.6 Plot of RIBE etch depth against time

This is most probably due to the difficulty of removing the native oxide layer with chlorine. It was not possible to remove it before etching by other means as there is no load-lock on the vacuum system, and it would therefore have regrown before etching began.

The control sample, chlorine gas without plasma, showed no discernible etch at all.

5.1.2.3 Scanning Electron Microscopy

The photolithographically masked sample was subjected to Scanning Electron Microscopy, to investigate the smoothness and the anisotropy of the etch.

Figure 5.7 shows a section of etched surface which looks very smooth, taken under high tilt, although the edge of the masked area is irregular over a range of 60 nm, the talystep measured depth of the etch.

Fig. 5.7 SEM photograph of the RIBE etched surface

Figure 5.8 shows a corner of the masked area, taken under high tilt. Although the edges appear straight and vertical, there seems to have been some lifting of the mask at the corner.

Fig. 5.8 SEM photograph of a corner of a masked area

5.2 Chemically Assisted Ion Beam Etching

This was performed with an argon ion beam and chlorine gas.

5.2.1 Experimental Procedure

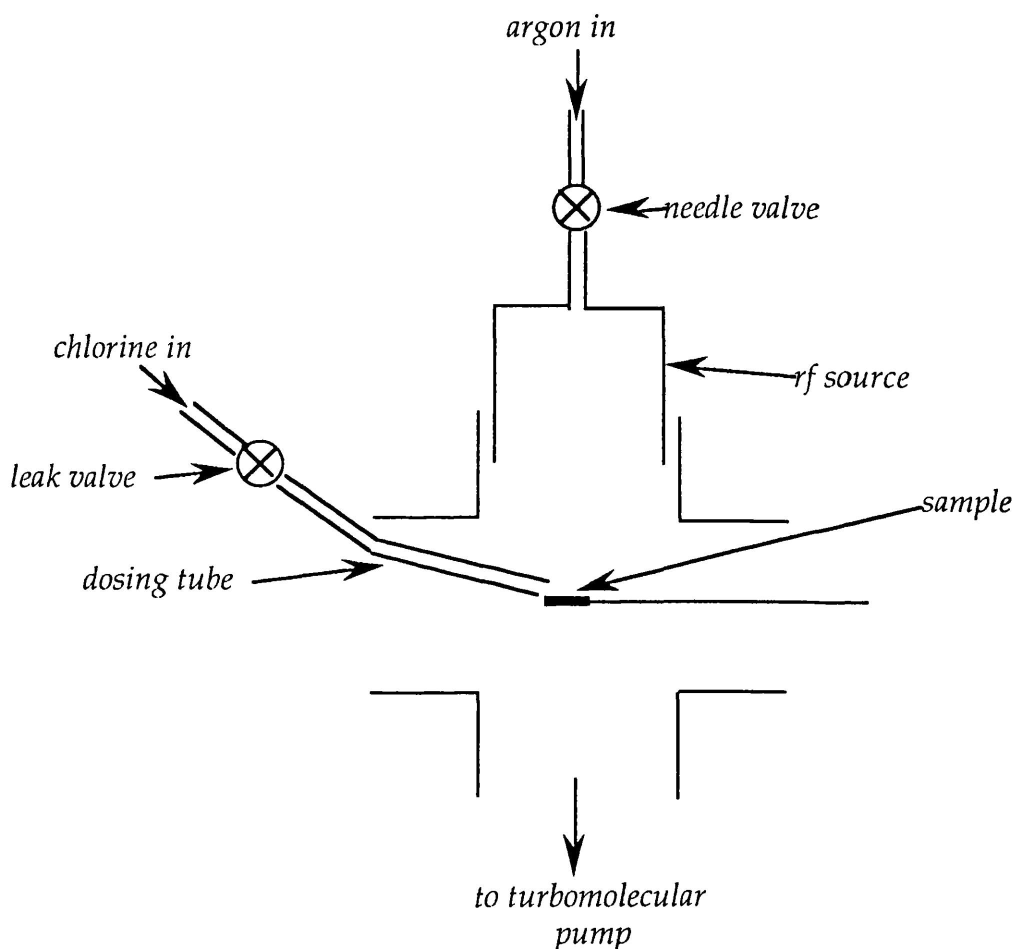

Fig. 5.9 Schematic of experimental setup for CAIBE

A quartz dosing tube was added to the system described in section 5.1.1, designed to deliver chlorine gas directly to the surface of the sample, via the leak valve.

Preliminary control tests were performed with the Ar^+ beam alone.

The first 1 hour test actually etched the sample to a depth of 40 nm, but a repeat the following day showed no etch at all. This implies that chlorine had

been adsorbed on the surface of the liner of the source, which was removed by the argon during the first run.

1st Ar^+ etch

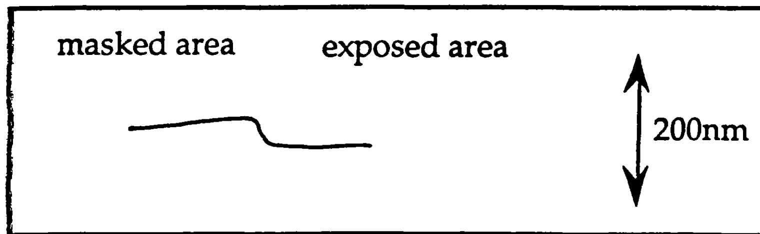

2nd Ar^+ etch

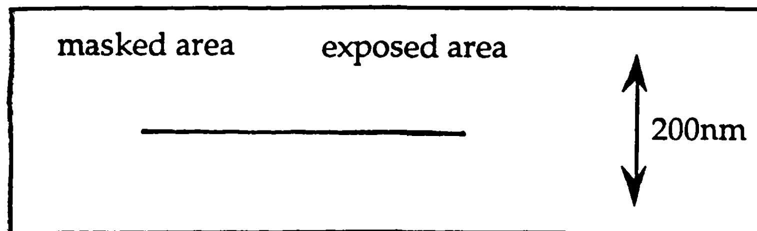

Fig. 5.10 Talystep traces of "etching" by Ar^+ bombardment

It can be concluded that at the energy of the ions in the beam from this source, no physical sputtering by Ar^+ ions occurred.

For each run: the system was first evacuated to a base pressure of $2x10^{-7}$ mbar. Then the leak valve was opened to admit chlorine to a predetermined pressure. Then the needle valve was opened to argon and the plasma was ignited. The etch was performed for 1 hour for each run.

Run	Cl_2 pressure	Ar^+pressure	Power	Time
1	$1x10^{-6}$ mbar	$6x10^{-4}$ mbar	300W	60 mins
2	$2x10^{-6}$ mbar	$6x10^{-4}$ mbar	300W	60 mins
3	$4x10^{-6}$ mbar	$6x10^{-4}$ mbar	300W	60 mins

At chlorine pressures greater than $4x10^{-6}$ mbar it was observed that the colour of the plasma changed from pink (argon) to blue implying that some chlorine was being reflected up into the source. This would have meant that the etching process was no longer purely CAIBE.

5.2.2 CAIBE Etching Results

5.2.2.1 The Contamination

A contamination layer similar to that observed in the RIBE series of etches was again observed. This was removed in the same manner as described previously.

5.2.2.2 Talystep Measurements, after Cleaning

(i) $p_{Cl} = 1x10^{-6}$ mbar

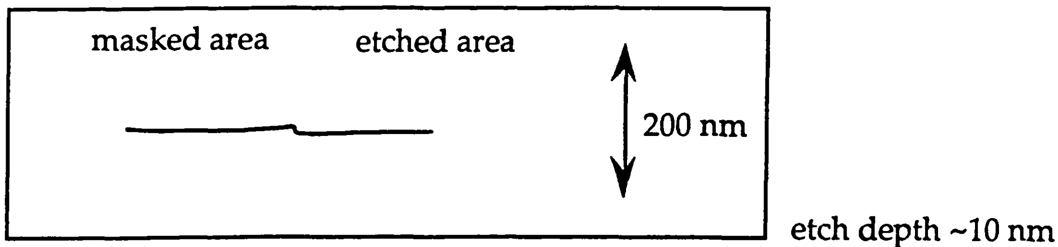

etch depth ~10 nm

(ii) $p_{Cl} = 2x10^{-6}$ mbar

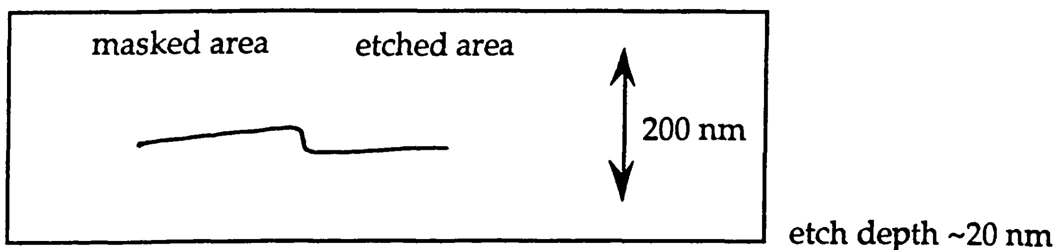

etch depth ~20 nm

(iii) $p_{cl} = 4 \times 10^{-6}$ mbar

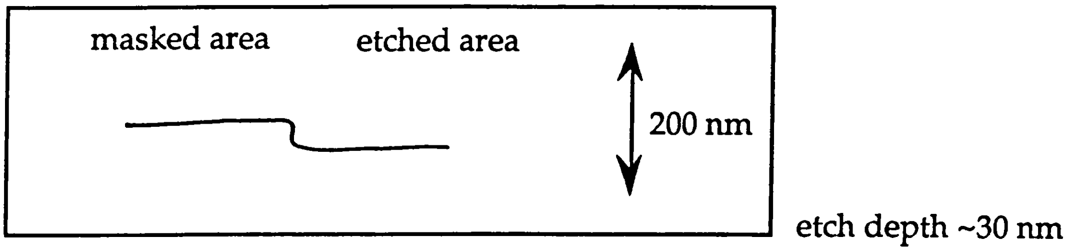

Fig. 5.11 Talystep traces of CAIBE etches with various Cl_2 flow rates

A plot of etch depth against chlorine flow rate is nearly linear, with an incubation period again evident, due to the native oxide layer.

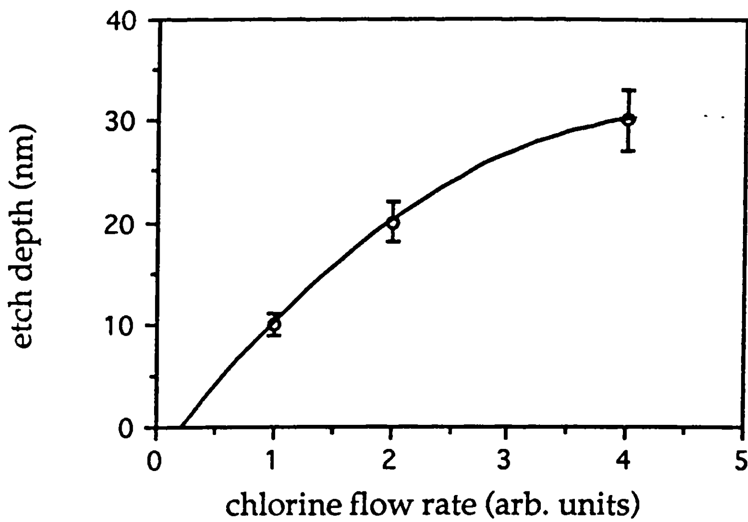

Fig. 5.12 Plot of CAIBE etch depth against Cl_2 flow rate

5.3 Combining Results

In order to compare the etching by the two methods, total chlorine flux for each etching run must be calculated.

5.3.1 Calculation of chlorine flux

$$\text{Impingement rate} = \frac{1}{4}n\bar{c} = \frac{1}{4}\frac{p}{kT}\sqrt{\frac{8RT}{\pi M_{molar}}}$$

$$= \frac{1}{4}\frac{pN_A}{RT}\sqrt{\frac{8RT}{\pi M_{molar}}}$$

$$= p\sqrt{\frac{N_A^2}{2\pi RTM_{molar}}}$$

$$= p\,\frac{2.635\text{x}10^{26}}{\sqrt{M_rT}}\ \text{m}^{-2}\text{s}^{-1} \quad \text{with p in mbar}$$

[5.2]

5.3.1.1 Chlorine flux for RIBE

In this case p = 6x10^{-4} mbar
T = ~400K
M_r= 70.9 (for Cl_2)

Hence the impingement rate = 9.39x10^{20} molecules s^{-1}

time	total flux (molecules)
15 min	8.45×10^{23}
30 min	1.690×10^{24}
40 min	2.253×10^{24}
60 min	3.380×10^{24}

5.3.1.2 Chlorine flux for CAIBE

In this case time = 60 min for all cases.

The pressure was measured by the Penning gauge, 23 cm from the sample, but the exit of the dosing tube was only 1 cm from the surface of the sample. To find the chlorine flux at the surface of the sample an enhancement factor is required. It is difficult to know precisely what this should be, but it is generally chosen to be between 50 and 100. In this case, due to the oblique angle between the dosing tube and the sample surface, the lower limit was chosen.

$$\text{Chlorine flux} = p\,\frac{2.635\times10^{26}}{\sqrt{M_r T}}\ m^{-2}s^{-1} \times t \quad = 5.633\times10^{27}\,p \ \text{molecules}$$

p	Flux (without enhancement)	Total flux (molecules) (with enhancement)
1×10^{-6} mbar	5.633×10^{21}	2.82×10^{23}
2×10^{-6} mbar	1.127×10^{22}	5.635×10^{23}
4×10^{-6} mbar	2.253×10^{22}	1.265×10^{24}

5.3.2 Combined Data

Figure 5.13 shows a plot of the combined data of etch depth against total chlorine flux from both methods of etching. All the data can be fitted to the same straight line, thus implying that the limiting factor in the etching process is the chlorine, and that therefore, in both methods it is primarily a chemical etch, with very little physical sputtering. This should mean that the damage incurred is minimal.

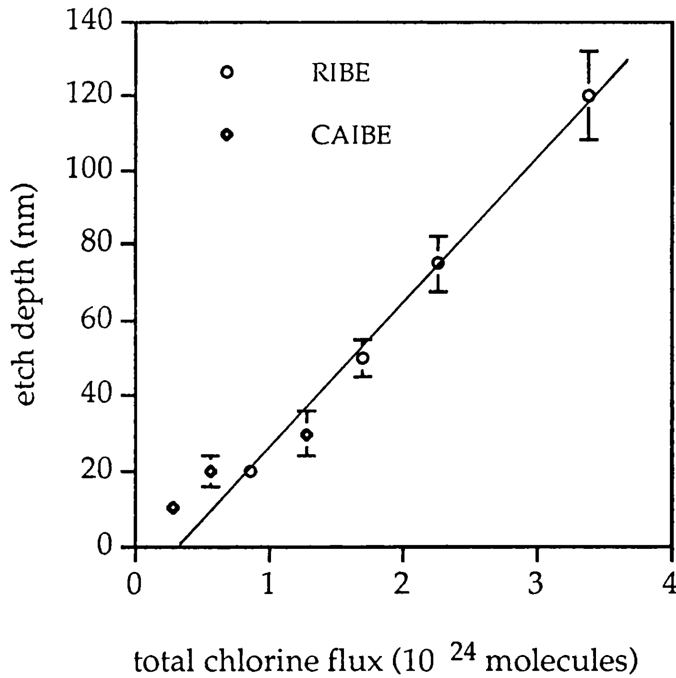

Fig. 5.13 Combined plot of etch depth against total chlorine flux

5.4 The Liner

Having concluded etching, the source was removed from the 6-way cross and the liner was taken out for examination.

The erosion, which was the origin of the contamination was very clear to see, and followed the pattern of the magnetic field. The eroded areas correspond to the earthed electrode rings, and mark the positions of the magnets. This is clearly shown in the photograph, figure 5.14.

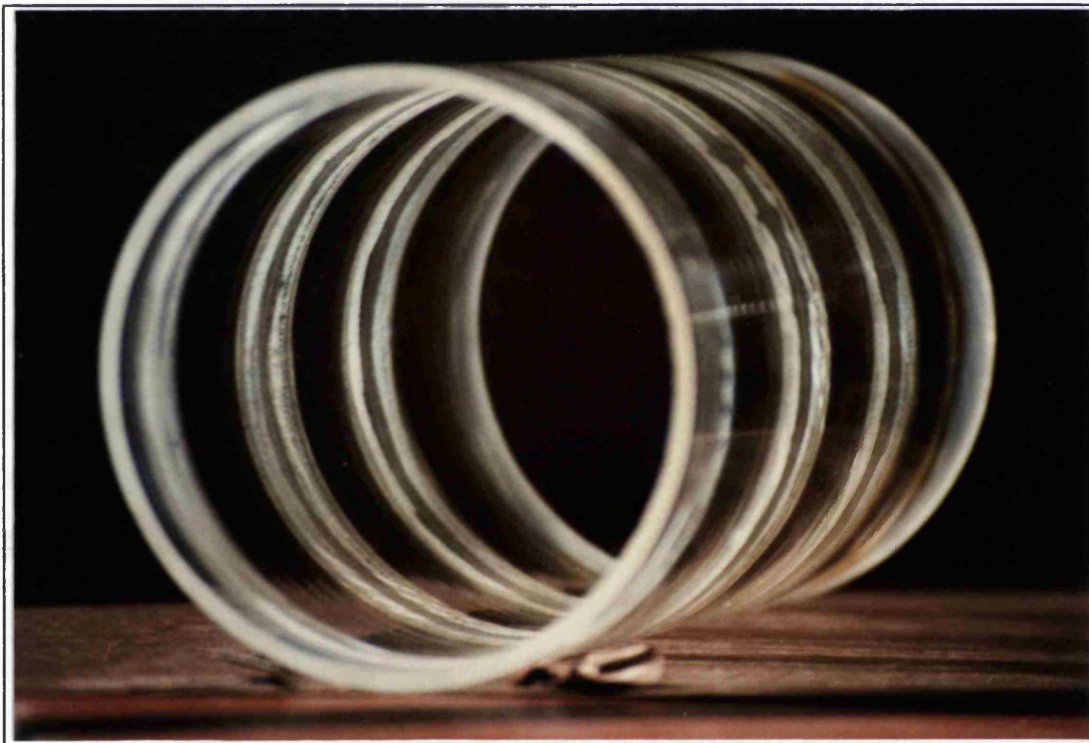

Fig. 5.14 Photograph of silica liner showing erosion

5.5 Evaluation of the Novel Source as an Etcher

For RIBE, the etching rate is 2nm min^{-1} at a Cl_2 pressure of 6x10^{-4} mbar, but the maximum etching rate that could be obtained for CAIBE was ~0.5nm min^{-1}.

Germann *et al* [5.3], using IBE, with Ar^+ at an energy of 150eV, and incurring considerable damage, also quote an etch rate 2nm min^{-1}. Furuhata *et al* [5.4], using Cl_2 at a pressure of 4.2 x 10^{-4} Torr and substrate heating report an etching rate of order 0.1μm min^{-1}, but at room temperature it was ~3nm min^{-1}.

Yamada *et al* [5.5], using RIBE report an etching rate of 0.15μm min^{-1}, but with a Cl_2 gas pressure of 2.6 x 10^{-3} mbar and a beam extraction voltage of 400V, much higher pressure and much greater energy than were used with the novel source. However, Tadokoro *et al* [5.6] had a higher etching rate, 0.2μm min^{-1} using an ECR plasma ion source at 6 x 10^{-4} Torr with the substrate heated to 100°C and an extraction voltage of 200V. They give no indication of any damage caused, concentrating mainly on the anisotropy of the etching process. Lishan and Hu [5.7] achieved an etching rate of 0.1μm min^{-1} with a microwave plasma generated Cl_2 beam at a pressure of 4 x 10^{-4} Torr, with the sample at a low temperature (50°C). They used no extraction voltage, but simply allowed the plasma to flow out, and positioned the sample downstream of the plasma chamber. This is the system most nearly similar to the configuration of the novel source.

In the CAIBE configuration, the etching rate for the novel source is very much lower than for other comparable systems. It is very close to the etching rate obtained by non-plasma methods.

Meguro *et al* [5.8], using a digitised form of CAIBE with Cl_2 and a 100eV electron beam, achieved an etching rate equivalent to ~3nm min^{-1}. They found the etch rate insensitive to Cl_2 cover. Skidmore *et al* [5.9], with a more conventional CAIBE system, Cl_2 pressure of 8 x 10^{-4} Torr and 200eV Ar^+ beam, achieved an etching rate of 60 nm min^{-1} but this is a much higher Cl_2 flow and much higher Ar^+ energy than were used with the novel source.

The etching rate for the novel source in the CAIBE configuration was considerably lower than these at a maximum of ~0.5 nm min^{-1}.

It is very likely that the presence of the contamination layer contributed to the slow etching rate. Since the etch depth increased linearly with time, and

the contamination layer was present, to a similar depth, for all etching times, it is clear that etching continued to take place after the formation of the contamination layer. It seems reasonable to assume that this layer was being continuously eroded and simultaneously deposited during the etching process, thus inhibiting the etching of the GaAs surface.

Thus in conclusion, although the resulting etched surface appears very smooth, after removal of the contamination layer, the presence of this layer makes this novel source far from ideal for *in situ* etching, as presently configured. Further development would be needed, to determine a way of avoiding the self-erosion.

5.6 References

5.1 B. E. Thompson, K. D. Allen, A. D. Richards and H. H. Sawin *J. Appl. Phys.* **59** 1890 (1986)

5.2 D. P. Woodruff and T. A. Delchar *Modern Techniques of Surface Science* C. U. P. (1986)

5.3 R. Germann, A. Forchel, M. Bresch and H. P. Meier *J. Vac. Sci. Technol.* **B7** 1475 (1989)

5.4 N. Furuhata, H. Miyamoto, A. Okamoto and K. Ohata *J. Appl.Phys.* **65** 168 (1989)

5.5 T. Yamada, T. Yuasa, K. Asakawa, M. Shimazu, M. Ishii and M. Uchida *J. Appl. Phys.* **64** 2286 (1988)

5.6 T. Tadakoro, F. Koyama and K. Iga *J. Vac. Sci. Technol.* **B7** 1111 (1989)

5.7 D. G. Lishan and E. L. Hu *Appl. Phys. Lett.* **56** 1667 (1990)

5.8 T. Meguro, M. Hamagaki, S. Modaressi, T. Hara, Y. Aoyagi, M. Ishii and Y. Yamamoto *Appl. Phys. Lett.* **56** 1552 (1990)

5.9 J. A. Skidmore, L. A. Coldren, E. L. Hu, J. L. Merz and K. Asakawa *Appl. Phys. Lett.* **53** 2308 (1988)

CHAPTER 6: DEVICE CHARACTERISATION OF ETCHED SURFACE

The purpose of this etching work has been to investigate the possibility of performing an etch which is damage-free, from the standpoint of electronic device fabrication. The definitive test is therefore to fabricate a device on the etched surface and test its characteristics. The simplest and most direct device to fabricate is a Schottky barrier diode, which is simply a metal-semiconductor contact.

6.1 Theory of Schottky Contacts

6.1.1 Barrier Height

When a metal makes intimate contact with a semiconductor, the Fermi levels in the two materials must be coincident at thermal equilibrium.

There are two limiting cases, (i) the ideal contact and (ii) contact when there is a very large density of surface states.

6.1.1.1 The Ideal Case

Figure 6.1 shows the electronic energy levels in the metal and n-type semiconductor.

Figure 6.1(a) shows the metal and semiconductor unconnected. If one then imagines the two being brought into electrical contact, electrons will flow from the higher level in the semiconductor to the metal until thermal equilibrium is established, and the Fermi levels are aligned. This is the situation in figure 6.1(b). The Fermi level in the semiconductor has been

lowered relative to the metal by an amount equal to the difference between the two work functions. The work function is the energy difference between the vacuum level and the Fermi level.

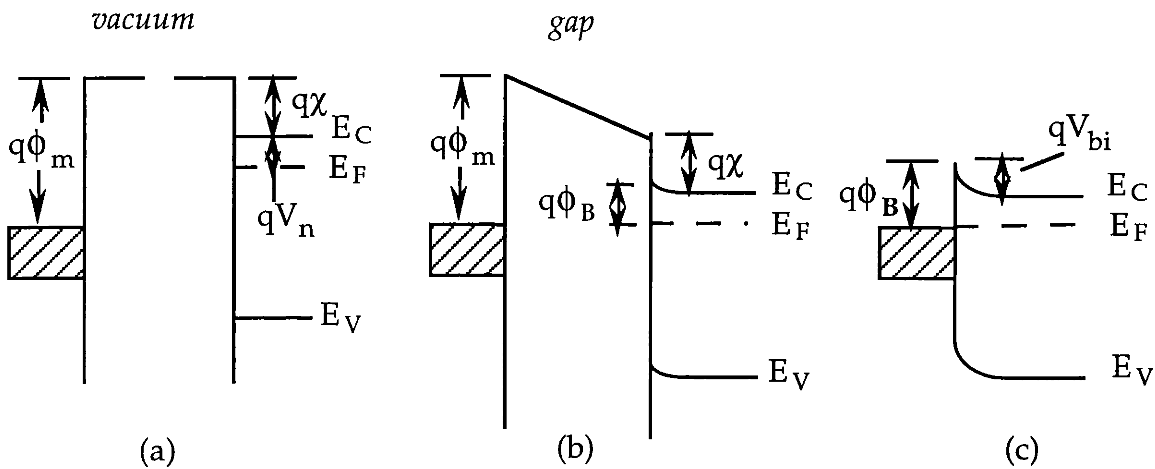

Fig. 6.1 Energy levels in Ideal Schottky Contact

When the two surfaces are brought into intimate contact, there will be a build-up of negative charge at the metal surface, and an equal build-up of positive charge at the semiconductor surface. This situation is shown in figure 6.1(c). The height of the potential barrier will be the difference betwen the work function of the metal, ϕ_m and the electron affinity, the difference between the bottom of the conduction band and vacuum, χ, of the semiconductor.

$$q\phi_B = q(\phi_m - \chi)$$

The build-up of charge at the semiconductor surface leads to a depletion layer of width W, whose width will depend on the doping level.

6.1.1.2 With a Large Density of Surface States

Figure 6.2 shows the electronic energy levels in a metal and a semiconductor, where a large density of surface states is present on the semiconductor surface.

In figure 6.2(a) the metal and semiconductor are unconnected. In this case, unlike in the ideal case, there is already some band bending apparent at the semiconductor surface as the bulk of the semiconductor comes to equilibrium with the surface states. What happens as the two are brought into theoretical contact is illustrated in figure 6.2(b). The Fermi level of the semiconductor falls by an amount equal to the contact potential, relative to the metal.

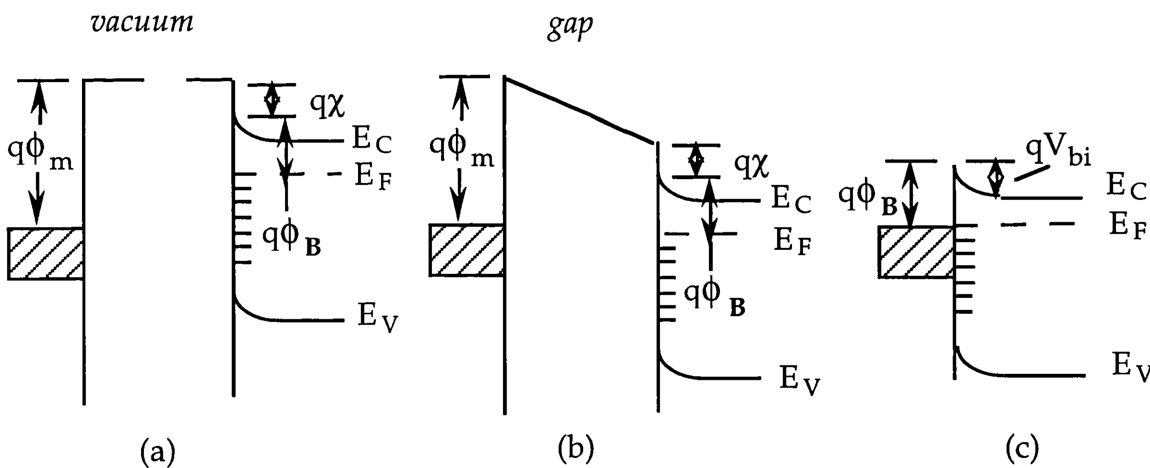

Fig. 6.2 Energy levels with a Large Number of Surface States

If the density of surface states is sufficiently large to accommodate any additional surface charge as the two surfaces come into intimate contact, as shown in figure 6.2(c), the space charge in the semiconductor will be unaffected. Thus in this case, the barrier height is determined by the property of the semiconductor surface, and is independent of the metal work function [6.1,6.2].

Thus, the barrier height can be a sensitive indicator of the condition of the semiconductor surface.

6.1.2 Current Transport Processes

Current transport in metal-semiconductor contacts is mainly due to majority carriers. There are four basic transport processes under forward bias.
(1) Transport of electrons from the semiconductor over the potential barrier into the metal. This is the dominant process for Schottky diodes with a moderately doped semiconductor operated at room temperature.
(2) Quantum-mechanical tunneling of electrons through the barrier. This is important for a heavily doped semiconductor and is responsible for ohmic contacts.
(3) Recombination in the space-charge region.
(4) Hole injection from the metal to the semiconductor, equivalent to recombination in the neutral region.

Since, under the conditions of characterisation of the Schottky diodes formed on the GaAs surfaces, (1) will be by far the dominant process, only the theories for this contribution will be given here.

6.1.2.1 Thermionic Emission Theory

There are three basic assumptions made in the derivation of the theory by Bethe [6.3]:
(i) the barrier height, $q\phi_B$, is much larger than kT;
(ii) thermal equilibrium is established at the plane that determines emission;
(iii) the existence of a net current flow does not affect this equilibrium.

The current density $J_{s\to m}$, from the semiconductor to the metal is given by the concentration of electrons with sufficient energy to surmount the potential barrier and moving in the x direction, (taking the x-direction as normal to the interface).

$$J_{s\to m} = \int_{E_F + q\phi_B}^{\infty} q v_x \, dn \qquad (1)$$

where $E_F + q\phi_B$ is the minimum energy requirement.

$$dn = N(E)F(E)dE$$

where N(E) is the density of states and F(E) is the distribution function. So

$$dn = \frac{4\pi(2m^*)^{3/2}}{h^3} \sqrt{E - E_C} \quad \exp[-(E - E_C + qV_n)/kT]dE \qquad (2)$$

where m* is the effective mass of an electron in the semiconductor and

$$qV_n = E_C - E_F$$

If all the energy of electrons in the conduction band is assumed to be kinetic energy then

$$E - E_C = 1/2\, m^*v^2$$

$$dE = m^*vdv$$

$$\sqrt{(E - E_C)} = v\sqrt{(m^*/2)}$$

Substituting these into equation (2) gives

$$dn = 2\left(\frac{m^*}{h}\right)^3 \exp\left(\frac{-qV_n}{kT}\right) \exp\left(\frac{-m^*v^2}{2kT}\right)(4\pi v^2 dv) \qquad (3)$$

This gives the number of electrons with speeds between v and v+dv over all directions.

$$v^2 = v_x^2 + v_y^2 + v_z^2$$

and

$$4\pi v^2 dv = dv_x dv_y dv_z$$

which, combined with (3) and substituted in (1) gives

$$J_{s\rightarrow m} = \left(\frac{4\pi q m^* k^2}{h^3}\right) T^2 \exp\left(\frac{-qV_n}{kT}\right) \exp\left(\frac{-m^*v_{0x}^2}{2kT}\right) \qquad (4)$$

Since v_{0x} is the minimum velocity required to surmount the barrier,

$$1/2 m^* v_{0x}^2 = q(V_{bi} - V)$$

Substituting this into (4) gives

$$J = A^*T^2 \exp\left(\frac{-q\phi_B}{kT}\right) \exp\left(\frac{qV}{kT}\right) \qquad \text{since } \phi_B = V_n + V_{bi}$$

and $A^* = \left(\frac{4\pi q m^* k^2}{h^3}\right)$ is the effective Richardson constant.

For GaAs, which is a direct band-gap semiconductor, $A^* = Am^*/m_o$, while A, the Richardson constant is 120 A cm^{-2} K^{-2}.

Combining diffusion theory with thermionic emission theory for the transport of electrons over the barrier, changes A* to A**, which is in fact only a small change, ~10%, and within the accuracy of this work, unimportant since this would only change the value of ϕ_B by 0.01%.

6.1.3 Measurement of Barrier Height and Ideality Factor

When a bias is applied to the Schottky barrier, there is an image-force-induced lowering of the barrier height, $\Delta\phi$, dependent on V. Thus the expression for the current density becomes

$$J = A^{**}T^2 \exp\left(\frac{-q\phi_B}{kT}\right) \exp\left(\frac{q(\Delta\phi + V)}{kT}\right)$$

This can be written as

$$J = J_s \left[\exp\left(\frac{qV}{nkT} - 1\right)\right]$$

where n is defined as

$$\frac{q}{kT} \frac{\partial V}{\partial(\ln J)}$$

and

$$J_s = A^{**}T^2 \exp\left(\frac{-q\phi_B}{kT}\right)$$

if $qV/nkT >> 1$ this approximates to

$$J \approx J_s \exp\left(\frac{qV}{nkT}\right)$$

Thus a graph of ln$J$ against V should have a linear region where V>3kT/q. The slope of this linear region yields n, the ideality factor, and the intercept of the line at V=0 is J_S which yields the barrier height.

6.2 Fabrication of Schottky Diodes

6.2.1 Preparation of Samples

6.2.1.1 Etching

Etched samples were prepared from a wafer of n-type GaAs of characteristics: Si-doped................. 1.4 - 1.8 x 10^{18} cm^{-3}
.... {100} orientation
The novel source was set up in the RIBE configuration, and etches were performed under similar conditions to the previous experiments.

6.2.1.2 Cleaning

As in all previous etches, a contamination layer formed. To ensure that the cleaning process to remove the contamination did not adversely affect the surface, two control samples were also prepared, from the same wafer.

Two samples, one etched and one unetched were placed in isopropyl-alcohol in a sonicator for a total of 30 minutes, removing them after each 10 minutes for gentle rubbing with a cotton bud. A third sample, unetched, was left untouched in a still Petrie dish of isopropyl-alcohol.

Finally, all three samples were put in a dish of 10% NH_3 solution, to remove the native oxide layer, as recommended in Chapter 3, section 3.2.1.4, and dried with dry nitrogen.

6.2.2 Deposition of Metal Contacts

6.2.2.1 Ohmic Contacts

On removal from the NH_3 solution and drying, all three samples were immediately transferred to the evaporator, where 10nm of Al, followed by 100nm of Au were deposited on the back surfaces.

The samples were all then annealed for 90 s at 450°C, to induce a sufficiently highly doped layer for the tunneling current to make an ohmic contact.

6.2.2.2 Schottky Contacts

All three samples were again put into NH_3 solution for a few minutes to remove the native oxide layer which would have regrown during the annealing process. They were then immediately transferred to the evaporator after drying where 100nm of Au was deposited through a shadow mask, illustrated in figure 6.3, onto the front surface .

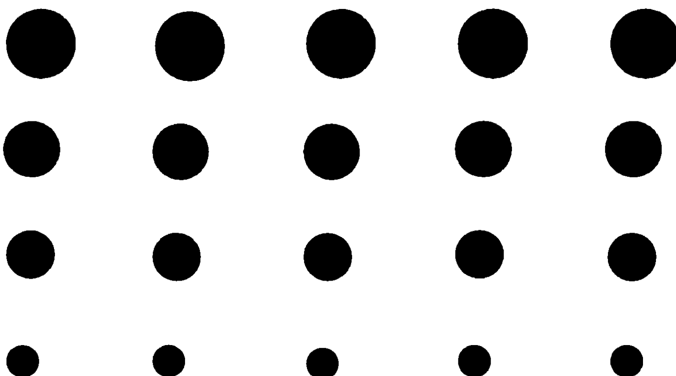

Fig. 6.3 Diagram of mask used to fabricate Schottky contacts

6.3 Evaluation of Schottky Diodes

6.3.1 I-V Characteristics

I-V characteristics were measured for sample dots of all sizes on each of the three samples, using a curve tracer. The curve tracer was designed such that the potential required to drive various standard current values was always measured. Current densities were then calculated from the known areas of the various dots deposited, and graphs of current density, *J*, against V were plotted. Figure 6.4 shows the *J*-V curves in both forward and reverse bias, illustrating the expected diode characteristics.

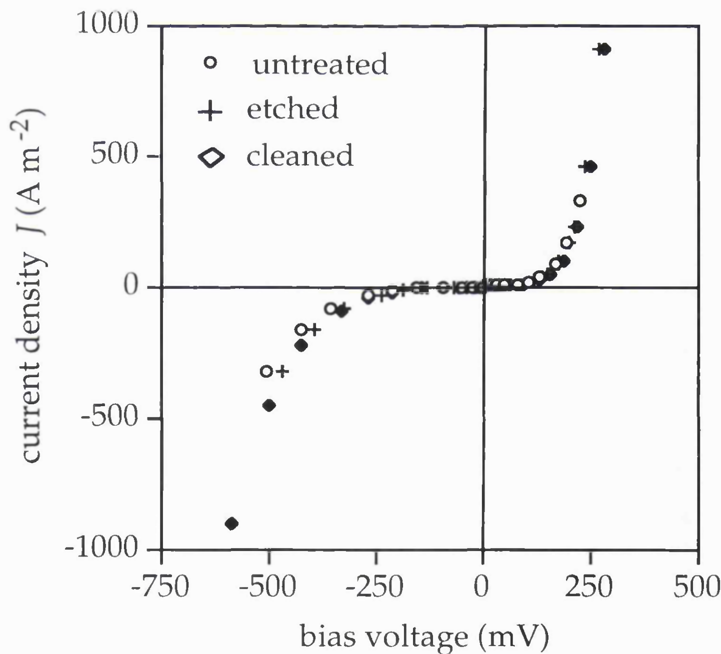

Fig. 6.4 J-V characteristics for representative diodes formed on each sample

It can clearly be seen that all three samples are very similar, and show good diode characteristics.

6.3.2 Analysis

Graphs of ln(J) against V were plotted, to find the slope and intercept of the linear sections.

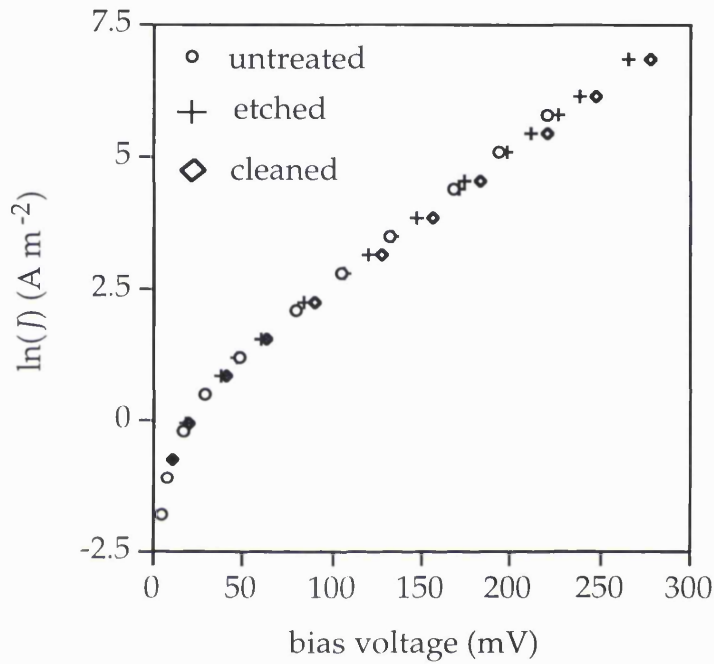

Fig. 6.5 Plot of ln(J) against V for the same diodes as Fig. 6.4

6.3.2.1 Ideality Factors

$$n = \frac{q}{kT} \frac{\partial V}{\partial(\ln J)}$$

For the untreated sample, $\frac{\partial V}{\partial(\ln J)} = 0.0384$

hence n = 1.52

For the etched sample, $\frac{\partial V}{\partial(\ln J)} = 0.0393$

hence n = 1.55

For the cleaned but unetched sample, $\frac{\partial V}{\partial(\ln J)} = 0.0406$

hence $n = 1.61$

6.3.2.2 Barrier Heights

$$J_S = AT^2 \exp(-q\phi_B / kT)$$

$$(J_S / AT^2) = \exp(-q\phi_B / kT)$$

$$\ln(AT^2/J_S) = (q\phi_B/kT)$$

$$\text{hence} \quad \phi_B = [\ln(AT^2) - \ln(J_S)](kT/q)$$

It is very difficult to read $\ln(J_S)$ accurately from the graph, so it was calculated from $\partial V/\partial(\ln J)$ and one easy-to-read point. The result of this was very close to the apparent value.

with $A = 1.2 \times 10^6$ A m^{-2} K^{-2} and $T = 293$K $\quad \ln(AT^2) = 25.36$

For the untreated sample, $\ln(J_S) = 0.03$
hence $\phi_B = 0.6395$ V

For the etched sample, $\ln(J_S) = 0.24$
hence $\phi_B = 0.634$ V

For the cleaned but unetched sample, $\ln(J_S) = 7 \times 10^{-3}$
hence $\phi_B = 0.640$ V

6.3.3 Summary of Characteristics

	Ideality Factor, n	Barrier Height, ϕ_B
Untreated sample	1.52	0.64 V
Etched sample	1.55	0.63 V
Unetched cleaned sample	1.61	0.64 V

6.4 Evaluation of Surface Characterisation

The ideality factors of 1.5 - 1.6 are high compared with the best values for GaAs of 1.04, and the barrier height of 0.64V is low compared with the ideal value for Au-GaAs of 0.9V, but both of these anomalies can be expected for a highly doped semiconductor. The wafer used in this characterisation work was doped to $\sim 10^{18}$ cm^{-3} which is indeed rather high.

The important point to note is the high degree of consistency among the three samples, particularly in the values of the barrier height, which indicate the density of surface states. The density of surface states has not been changed at all by either the etching or the cleaning process.

This result compares very well with other etching methods.

Yamasaki *et al* [6.4] investigated the effect of rf sputter etching on the GaAs surface. Their material was n-type GaAs (Si-doped -- 3×10^{17} cm^{-3}). They found the barrier height dropped from 0.7V to 0.44V with 100W of rf power, whilst the ideality factor increased from 1.1 to 1.8. T. Hara *et al* [6.5], with reactive ion etching of a previously deposited SiO_2 layer, found that the barrier height of the newly exposed GaAs surface had fallen from 0.745V for the virgin surface to 0.52V for a rf power of 300W. Their carrier concentration

in the virgin sample was 1.9 x 10^{17} cm^{-3}. Noh *et al* [6.6] using an Ar ECR microwave plasma, found the ideality factor increased from 1.04 to 1.24, with an initial carrier concentration of 1.9 x 10^{17} cm^{-3}, whist the barrier height fell from 0.767V to 0.67V (converting their values to those which would have been obtained with A = 120 A cm^{-2} K^{-2}, for ease of comparison).

In all of these cases, a considerable change in both ideality factor and barrier height were found subsequent to the etching process, (12% - 35% in barrier height, 24% - 64% in ideality factor).

In the etching performed with this novel source, the change in barrier height is 1%, and the change in ideality factor is 2%. Thus the damage induced by etching with this novel source is indeed ultra-low [6.7].

6.5 References

6.1 S. M. Sze *Physics of Semiconductor Devices* Wiley (1981)

6.2 H. K. Henisch *Rectifying Semiconductor Contacts* Clarendon, Oxford (1957)

6.3 H. A. Bethe *M. I. T. Radiat. Lab. Rep.* 43-12 (1942)

6.4 K. Yamasaki, K. Asai, K. Shimada and T. Makimura *J. Electrochem. Sci.: Solid State Sci and Technol.* **129** 2760 (1982)

6.5 T. Hara, H. Suzuki, A. Suga, T, Terada and N. Toyoda *J. Appl. Phys.* **62** 4106 (1987)

6.6 S. K. Noh, K. Ishibashi, Y. Aoyagi, S. Namba and Y. Yoshizako *J. Appl. Phys.* **67** 2591 (1990)

6.7 J. Beckman and R. B. Jackman *Vacuum* **44** 257 (1993)

CHAPTER 7: THIN FILM DIAMOND

7.1 Importance of Diamond

Diamond is a material with many extreme properties, which make it useful for many varied applications. It is extremely hard, with a low coefficient of friction and is chemically highly resistant. This makes it a very useful material for protective coatings in applications as diverse as machine tools and artificial joints. It has the highest thermal conductivity of any material, 10 times that of copper, and is therefore an ideal heat diffuser for high temperature, high power semiconductor devices.

Diamond is also a semiconductor material in its own right, with a very wide band-gap, 5.5eV, (compared with 1.1eV for silicon and 1.4eV for GaAs), high hole mobility and high breakdown voltage. Thus there is a great deal of interest in developing doped-diamond materials for electronic purposes, to produce high power, high frequency devices compatible with high temperature, chemically harsh and/or high radiation environments [7.1].

7.2 CVD of Diamond

It has been shown within the last decade that diamond can be grown by a variety of CVD methods, but they all have certain common characteristics. The carbon containing precursor may be one of numerous common gases, (CH_4, C_2H_2, CO, CO_2 and others have been used), but it must in all cases be greatly diluted, to <1%, in hydrogen. The other important characteristic is the need for the presence of atomic hydrogen in the vicinity of the growing surface. The exact role of H in the nucleation and growth of diamond is still a matter of some controversy, but it is certain that without it only graphitic forms of carbon will grow.

The temperature of the growing surface is also a very important parameter. If the temperature is either too low or too high, only graphitic forms will grow. The temperature must be within a given window, but what this temperature range is, is also somewhat controversial. It is actually quite difficult to monitor exactly the temperature of the growing surface, and different groups have used widely differing methods, such as thermocouples attached to the underside of the sample or to the sample holder, or pyrometers. This may be the cause of the disparity. However, on average, it seems to be about 1000°C ± 200°C [7.7,7.9,7.15,7.19].

Angus and Hayman [7.2] suggest that in the presence of atomic hydrogen the diamond surface is likely to be saturated with hydrogen. Because the H–H bond energy is greater than the C–H bond energy, atomic hydrogen will both add to vacant surface sites, S·, and abstract hydrogen from filled sites, S–H:–

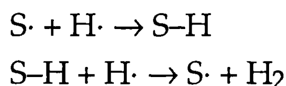

$$S\cdot + H\cdot \rightarrow S\text{–}H$$
$$S\text{–}H + H\cdot \rightarrow S\cdot + H_2$$

Both these reactions are exothermic. Because of the dynamic interaction between atomic hydrogen and the surface, there will be a steady-state concentration of free surface sites, S·, which can undergo reactions with carbon-containing species, R, for example:–

$$S\cdot + R\cdot \rightarrow S\text{–}R$$

There has been much speculation whether the intermediate for diamond growth is a single-carbon-species, such as the methyl radical (CH_3) or CH_3^+ ions, or a two-carbon-atom species, such as acetylene (C_2H_2).

Jackman *et al* [7.3] have demonstrated that neither methane nor hydrogen will adsorb on a clean silicon substrate, without activation, in the case of their work, by a hot filament. They also demonstrated that in the presence of a filament heated to 2200K, acetylene and ethylene (C_2H_4) desorbed from the surface after it had been exposed to activated methane, implying that these species, which are known to form from methane when activated, can also stick to the growing surface. Exposure to atomic hydrogen can convert ethylene to acetylene, by hydrogen abstraction, and then to C_3 forms through a hydrogen driven addition reaction between adsorbed acetylene and methyl species. Thus in this schema, both single-carbon-atom species and two-carbon-atom species can contribute to growth.

The aim for electronic applications is to grow heteroepitaxial, single crystal, diamond films. However, the lattice constant of diamond, 3.57Å, is

very much smaller than almost any other cubic crystal, so epitaxial growth is very difficult to achieve. (Cubic boron nitride has a lattice constant of 3.62Å, only a little larger than diamond, but is itself very difficult to grow, and is not suitable as a substrate for diamond. It is grown as a wide band-gap material in its own right). The most common substrate used is Si, (lattice constant 5.43Å) which has a considerable mismatch. To encourage nucleation and growth various surface pretreatments have been used, commonly polishing with diamond powder, but biasing in hydrocarbon plasma has also been used very successfully [7.4]. It is believed that an intermediate layer of SiC promotes epitaxial growth since the lattice constant of SiC is 4.35Å, much closer to that of diamond than silicon itself , and the cubic structure is the same. However, it is still a considerable mismatch by normal epitaxial standards (22% compared with less than 5% for other heteroepitaxial systems). Nevertheless, highly oriented polycrystalline diamond films can be grown, where the orientation is close to that of the substrate (within 3° or 4°), particularly on Si(100), and can be considered epitaxially textured [7.5]. These films are not yet single crystal. The individual crystallites, as they grow and merge still have clear grain boundaries between them as they do not all have the same low angle to the substrate. These low angle grain boundaries inhibit carrier mobility, so that CVD diamond film is not yet of good electronic material quality [7.6].

The variety of CVD methods is in the means chosen to activate the hydrogen/hydrocarbon mixture.

7.2.1 Hot Filament Assisted CVD of Diamond

This is one of the simplest methods. The substrate is held a few mm from a filament, of tungsten or tantalum [7.7], heated to between 2000°C and 2500°C. The gas mixture is passed over the filament to impinge on the substrate surface. The substrate is heated to between 800°C and 1000°C, some or all of this heating coming from the filament. Because of its simplicity this method is much used for research into the growth mechanisms themselves, including the required concentration of H and its role in diamond growth [7.8-7.15], but it is not a suitable method for bulk production of uniform diamond films. There are also the problems of contamination of the film from the material of the filament, due to high temperature reactions between the

metallic filament and hydrogen, forming volatile products which can be deposited on the growing surface, and degradation of the filament itself by carburisation, which can happen in a few hours [7.7].

7.2.2 Plasma-Assisted CVD of Diamond

7.2.2.1 Microwave Plasma-Assisted CVD of Diamond

This has been a very successful method of growing CVD diamond film of very high quality, using microwave plasmas [7.16-7.18]. The advantages of microwave plasma-assisted CVD for diamond film are very high plasma densities leading to relatively high concentrations of atomic hydrogen and methyl and other organic radicals, together with very low sheath potentials, due to the high frequency (of order GHz) of microwaves. The disadvantages of microwaves are difficulty in scaling up, and the extensive shielding of microwave apparatus needed, as microwaves are hazardous to life. The size of the plasma ball is related to the wavelength and for the standard 2.45GHz is only a few centimetres diameter. To increase the size would mean decreasing the frequency and retuning the entire apparatus. This has been done, but is expensive to achieve.

7.2.2.2 Radio-Frequency Plasma-Assisted CVD of Diamond

RF plasmas have been tried in plasma-assisted CVD of diamond, both inductive [7.19-7.25] and capacitive [7.26-7.28], but with only limited success so far. It appears that there must be a good reason for the greater success of microwave over RF. Microwave plasmas are more dense by an order of magnitude or more, resulting in a much higher concentration of atomic hydrogen and hydrocarbon radicals, which are known to be needed for CVD diamond growth. Also, the plasma and sheath potentials in microwave plasmas are lower than in most RF plasmas. It appears that there is an energy window for diamond growth of around 23eV [7.29]. The advantages which

could be obtained by using radio-frequency are the much greater volume of uniform plasma which can be sustained, allowing for either large or even multiple wafer processing, and the safety and simplicity of RF technology. However, conventional capacitively coupled RF plasma sources have high sheath potentials and insufficiently high plasma densities, whilst inductively coupled RF plasma sources, while giving lower sheath potentials use ten times as much power, and the induction coils which sustain the plasma also heat the substrate, making independent temperature control of the substrate difficult.

7.2.2.3 Comparison of Characteristics of Plasma Sources

Plasmas are usually characterised by the electron temperature, the energy the electrons absorb from the exciting electric field, the plasma density, the concentration of charged particles in the plasma, and the ion energy. It is instructive to compare the values of these parameters for different plasma sources.

Table of comparisons for plasma characteristics

Plasma Source	**Electron Temp**	**Plasma Density**	**Ion Energy**
Microwave	10eV	$2 \times 10^{11} cm^{-3}$	10 - 20eV [2.12]
Capacitively Coupled RF	3eV	$4 \times 10^{9}\ cm^{-3}$	~150eV [2.13]
This work	12-16eV	$1 \times 10^{10} - 7 \times 10^{10} cm^{-3}$	20 - 25eV

From the above table, it can clearly be seen that conventional capacitively coupled RF plasma sources form plasmas very different from those formed by microwave excitation. It can also be seen that the novel source

used in this study forms a plasma very similar to that of microwave sources. The figures for the source used here come from Chapter 4.

In view of the similarities between the novel source plasma characteristics, and those of microwave plasmas, it should be possible to use the source in plasma-assisted CVD of diamond. If successful, the advantages of easy scale-up for this source would make it a useful tool in the development of thin film diamond.

7.2.3 Quality of CVD Diamond

Actual devices have been manufactured, but so far the most successful have been on homoepitaxially grown, boron-doped, thin films, which can be single crystals. Theoretically, diamond devices could be considerably more efficient at high frequency and high power than currently available devices [7.30], once the problems of forming suitable rectifying and ohmic metal contacts have been solved. The main difficulty is in forming the ohmic contacts.

For electronic purposes, growing diamond as a thin film on cheaper substrate materials, such as silicon has the best commercial promise. The most successful method to date is microwave plasma assisted chemical vapour deposition (MPACVD). But the best growth to date is polycrystalline, and attempts to form metal contacts on these films have proved that their electronic quality is still well below that of the single crystal films [7.31,7.32]. Also, this method has its limitations, as described above.

There are also still many problems with doping diamond films. Boron doping is the most successful to date, giving p-type diamond. No dopant has yet been found successfully to produce n-type diamond, which is a great limitation on the use of this material for electronics.

7.2.4 Surface Preparation

Because of the extreme lattice mismatch between silicon and diamond, it is actually very difficult to initiate diamond growth on silicon substrates.

It has been found that some form of surface pretreatment is necessary.

Various pretreatments have been tried. Scratching the surface, either with a simple abrasive, such as SiC [7.43], or with fine diamond powder have both been successful in initiating the nucleation of diamond, although diamond powder is the more successful. It has even been reported that contamination of the surface with hydrocarbons [7.44] can enhance nucleation.

7.2.4.1 Bias-enhanced nucleation

It has been known for some years that putting a bias on the substrate will affect the way in which diamond grows. In 1991 Stoner *et al* [7.4] grew textured diamond on β-SiC by imposing a bias of -250V with respect to the chamber, while using a gas mixture relatively rich in methane for 30min, and subsequently growing without bias under reduced methane concentration.

The exact mechanisms involved are not yet completely understood, but the problem has been much studied.

Stoner *et al* [7.46] performed a careful and thorough surface analysis of the effect that a negative bias of -250V would produce. They found that applying a negative bias of -250V to an unscratched Si substrate, in a MWCVD reactor with a gas mixture of 2% methane in hydrogen, at a pressure of 15 Torr, with a microwave power of 600W, increased the nucleation density by up to 5 orders of magnitude. The nucleation density depended on the length of time for which the bias was applied, increasing with increased exposure, up to a maximum period of 2 hours. Normal growth conditions were reverted to when the bias was turned off, and good quality diamond crystals grew.

If the bias remained on throughout growth, poor quality film resulted. This implied that conditions suitable for nucleation are unsuitable for growth.

Surface analysis tehniques revealed that an amorphous SiC interfacial layer developed before significant diamond nucleation occurred. A non-textured diamond film therefore resulted from this process.

Chang *et al* [7.47] investigated the effect of changing the bias applied to the substrate. They found that a low negative bias resulted in a mixture of diamond and amorphous carbon, and a high negative bias grew no diamond. A positive bias improved the quality of the diamond film. This confirms the finding of Stoner *et al* [7.46] that continuous negative bias results in poor quality film.

An ingenious method of combining the textured film growth made possible by applying a bias to β-SiC, with growing diamond on a Si substrate was devised by Wolter *et al* [7.5]. A pre-bias carburisation step, under a 2% methane in hydrogen MW plasma, with the substrate immersed in the plasma, was followed by just 3 mins at a bias of -250V, with the methane concentration increased to 5%, and the substrate at the very edge of the plasma. Growth was continued with the methane concentration reduced to 0.5%, and the substrate moved slightly downstream of the plasma.

This resulted in textured diamond film growth on the silicon substrate, with the orientation of the diamond crystals following the orientation of the silicon wafer.

They hypothesised that the carburisation step induced the growth of an epitaxial SiC conversion layer, and that the subsequent diamond nucleation was epitaxial to the SiC.

John *et al* [7.48] investigated the layer induced by biasing, which is known to increase nucleation. They found that it consisted of carbon-hydrogen groupings based on both sp^2 and sp^3 C–H bonding. This is entirely consistent with the Raman spectra showing lines typical of polyacetylene in the early stages of film growth. These are transformed under subsequent unbiased dilute-methane growth conditions into diamond. However, they utilised a microwave power of 120W in their experiments, contrasted with the 600W of Stoner *et al* [7.46]. There has not as yet been an investigation on the effect of microwave power on the nucleation mechanism, but these two studies seem to indicate that it does make a considerable difference. At 600W, SiC was formed, at 120W hydrogenated carbon was formed.

Beckmann *et al* [7.49] found that growth following bias pretreatment resulted in fine grained diamond film, with a nucleation density $>10^{10}cm^{-2}$.

7.3 Characterisation of Carbons by Raman Spectroscopy

The Raman spectrum of large single crystal graphite shows a strong line at a shift of 1580 cm^{-1} from the C-C stretching mode of the hexagonal sheets, designated the G (for graphite) line, with a much weaker line at 2724 cm^{-1}. The latter is taken to be a two-phonon band, 2x1357 cm^{-1}, 1357 cm^{-1} being a line which appears strongly in polycrystalline graphite, and designated the D line, (as it was thought to be related to the diamond-like sp^3 carbon bond) but not in the large grain crystals. This line is assigned to a first-order phonon at the M point, the 1000 zone boundary of the hexagonal Brillouin zone. The small size of the particles causes a breakdown of the $k = 0$ selection rule.

For other disordered graphitic carbons, such as the glassy carbons, (so called from their non-crystalline structure), these same two lines, 1357 cm^{-1} and 1580 cm^{-1} also appear, although sometimes shifted slightly and much broadened, and are therefore designated the D and G bands respectively. The classification of the carbon can be made on the width and wavenumber of the G band, and on the D/G intensity ratio [7.33].

The classification can be summarised in the following table:

Carbon Type	I_D/I_G	$\Delta\nu_G$ (cm^{-1})	ν_G (cm^{-1})	ν_D(cm^{-1})
Diamond				1332
Natural graphite crystal	0	13	1580	
HOPG	0	13	1576	
Polycrystalline graphite	0.2	28	1580	1357
Glassy Carbon A	0.91	79	1591	1343
Glassy Carbon B	1.32	61	1591	1343

The Raman spectrum of pure natural diamond has only one, very sharp line, at 1332 cm^{-1}, close to the D line of graphitic carbon, since the tetragonal structure of diamond has only one possible bond length, and the structure has cubic symmetry, whilst highly ordered pyrolitic graphite, (HOPG), like large grain crystalline graphite has only the G line. The main difference between

these latter two is a small wavenumber shift for HOPG from 1580 cm^{-1} to 1576cm^{-1}.

A line at 1620 cm^{-1} can also be seen in microcrystalline graphite, whose strength increases as the crystal size decreases. This line is also a first-order phonon at a zone boundary, due to second-neighbour forces [7.34].

7.4 Diamond-like Carbon (DLC) film

Diamond-like carbon films are amorphous, hydrogenated carbon films, (a-C:H). The carbon atoms are strongly linked, in a combination of sp^2 and sp^3 bonding, with some of the sp^3 bonds hydrogen terminated. The exact structure is very variable, as it is not a crystal lattice. These films have interesting properties; they are very hard, they are good electrical insulators, they have high thermal conductivity, are chemically inert and are transparent in the infra-red [7.35]. Indeed, many of their properties are so similar to those of diamond film that when they were first fabricated it was thought that they were a form of diamond. (Hence the name they are commonly known by). However, the actual values of these properties, when measured, vary considerably from film to film, depending on growth conditions [7.36], unlike true diamond, whose properties vary very little, whether one measures natural diamond or polycrystalline diamond film, and the method of film growth also affects the actual properties of the diamond very little.

7.4.1 Applications of DLC films

Diamond-like carbon films have many applications, as do diamond films. They are used as wear reduction coatings in medical applications, both for precision surgical tools, and for artificial joints, since as well as being very hard, DLC is biologically compatible[7.37]. They are also used in electronic applications, as insulating passivation layers [7.38], and in opto-electronic devices [7.39,7.40].

7.4.2 Growth of DLC by RF Plasma Assisted Chemical Vapour Deposition

The conditions required for the deposition of a-C:H films are rather different from those required for the deposition of diamond.

The deposition process consists of several steps. Hydrocarbon radicals adsorb on the surface, with a sticking coefficient strongly dependent on surface temperature. If the temperature is raised, the species gain too much energy and rapidly desorb again. Thus DLC is usually grown at near room temperature, in contrast to diamond, grown at the elevated temperature of between 850°C and 950°C. Indeed, at temperatures above a few hundred degrees Celsius, DLC decomposes.

The next step occurs when ions bombard the growing surface, and if they have sufficient energy, will penetrate, either lodging in an interstitial, or dislodging another atom into an interstitial and taking its lattice position. In either case, this increases the density locally, and causes the formation of sp^3 bonds. However, if the energy of the incoming ion is too great, as well as penetrating the surface, and disloding an atom from its position, it could give rise to a thermal spike on losing the extra energy. This would then lead to relaxation of the denser region, and the sp^3 bonds would reconvert to sp^2 bonds [7.41]. The energy of the ions is usually estimated from the self-bias which develops, from the relationship $E_i \approx 0.4\ V_b$. The optimum value of E_i is ~120eV per carbon atom in the ion, and therefore depends on the source gas. This corresponds well with the finding that for $|V_b| < 100V$ only soft polymeric coatings are grown, (as the ions have insufficient energy to penetrate the surface), and for $|Vb| > 600V$ only graphitic material is deposited [7.42]. This work was with methane as the source gas.

A range of source gases, including methane, acetylene and benzene have been used. These are usually, but not always, diluted with hydrogen, either lightly, 75% methane:25% hydrogen [7.42] or quite strongly. Grant *et al* [7.37] varied the methane concentration between 2% and 100% to optimise the concentration for coating hardness and adhesion, and found that 16% to 18% of methane in hydrogen gave the best hardness and adhesion. This again is in contrast to diamond, where the methane concentration is ≤ 1%.

Gas pressures for the deposition of DLC are in the range 0.01-1 torr, again very different from diamond, where pressures of 5-30 torr are required.

These necessary conditions of pressure, ion energy and temperature make the standard capacitively coupled RF plasma reactor very suitable for the deposition of DLC. Such reactors are commonly used for the deposition of DLC.

7.8 References

7.1 W. Zhu, B. R. Stoner, B. E. Williams and J. T. Glass *Proc. of IEEE* **79** 621 (1991)

7.2 J. C. Angus and C. C. Hayman *Science* **241** Articles 913 (1988)

7.3 R. B. Jackman , L. H. Chua and J. S. Foord *Surf. Sci.* **292** 47 (1993)

7.4 B. R. Stoner and J. T. Glass *Appl. Phys. Lett.* **60** 698 (1992)

7.5 S. D. Wolter, B. R. Stoner, J. T. Glass, P. J. Ellis, D. S.. Buhaenko, C. E. Jenkins and P. Southworth *Appl. Phys. Lett.* **62** 1215 (1993)

7.6 J. A. von Windheim, B. A. Fox, D. M. Malta and H. A. Wynands *Diamond Films '93* (in press)

7.7 H. Matsubara and T. Sakuma *J. Mater. Sci.* **25** 4472 (1990)

7.8 A. A. Morrish and P. E. Pehrsson *Appl. Phys. Lett.* **59** 417 (1991)

7.9 S. Iijima, Y. Aikawa and K. Baba *J. Mater. Res.* **6** 1491 (1991)

7.10 D-W. Kweon, J-Y. Lee and D. Kim *J. Appl. Phys.* **69** 8329 (1991)

7.11 W. L. Hsu *Appl. Phys Lett.* **59** 1427 (1991)

7.12 K-H. Chen, M-C. Chuang, C. M. Penney and W. F. Banholzer *J. Appl. Phys.* **71** 1485 (1992)

7.13 F. G. Celii and J. E. Butler *J. Appl. Phys.* **71** 2877 (1992)

7.14 K. Tankala annd T. DebRoy *J. Appl. Phys.* **72** 712 (1992)

7.15 E. Kondoh, T. Ohta, T. Mitomo and K. Ohtsuka *J. Appl. Phys.* **72** 705 (1992)

7.16 P. John, D. K. Milne, W. C. Vijayarajah, M. G. Jubber and J. I. B. Wilson *Dia. and Rel. Mat.* **3** 388 (1994)

7.17 K. Kobashi, K. Nishimura, Y. Kawate and T. Horiuchi *Phys. Rev. B* **38** 4067 (1988)

7.18 M. Nunotani, M. Komori, M. Yamasawa, Y. Fujiwara, K. Sakuta, T. Kobayashi, S. Nakashima, S. Minomo, M. Taniguchi and M.Sugiyo *Jap. J. Appl. Phys.* **30** L1199 (1991)

7.19 S. Matsumoto *J. Mater. Sci. Lett.* **4** 600 (1985)

7.20 S. Matsumoto, M. Hino and T. Kobayashi *Appl. Phys. Lett.* **51** 737 (1987)

7.21 D. Meyer, N. J. Ianno, J. A. Woollam, A. B. Swartzlander and A. J. Nelson *J. Mater. Res.* **3** 1397 (1988)

7.22 D. Meyer, R. O. Dillon and J. A. Woollam *J. Vac. Sci. Technol.* **A7** 2325 (1989)

7.23 R. A. Rudder, G. C. Hudson, J. B. Posthill, R. E. Thomas and R. J. Markunas *Appl. Phys. Lett.* **59** 791 (1991)

7.24 R. A. Rudder, G. C. Hudson, J. B. Posthill, R. E. Thomas, R. C. Hendry, D. P. Malta, R. J. Markunas, T. P. Humphreys and R. J. Nemanich *Appl. Phys. Lett.* **60** 329 (1992)

7.25 R. J. Graham, J. B. Posthill, R. A. Rudder and R. J. Markunas *Appl. Phys. Lett.* **59** 2463 (1991)

7.26 S. R. Lee and B. Gallois *Dia. and Rel. Mater.* **1** 235 (1992)

7.27 Y. Shimada, K. Kobayashi, N. Mutsukura and Y. Machi *Dia. and Rel. Mater.* **2** 656 (1993)

7.28 Y. Shimada, K. Kobayashi, N. Mutsukura and Y. Machi *Plasma Sources Sci. Technol.* **2** 18 (1993)

7.29 J. Wei, H. Kawarada, J-I Suzuki, J. S. Ma and A. Hiraki *Jap. J. Appl. Phys.* **30** 1279 (1991)

7.30 R. T. Trew, J-B. Yan and P. M. Mock *Proc. IEEE* **79** 598 (1991)

7.31 M. W. Geis *Proc. IEEE* **79** 669 (1991)

7.32 G. Sh. Gildenblat, S. A. Grot and A. Badzian *Proc. IEEE* **79** 647 (1991)

7.33 D. S. Knight and W. B. White *J. Mater. Res.* **4** 385 (1989)

7.34 R. J. Nemanich and S. A. Solin *Phys. Rev.B* **20** 392 (1979)

7.35 F. López, M. V. Garcia-Cuenca, C. Serra and J. L. Morenza *Dia. & Rel Mat.* **2** 229 (1993)

7.36 P. W. Pastel and W. J. Varhue *J. Vac. Sci. Technol.* **A9** 1129 (1991)

7.37 D. M. Grant, I. R. McColl, M. A. Golozar, J. V. Wood and N. St. J. Braithwaite *Dia. & Rel Mat.* **1** 727 (1992)

7.38 M. Frischholz, Th. Mandel, R. Helbig, G. Schmidt and A. Hammerschmidt *Dia. & Rel Mat.* **2** 718 (1993)

7.39 C. O. Morosanu, T. Stoica, C. De Martino, F. Demichelis and A. Tagliaferro *Dia. & Rel Mat.* **3** 814 (1994)

7.40 Rusli, S. R. P. Silva and G. A. J. Amanatunga *Dia. & Rel Mat.* **3** 817 (1994)

7.41 J. Robertson *Dia. & Rel Mat.* **3** 361 (1994)

7.42 E. H. A. Dekempeneer, J. Smeets, J. Meneve, L. Eersels and R. Jacobs *Dia. & Rel Mat.* **3** 613 (1994)

7.43 K. Mitsuda, Y. Kojima, T. Yoshida and K. Akaashi *J. Mater. Sci.* **22** 1557 (1987)

7.44 A. A. Morrish and P. E. Pehrsson *Appl. Phys. Lett.* **59** 417 (1991)

7.45 B. A. Fox, B. R. Stoner, D. M. Malta, P. J. Ellis, R. C. Glass & F. R. Sivaslian *Dia. & Rel Mat.* **3** 382 (1994)

7.46 B. R. Stoner, G.-H. M. Ma, S. D. Wolter and J. T. Glass
Phys. Rev. B **45** 11067 (1992)
7.47 J. J. Chang and T. D. Mantei *J. Appl. Phys.* **71** 5724 (1992)
7.48 P. John, D. K. Milne, I. C. Drummond, M. G. Jubber, J. I. B. Wilson and J. A. Savage *Dia. and Rel. Mat.* **3** 486 (1994)
7.49 R. Beckmann, B. Sobisch, W. Kulisch and C. Rau *Dia. and Rel. Mat.* **3** 555 (1994)

CHAPTER 8: CARBON DEPOSITION WITH MODIFIED SOURCE

As the plasma characteristics of the novel source, as characterised in Chapter 4, and, as shown in the comparisons with microwave plasmas in the previous chapter, are very suitable for plasma-assisted CVD of diamond, this new application was evaluated.

8.1 Modification of the Source

The propensity of the source for self-erosion was exploited to deposit thin films of carbon on silicon substrates.

The most usual method used to deposit thin diamond films is microwave plasma CVD, but if a method of utilising RF plasma could be successfully devised, this would be a considerable advantage, as explained in Chapter 7. If a method could be found also which did not require premixing hydrogen and methane flows to the exact level of dilution needed, 1% methane in hydrogen, to promote diamond rather than graphitic growth, this simplification would be a great advance.

With the liner of the source graphite instead of silica, and with hydrogen as the gas used for the plasma, erosion of the graphite by the hydrogen plasma should produce an admixture of hydrocarbons. This mixture could meet the requirements for diamond growth.

8.1.1 Preliminary Tests

Some preliminary tests were carried out to determine the response of the novel source to hydrogen.

It was found that the plasma could only be sustained with higher powers at higher pressure. Figure 8.1 shows the minimum pressure required to sustain a plasma at various input powers.

It was also found that the maximum power input available was 400W, although with argon the power supply maximum was 500W.

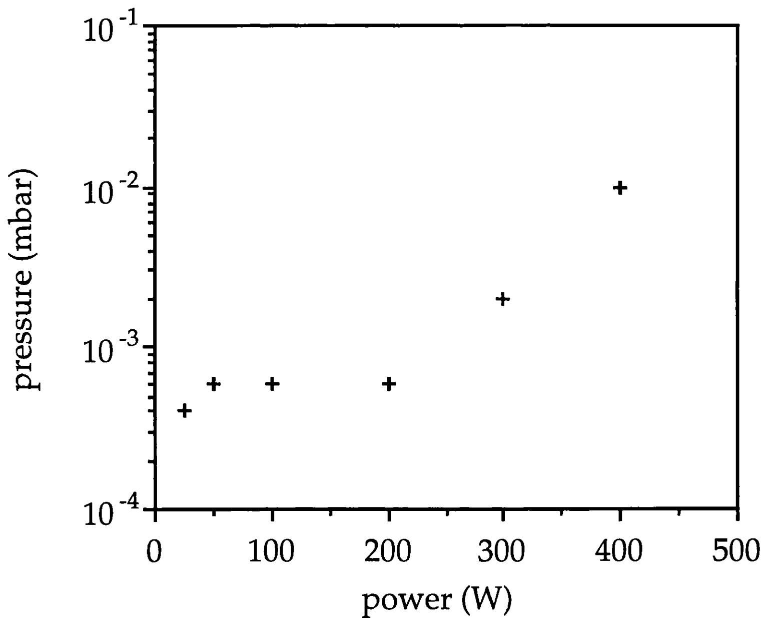

Fig. 8.1 Minimum Pressure against power for hydrogen plasma

Further, it was observed that at higher pressures, $\sim 10^{-2}$ mbar, the plasma was contained in rings inside the plasma chamber of the source. This is illustrated in figure 8.2.

Fig. 8.2 Photograph of high pressure hydrogen plasma showing rings.

8.1.2 Preparation of Liner

To prepare a graphite liner, the silica liner was removed from the source and coated. After some trial and error, a recipe was evolved which produced a smooth stable coating.

Aquadag, diluted with D.I. water until a smooth creamy texture was achieved, was painted onto the inside of the liner. The liner was then baked for one hour at 140°C and allowed to cool slowly. The liner was then replaced in the source.

8.2 First Carbon Deposition

8.2.1 Unprepared Silicon

Samples of virgin silicon were exposed to the plasma, for some time, under moderate conditions of power and pressure, (300W RF power and a pressure of 2×10^{-3} mbar), without heating. There was no evidence of any deposit formed.

Further samples of untreated silicon were then exposed to the plasma, under similar conditions, but with the silicon substrate heated by passing current directly through the sample from tantalum foil connections. A heating current of 8A produced adequate heating of the sample, as tested with a thermocouple in contact with the sample surface.

After one hour a coating was formed.

The heating was not uniform, because of differences in the degree of contact of the tantalum connectors, and thus a temperature gradient was established, from ~800°C at one end to ~600°C at the other.

It was observed that the coating was thick and black at the hotter end, brownish at the cooler end.

The coating was clearly graphitic and not diamond.

8.2.2 Hot Prepared Silicon

The silicon was scratched with carburundum (SiC) powder, as it has been well established that carbon nucleation is much increased by scratching the surface.

A series of one hour depositions was performed, varying both power and pressure, as detailed in the table below. All these depositions produced films, which varied in appearance with the temperature gradient across the sample.

These samples, together with the unscratched sample, were then prepared for Raman spectro-scopic analysis, by separating the regions grown under different temperature conditions.

Power	Pressure	Appearance of Deposition
150W	$>10^{-2}$ mbar	Barely visible
330W	6×10^{-3} mbar	Sooty in middle, clear at ends
330W	10^{-2} mbar	Sooty in middle, clear at end
400W	$>10^{-2}$ mbar	Sooty in middle, clear at end

8.2.2.1 Analysis by Raman Spectroscopy

From the Raman spectra obtained from the carbon depositions, shown in figures 8.3 (a) - (i), measurements of ν_G, ν_D, I_D/I_G and $\Delta\nu_G$ were made. These are given below, together with the classification of the deposit grown, from comparison with the table given in Chapter 7.

P(W)	p(mbar)	T(°C)	I_D/I_G	$\nu_D(cm^{-1})$	$\nu_G(cm^{-1})$	$\Delta\nu_G(cm^{-1})$	Classification
330	6×10^{-3}	600	0.83	1350	1580	29.4	polycrystalline C
		700	1.31	1343	1580	59	glassy carbon B
		800	1.07	1343	1585	76.5	glassy carbon A
330	1×10^{-2}	600	0.76	1350	1580	28	polycrystalline C
		700	1.28	1341	1580	59	glassy carbon B
		800	1.11	1347	1590	73.5	glassy carbon A
400	$>10^{-2}$	600	0.83	1350	1580	28	polycrystalline C
		700	1.33	1344	1580	61.8	glassy carbon B
		800	1.1	1344	1585	76.5	glassy carbon A

From this it can be seen that the definitive parameter is temperature. All the spectra also show a clear indication of the line at 1620 cm^{-1}, implying that the crystals are very small.

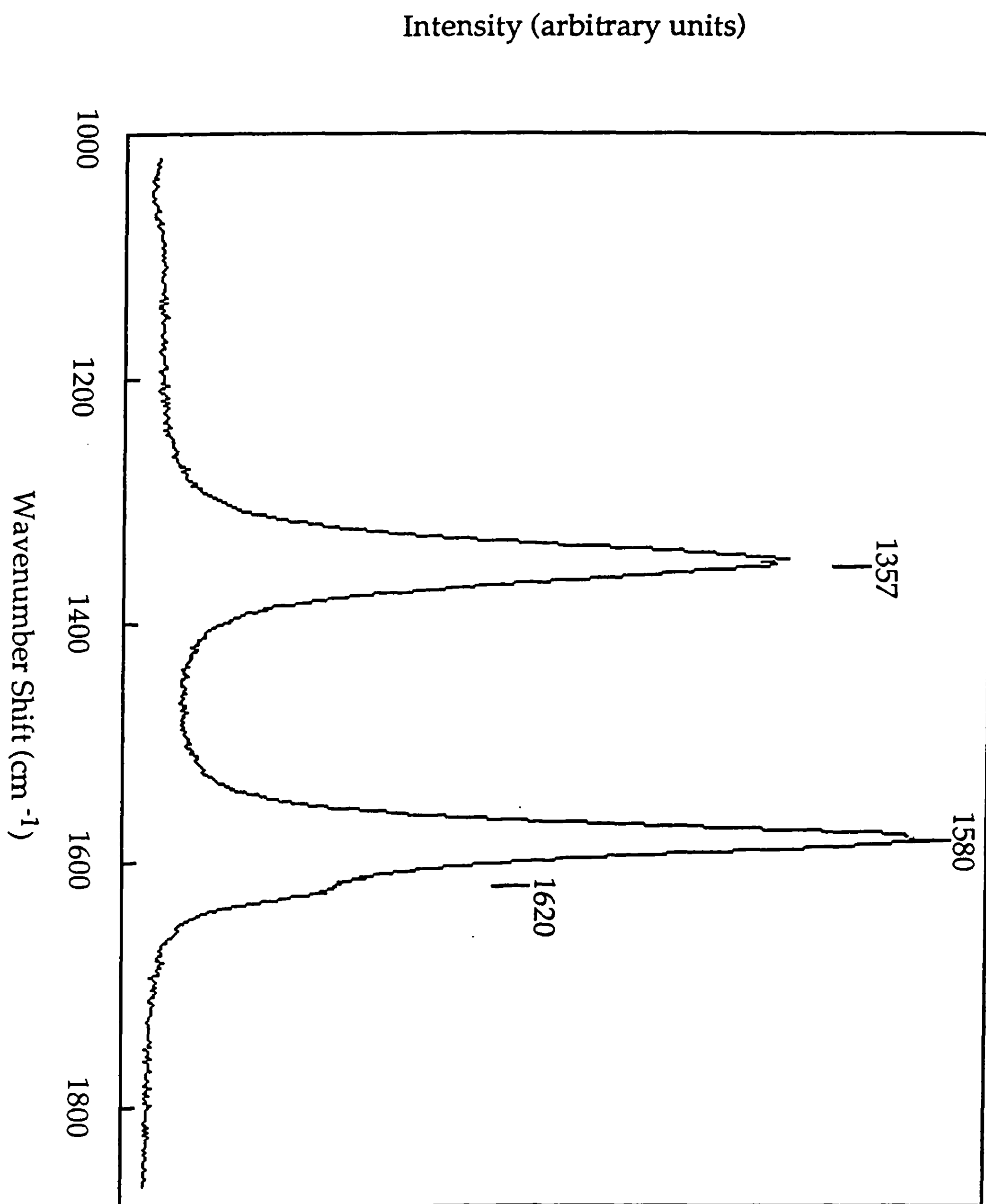

Conditions: Power 330W

Pressure 6×10^{-3} mbar

Temperature 600°C

Figure 8.3(a) Raman Spectrum from polycrystalline carbon

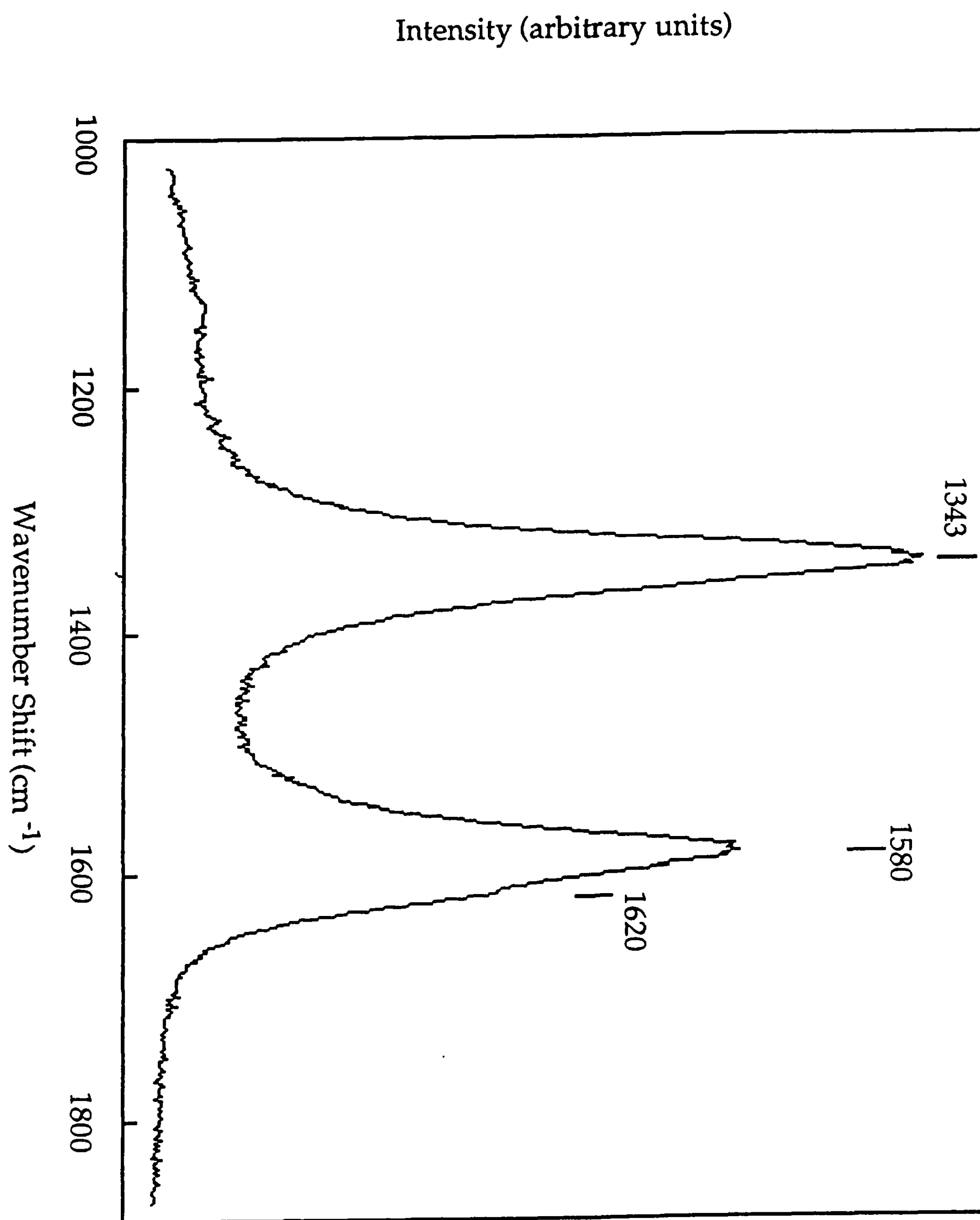

Conditions: Power 330W

Pressure 6×10^{-3}mbar

Temperature 700°C

Figure 8.3(b) Raman spectrum of glassy carbon B

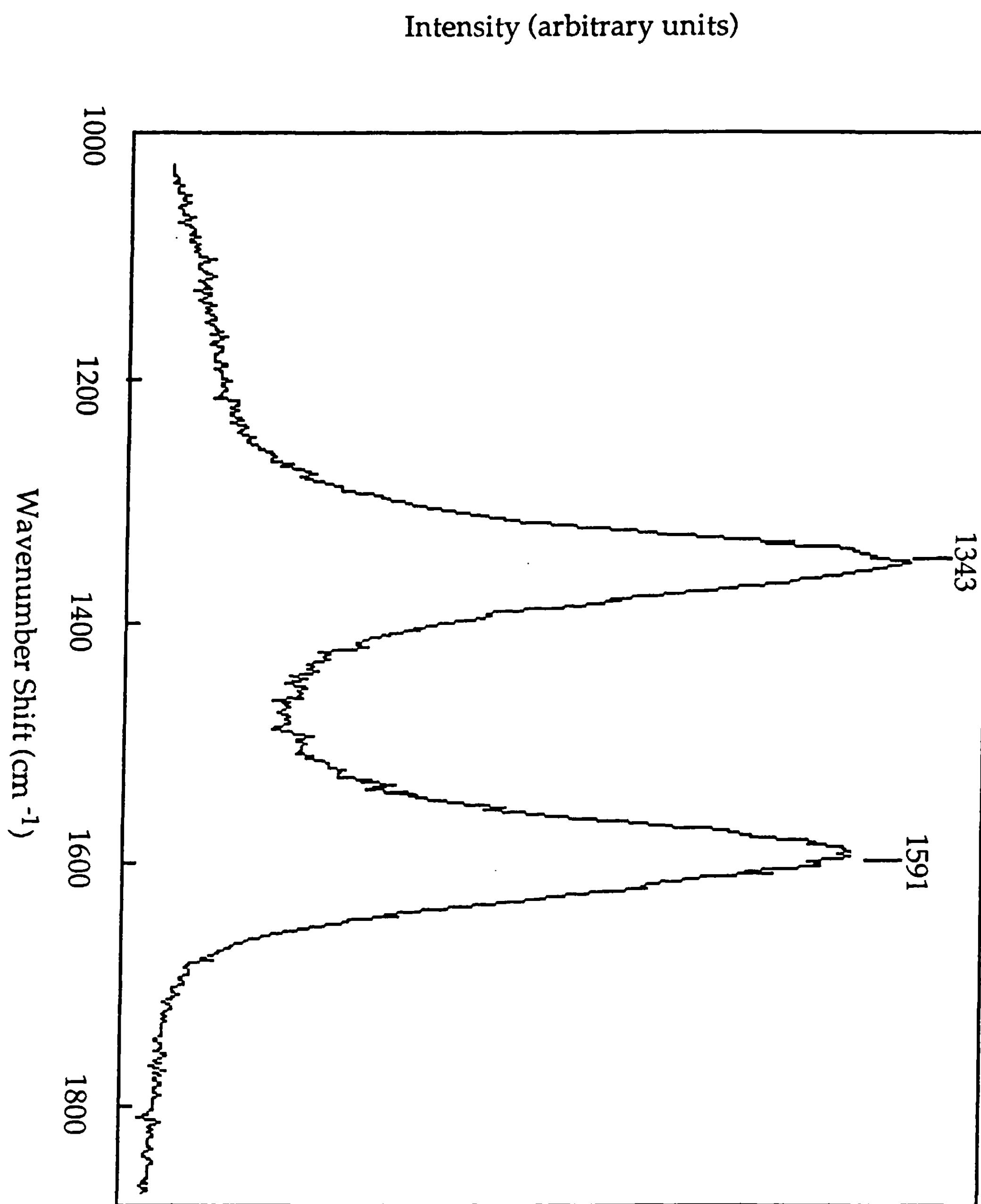

Conditions: Power 330W

Pressure 6×10^{-3}mbar

Temperature $800^{o}C$

Figure 8.3(c) Raman spectrum from glassy carbon A

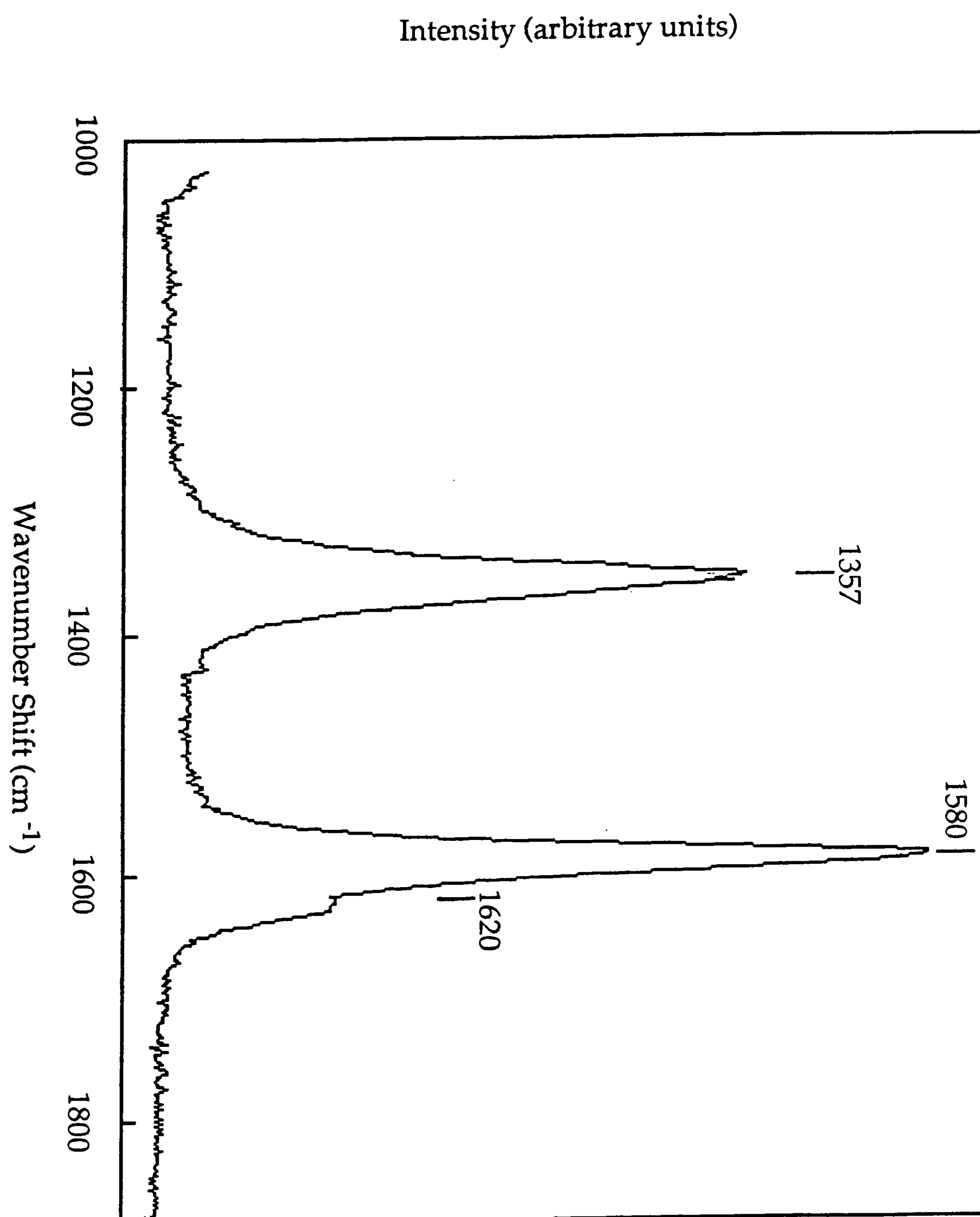

Conditions: Power 330W

Pressure 10^{-2}mbar

Temperature $600^{o}C$

Figure 8.3(d) Raman spectrum from polycrystalline carbon

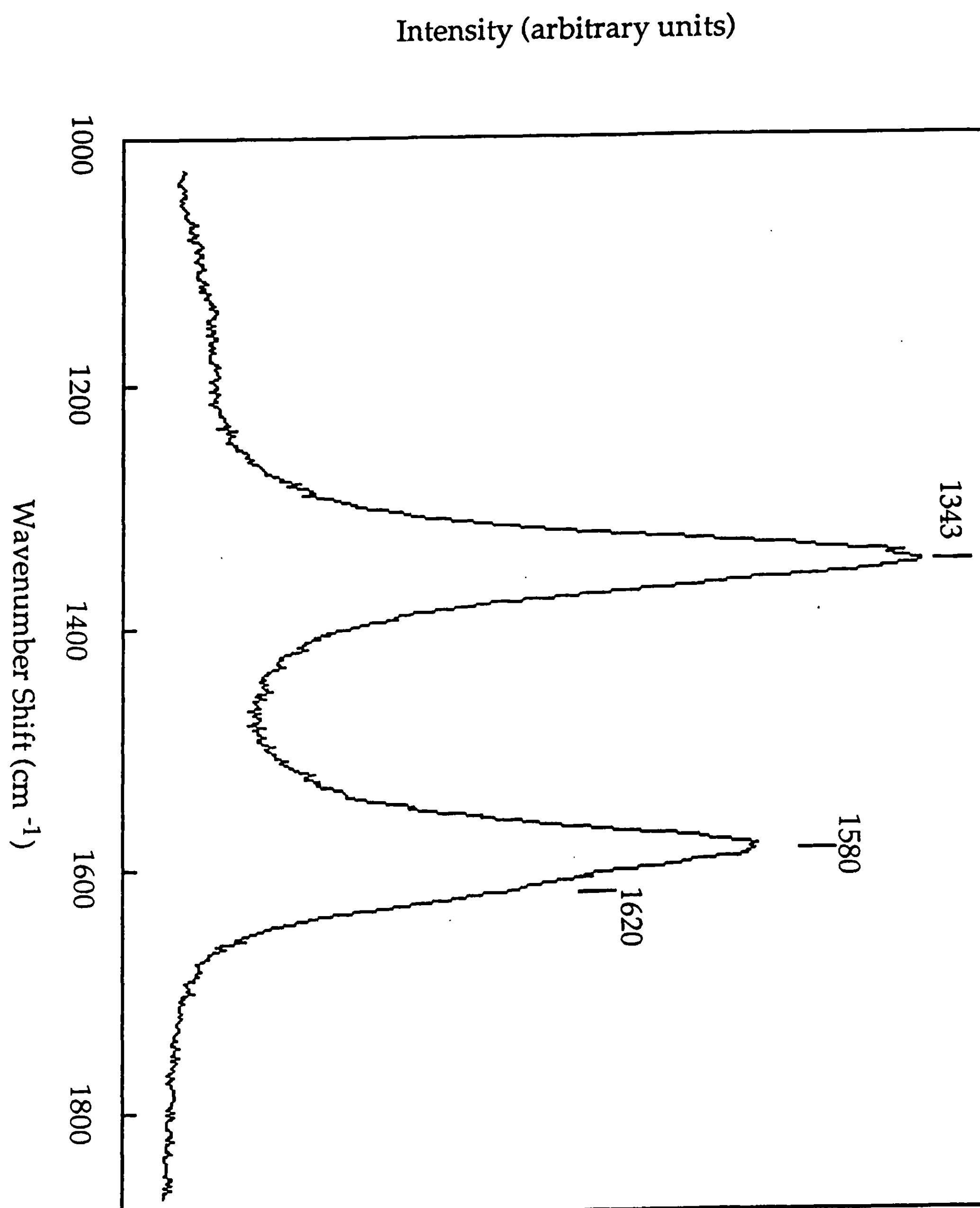

Conditions: Power 330W

Pressure 10^{-2}mbar

Temperature $700^{\circ}C$

Figure 8.3(e) Raman spectrum from glassy carbon B

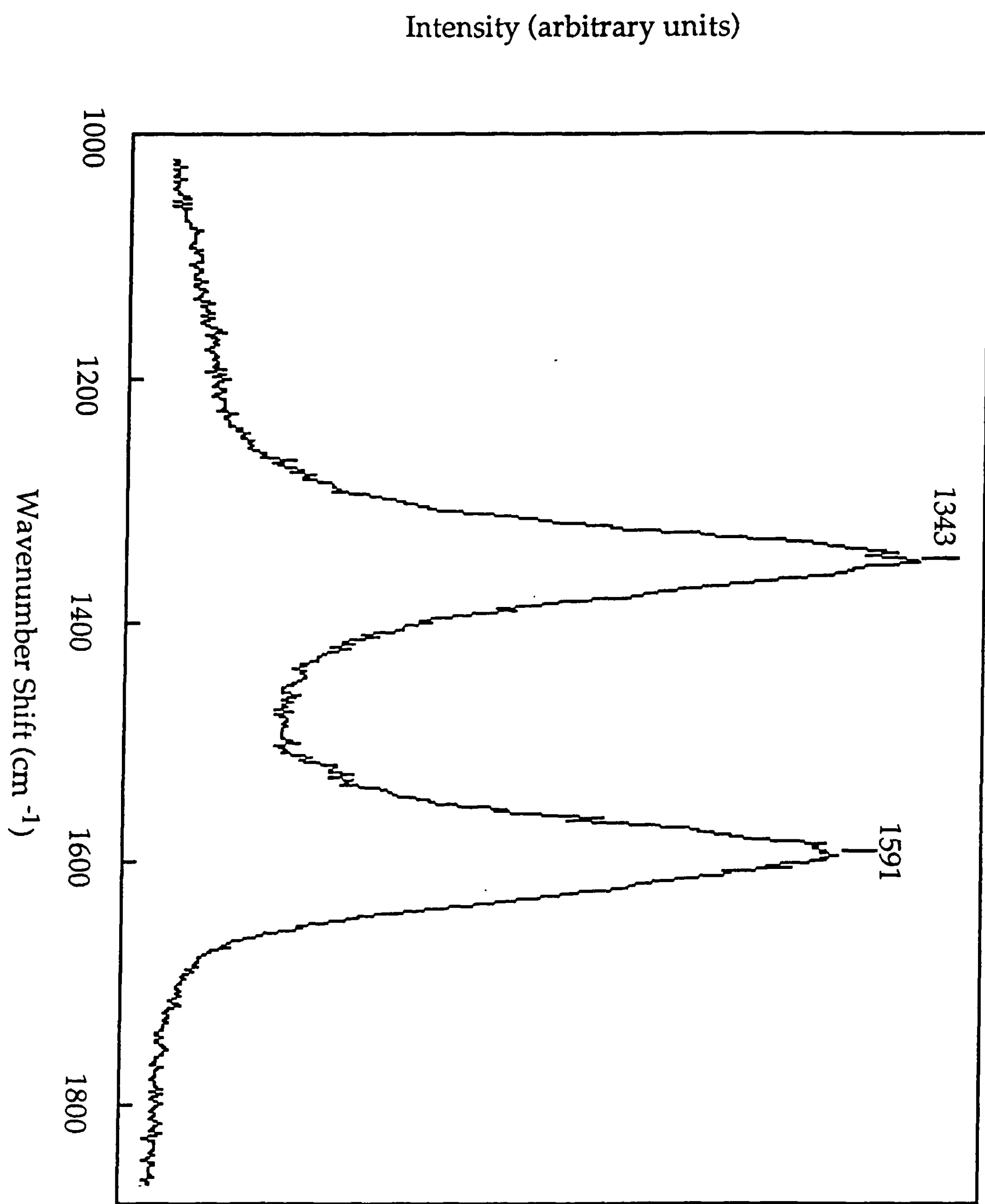

Conditions: Power 330W

Pressure 10^{-2}mbar

Temperature 800°C

Figure 8.3(f) Raman spectrum from glassy carbon A

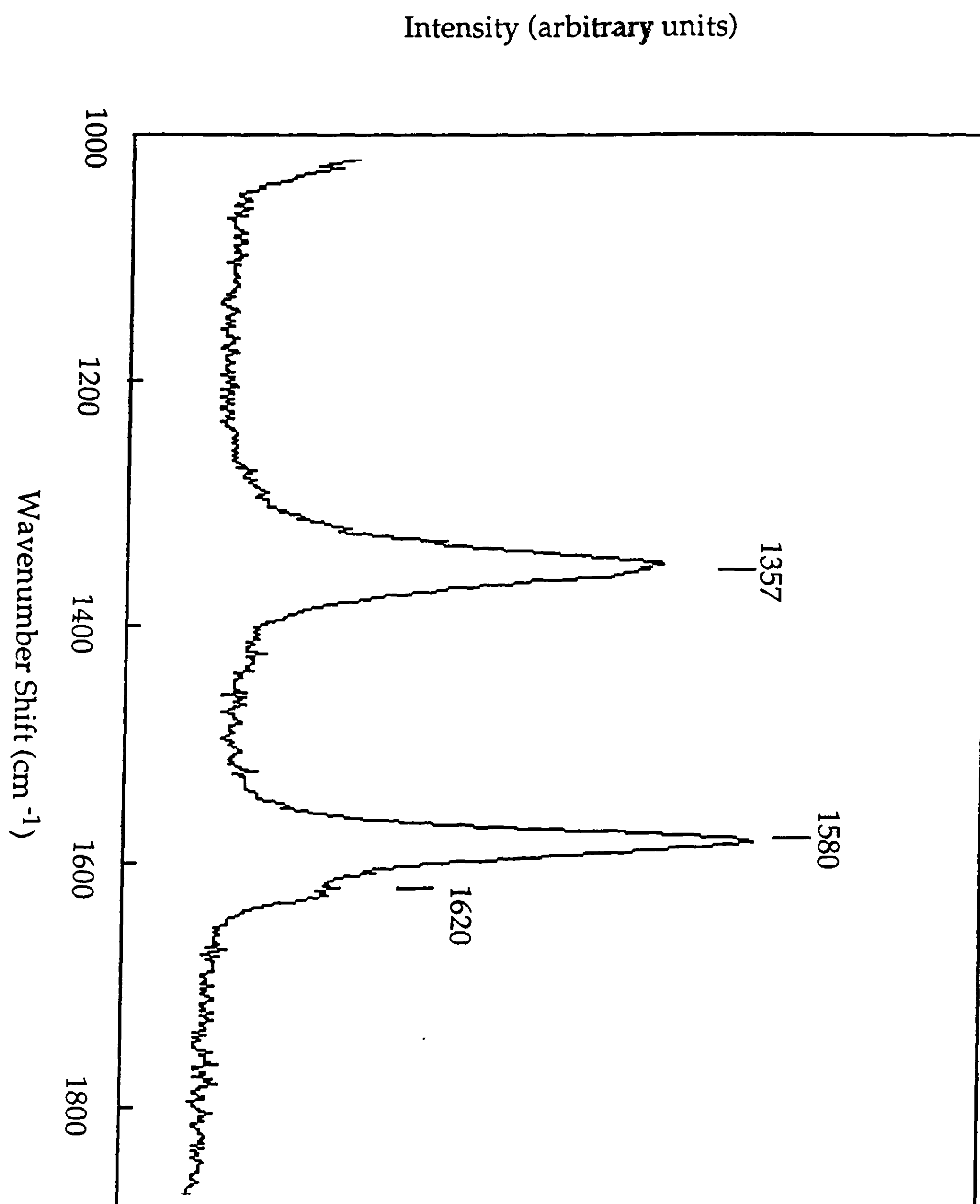

Conditions: Power 400W

Pressure $>10^{-2}$ mbar

Temperature $600^{o}C$

Figure 8.3(g) Raman spectrum from polycrystalline carbon

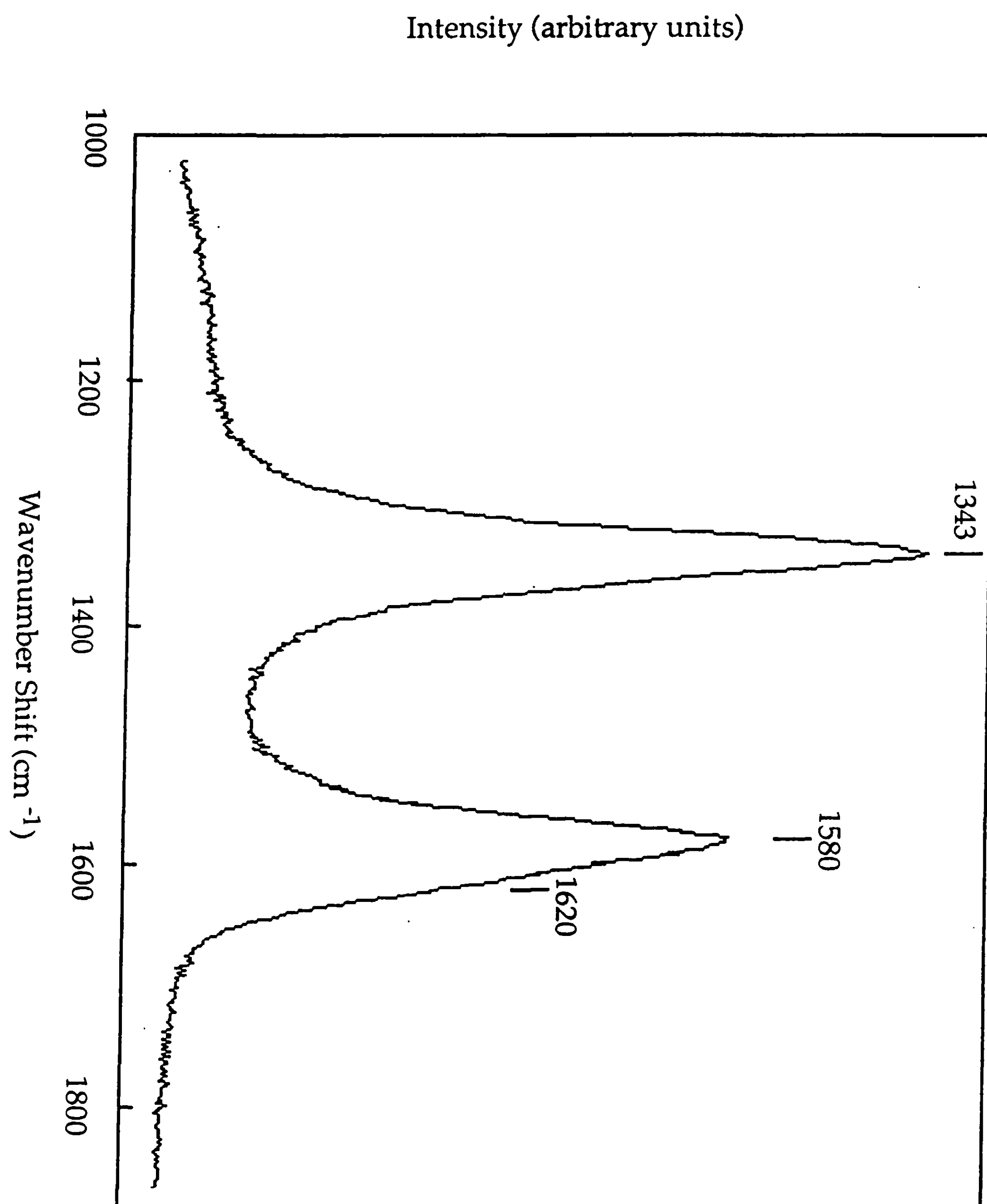

Conditions: Power 400W

Pressure $>10^{-2}$ mbar

Temperature 700°C

Figure 8.3(h) Raman spectrum from glassy carbon B

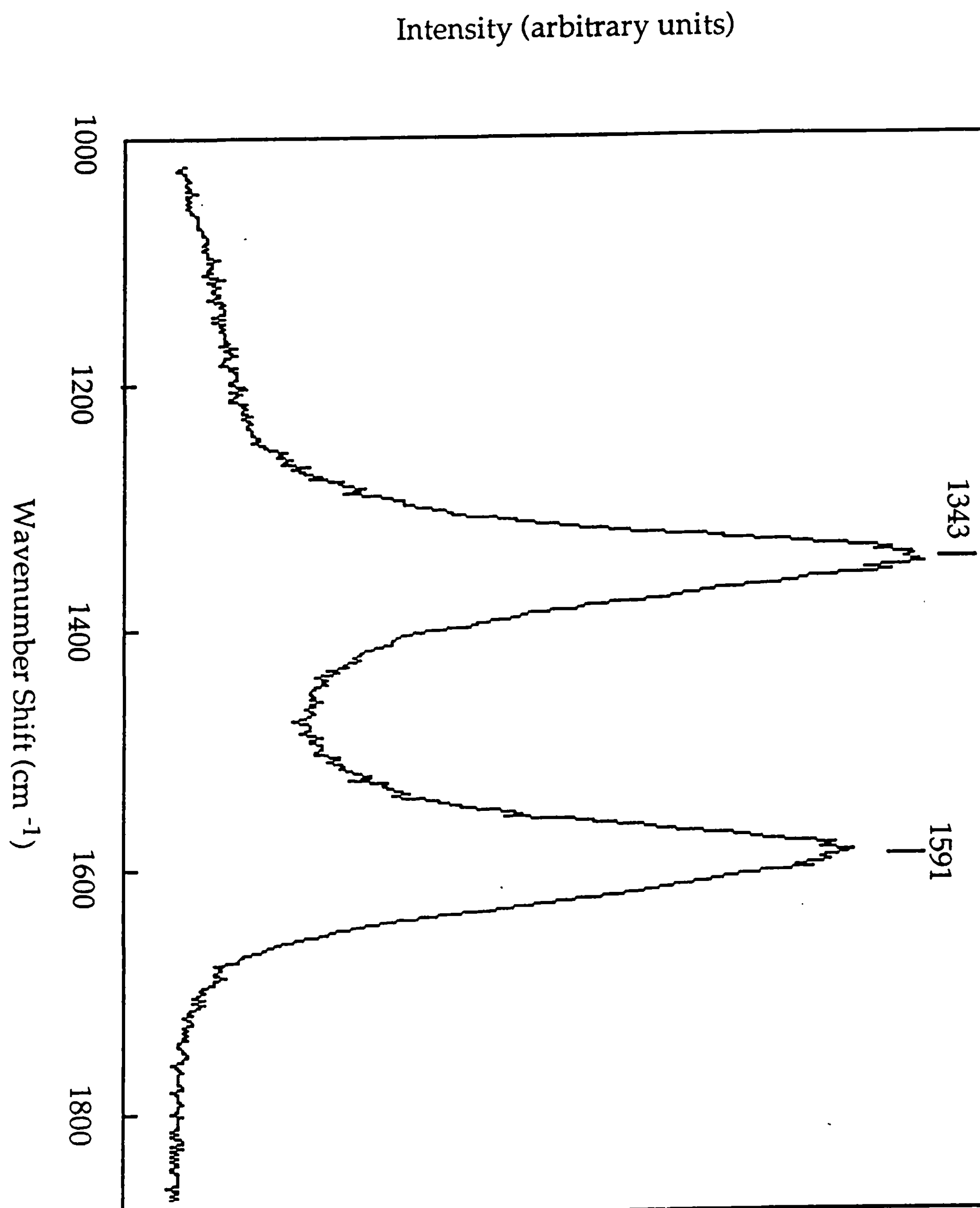

Conditions: Power 400W

Pressure >10^{-2}mbar

Temperature 800°C

Figure 8.3(i) Raman spectrum from glassy carbon A

Close examination of the spectra also shows that there is probably a small polycrystalline component at 700°C, which increases as the temperature decreases. The main difference at different conditions of power and pressure is in the intensity of the lines, and in the intensity of the line from the underlying silicon. This gives a measure of the thickness of the coverage. At higher power the coverage is much less. The most effective combination was high pressure and 330W power.

8.2.3 Atomic Hydrogen Addition

One possible cause of only graphitic deposits was an insufficiency of atomic hydrogen being generated. Several methods of increasing the atomic hydrogen concentration were tried, such as using an extra filament, in addition to the plasma, and hydrogen flow directly over a filament onto the sample from a dosing tube, but without success. All coatings formed were graphitic, a mixture of glassy carbons and graphite crystals.

8.3 Mass Spectroscopic Analysis

Another property of the plasma must have been the cause. An analysis of the output of the modified source was undertaken, using a mass spectrometer.

Since a mass spectrometer can only be operated at 10^{-5}mbar or less, and a hydrogen plasma could only be maintained at $>10^{-3}$mbar, a form of differential pumping was devised.

A metal plate, with a small central orifice (1mm diameter) was made to fit over the exit from the source, in the position originally designed for a grid.

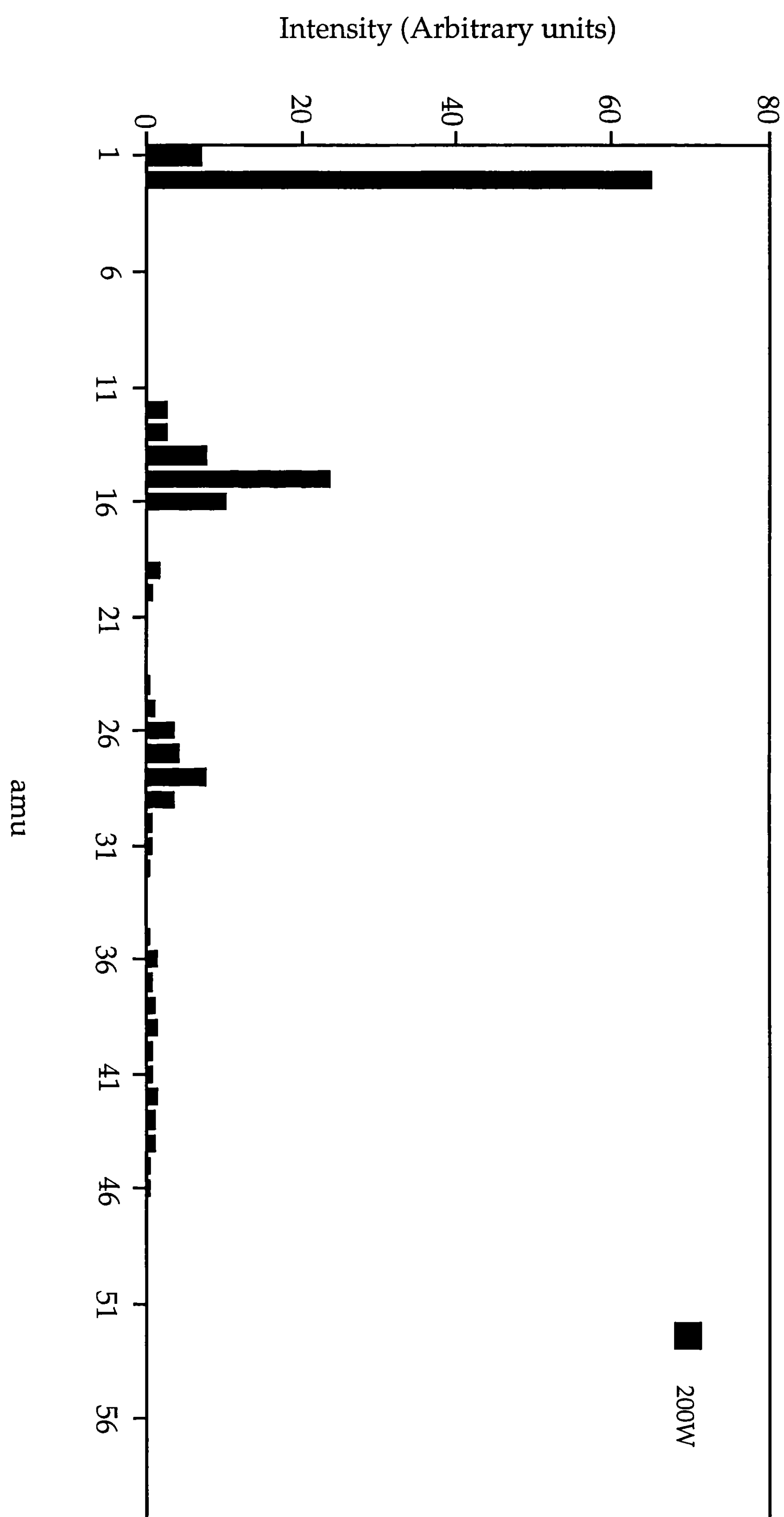

Figure 8.4 Amalgamated Mass Spectrum with Source in Original Configuration

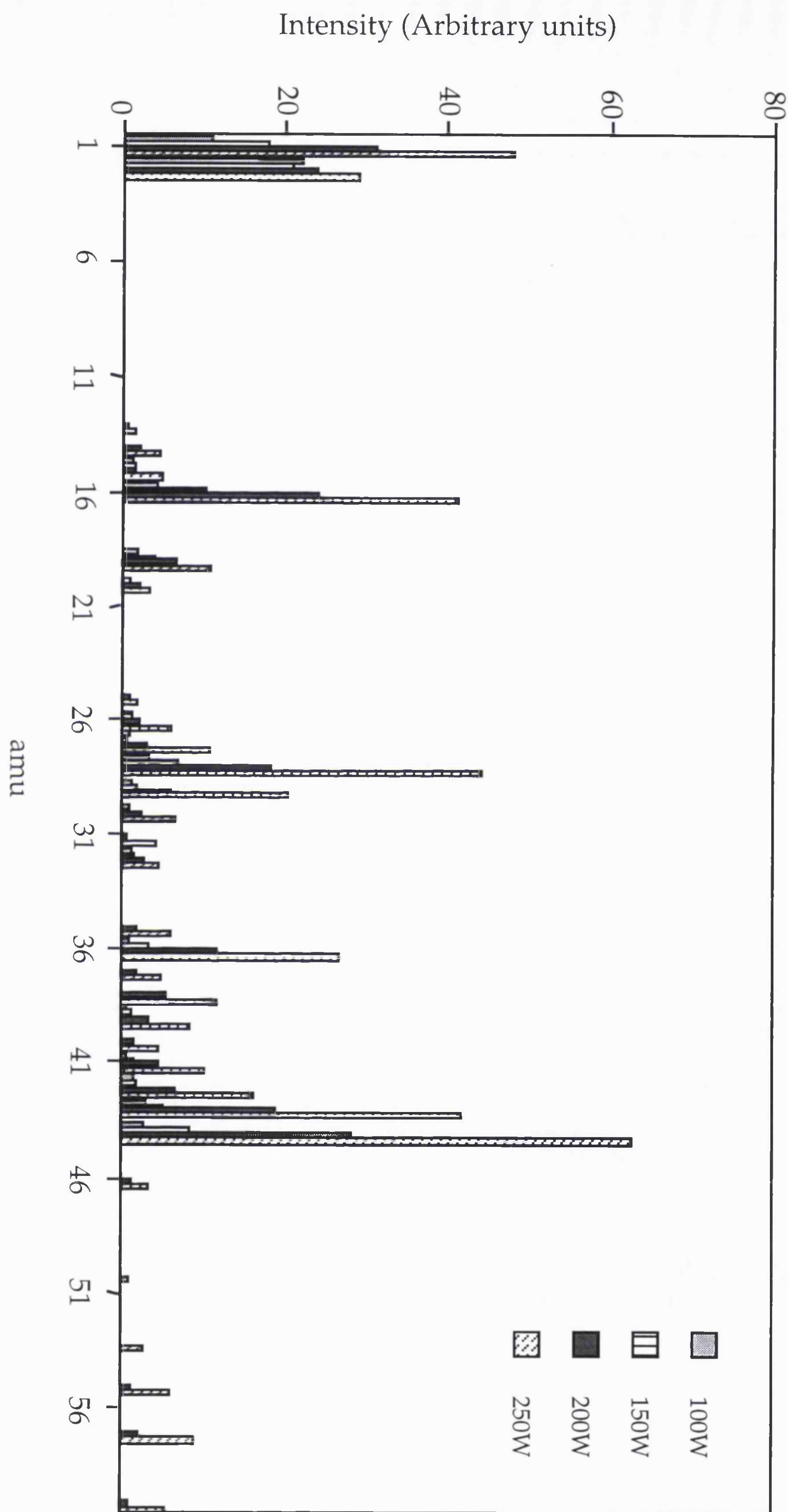

Figure 8.5 Amalgamated Mass Spectra with Source in Magnetically modified configuration

8.3.1 With Source in Original Configuration

Using a Spectramass mass spectrometer, background spectra and spectra with the rf power set to 200W were taken.

Careful analysis of the spectra obtained, shown amalgamated in fig. 7.4, (with the signal from water removed for clarity), yielded a complex mix of hydrocarbons including methane, ethane, propane and propene, the latter two being C_3H_x compounds, not generally considered suitable for diamond growth. There was also relatively little atomic hydrogen. The water was released from the aquadag painted on the liner, as carbon was removed by the action of atomic hydrogen, and produced a signal an order of magnitude stronger than any other. It was surmised that much of the atomic hydrogen generated immediately reacted with the carbon on the liner, producing the large quantities of hydrocarbon found.

8.3.2 With Further Modification of the Source

To reduce the strength of the reaction of atomic hydrogen with the liner, a further modification of the source was carried out. More than half the Sm-Co magnets were removed. The number of rows of magnets was reduced from 12 to 6, and where previously there had been 3 magnets at each position, this was reduced to 2. This modification should also actually increase the plasma density [2.28].

An extended series of mass spectra were now taken with this new magnetic configuration, and with the source repositioned on a side-arm of the six-way cross, facing the mass spectrometer head.

With this configuration, it can be seen from the spectra shown in fig. 8.5, that increasing the input rf power, rapidly increases the output of both atomic hydrogen and hydrocarbons. In particular, the heavier hydrocarbons still predominate at higher powers, where the atomic hydrogen concentration is best, including the appearance of C_4H_x compounds.

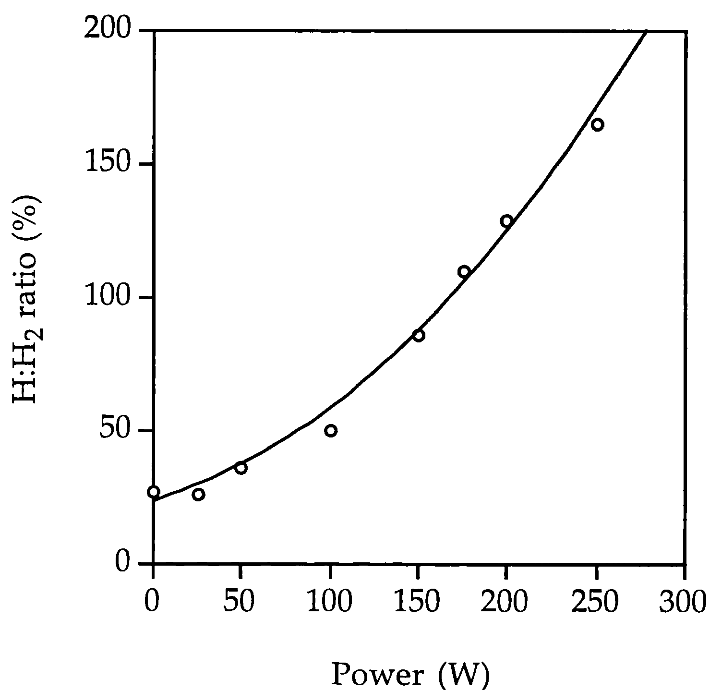

Fig. 8.6 Graph showing the increase in the ratio of atomic hydrogen with rf power

An important feature is the rapid increase in the atomic hydrogen signal compared with molecular hydrogen as the rf power increases, shown in fig. 8.6.

A growth run was attempted with this magnetic configuration, but, not surprisingly, only graphitic forms were again produced.

Summary

In conclusion, the source with hydrogen plasma and a carbon liner, is too efficient at stripping carbon, and makes too rich a hydrocarbon mixture for diamond growth.

CHAPTER 9: DIAMOND DEPOSITION

The idea of using a carbon liner was abandoned, and the liner was thoroughly cleaned, all traces of carbon being removed by baking in air at 800°C.

A gas cylinder of premixed 1% methane in hydrogen was obtained from Gas and Equipment Ltd., and used as the gas supply for the next series of depositions.

9.1 Heating the Sample

9.1.1 Direct Heating

The sample was held only by tantalum clips, through which a heating current could be passed, as in the previous series of depositions. A thermocouple was attached to the centre of the sample.

The sample was then positioned at the aperture of the source.

Plasma conditions were:– pressure 2mbar
rf power 250W

Without any heating current through the sample, the temperature of the sample rose to 185°C, as measured by the thermocouple.

The current supply was then switched on, and nothing happened.
The plasma was switched off, and the sample heated to red-hot. Then the plasma was ignited, and the heating current disappeared. It was surmised that a plasma at this density is too good an electrical conductor, and an indirect method of heating must be devised.

9.1.2 Indirect Heating

A sample holder, to contain a heating filament, was designed and made of pyrophyllite. A coiled filament of 0.5mm diameter tantalum wire was made for the heating filament, and the recess in the holder for the filament coil was lined with tantalum foil to reflect the radiant heat away from the ceramic and onto the sample. This is illustrated in fig. 9.1.

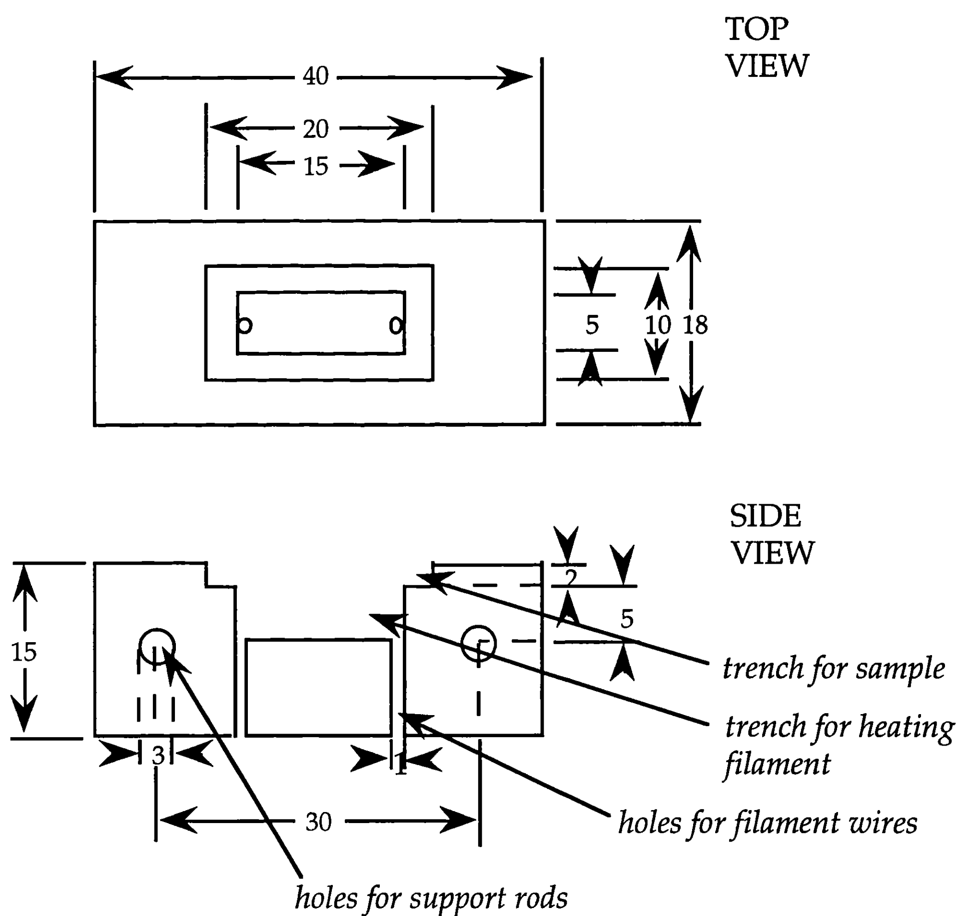

Fig. 9.1 Design for ceramic sample holder/heater

9.1.3 Temperature Measurement

It proved impossible to attach a thermocouple to the sample in this holder, so calibration curves were drawn relating filament power consumption to sample surface temperature, as monitored by a disappearing filament pyrometer, *in vacuo*. Two different types of silicon wafer were used in these depositions, of different thicknesses, one of 0.25mm thickness, the other of 0.5mm thickness.

N. B With the plasma ignited, it would not have been possible to see the glow of the hot sample. Flowing gas cools the sample, but the plasma itself heats the sample, as demonstrated in Section 9.1.1. These two effects nearly cancel each other, so monitoring in vacuo *is accurate to within ~20°C.*

The calibration curves are shown as figures 9.2 (a) for the thinner silicon, and 9.2 (b) for the thicker silicon.

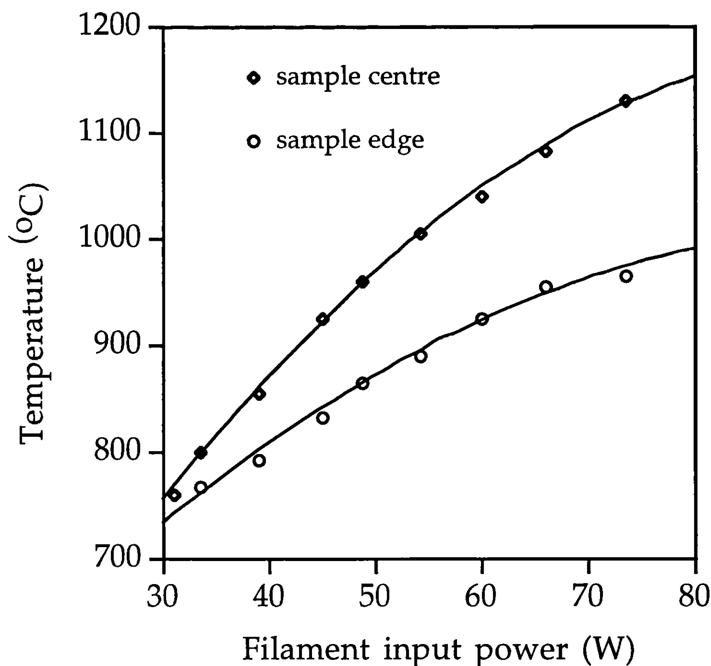

Fig. 9.2 (a) Temperature calibration curve for 0.25mm thick silicon wafer

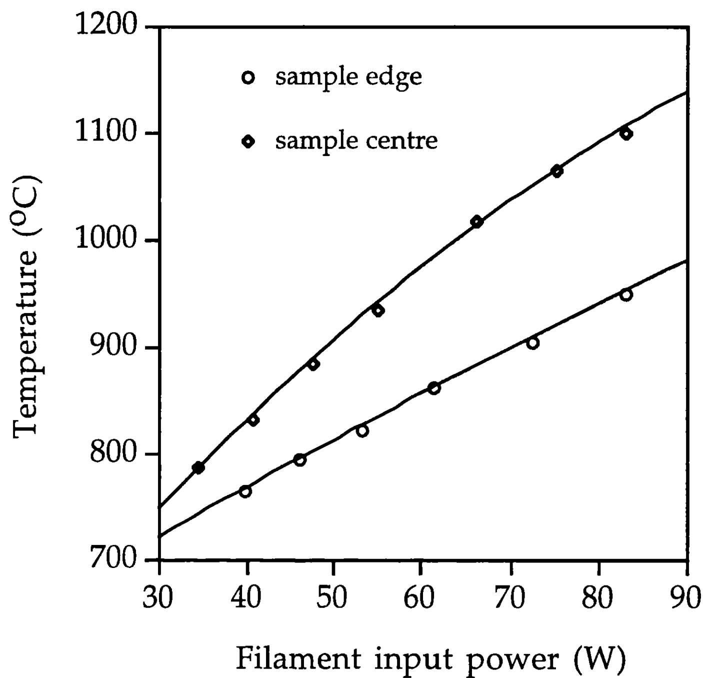

Fig. 9.2 (b) Temperature calibration curve for 0.5mm thick silicon wafer

9.2 Diamond Depositions: Substrate Preparation Method 1

9.2.1 Sample Preparation

This series of depositions was characterised by the method of sample preparation. All samples were scratched vigorously with diamond powder, (<1μm), mixed to paste with de-ionised water, between two pieces of silicon, and then sonicated for 30 minutes in acetone to remove all traces of diamond from the surface, leaving a surface which was very craggy under high magnification, but which did not show any residual diamond particles. This is shown in figure 9.3.

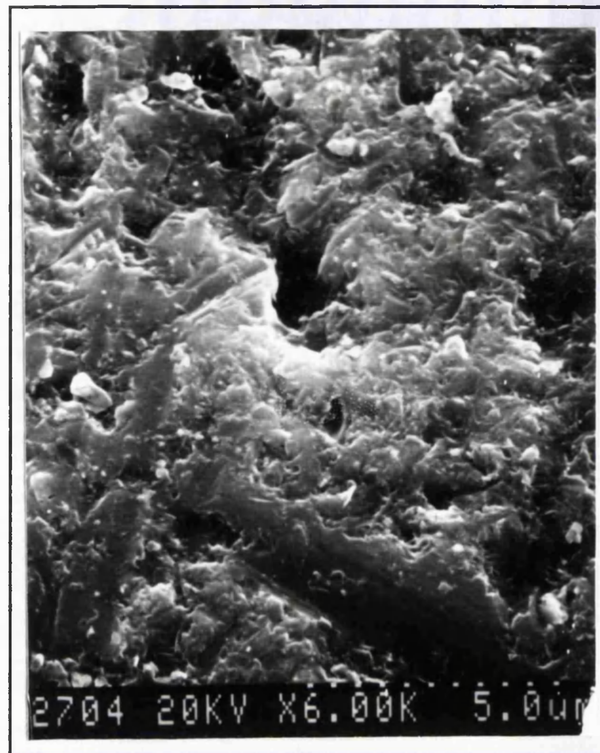

Fig. 9.3 SEM photograph of control sample of scratched silicon.

9.2.2 Experimental Procedures

Deposition run conditions were as follows:–

	RF power (W)	Pressure (mbar)	Filament power (W)	Temp. ^{o}C (centre)	Temp. ^{o}C (edge)	Time (hours)
(i)	200	15	54	1000	895	5
(ii)	200	15	57.5	1025	915	5
(iii)	200	15	73	1125	970	5
(iv)	200	15	63.5	1065	940	9
(v)	250	8	51	975	875	17

9.2.3 Scanning Electron Microscopy

All samples were examined under the Scanning Electron Microscope.

Samples (i) and (ii) seemed to have grown only glassy carbon, as the appearance was similar to that of the samples described in Chapter 8.

Sample (iii) had many small crystals near the edge, but not near the centre, where the temperature was higher.

Sample (iv) with a lower temperature and a longer time, showed many small crystals, but without the characteristic diamond faceting.

9.2.4 Raman Spectroscopic Analysis

Sample (iv) was subjected to Raman spectral analysis. The spectra obtained are shown in figures 9.4 (a) and (b). Figure 9.4 (a) is from the centre of the sample, showing only graphitic signals, but figure 9.4 (b), from the edge of the sample, where it is cooler, shows a complex signal implying some pre-diamond nucleation. The 1345cm^{-1} and the 1590cm^{-1} lines are the D and G lines of graphite, but 1300cm^{-1} is close to the 1330cm^{-1} of diamond whilst the band from 1400cm^{-1} to 1430cm^{-1} is most probably due to polyacetylene, more clearly shown in the spectra from sample (v), figures 9.5 (a) and (b).

In the light of this analysis, conditions were changed slightly for the next deposition, sample (v), as can be seen from the table above. A lower pressure and a higher rf input power was used, to improve the $H:H_2$ ratio, thus encouraging the diamond growth over the graphite, and the temperature was reduced further, to be similar to that at the edge of sample (iv). The time was increased by a factor of ~2.

This sample was then also subjected to Raman spectral analysis. The spectra are shown in figures 9.5 (a) and (b). Figure 9.5 (a) is from the centre of the sample, where the coverage was of many very small crystals. There is little evidence of graphite, but a strong diamond signal, at 1330cm^{-1}, broadened due to the small size of the crystals. Figure 9.5 (b) is from the edge of the sample, where the coverage was sparser. The 1570cm^{-1} line indicates large graphite crystals, while the 1330cm^{-1} diamond line is much narrower, also indicating

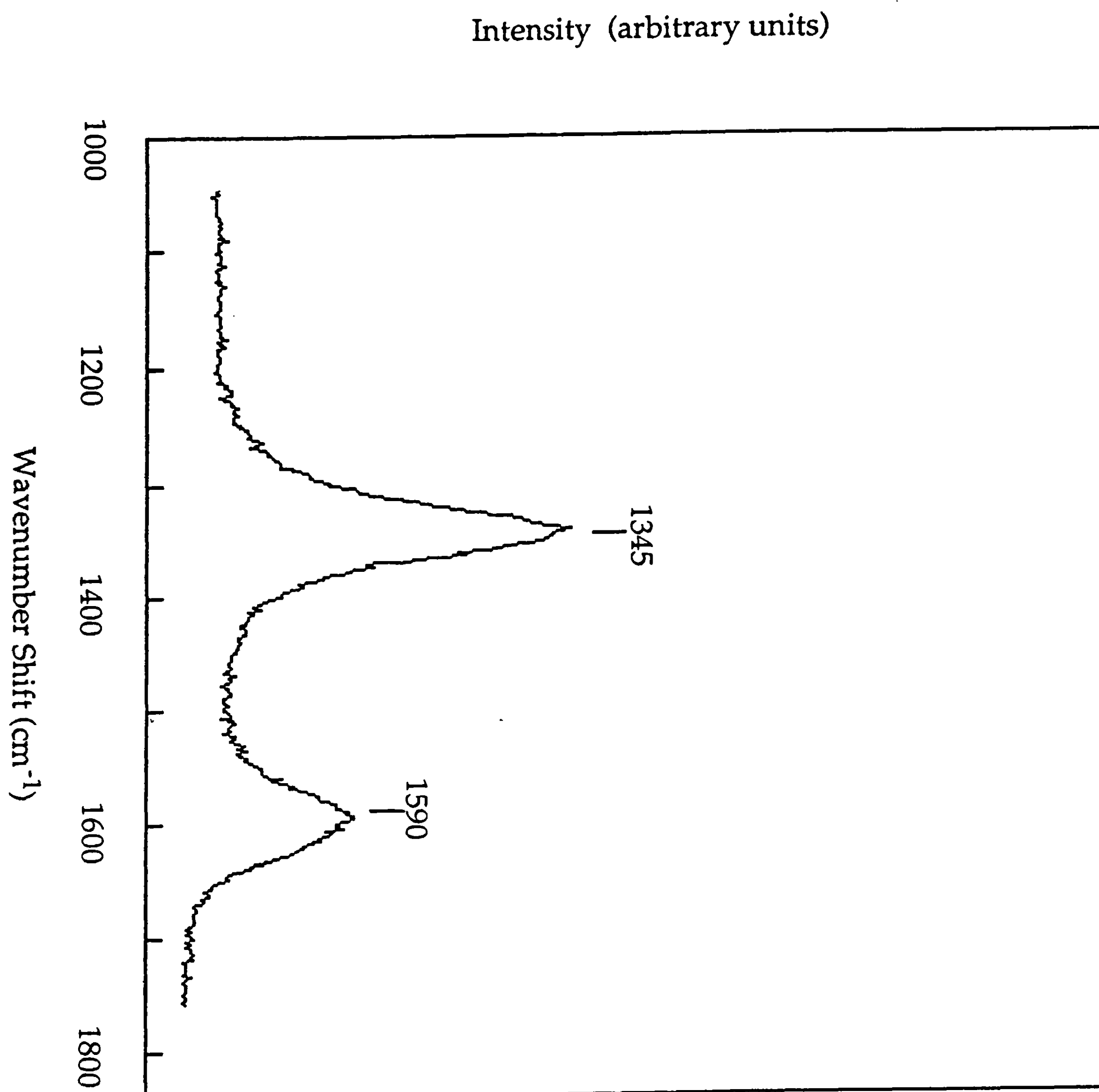

Fig. 9.4 (a) Raman spectrum from centre of sample (iv)

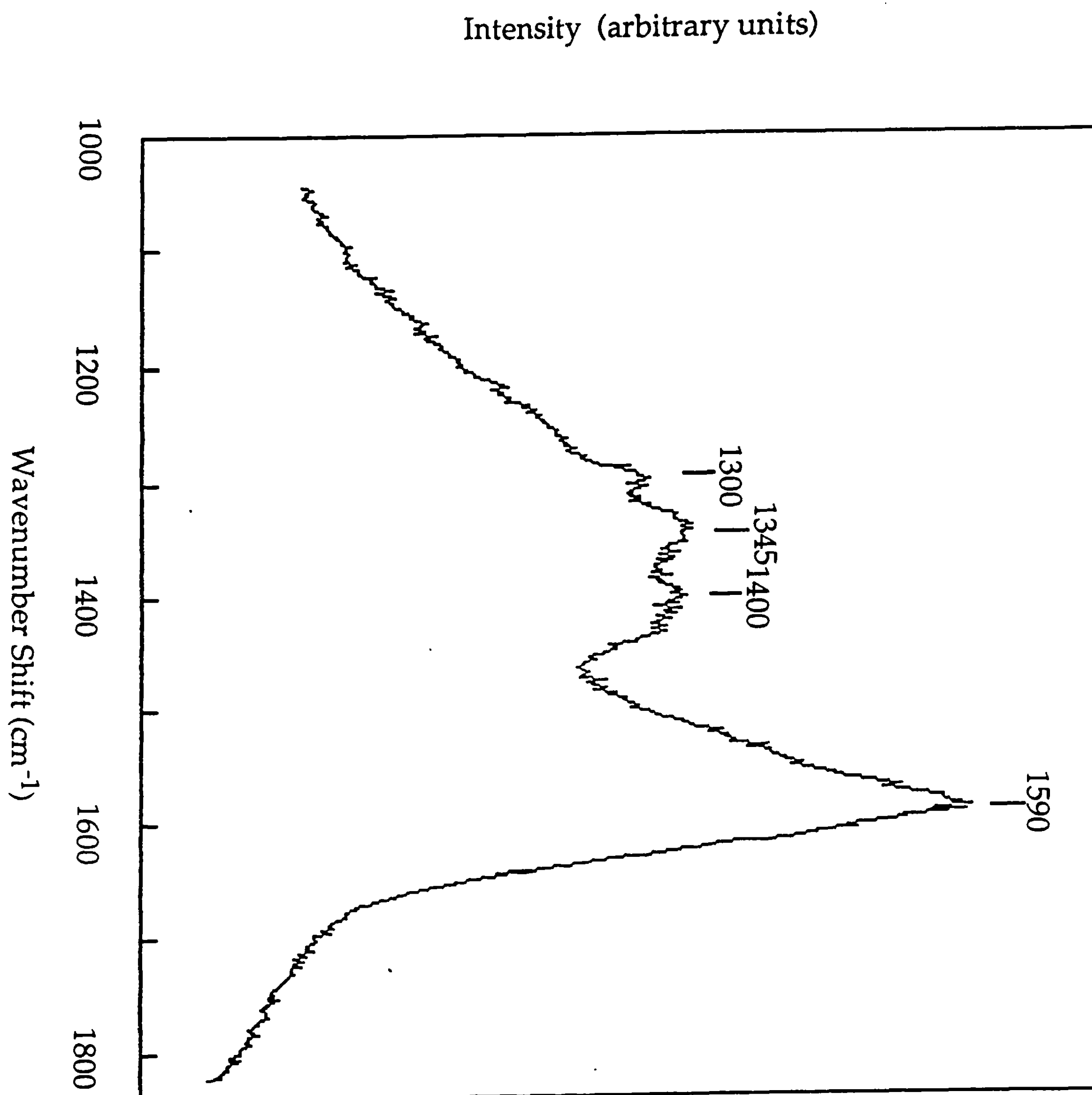

Fig. 9.4 (b) Raman spectrum from edge of sample (iv)

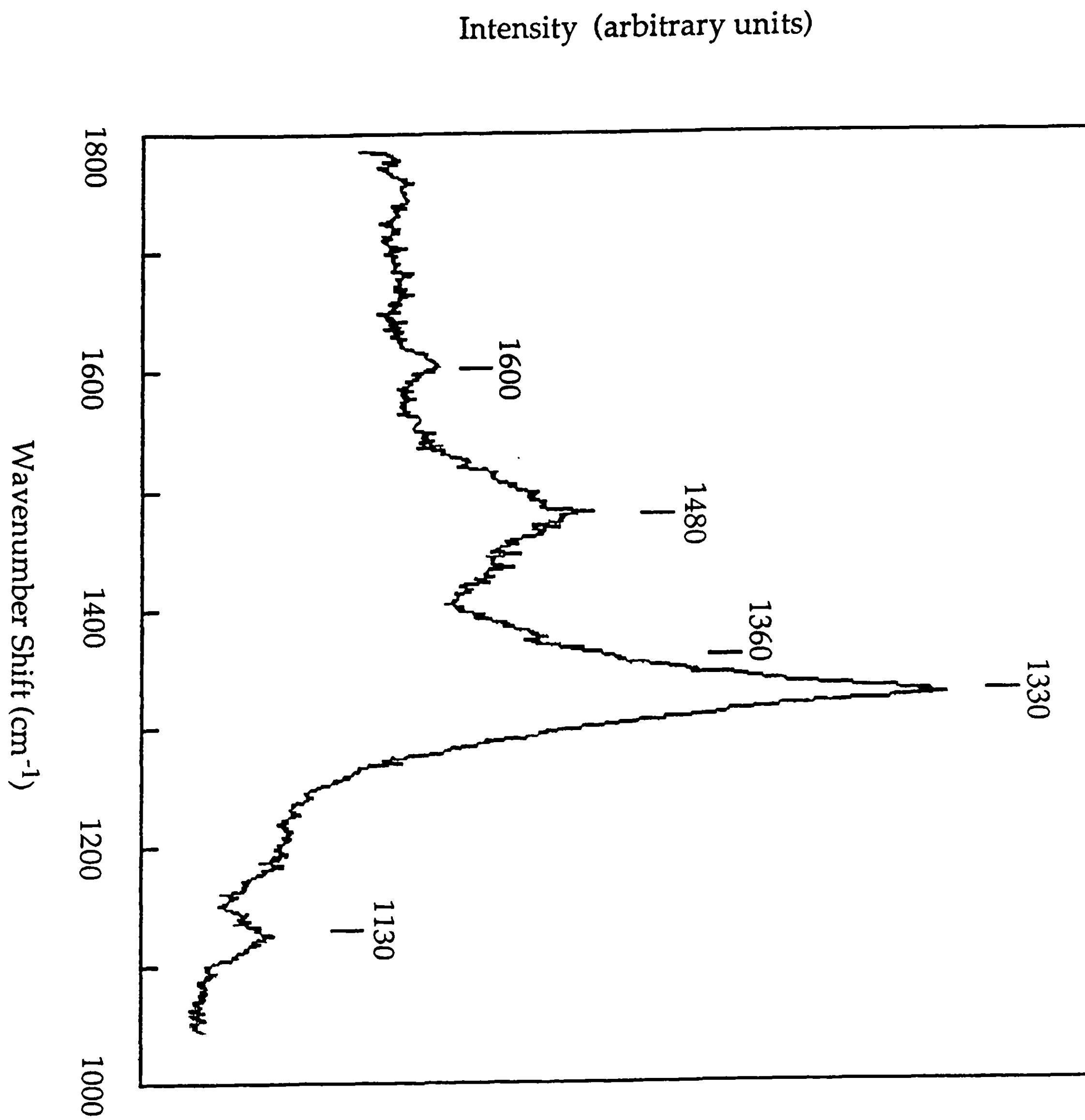

Fig. 9.5 (a) Raman spectrum from centre of sample (v)

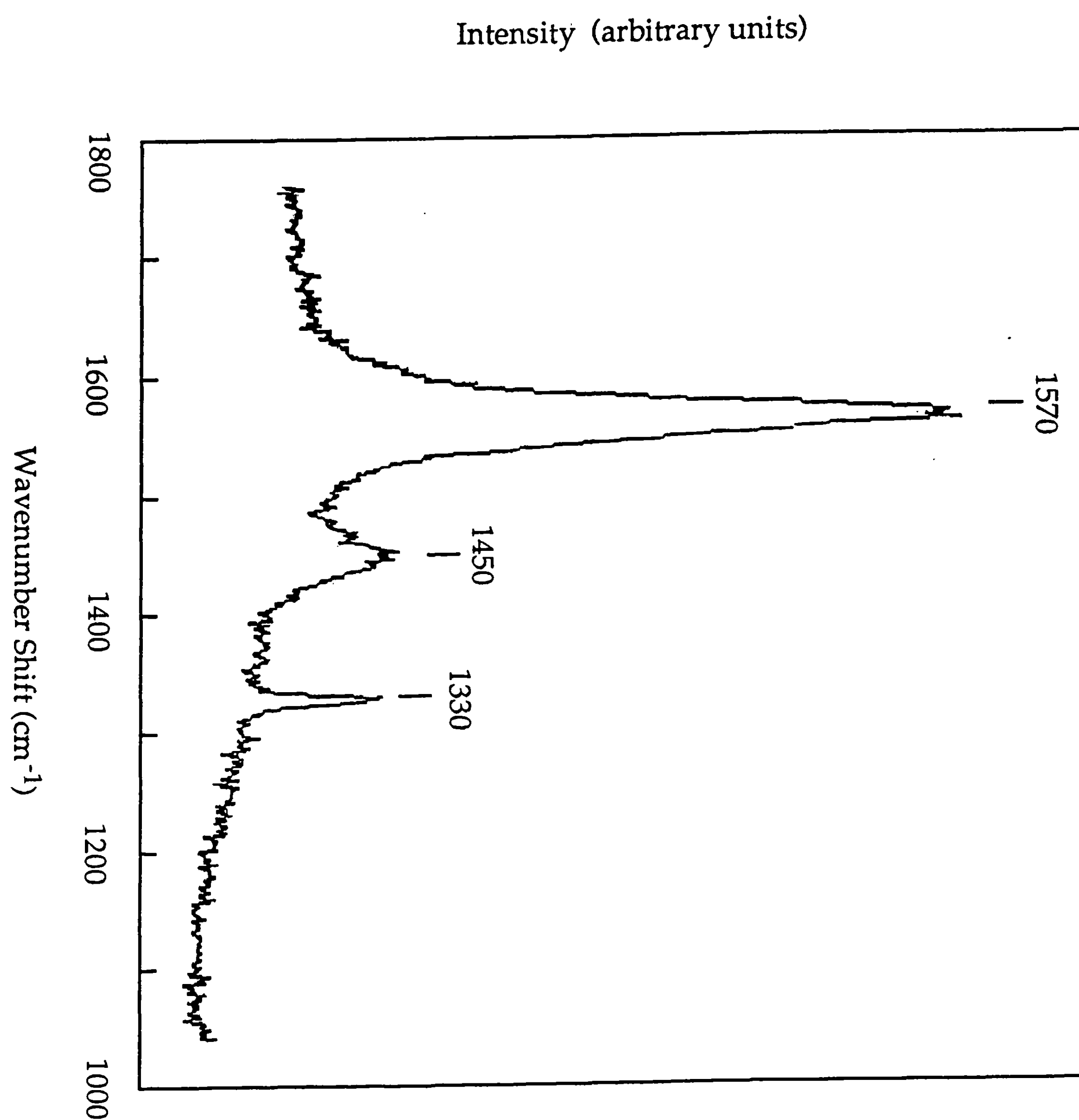

Fig. 9.5 (b) Raman spectrum of edge of sample (v)

larger crystals. The 1450cm^{-1} line has been attributed to polyacetylene [9.1], a possible pre-nucleation stage for diamond growth.

When looked at under the SEM, this sample showed a considerable coverage of tiny crystallites, together with a few larger ones, as can be seen in figure 9.6.

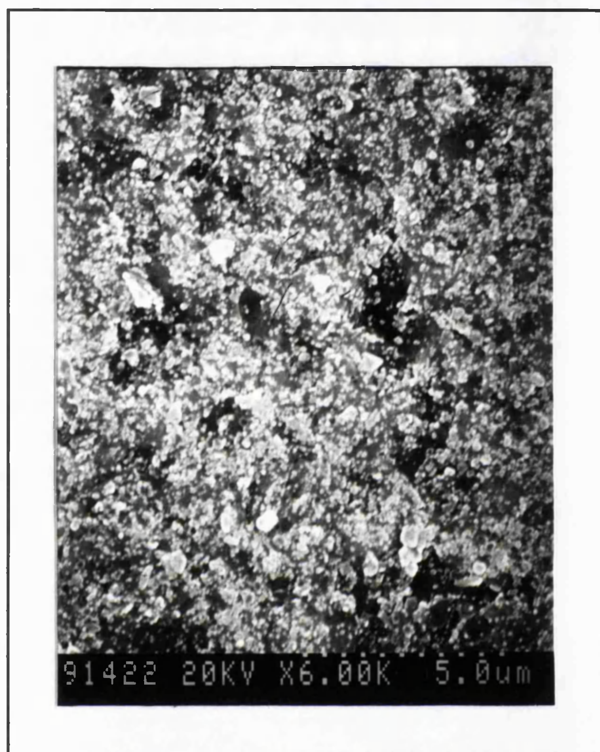

Fig. 9.6 SEM photograph of sample (v), grown with rf power 250W for 17 hours

9.2.5 Summary of Results

This is the first time that diamond crystallites of such quality have been grown so profusely with a capacitively coupled RF plasma source[9.2]. Clearly, the conditions in the plasma from this novel source are indeed sufficiently close to those of a microwave plasma, as the characterisation detailed in Chapter 4 suggested.

9.3 Diamond Depositions: Substrate Preparation Method 2

9.3.1 Sample Preparation

This series of experiments was characterised by an alternative method of sample surface preparation. Although diamond crystallites had been grown by the end of the previous series of experiments, the extremely rough surface meant that a good diamond film could not be grown. Following advice from a more experienced grower of CVD diamond film (by MWPECVD), the samples were polished gently with a cotton bud dipped in diamond powder. Then the sample was sonicated as before. The sample surface remained smooth and shiny to the eye, although was clearly roughened on a microscopic scale. This is illustrated in figure 9.7.

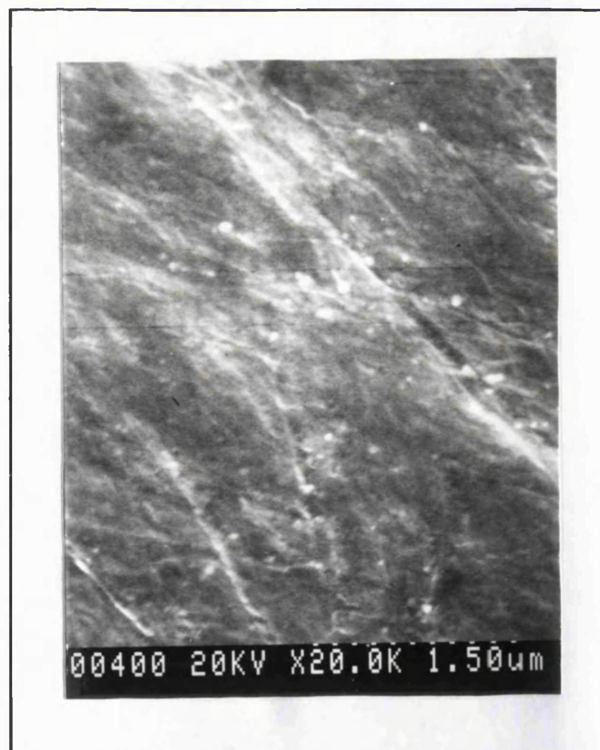

Figure 9.7 SEM photgraph of control sample of diamond polished silicon (111)

9.3.2 Experimental Procedures

A range of temperatures and rf power inputs were used, but the pressure was maintained at 8 mbar throughout, since employment of this pressure had led to success in previous experimental runs.

Deposition run conditions were as follows:–

	RF Power (W)	Temp. °C	Time (hours)
(i)	250	835	30
(ii)	250	880	16
(iii)	250	925	30
(iv)	250	980	16
(v)	300	780	18
(vi)	300	860	18
(vii)	300	880	17
(viii)	300	935	16
(ix)	300	1000	17
(x)	300	1080	16
(xi)	400	800	20
(xii)	400	880	20

All of these above growth conditions grew crystallites, at densities which depended on both temperature and rf input power.

9.3.3 Growth at 250W RF Input Power

These samples were as near as possible a repeat of the conditions of the most successful run of the previous series, to investigate first the improvement that the new surface treatment produced.

9.3.3.1 Scanning Electron Microscopy

The SEM photographs of figure 9.8 (a) - (d) show varying stages of film growth as the temperature is increased. At the lowest temperature, 835°C, there is considerable coverage of individual crystallites, which, although extremely small, have sharp octohedral tendencies. As the temperature increases, these become fewer in number. At the same time, there can be seen an underlying filmic cover, which becomes denser as the temperature increases.

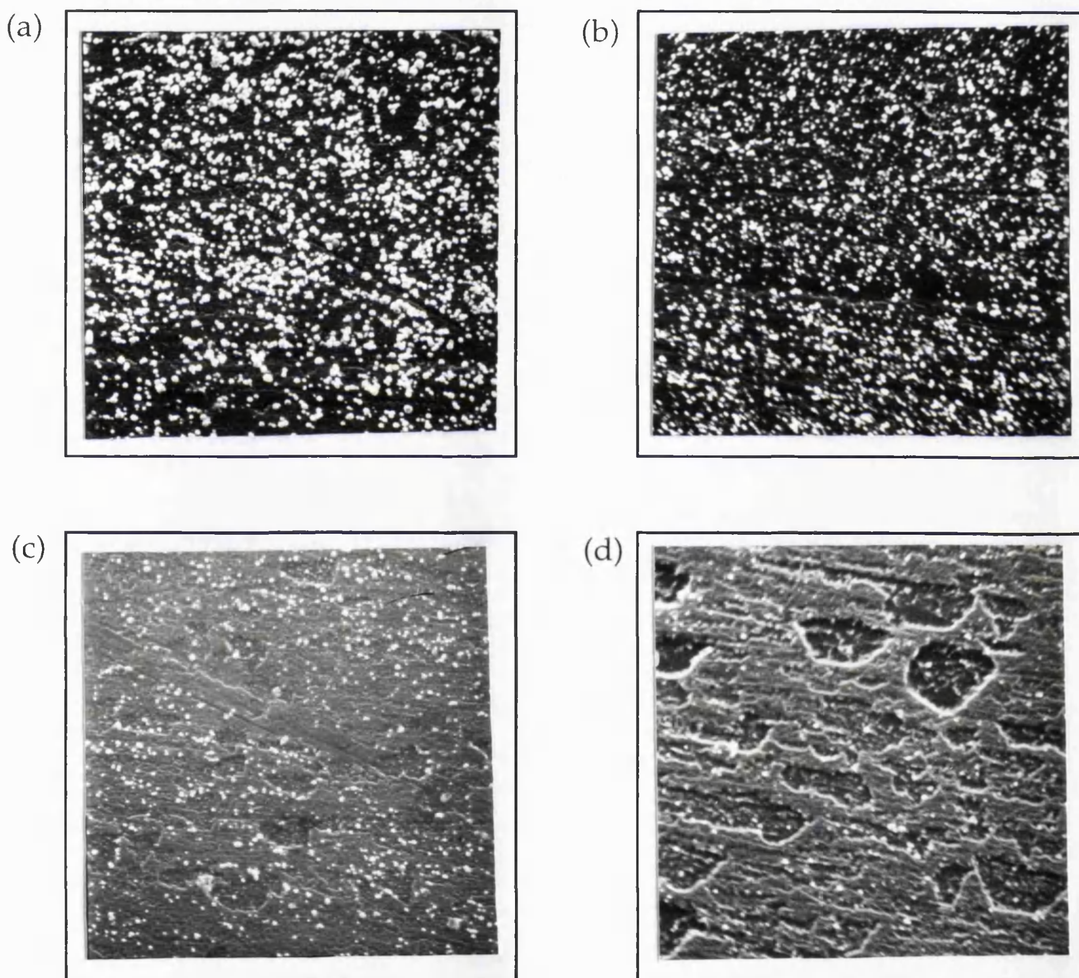

Figure 9.8 SEM photographs (all at 10K magnification) of film growth at 250W RF Power.
(a) 835°C, (b) 880°C, (c) 925°C, (d) 980°C

9.3.3.2 Raman Spectroscopy

Figure 9.9 (a) - (d) shows the Raman spectra corresponding to these film growths. It will be noticed that on most of these spectra numerous lines appear at slightly varying frequencies. These are attributed to C–H bonds, mostly in the form of *trans*-polyacetylene, (*trans* - $(CH)_x$). The exact frequencies at which these lines appear depend on both the wavelength of the exciting light and on the length of the polymer chain [9.1], but when using red light, as here, the frequencies most likely to be found will be 1120 cm^{-1}, 1160 cm^{-1}, 1185 cm^{-1}, 1200 cm^{-1}, 1250-1280 cm^{-1}, 1460cm^{-1}, 1550 cm^{-1} and 1575 cm^{-1} [9.1].

Thus, although the SEM photograph of the sample grown at 835°C shows many crystallites, any diamond signal they may be producing is swamped by the background of polyacetylene and amorphous carbon. The Raman signal from diamond is very weak compared with other forms of carbon, as the scattering efficiency is only ~1/50 that of graphite [7.33].

In figure 9.9 (b), at a temperature of 880°C, the diamond line at 1332 cm^{-1} can just be discerned as a shoulder on a strong peak at 1360 cm^{-1}, due to very fine graphite crystals. Nemanich and Solin [7.34] have shown that the D line of graphite, (as defined in Chapter 7, section 7.3), which does not appear in large crystals, appears in poly-crystalline graphite, and the D/G intensity ratio increases as the crystal size diminishes. This spectrum also has lines at frequencies corresponding to the G line. The other lines correspond to polyactylene, as in the previous spectrum. As the temperature is again increased to 925°C, the contribution centred on 1332 cm^{-1}, a small broad band, is now much clearer, as the graphitic contribution has all but disappeared, while some of the polyacetylene lines have shifted. This spectrum is surprising since the number of visible crystallites is actually fewer than at lower temperatures. At the highest temperature utilised with this RF power, 980°C, there are very few crystallites indeed, and they are extremely small. The underlying film growth is smooth, but not quite complete, there are some gaps. The Raman spectrum however, shows small peaks at 1440 cm^{-1} and 1600 cm^{-1}, which are polyacetylene still, with a very strong signal centred on 1334 cm^{-1}. There are no polyacetylene lines at this frequency, and although the D line of graphite, nominally at 1357cm^{-1} can suffer either blue or red shifts, depending on whether the material is being stressed or compressed, these shifts are of only a few wavenumbers.

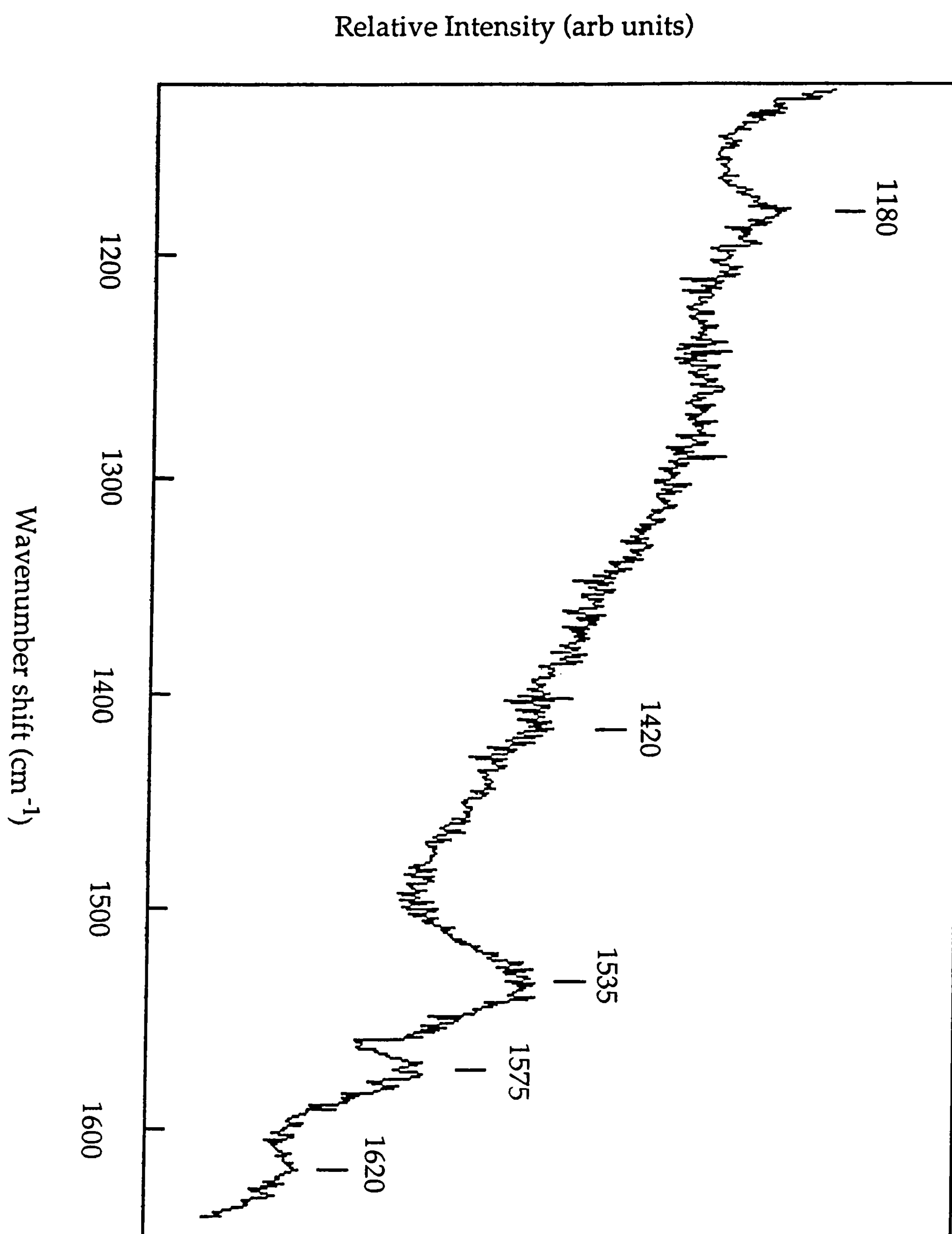

Figure 9.9 (a) Raman spectrum from sample grown at 835°C, 250 W

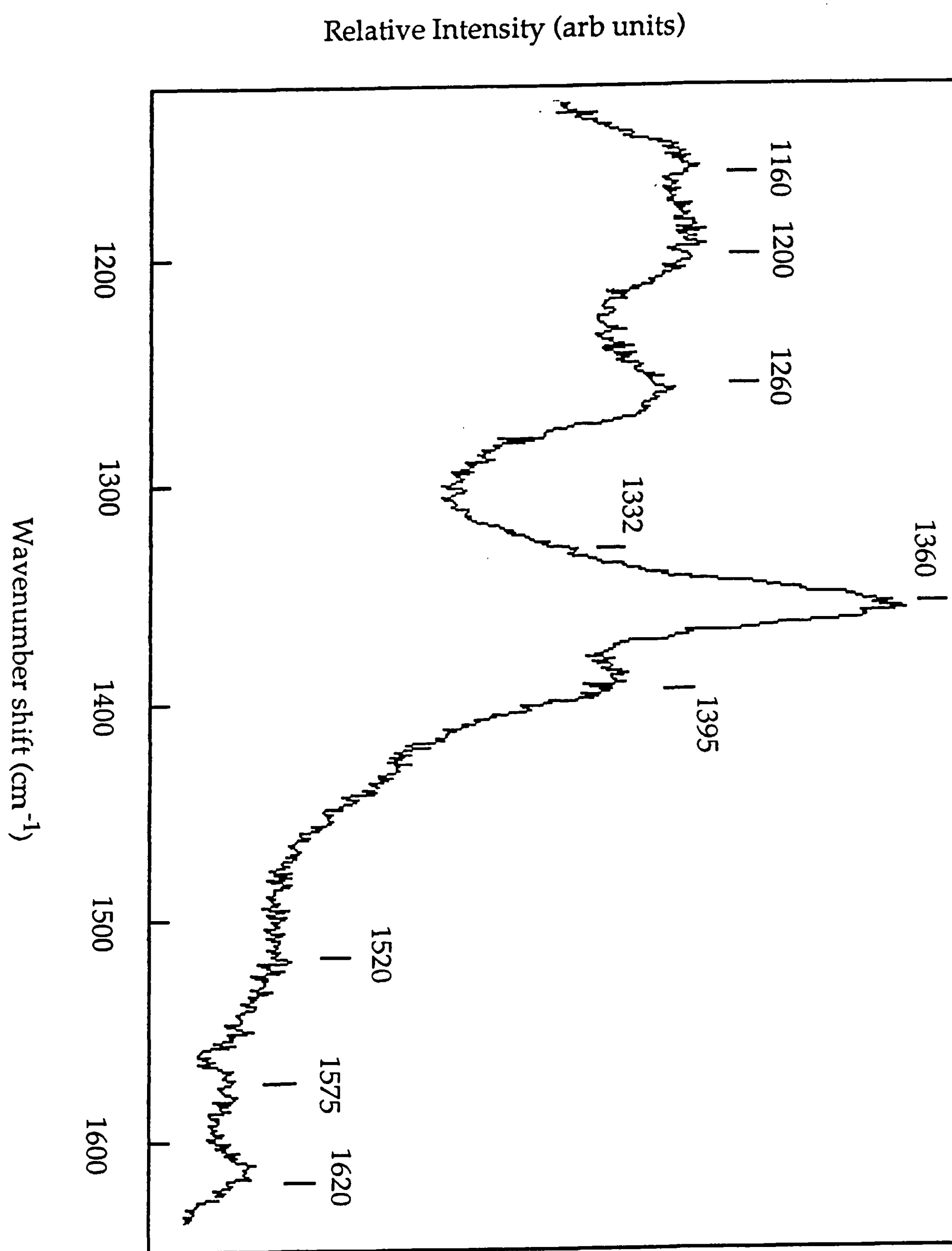

Figure 9.9 (b) Raman spectrum from crystallites grown 880°C, 250W

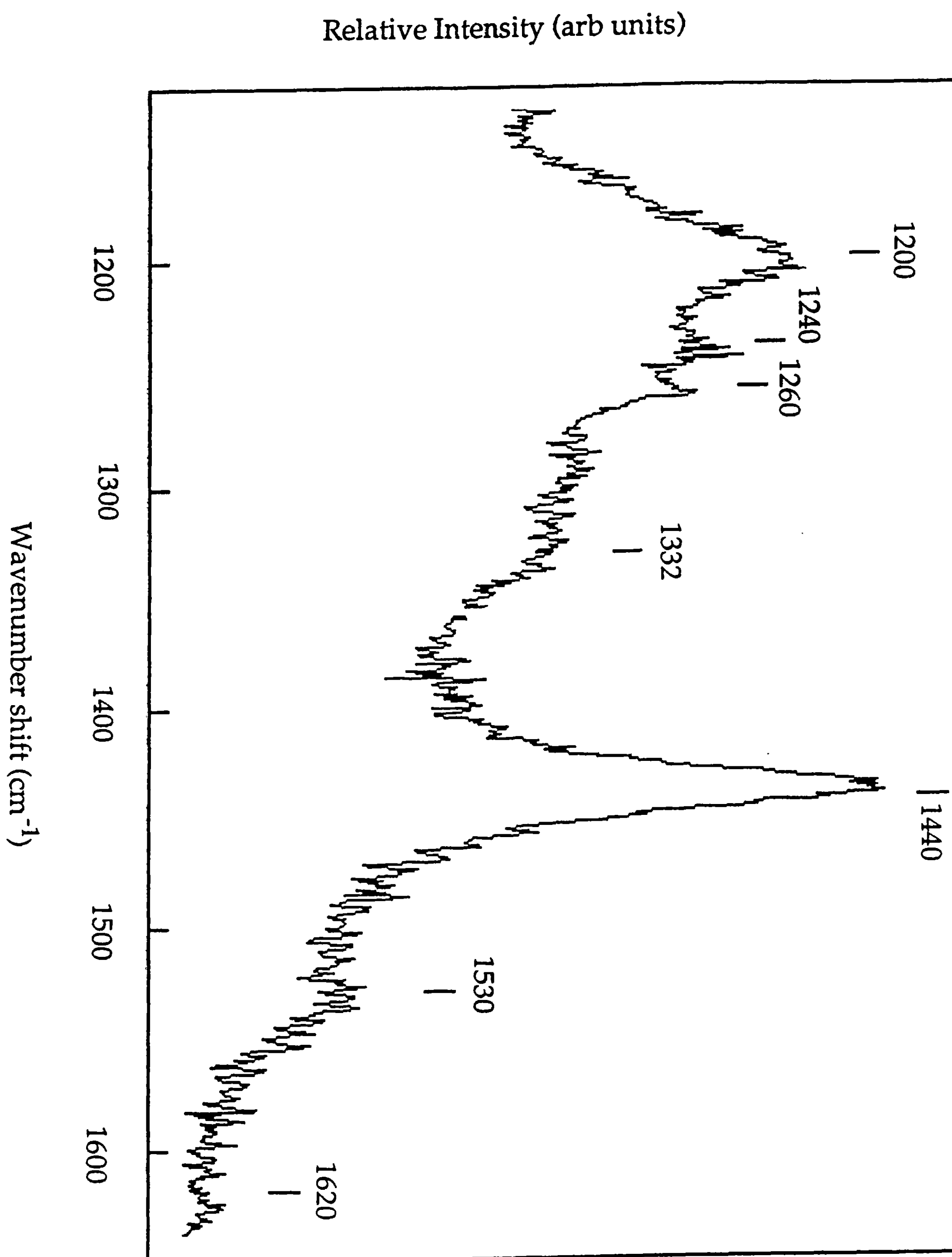

Figure 9.9 (c) Raman specrtum from sample grown at 925°C, 250W

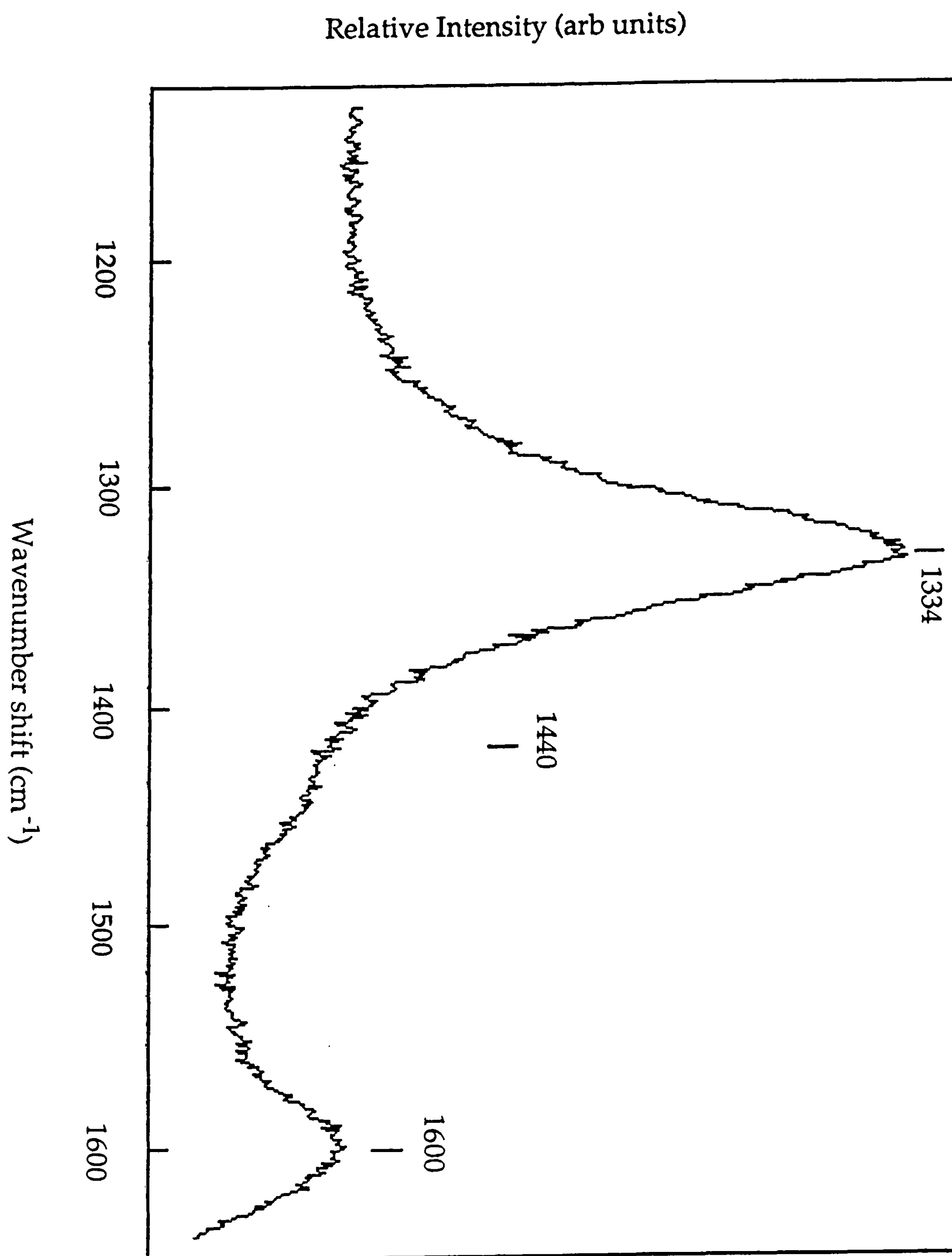

Figure 9.9 (d) Raman spectrum from sample grown at 980°C, 250W

By considering the vibrations which are active vibrations in Raman spectroscopy as simple harmonic oscillators, Fitzer and Rozploch [9.7] have shown that there is a simple proportional relationship between the Raman frequency and the bond length between carbon atoms:

$$\frac{v_G}{v_D} = \frac{b_D^2}{b_G^2}$$

where v_i is the Raman wavenumber, and b_i is the bond length.

This means it is possible, if one bond length is known, for example from x-ray diffraction, then other bond lengths may be calculated from the wavenumber of the Raman line. Therefore, since the wavenumber of the line seen here is the same as that for diamond, the bond length must also be that of diamond. The same authors also clearly demonstrated that it is not possible to find this bond structure in graphite.

Thus it would appear that the only possible interpretation is that the film cover, at lower temperatures polyacetylene, at the elevated temperature of 980°C is actually very fine grained diamond film.

The improved surface trreatment has improved the quality of the diamond grown, as can be seen by comparing the Raman spectra for otherwise very similar conditions, such as fig. 9.5(a) and fig. 9.9(d).

9.3.4 Film Growth at 300W RF Input Power

Although the sample which gave rise to the Raman spectrum of fig. 9.9(d) showed a considerable diamond growth, the quality was still rather poor.

The next parameter to change was therefore the rf in;ut power. Increasing the power to 300W, should, by the curve of fig. 4.7, increase the plasma density by about 20%, thus greatly increasing the atomic hydrogen concentration. This should improve the growth of diamond over graphite, thus improving the quality.

Again, temperature settings for the first run were chosedn to be close to the most successful conditions of the previous experimnets at 250W, and then

varied, both up and down, to investigate the effects of both temperature and power.

9.3.4.1 Scanning Electron Microscopy

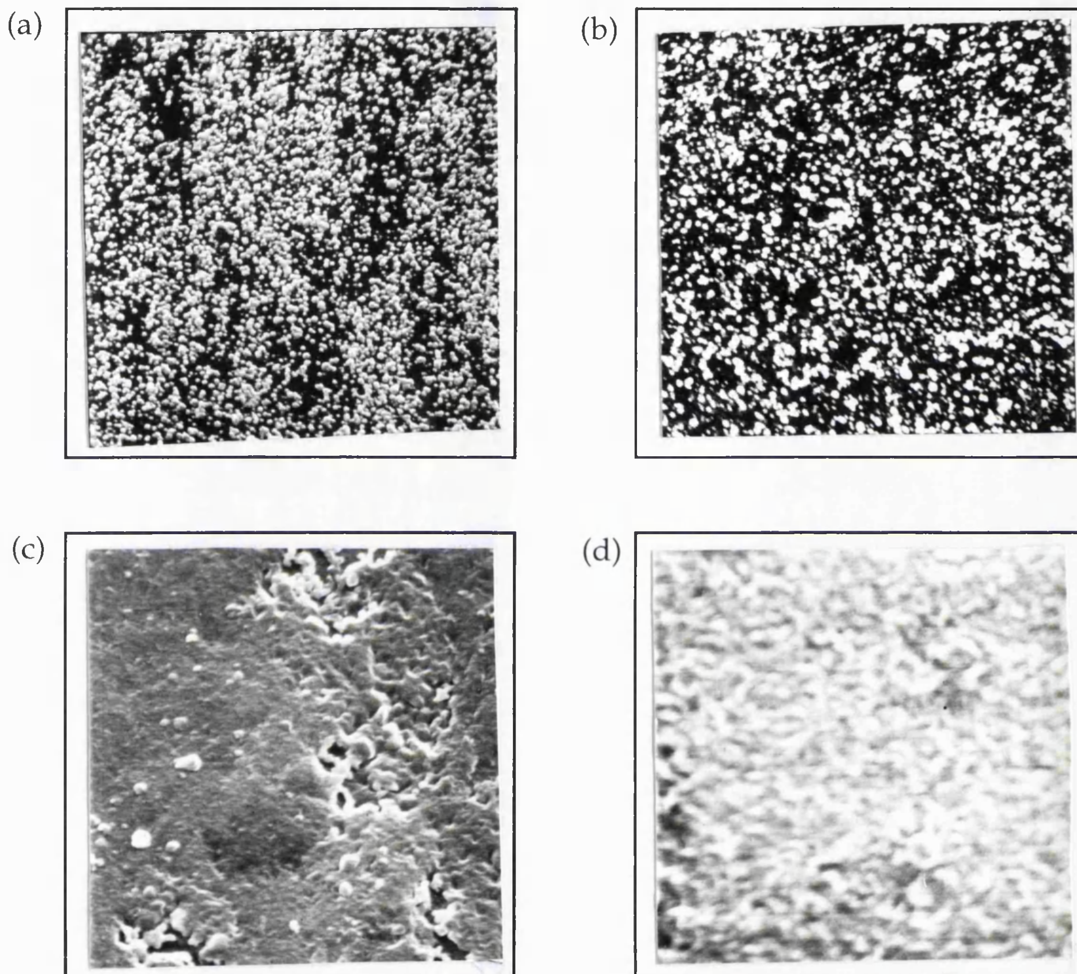

Figure 9.10 SEM photographs of films grown with 300 W RF input power.
(a) 880°C, (b) 935°C, (c) 1000°C, (d) 1080°C

The SEM photographs of figure 9.10 show varying stages of film growth, again as the temperature is increased. At the lowest temperature shown, there is a dense coverage of sharply defined crystallites, which changes as the temperature is increased firstly to a very smooth, fine textured film, and then to a film with an apparently 'rippled' surface. The crystallites grown at 880°C

look like tiny diamonds, but the almost continuous film grown at 1000°C does not look like any commonly grown diamond film. There are almost no individual crystallites visible at this temperature, and none at all at the even higher temperature of 1080°C, where the texture of the film has changed. If the film is composed of tiny crystallites which have merged, then that grown at the higher temperature must be composed of slightly larger such crystallites, which give the film its texture. These films were also subjected to Raman spectral analysis, to investigate their composition.

9.3.4.2 Raman Spectroscopy

The Raman spectra from the samples grown at 300W RF input power are shown in figure 9.11 (a) - (d). They all show a strong diamond line at 1330 or 1331 cm^{-1}, with a small peak at the position of the graphite G line. Thus it appears that both the sharply defined individual crystallites and the continuous film growth are formed of diamond. As the graphite line is 50 times more intense than the diamond line, as discussed above, this means that these films contain less than 0.5% of non-diamond material. In figure 9.11 (d), the spectrum from the more coarsely grained film, the G line is quite sharp with a very clearly defined shoulder at 1620 cm^{-1}, which is due to the very small size of the crystals, as discussed in Chapter 8.

The diamond lines are however quite broad; natural diamond has a very narrow line, of order 2 cm^{-1}. The broadness of these lines can similarly be attributed to the very small size of the individual crystals which form the film [9.3]. If this is indeed the case, then the smoother film grown at 1000°C should produce a broader line than the coarser film grown at 1080°C. This hypothesis is borne out by measurements of the FWHM of the diamond peaks on these spectra, tabulated below.

A Raman spectrum was also taken from the sample grown at 850°C, although the SEM of these crystallites is not illustrated. This spectrum is shown as figure 9.11 (e), and it can be seen that at this lower temperature, even at the higher power of 300W, some polyacetylene lines appear, although there is a very clear and considerable contribution from diamond.

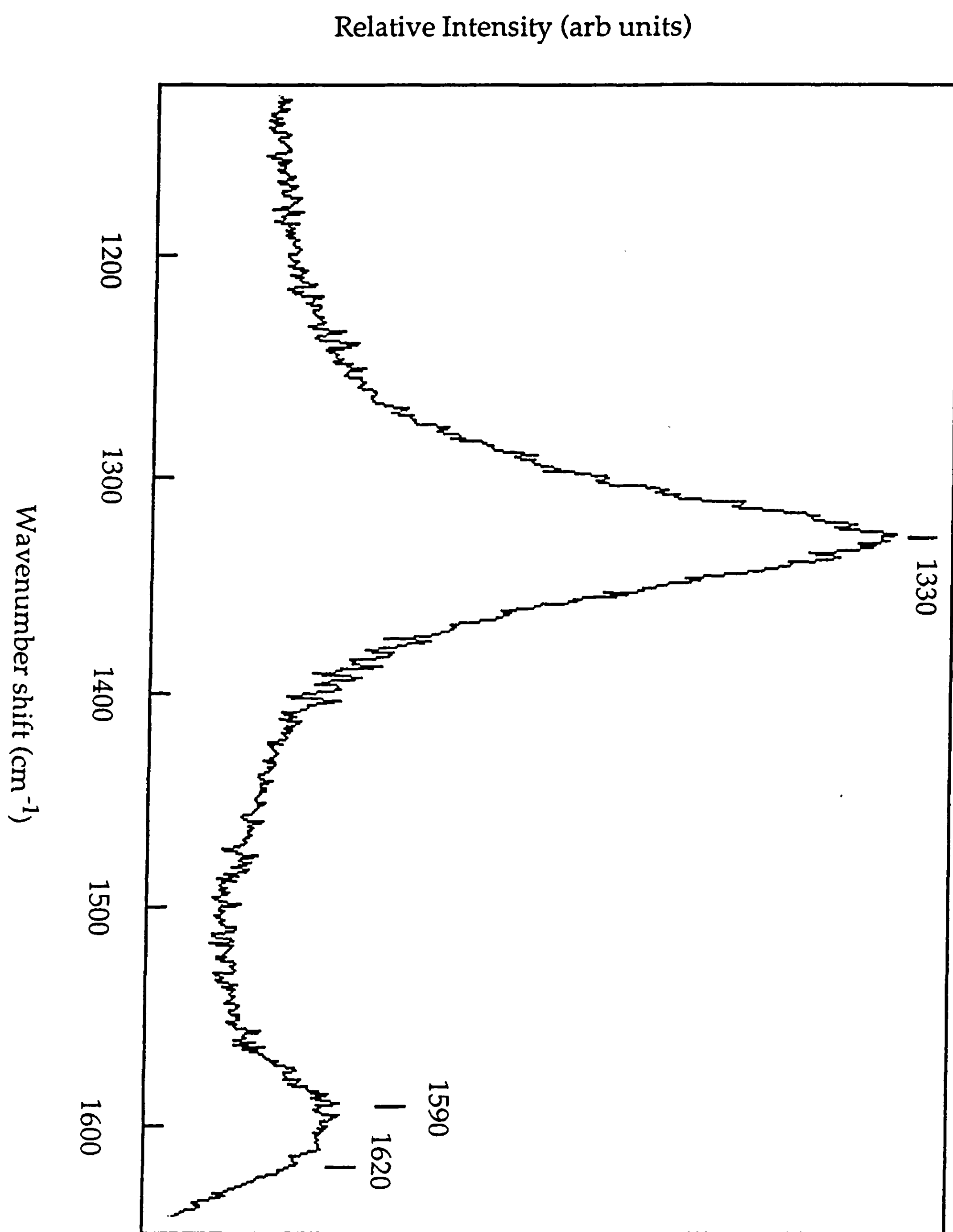

Figure 9.11 (a) Raman spectrum from sample grown at 880°C, 300W

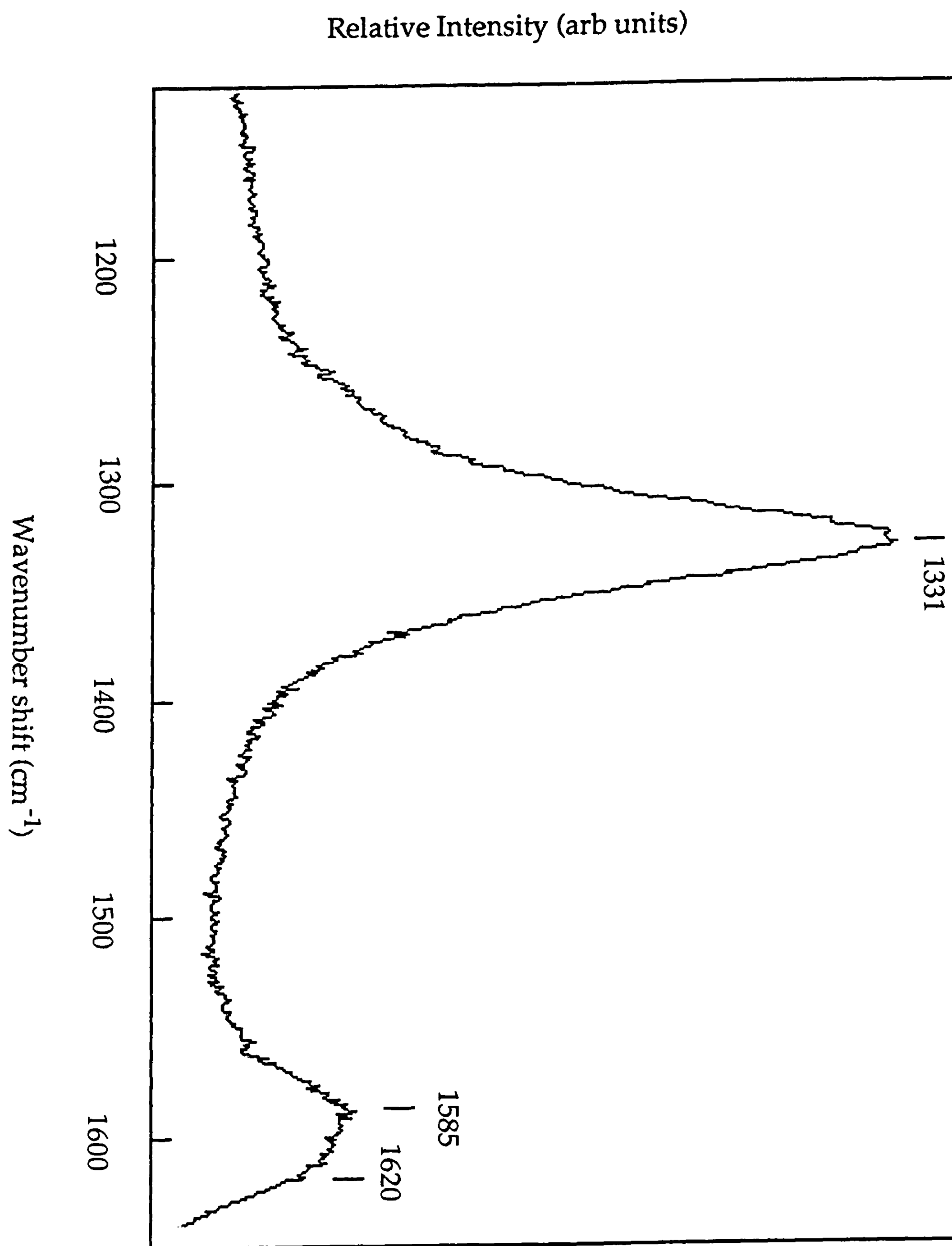

Figure 9.11 (b) Raman spectrum from sample grown at 930°C, 300W

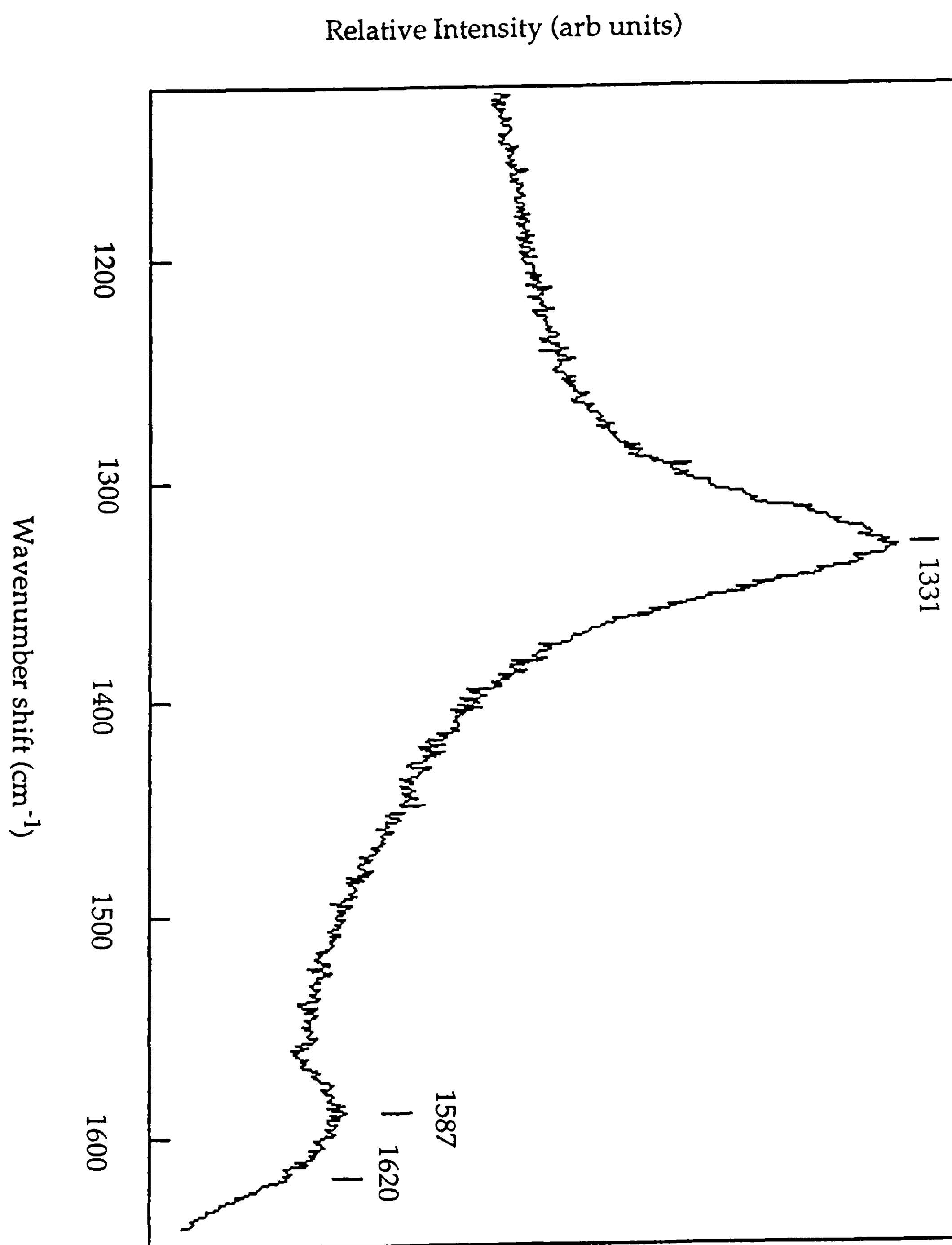

Figure 9.11 (c) Raman spectrum from sample grown at 1000°C, 300W

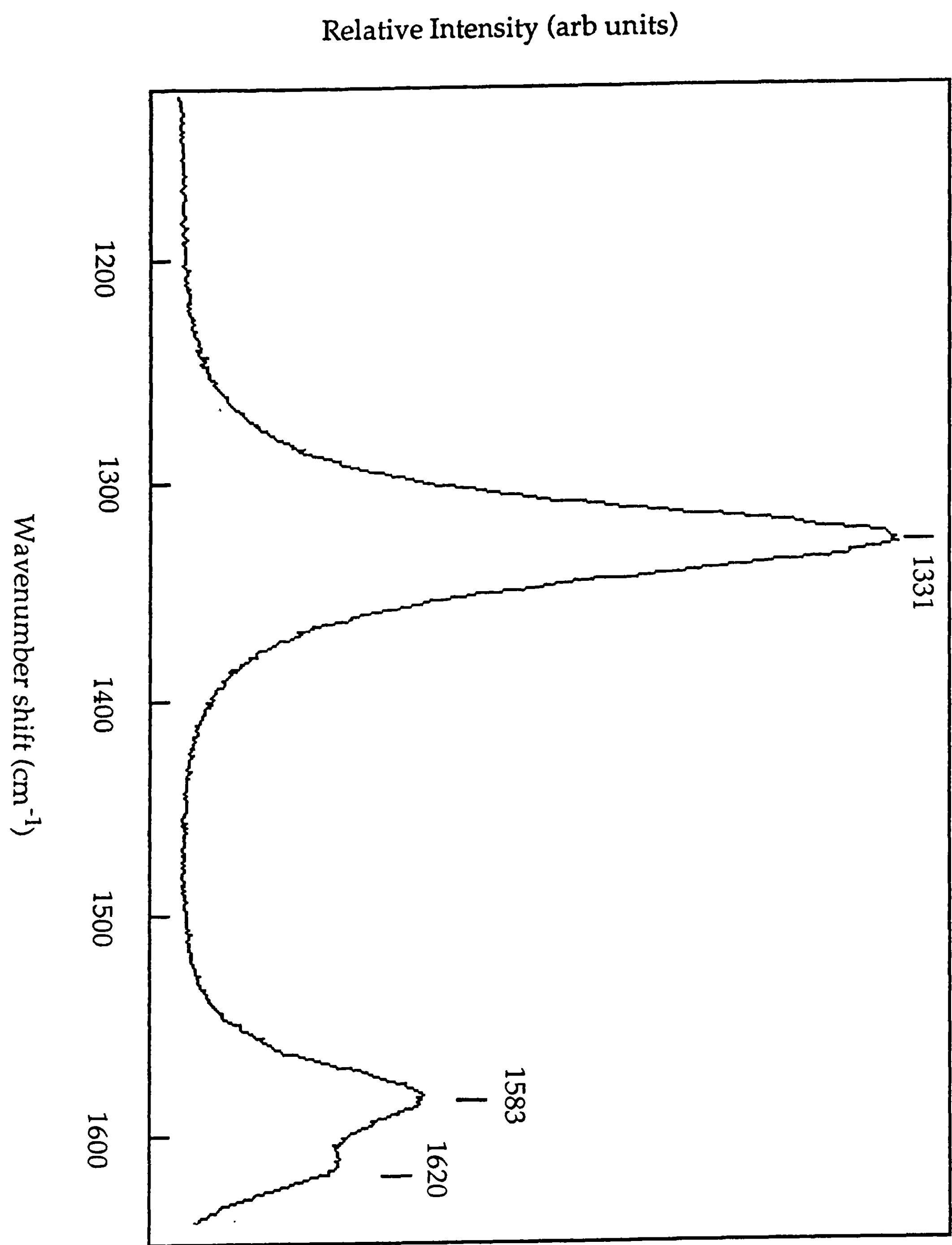

Figure 9.11 (d) Raman spectrum from sample grown at 1080°C, 300W

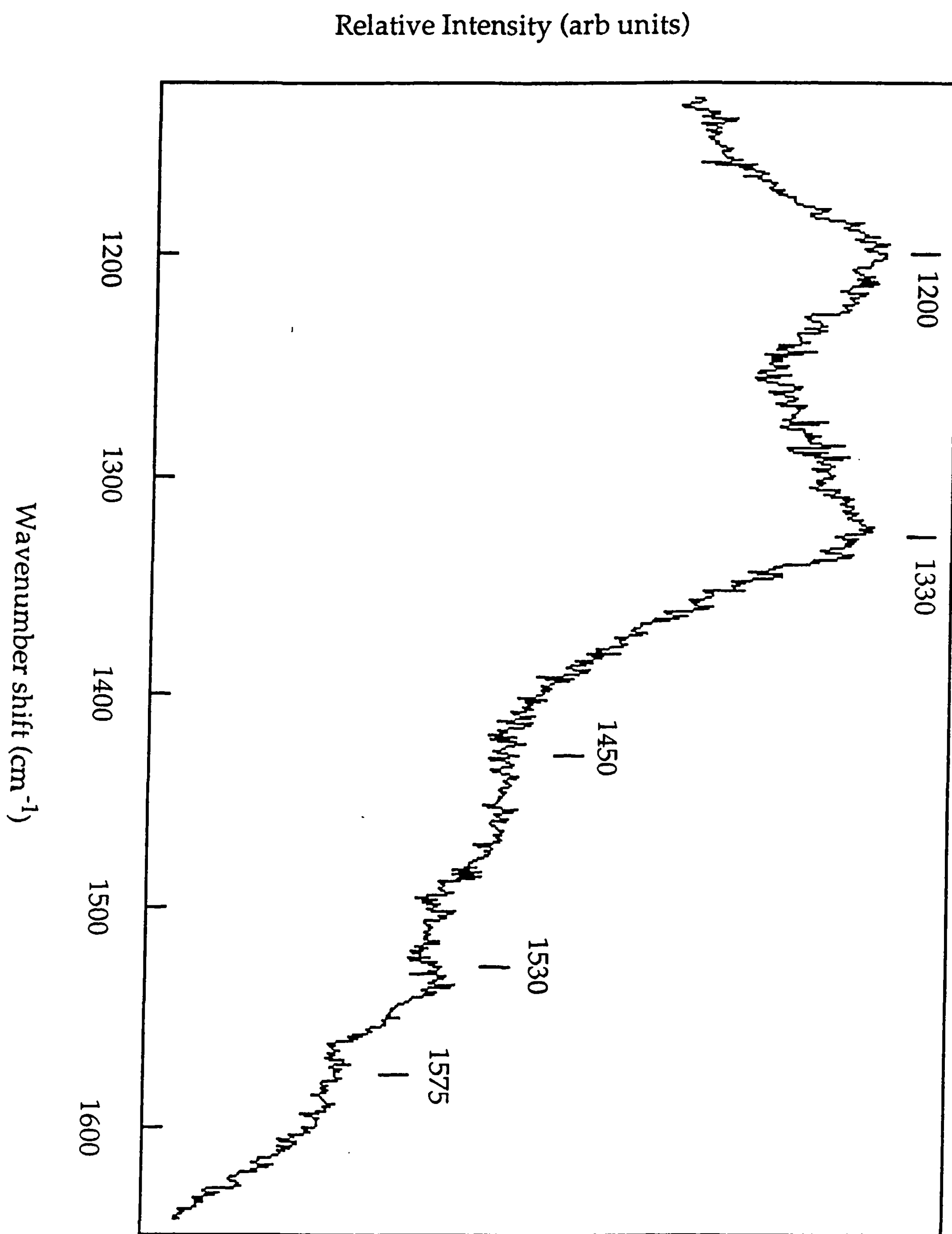

Figure 9.11 (e) Raman spectrum from sample grown at 850°C, 300W

9.3.5 Comparison of Growth at Different RF Input Powers

From the previous discussions, it is clear that both the substrate surface temperature and the input power to the plasma affect the quality of film grown. A comparison of the type of growth obtained at each temperature, with each power is summarised below.

Temperature	250W	300W
860°C	Some evidence of diamond, with much polyacetylene	Much diamond, with some polyacetylene
880°C	Some diamond (more than above), and some polyacetylene.	Strong diamond signal, some microcrystalline graphite, nothing else.
930°C	Some diamond, some polyacetylene, very small amount of microcrystalline graphite.	Strong diamond signal, some microcrystalline graphite, nothing else.
980-1000°C	Strong diamond signal, ($1334cm^{-1}$), small peak at $1440cm^{-1}$ (polyacetylene), and small amount of microcrystalline graphite.	Strong diamond signal, high background, small amount of microcrystalline graphite.
1080°C		Very strong, narrower, diamond peak, small microcrystalline graphite peak, low background.

The defects in the polyacetylene chains due to the presence of C–C bonds of diamond and graphite will strongly affect the Raman frequencies found [9.1]. Thus, although the lines seen here, and attributable to neither

diamond nor graphite, do not fit precisely with the frequencies assigned to poly-$(CH)_x$, they are nevertheless attributable to C–H bonding.

It is clear from the above table that the higher, 300W, RF input power always grows better quality diamond than the lower, 250W, at similar temperatures. At 250W, until the temperature is very high, the diamond signal is almost hidden by the many lines of polyacetylene. Even at the highest temperature employed at this power, 980°C, some evidence of polyacetylene is still seen. However, at an input power of 300W, only at the lowest temperature employed, 860°C, was anything other than diamond and a very small (<0.5%) contribution from microcrystalline graphite observed. This improvement in quality is most likely due to the much higher concentration of atomic hydrogen at the higher RF input power, (see Chapter 8, section 8.3.2).

9.3.5.1 Assessment of Film Quality

One measure of the quality of diamond is the width of the characteristic diamond line, measured as the FWHM (full width at half maximum). A table of these measurements is given below.

Temperature (°C)	RF Power(W)	FWHM (cm^{-1})	Type of Growth
925	250	—	very small crystallites (<0.1μm) with pre-diamond film growth
980	250	80	mostly thin film cover with few very small crystallites
880	300	60	crystallites (~0.2μm)
935	300	55	crystallites (possibly some film)
1000	300	70	smooth, nearly complete film
1080	300	40	rippled film (composed of slightly larger crystallites)

The broadness of all the diamond peaks is mainly due to the very small size of the individual crystals which form the film. The line may also be broadened by defects in the crystals [9.6], and with film composed of such small crystals, dislocations and grain boundaries will be numerous. For crystallites of ~1μm across, the FWHM of the 1332 cm^{-1} diamond line is commonly found to be 15 to 20 cm^{-1} [7.17, 7.18, 7.47]. The crystallites in the film grown here are only 0.1 to 0.2 μm across, and therefore an even broader line is to be expected. It has frequently been noted that the crystal size is very small at the interface, and that as growth of the layer continues, the crystals become larger [7.17]. Thus, the small crystal size in these very thin films is not necessarily a problem. Another aspect of the quality of the film grown is the quantity of non-diamond material incorporated in it. The Raman spectra of these films show only a very small contribution from microcrystalline graphite, and no amorphous phase at all. There is just a very fine grained diamond film.

This is comparable to what can be achieved with bias-enhanced nucleation and a microwave plasma, and is therefore a very exciting result. Diamond film of such high quality has not been grown with an RF plasma before.

9.3.6 Nucleation Density

9.3.6.1 Variation with Temperature

As mentioned in section 9.3.2, the nucleation density was found to depend strongly on both temperature and RF input power to the plasma[9.4]. At temperatures above ~900°C, the crystallites have merged to form continuous film, hence the nucleation density has saturated, illustrated in figure 9.13 .

But at lower temperatures, the effect of substrate temperatue is very marked, a difference of only 100°C making a difference in nucleation density of 2 orders of magnitude. This finding corresponds closely to the results of Fayette *et al* [9.5], who also found an increase in nucleation density of 2 orders of magnitude over a narrow range of temperature, with saturation being reached at 850°C in their study (growth by MWPECVD). The increase in size of the crystallites, as evinced by the narrowing of the Raman line, at higher

temperatures, after nucleation density saturation has been achieved, implies an increase in actual growth rate. This does not appear to be the case at lower temperatures, where the nucleation density is still increasing, as the size of the crystallites grown for the same period of time, is the same. Fayette *et al* [9.5] also found an increase in growth rate with temperature.

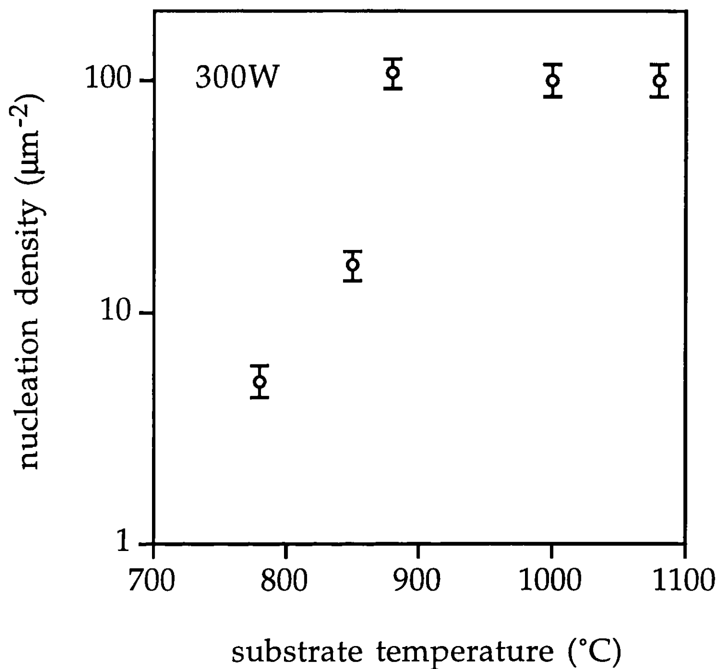

Figure 9.13 Graph showing variation of nucleation density with temperature

9.3.6.2 Variation with Input Power

The nucleation density also depends quite strongly on the RF input power, which affects the quality of the plasma and the gas species activation. From figure 9.14, showing nucleation densities for a range of RF input powers at 880°C, it can be seen that the nucleation density at first increases rapidly with increasing power, but then appears to be approaching a saturation level. This maximum nucleation density is at least as high as can be achieved with bias-enhanced nucleation in MWPECVD systems. This effect is expanded upon below.

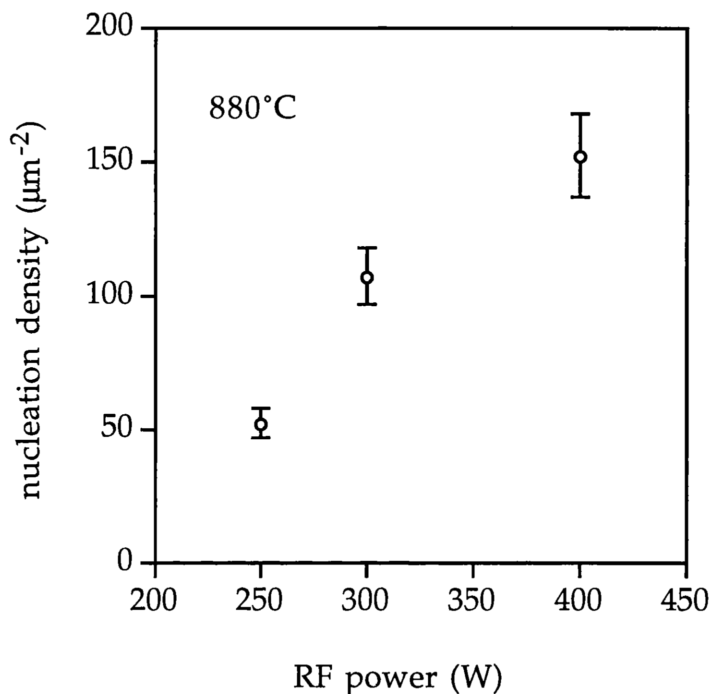

Figure 9.14 Graph showing variation of crystallite density with rf input power

9.3.7 Growth at 400W RF Input Power

As the rate of increase of plasma density with power slows down above 300W, to achieve a noticeable increase the power was increased to 400W. This increase in power above 300W also increases the ion energy, as was noted in Chapter 4. An increase in ion energy could be equivalent to adding a negative bias to the substrate. I was interested to see if indeed the diamond growth would be different under these more extreme conditions.

There was an increase in both nucleation density and growth rate at this higher power, the latter shown by the larger crystal size, illustrated in figure 9.15. There was also a considerable change in the quality of the growth.

The samples grown at 400W RF input power were then subjected to Raman spectral analysis. The spectra produced are shown as figures 9.16 (a) and (b). Both show the 1330 cm^{-1} diamond line. (These spectra were taken using an Ar (green) laser beam.) The spectrum from the sample grown at

880°C shows both a broad band centred on 1330 cm^{-1}, from the diamond crystallites, and also broad bands centred on the D and G lines of polycrystalline graphite. These bands are all of approximately the same intensity, which actually means that about 2% of the growth is graphitic. This is rather more than at the lower input power of 300W. A probable explanation for the increase of the graphitic signal, is the increased ion impact energy at this RF power, which could be graphitising the surface of the diamond crystallites after they have formed [7.1].

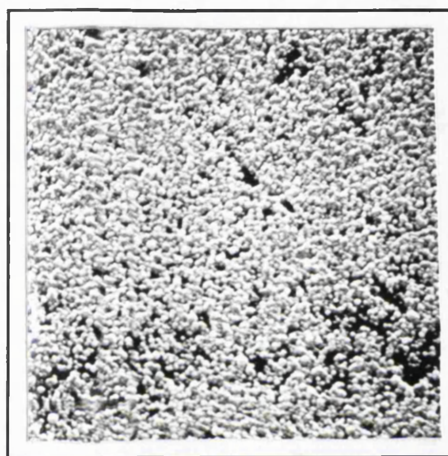

Figure 9.15 SEM photograph of crystallites grown at 800°C, 400W

The spectrum from the sample grown at 800°C, (figure 9.16 (a)), which looks like a dense coverage of well formed crystallites, as shown in figure 9.15 is, remarkably, similar to that from an unscratched, biased at -275V, microwave plasma enhanced CVD sample, grown at AEA Technology, Harwell, shown as figure 9.17. This implies that the growth conditions induced by the use of this higher power are similar to those produced by biasing the substrate. Putting a bias on the substrate is often used to enhance the nucleation of diamond on non-diamond substrates, and encourage oriented crystal growth. In fact, the crystals grown here also seem to have a clear orientation, but as the substrate surface was Si(111) and was lightly polished with diamond powder, they are not as strongly oriented as they could be, and neither is the orientation such as to produce the smoothest film. Highly oriented diamond film on Si(100) surfaces is likely to display superior electronic properties to irregular, variable films.

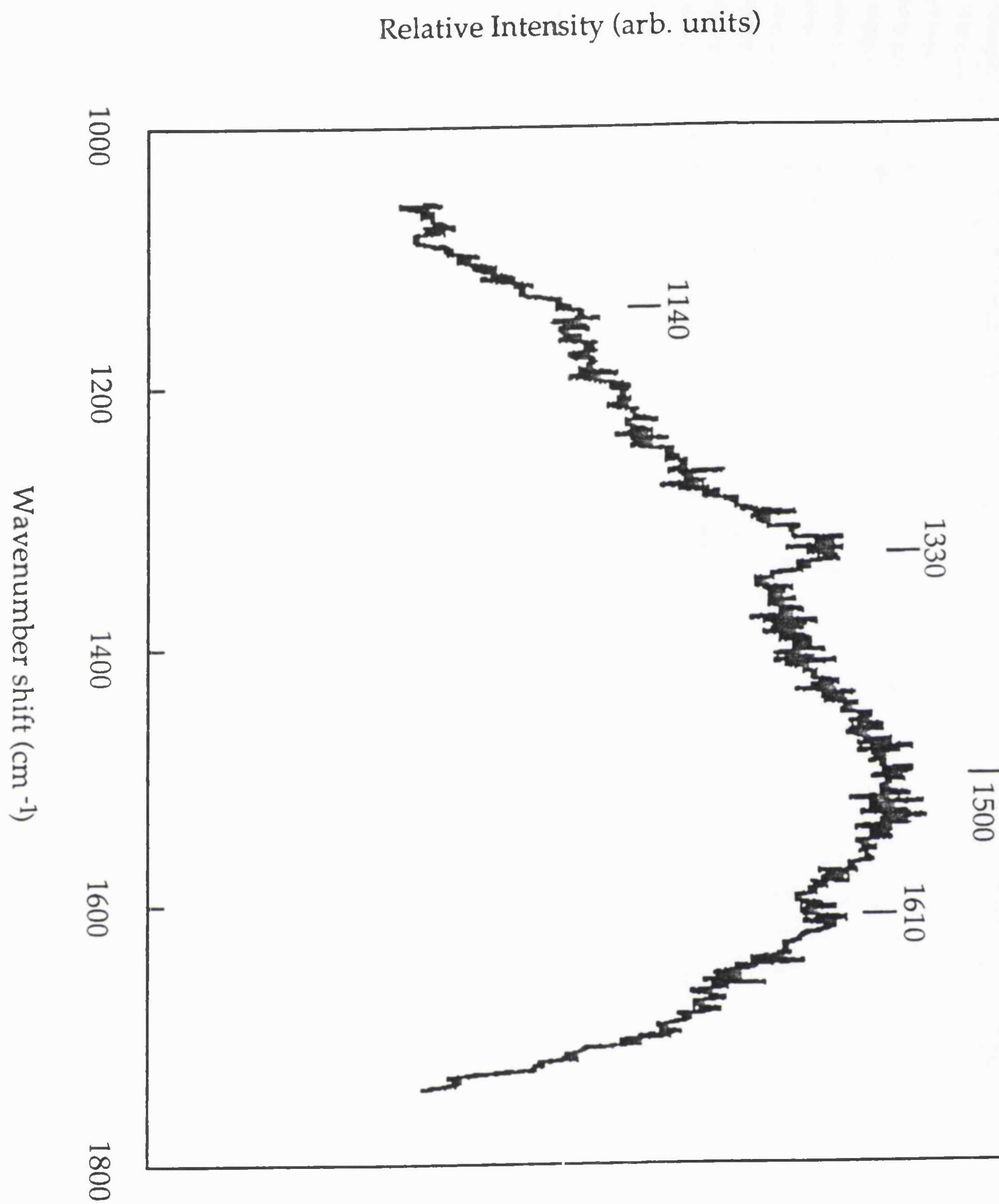

Figure 9.16 (a) Raman spectrum from sample grown at 800°C, 400W

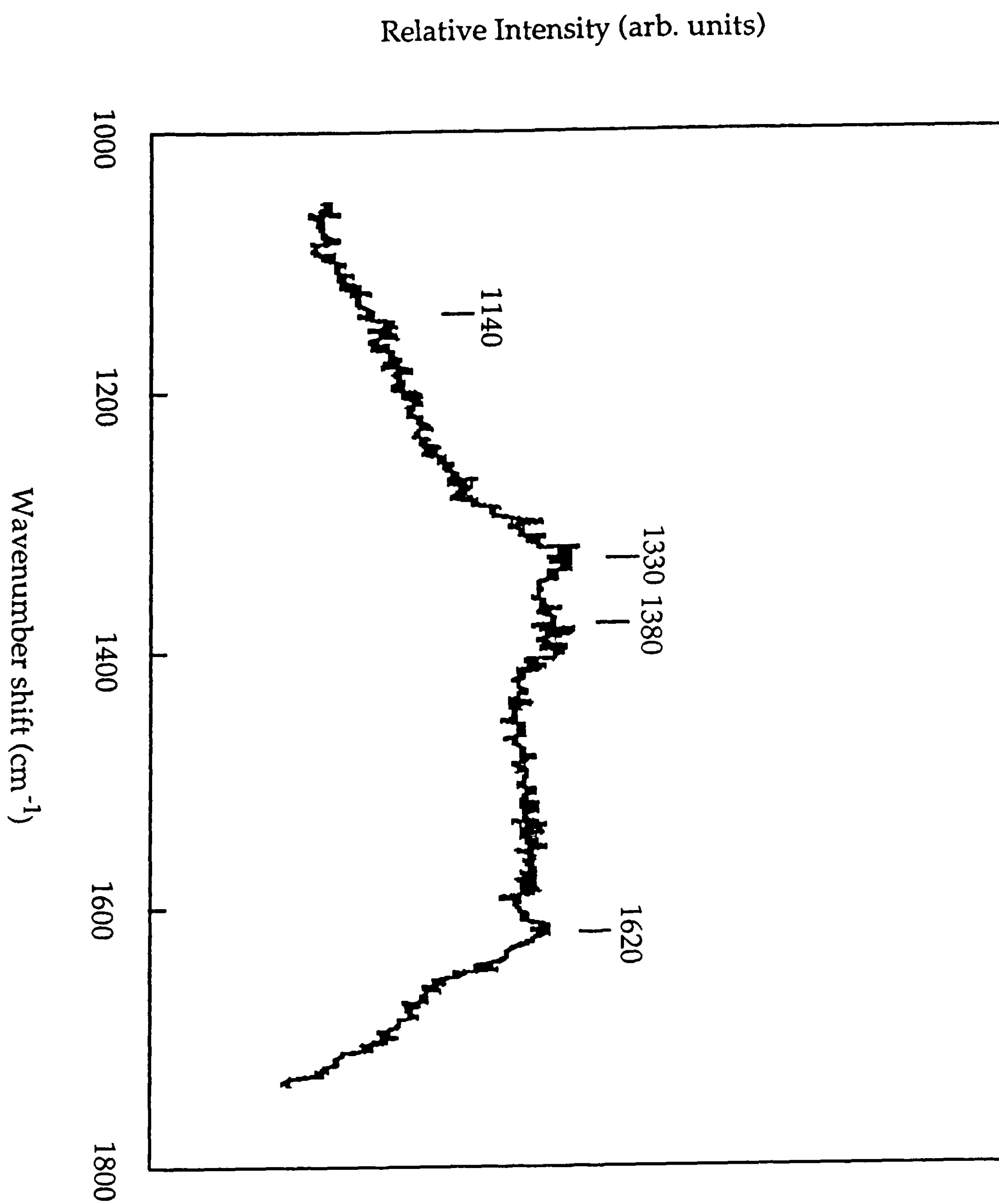

Figure 9.16 (b) Raman spectrum from sample grown at 880°C, 400W

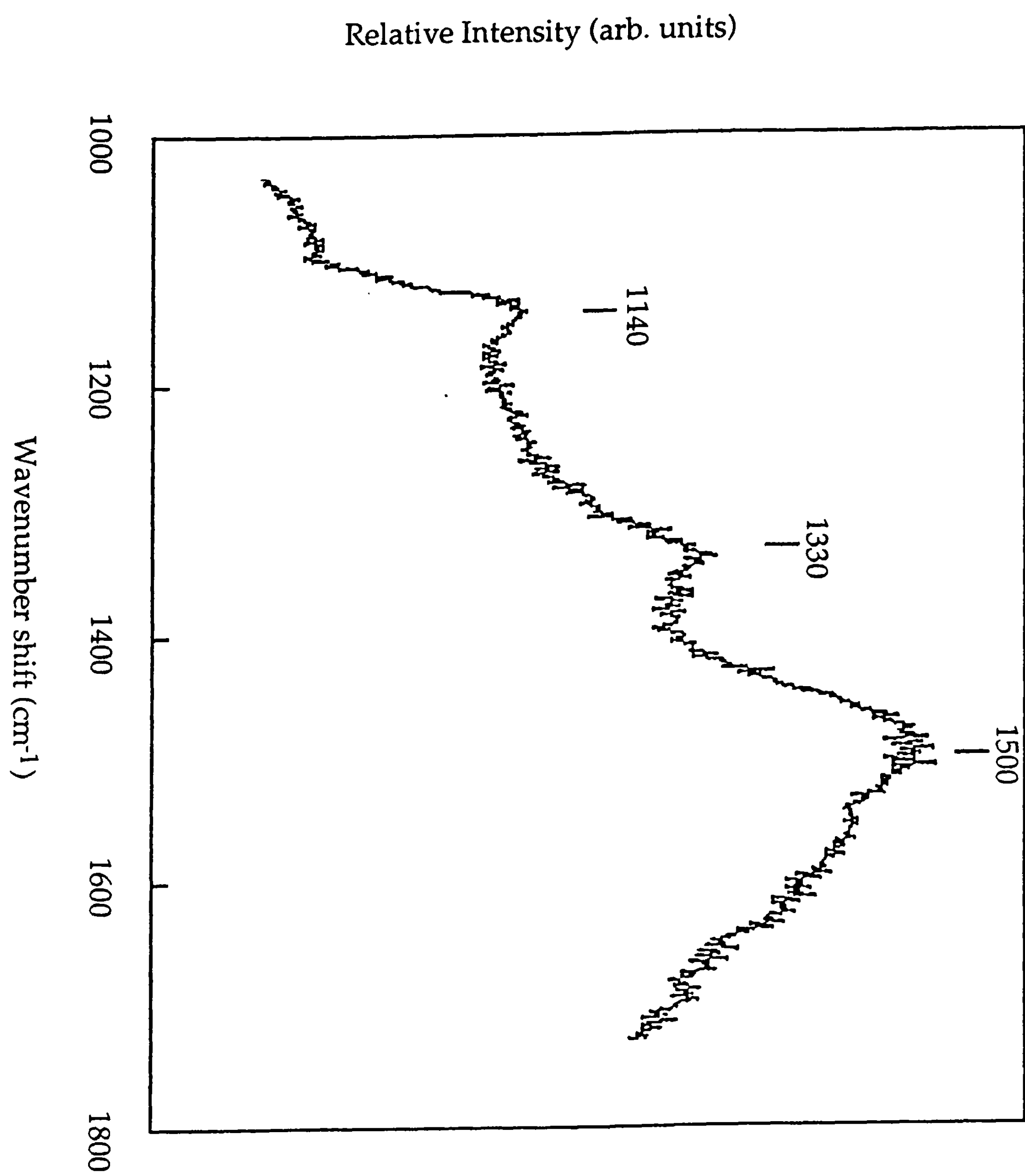

Figure 9.17 Comparison spectrum from microwave grown "bias-enhanced" nucleation

The density of individual crystallites in the diamond film grown here with the RF plasma source is in the range of $1 \rightarrow 1.5.10^{10}cm^{-2}$. The nucleation density of the very fine-grained continuous film can be estimated from the assumed size of the crystallites which make up the film, (derived from the FWHM of the diamond line) and the assumption that they have grown together, and so the separation of the individual grains must be approximately equal to their diameter. This nucleation density is very comparable to that achieved with bias-enhanced nucleation as discussed in Chapter 7, section 7.2.4.

9.3.7.1 Comparison of this work to Bias-enhanced Nucleation (BEN)

It has been shown that the nucleation density of diamond crystallites depends strongly on the RF power input, and that the densities achieved ($>10^{10}$ cm^{-2}) are comparable with the best achieved with MWPECVD, with BEN. However, nucleation on a pristine surface has not been attempted.

It has also been demonstrated that the quality of diamond film growth depends strongly on the RF power input. Although a higher power should mean a greater atomic hydrogen concentration, this may be offset by the higher ion impact energy.

It was shown in Chapter 4 that the plasma density continues to increase almost linearly as input power increases, but that the electron temperature reaches a maximum at about 300W input power. The apparent ion energy, as demonstrated by the "stopping potential" (Chapter 4), increases with increased input power. It is therefore clear that the relationship between plasma quality and input power is far from simple.

However, the increase in nucleation density, together with the fall in film quality as the input power is increased from 300W to 400W mimics the effects of applying a negative bias to the substrate during MWPECVD "BEN". The similarity of the micro-Raman spectra from the high power nucleation and BEN support this claim.

Since it was possible to grow very high quality diamond film with an input power of 300W, with a reasonably high nucleation density, and it was also found that diamond-containing film, with a very high nucleation density, was grown with an input power of 400W, under conditions which appeared to

be similar to BEN, from the evidence of the Raman spectra, there seems to be an excellent prospect for using this technique to grow diamond film of electronic quality. Thus the many advantages of utilising RF excitation rather than microwave can now be exploited in the development of high grade diamond film.

Summary

Until now it has not been possible to grow good quality diamond film by means of RF plasma enhanced CVD, but only by means of microwave PECVD.

However, as the plasma characteristics of this novel source are so very different from those of a conventional RF plasma reactor, and so similar to those required for the promotion of diamond growth, i.e. amicrowave plasma, a series of experiments were undertaken to verify the feasibility of using this technique.

Since the main purpose was a feasibility study, the standard gas mixture of 1% methane in hydrogen, known to be successful in many other growth methods was used, rather than also varying the gas mixture, which would at this stage have added unnecessary complications to the study. Other parameters, such as gas pressure and substrate surface temperature are less clearly defined. A wide range in both of these have been shown to succeed in promoting the growth of diamond film, under varying plasma conditions. Also, the input power which would be needed was completely unknown, since no plasma source of this type had previously been used for this application. Thus, all these parameters were investigated for the optimum values, and their general effect on the growth of diamond film.

The first tests were done at the lowest power known to create a reasonable concentration of atomic hydrogen, namely 200W, and at a high pressure as utilised in microwave plasmas. A series of experiments were then performed with a range of substrate surface temperatures, but without success. Some non-graphitic material was grown, related to diamond precursors, but not actually diamond.

The power was then increased to 250W, and the pressure reduced, to increase the atomic hydrogen concentration, and this was highly effective. Diamond crystallites were grown, although in a matrix of non-diamond material, graphite and polyactylene.

A further series of experiments was undertaken, with an improved surface pretreatment, optimising the surface temperature, and the RF power input was also increased, first to 300W and then to 400W, to optimise this parameter as well, and thereby to improve the quality of diamond film grown.

These culminated in the first high quality diamond film to be grown with RF plasma enhanced CVD, as evidenced by Raman spectrosopy. It was found that at a RF power of 400W, a nucleation layer similar to that produced by bias-enhanced nucleation formed, whilst at 300W, very high quality diamond film, with very little graphite (<0.5%) and no amorphous carbon content, was grown.

Thus it has been clearly demonstrated that this technique can be used to grow diamond film, of very high quality.

9.4 References

9.1 S. Lefrant, E. Mulazzi and C. Mathis *Phys. Rev. B* **49** 13400 (1994)

9.2 J. Beckman, R. B. Jackman and J. S. Foord *Dia. & Rel. Mat.* **3** 602 (1993)

9.3 L. Fayette, B. Marcus, M. Mermoux, L. Abello and G. Lucazeau *Dia. & Rel. Mat.* **3** 438 (1994)

9.4 R. B. Jackman, J. Beckman and J. S. Foord *Mat. Sci. and Eng. B* (submitted)

9.5 L. Fayette, M. Mermoux and B. Marcus *Dia. and Rel. Mat.* **3** 480 (1994)

9.6 P. K. Bachmann and D. V. Wiechert *Dia. and Rel. Mat.* **1** 422 (1992)

9.7 E. Fitzer and F. Rozploch *High Temperatures–High Pressures* **20** 449 (1988)

CHAPTER 10: CONCLUDING THOUGHTS

The advantages and disadvantages of currently available systems, for the etching of electronic materials, both the traditional wet etching, and the more recently developed dry etching, in all its varieties, were studied. Similarly, currently available systems for the deposition of these materials were also studied. Many of the most modern systems use plasmas or beams derived from plasmas, and the properties of these plasmas affect strongly the performance of the system. The theory of plasma generation and of source construction, together with currently available designs were therefore also studied. Thus the specifications for the ideal plasma and broad beam ion source were developed. These are: high plasma density, leading then also to high beam flux, and ultra-low ion beam energy, below the threshold for induced damage, which for GaAs is as low as 20eV.

A novel capacitively coupled, radio-frequency plasma and broad beam source was designed and built, to attempt to meet these specifications. This source does not have parallel plate electrodes, as is usual in capacitively coupled sources, but ring electrodes which surround the plasma chamber. It is also magnetically enhanced. In the initial characterisation studies, using only argon, it appeared to meet these specifications very closely. The plasma density was found to be $\sim 10^{11}$ ions/cm^3, the beam current density was $\sim$1mA/cm^2, and the ion energy was between 20eV and 25eV.

Etching of GaAs was then performed with this novel source, in two etching configurations, reactive ion beam etching (RIBE),where chlorine was used in the plasma chamber to create a beam of reactive chlorine ions, and chemically assisted ion beam etching (CAIBE), where argon was used in the plasma chamber, to create an ultra-low energy beam of inert argon ions, to promote etching by chlorine gas, separately introduced. GaAs is an important III-V semiconductor material, for optoelectronic applications, but is easily damaged by energetic ion bombardment.

The etch depths achieved were not very great, less than 100nm per hour, but for state of the art optoelectronic applications this is actually not a disadvantage, as etching depths of only a few mono-layers are often required. Thus a slow etch rate allows for greater control of the exact etch depth.

The etched surfaces were then characterised by scanning electron microscopy, and appeared to be clean and smooth. The anisotropy of the etch was not however as good as can be achieved with higher energy sources.

A more sensitive test of the surface condition, and also of some underlying damage, is to characterise Schottky diodes formed on the surface. The barrier height in particular, is extremely sensitive to the surface states. This was performed, and the characteristics of the diodes were compared with those of diodes formed on an unetched sample from the same wafer. All the diodes were virtually identical. This demonstrates that the source is indeed capable of performing damage-free etching, as required. This was in contrast to all other dry etching techniques, which all introduce considerable damage.

However, the source also had a propensity to etch its own lining, depositing the silica products as a lightly adhering contamination layer. Thus, although the contamination was easily removed, it was not considered an ideal etcher. Some design changes would be required to improve its performance in this respect, such as a change to the magnetic configuration, to keep the plasma away from the lining, and maybe forming the lining from a material more resistant to etching by chlorine.

Diamond is a most interesting material, with properties of thermal conductivity, hardness, chemical resistance and electronic band-gap which are all extreme. Its applications in the field of electronics, in high frequency optical detectors and emitters, and high temperature electronic devices are only just beginning to be realised. The standard method for growing thin film diamond for electronic applications is microwave plasma-assisted chemical vapour deposition (MWPECVD). A high concentration of atomic hydrogen is required in the plasma, with a very dilute concentration of hydrocarbon ($\leq$1%), commonly methane. However, microwaves suffer from several disadvantages: the dimensions of the most active region of the plasma, the "plasma ball", are quite small, and depend on the wavelength, thus scaling up is complicated and costly; the plasma is often difficult to strike; microwaves are hazardous, thus the equipment must be shielded. Radio frequencies suffer from none of these disadvantages. The volume of uniform plasma which can be sustained is greater than any present-day equipment would need, due to the much longer wavelength. Radio-frequency waves are not known to present any hazard either. Inductively coupled RF plasma-enhanced CVD of diamond has been moderately successful, but very high input power is required, and substrate

surface temperature is difficult to control, as the substrate heats inductively. The only problem up until now has been that good quality diamond could not be grown with capacitively coupled radio-frequency plasma-assisted chemical vapour deposition. Capacitively coupled radio-frequency plasma-assisted CVD has only been used for the growth of diamond-like carbon (DLC), an amorphous hydrogenated carbon film, which has some properties of hardness, low friction, insulation etc. similar to those of diamond.

Since the plasma characteristics from the novel source used in this study are very similar to those required for diamond growth, a series of experiments were undertaken to demonstrate the feasibility of this novel arrangement for diamond growth.

At first, it was surmised that it might be possible to utilise the self-etching, and create a plasma of the correct constituents using a graphite lining and only hydrogen gas. This imaginative route was unsuccessful, as the source was too efficient at self-etching. A very high concentration of hydrocarbons, far in excess of the $\leq 1\%$ required was found to be present in the plasma. Also, much of the hydrocarbon formed was of too heavy a type. Diamond apparently only grows with single or double carbon atoms as source, such as methane or acetylene. However, it was found that the source produced a very high proportion of atomic hydrogen, which, as stated above, is a most important factor in the promotion of the growth of diamond over graphite.

A conventional 1% methane in hydrogen gas mixture, known to be successful in other diamond growth methods, was then used in the source, cleaned free of carbon. At an input power of 250W some diamond crystallites were grown. Conditions of power and substrate surface temperature were then varied to find the optimal values of these parameters.

It was found that at an input power of 300W very high quality continuous diamond film could be grown, and with an input power of 400W a nucleation layer very similar to that produced by bias-enhanced nucleation could be grown.

This novel design of a magnetically enhanced, capacitively coupled radio-frequency plasma source, seems to have solved many of the problems inherent in more conventional designs.

Because of the similarity in Raman signatures between the growth at high power (400W) and a bias enhanced nucleation, it would be interesting to

see if the source would promote nucleation of diamond on a pristine silicon surface.

Since biasing is the most successful technique so far in the growth of highly oriented thin diamond film, this development, if successful, could lead to this novel source also growing highly oriented film. This type of film is the most useful to date for electronic applications, having a much higher carrier mobility than randomly oriented thin film, up to five times higher.

However, some further changes to the design would be needed before such speculative work could be embarked on. Prolonged use of the source has revealed some problems, chiefly in the design of the housing. At present, the entire source is, in effect, immersed in the gas, although the plasma is only struck in the expected chamber. But, as the entire system is heated by the plasma, to well above 100°C inside, contamination effects have been found on the outside of the source, around the electrodes and electrical connections. These have affected subsequent operation of the source, which has had to be removed and cleaned between experimental runs. In the long run, this would not be a selling point for the system. A new housing should be designed to isolate the outside of the source from the plasma chamber. Such further development of the source, to prepare it for an attempt at the growth of high quality diamond film, would probably be an entire further project in itself.

However, I am sure that if these improvements could be made, such a source as this would have a future in the field of thin film diamond growth. The present source was built at a cost of ~£10 000, and a new, improved source could doubtless be built for a sum of the same order of magnitude. A newly developed microwave plasma-assisted CVD system, for 8" wafers, using a lower frequency than the present standard in order to get the larger volume, costs ~$250 000! Thus, RF plasma sources could have a genuine commercial future.